NON-LEGGED LOCOMOTION ON COMPLEX 3-D TERRAIN AND WET FLOWABLE SUBSTRATES

by
Divya Ramesh

A dissertation submitted to The Johns Hopkins University in conformity with the requirements for the degree of Doctor of Philosophy

Baltimore, Maryland
October 2024

Abstract

Animals can traverse any complex 3-D terrain and substrate by modifying their primary locomotion strategy or transitioning to other strategies. Robots, unlike animals, often struggle to traverse similar environments due to lack of understanding of robot-obstacle/substrate interaction to generate propulsion. Understanding this interaction will help develop control strategies for robots to locomote similarly to animals. Snake and amphibious fish locomotion are excellent for traversing complex 3-D terrains and wet flowable substrates respectively.

Snakes can successfully traverse such terrains via 3-D body bending to generate the right propulsion. Snake robots still struggle to traverse such terrains due to lack of understanding in controlling 3-D body bending to push against obstacles to generate and control propulsion. Previous studies show that generalist snakes likely sense body-terrain contact forces via tactile sensing to adjust body bending in real-time. We took the robophysics approach to understand snake locomotion on complex 3-D terrain due to lack of knowledge of tactile sensing. We developed a sensorized snake robot capable of 3-D body bending and tactile sensing. We allowed this robot to traverse an obstacle using vertical bending and showed that it is useful for systematic studies due to high repeatability.

Despite challenges in traversing wet flowable substrates due to variable wetness, amphibious fishes can easily adapt to such variations via body and fin adjustments with substrate interaction. To understand how locomotor morphology, control, and kinematics permit performance, quantification of locomotor-substrate interaction and how propulsive forces are generated are necessary. Despite several studies on dry, wet, and saturated sand, only few animal studies focused on mud with no study in

interaction mechanics yet. We developed tools and methods to prepare, control, and maintain mud with different strengths similar to sand. We performed systematic studies of mudskipper and ropefish, and a preliminary study of bichir moving on different mud strengths with each animal representing a distinct strategy used by amphibious fishes on land. All three fishes had more sinkage and contact length as mud weakened. Mudskipper used its tail to propel against weaker mud. Bichir and ropefish vertically lifted some body sections likely to reduce drag on stronger mud.

Keywords: Locomotion, amphibious fish, snake, bio-inspired robot, robophysics

Primary reader and thesis advisor

Dr. Chen Li
Associate Professor
Department of Mechanical Engineering
Johns Hopkins University, Baltimore MD

Secondary readers

Dr. Jeremy Brown
Assistant Professor
Department of Mechanical Engineering
Johns Hopkins University, Baltimore, MD

Dr. Sandy Kawano
Assistant Professor
Department of Biology
George Washington University, Washington, DC

This thesis is dedicated to my family, partner, 4 legged one tail companion, and friends

Acknowledgment

I am extremely grateful to have worked with my advisor, Prof. Chen Li, during my Ph.D. Despite my coming into the program with minimal experience in Mechanical Engineering, he went to great lengths to help me cultivate my mechanical intuition. I cannot thank him enough for training me to be an independent researcher, a better communicator, and a good mentor. It has been a rewarding experience working with him and I am thankful to have him as my advisor.

I would like to thank Prof. Noah Cowan for teaching foundational courses that helped my research and providing constructive feedback for my research. I would like to thank Prof. Jin Seob Kim, Prof. Marin Kobilarov, Prof. Yannis Kevrekidis, Prof. Simon Leonard, and Prof. Enrique Mallada. The classes I have taken with them were not only interesting but also helped my intellectual growth. I would like to thank Prof. Feifei Qian for her support and for helping me navigate my Ph.D. journey.

Working in the Terradanamics lab provided me with an opportunity to work with many wonderful people. I am extremely grateful to Dr. Qiyuan Fu and Dr. Ratan Othayoth for guiding and mentoring me through my Ph.D. research. I would like to thank Dr. Yaqing Wang, Eugene Lin, Gargi Sadalgekar, Dr. Qihan Xuan, Kangxin Wang, Eric Lara, Kapi Ketan Mehta, and many others for their help in research and life. I would like to thank all of my mentees throughout my Ph.D. that have helped me learn and grow as a mentor. I wouldn't have been able to accomplish my goals without their help in various aspects of my research. Special thanks to Qiyuan, Gargi, and Yaqing for their help with animal care. I would also like to thank my lab members for taking care of the animals. Without their help with animal care, I wouldn't have been able to perform experiments with the animals.

I would like to thank my committee members Prof. Jeremy Brown and Prof. Sandy Kawano for their support and reading of my dissertation. I also thank Prof. Noah Cowan, Prof. Yannis Kevrekidis, Prof. Simon Leonard, Prof. Yun Chen, and Prof. Avanti Athreya for examining me at my Graduate Board Oral (GBO) exams. I would like to thank Prof. Noah Cowan, Prof. Jin Seob Kim, and Prof. Gretar Tryggvason for examining me at my Departmental Qualifier Exam (DQE).

I thank the academic staff at the Department of Mechanical Engineering and Laboratory for Computational Sensing and Robotics, especially Mike Bernard, Kevin Adams, Lorrie Dodd, Ashley Moriarty, Alison Morrow, and John Soos for their academic and logistical support during my Ph.D.

I would also like to thank the funding sources for Terradynamics Lab. My research would not have been possible without the funding that Chen and the lab received from the Arnold and Mabel Beckman Foundation Beckman Young Investigators Award, a Burroughs Wellcome Fund, Career Award at the Scientific Interface, a Johns Hopkins University Catalyst Award, the JHU Whiting School of Engineering start-up funds, and the Johns Hopkins University Bridge Grant.

I would like to thank my friends who have been my emotional support during my Ph.D. and helped me through my tough times, especially during the pandemic. Parmi Thakker, Tarana Kaovasia, Srushti Singh, Shivaanee Kothavale, Siddharth Kothiyal, Shreyash Kumar, and Samarth Marudheri offered me immense advice and support during my struggles in the initial years of my Ph.D. Prashanth Prakash and Rachit Saluja helped me vent during difficult times and provided emotional support. Deeksha Shama, Aditya Venkatraman, Kapi Ketan Mehta, and Arnab Chatterjee helped me get away from research, be my emotional support, and make wonderful

memories together. Lydia Al-Zogbi, Kaitlynn Pineda, Keshuai Xu, Benjamin Killeen, Jakub Piwowarczyk, Justin Ma, Arnab Chatterjee, and Michael Wilkinson were my support systems during my post-pandemic years at Hopkins. Without them, I would not have been able to complete the last stretch of my Ph.D. journey. A special thanks to my best friend, Lydia Al-Zogbi, for being there for me during the toughest and happiest times of my Ph.D. journey.

I couldn't have made it without the immense emotional support from my feline and canine friends: Fletcher Ramesh, Alpaca Xu, Fifi, Fili Pineda, Mr. Fitzwilliam Darcy, Casval, and Artesia. I am immensely thankful to have Buddy Barnes Ramesh in my life, without his happy face and wagging tail that I get to see every day when I go back home, I wouldn't have had the motivation to finish my Ph.D.

Ravi Shankar, my partner, has been moral support through the final years of my Ph.D. I am thankful to have met him during this journey and to have him support me during the difficult times. Finally, I would like to thank my family: my parents, Dr. Savithri Ramesh and Dr. Ramesh Ardhanari, and my twin sister, Rachita Ramesh. Without their constant encouragement and advice, I wouldn't have been able to make it to where I am today.

It is what it is.
Just go with the flow.

– Divya Ramesh

Table of Contents

List of Tables

List of Figures

Chapter 1

Introduction

1.1 Motivation and overview

The natural environment animals regularly interact with is often complex. It can be uneven terrain with boulders and rocks, terrain filled with twigs and tree branches, and substrates such as snow, boulders, pebbles, gravel, sand, silt, and clay (Fig. 1.1). Substrates such as boulders and pebbles are considered uneven terrain if their size is comparable to small animals (Fig. 1.1D). Substrates with particles that flow when

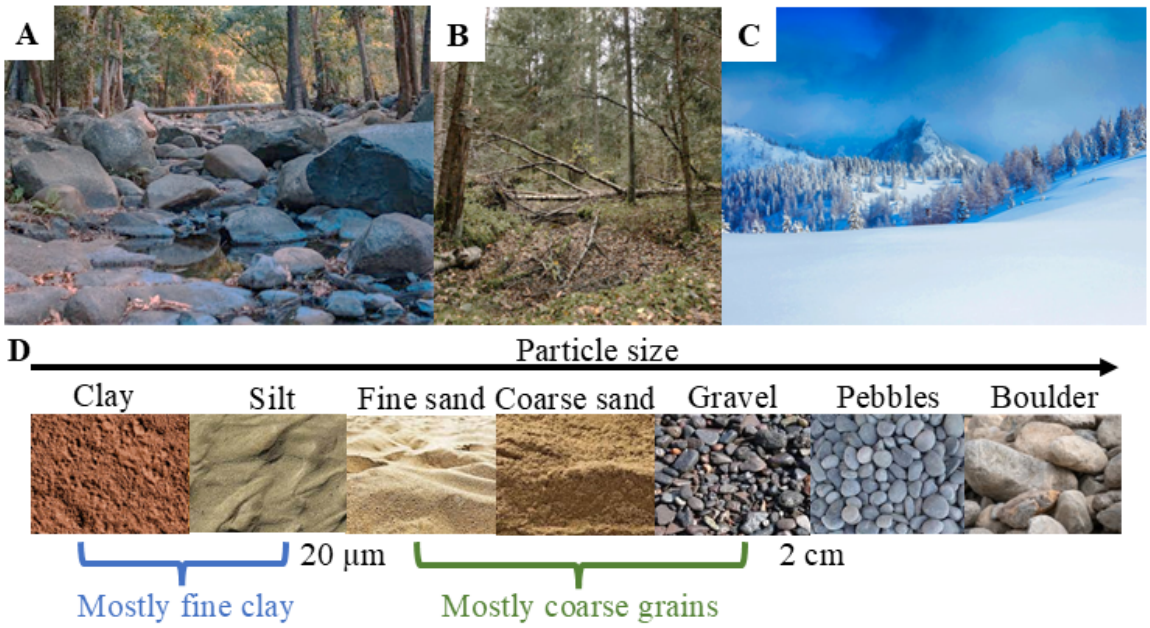

Figure 1.1: Natural environment and substrates. (A) Uneven terrain filled with obstacles such as rocks and boulders. **(B)** Terrain with twigs and tree branches. **(C)** Snow-filled environment. **(D)** Types of substrates varying with particle size found in the natural environment. Image Courtesy of (A-C) Pexels, and (D) Google Images, Getty Images, CMM Landscape Supply, Wikipedia, and Bryan's Lawn Maintenance.

force is applied are considered to be flowable substrates (Fig. 1.1D). These flowable substrates can either yield and behave similarly to a solid or flow similar a fluid depending on the forces relative to the yield strength (Coussot, 1997; Goldman, 2014; Li et al., 2009; Mazouchova et al., 2010; Sharpe, Kuckuk, and Goldman, 2015; Winter, Deits, and Hosoi, 2012). Wet flowable substrates in particular can also get wetter or dryer which causes variation in the yield strength at which the solid-fluid transition occurs. Hence, movement in the natural environment can be challenging.

Despite the environment being complex and challenging to move on, animals of different types, bodies, and shapes can move exceptionally well on both complex

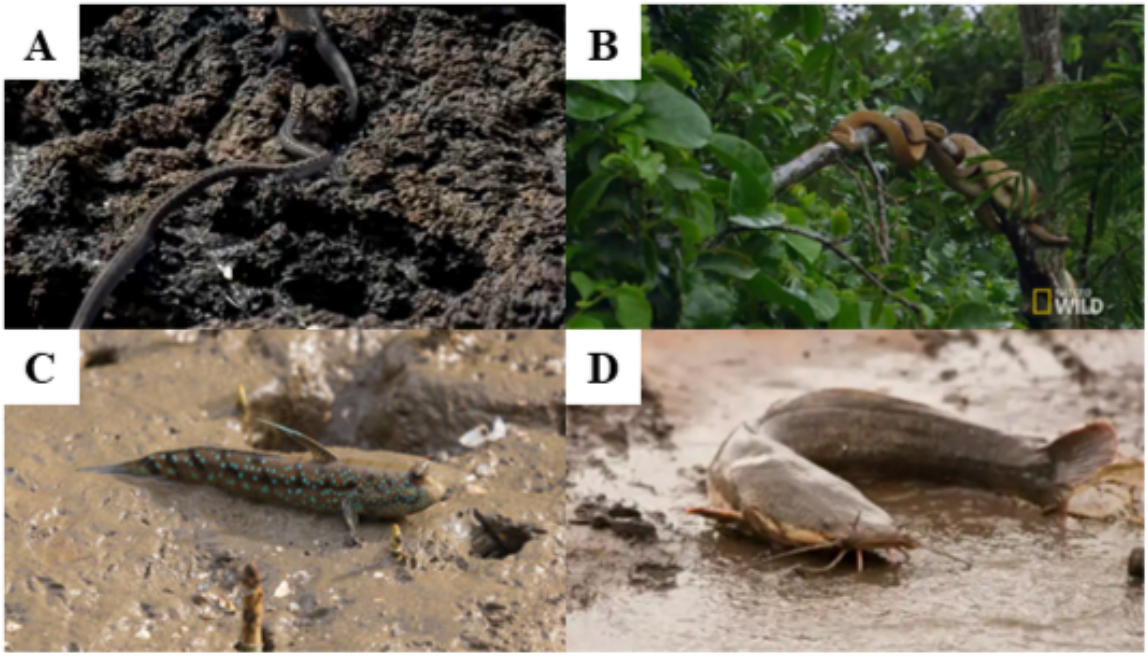

Figure 1.2: Animals moving in complex 3-D terrain and on wet flowable substrates. Snakes bending their body in 3-D to traverse **(A)** uneven terrain and **(B)** a tree branch. Amphibious fishes such as **(C)** mudskipper and **(D)** catfish walking on muddy areas at the water–land interface. Image Courtesy of (A) video from BBC, (B) video from National Geographic, (C) Getty Images, and (D) Practical fishkeeping website.

3-D terrain and substrates. They can either transition between different locomotion modes (Othayoth, Thoms, and Li, 2020; Fu et al., 2020; Astley and Jayne, 2009) or modify their primary locomotion mode with small changes (Marvi et al., 2014; Naylor and Kawano, 2022) to facilitate locomotion based on the obstacle/substrate-animal interaction. Some animals use body bending (Jurestovsky, Usher, and Astley, 2021; Fu, Astley, and Li, 2022) or tail bending (Naylor and Kawano, 2022; McInroe et al., 2016; Wang et al., 2013) to generate the right propulsive force based on the obstacle/substrate-animal interaction. Limbless and amphibious fish locomotion are excellent for traversing complex 3-D terrain and wet flowable substrates such as mud respectively (Fig. 1.2).

Bio-inspired robots have great potential in a variety of applications in 3-D terrains and on wet flowable substrates. Limbless and appendage-based robots can be used for soil testing along the rivers, rescue missions in muddy areas after rain and floods, and exploring muddy areas. Snake robots (Hirose, 1993; Liljebäck, Pettersen, and Stavdahl, 2010; Borenstein, Hansen, and Borrell, 2007; Wright et al., 2007) can also be used in various applications in unknown terrains filled with obstacles such as search and rescue during earthquakes to move between and over rubble, exploring unknown environments such as planet exploration, and inspection of industrial pipes. Unlike animals, robots still have difficulty moving in such environments due to a lack of understanding of the locomotor-obstacle/substrate interaction.

Generalist snakes can bend their body in 3-D likely using contact force (tactile) sensing via sensory feedback to generate the right forces to traverse any complex terrain in real time. Understanding how the terrain contact forces are exerted or redirected will help in the development of control strategies that use terrain contact

force feedback to help snake robots move easily on any complex 3-D terrain.

Amphibious fishes regularly make foray onto land at the water–land interface and adapt to mud at different strengths easily. The amphibious fish-mud interaction mechanics will help fully understand how locomotor morphology and kinematics permit performance. This will in turn help in developing better control strategies for robots moving on wet flowable substrates such as mud with different mud strengths. This interaction mechanics can be understood using resistive force theory which experimentally estimates drag and lift forces on the locomotor's body (Li, Zhang, and Goldman, 2013; Maladen et al., 2009) because no fundamental theories exist for understanding the locomotor-substrate interaction mechanics on flowable substrates. This requires tools and methods to control and maintain the mud strength which does not exist for mud yet unlike those well-established for sand (Li et al., 2009; Sharpe, Kuckuk, and Goldman, 2015).

Robophysial models can be used to perform systematic and controlled experiments and help obtain repeatable results (Aguilar et al., 2016). They are hence useful as active physical models of animals for studying locomotion. There is a lack of understanding of the use of vertical bending via tactile sensing in snakes and snake robots to generate propulsion and a lack of understanding of the emergence of the use of vertical bending in fishes to vertically lift parts of their body to propel against mud and lift some body sections to modulate ground friction with mud strength variation. A robophysical model will be useful in understanding the use of vertical bending to generate propulsion or modulate ground friction.

In this dissertation, we performed biological and robot experiments to understand non-legged animal locomotion on complex 3-D terrain and wet flowable substrates

such as mud. We have used force measurements to characterize mud and used a sensor model for dynamic force measurement. We will focus on the use of vertical bending by animals to generate propulsion and modulate ground friction. We have divided the objective into two studies based on the environment: (1) development of a robot to study the use of tactile sensing by snakes for 3-D body bending as sensory feedback in complex 3-D terrain and (2) understanding amphibious fishes moving on mud with variation in mud strength. To achieve (1), we have developed a robophysical model, a sensorized snake robot, that will help in understanding the principles behind tactile sensing in snakes in traversing 3-D terrain and show that it can be used to perform systematic and controlled experiments and obtain repeatable results for force measurements. To achieve (2), we have investigated three model organisms representing the three distinct strategies seen in amphibious fishes on mud with different mud strengths and performed force measurement experiments for resistive force theory. We have also developed a fish robophysical model to study the coordination of lifting and lateral bending. We will describe the relevant background and knowledge gaps in Sec. 1.2. We will then describe the research objective and questions we plan to investigate and how we approached them in Sec. 1.3.

1.2 Background

1.2.1 Limbless locomotion on uneven terrain

1.2.1.1 Snakes and snake robots use lateral bending to generate propulsive forces on vertical obstacle-filled terrain

Snakes use lateral bending to push against vertical obstacles such as rocks and tall plants to generate propulsion when navigating natural terrains filled with obstacles. Previous studies have shown that snakes use lateral undulation to push against vertical peg-like obstacles to generate propulsive forces to move forward (Schiebel, Hubbard, and Goldman, 2020; Kano et al., 2012; Gray and Lissmann, 1950; Kelley, Arnold, and Gladstone, 1997; Jayne, 1986; Moon and Gans, 1998) (Fig. 1.3A-C). Lateral undulation is a type of snake locomotion where the body bends in a wave-like pattern

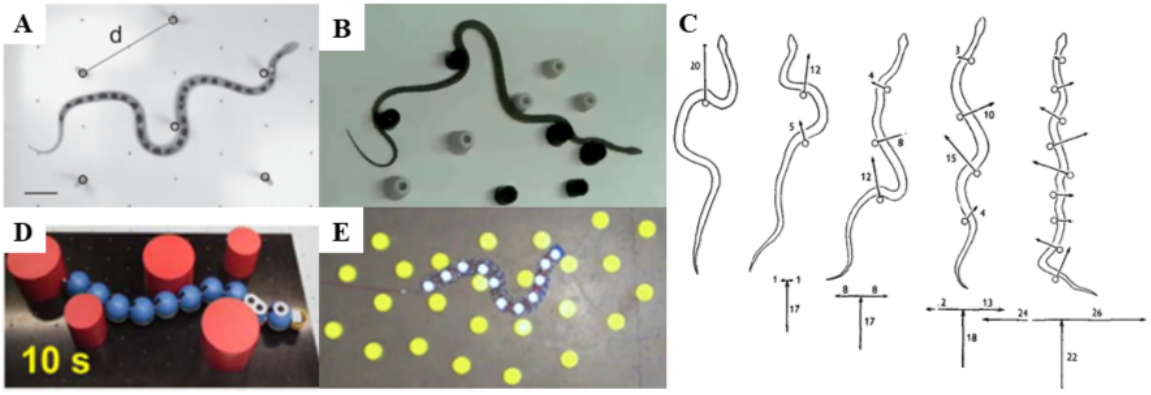

Figure 1.3: Lateral bending by snakes to push against vertical obstacles. **(A-C)** Snake laterally bending its body to push against discrete vertical obstacles such as pegs to generate propulsion to progress forward. **(D-E)** Snake robot using contact force sensing via sensory feedback to push against the vertical obstacles to generate enough propulsive forces to progress forward. Reproduced from (Schiebel, Hubbard, and Goldman, 2020; Kano and Ishiguro, 2013; Gray and Lissmann, 1950; Liljebäck et al., 2011).

and this pattern is propagated from head to tail to generate forward propulsion.

Based on the habitats they encounter, snakes can be categorized into specialists and generalists. Specialists are usually confined to a specific environment whereas generalists often encounter various terrains in their habitat (Schiebel, Hubbard, and Goldman, 2020). Specialist snakes such as desert specialists when moving on terrain filled with vertical obstacles do not change their wave pattern and remain similar to when moving on a flat surface (Schiebel, Hubbard, and Goldman, 2020). Generalist snakes, on the other hand, modify their waveform i.e, lateral bending, based on the density of the vertical obstacles (Schiebel, Hubbard, and Goldman, 2020; Kelley, Arnold, and Gladstone, 1997; Gray and Lissmann, 1950). They likely use the terrain contact force sensing as feedback to help maintain contact and control the direction of propulsion.

Studies have developed snake robots with terrain contact sensing capabilities and have been able to laterally bend and traverse over terrains with vertical obstacles (Kano and Ishiguro, 2013; Liljebäck et al., 2011; Liljebäck, Pettersen, and Stavdahl, 2010; Hirose, 1993) successfully similar to generalist snakes (Fig. 1.3D-E). These robots have been able to achieve this by using sensory feedback where they use terrain contact sensing to bend the body laterally (Kano and Ishiguro, 2013; Liljebäck et al., 2011). This suggests that snakes generate propulsion using lateral bending and it is a sensory-modulated process.

1.2.1.2 Use of vertical bending by snakes and snake robots to propel against complex 3-D terrain

Studies have investigated the use of vertical bending by snakes during traversal in arboreal environments such as cylinders representing perches with different slopes and pegs protruding out of the cylinder surface (Astley and Jayne, 2009; Astley and Jayne, 2007), array of horizontally placed cylinders representing branches (Jurestovsky, Usher, and Astley, 2021), and gliding (Yeaton et al., 2020) (Fig. 1.4A-C). The ground reaction forces measured over the horizontally placed cylinders (Fig. 1.4A) showed that snakes use vertical bending to push against the obstacles to generate large propulsive forces (Jurestovsky, Usher, and Astley, 2021).

A previous study in snakes found that snakes use vertical bending to lift parts of their body during lateral undulation to increase speed and efficiency on solid ground by modulating ground friction (Hu et al., 2009). Sidewinders also use a combination of vertical and lateral lifting to modulate friction and drag forces on sandy slopes but do not use vertical lifting directly for propulsion generation (Marvi et al., 2014). A recent study revealed that generalist snakes combine vertical bending and lateral bending during traversal in complex 3-D terrains in the natural environment and that vertical bending was used to potentially generate propulsion when the snake moved over a terrain filled with blocks of varying heights (Fu, Astley, and Li, 2022). Vertical and lateral bending combined increases the number of obstacle-body contact push points that help generate propulsive forces (Fu, Astley, and Li, 2022) (Fig. 1.4D). This suggests that snakes likely use sensory feedback to control body bending to push against the terrain in 3-D to generate contact forces along the desired direction.

Many snake robots for traversal on 3-D terrains have used methods such as

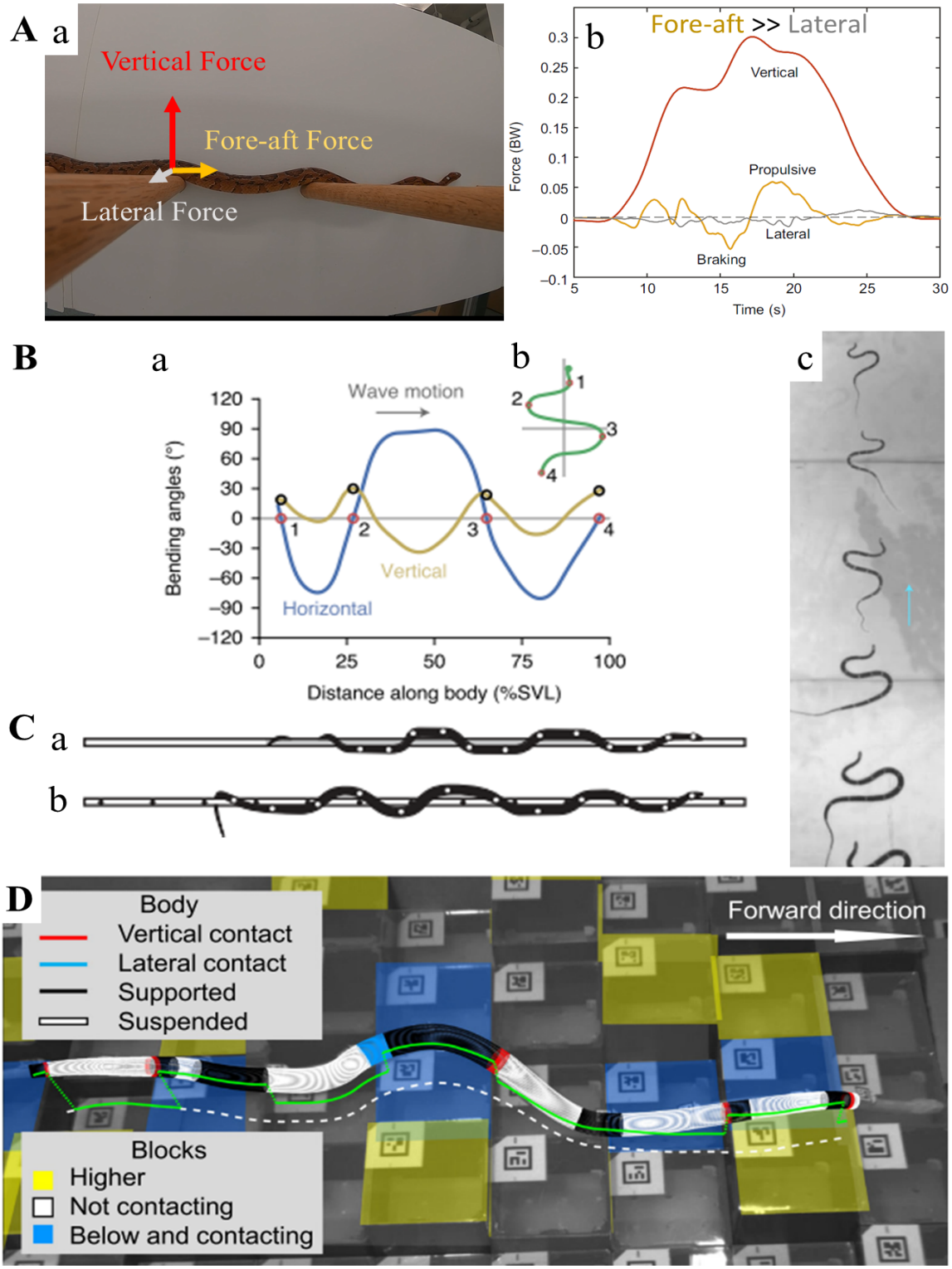
A a
Vertical Force
Fore-aft Force
Lateral Force
b
Fore-aft >> Lateral
Vertical
Propulsive
Lateral
Braking
Force (BW)
Time (s)
B
a
Wave motion
Bending angles (°)
Vertical
Horizontal
Distance along body (%SVL)
b
c
C
a
b
D
Body
Vertical contact
Lateral contact
Supported
Suspended
Forward direction
Blocks
Higher
Not contacting
Below and contacting

Figure 1.4: Vertical bending by snakes to push against lateral obstacles in an arboreal environment and in complex 3-D terrain. (A) Generation of propulsive forces via vertical bending by snakes when moving on an array of horizontally placed cylinders. (a) Snake moving over an array of cylinders. (b) Vertical, fore-aft, and lateral force as a function of time. **(B)** Snake using vertical bending during gliding. (a-b) Horizontal and vertical bending angles as a function of snout-vent length (SVL). (c) Overlaid snapshots of snake gliding. **(C)** Snake moving over (a) bare perch and (b) perch with pegs. **(D)** Snake moving over terrain with blocks of varying heights using vertical and lateral bending to increase obstacle-body contact push points. Reproduced from (Jurestovsky, Usher, and Astley, 2021; Yeaton et al., 2020; Astley and Jayne, 2009; Fu, Astley, and Li, 2022).

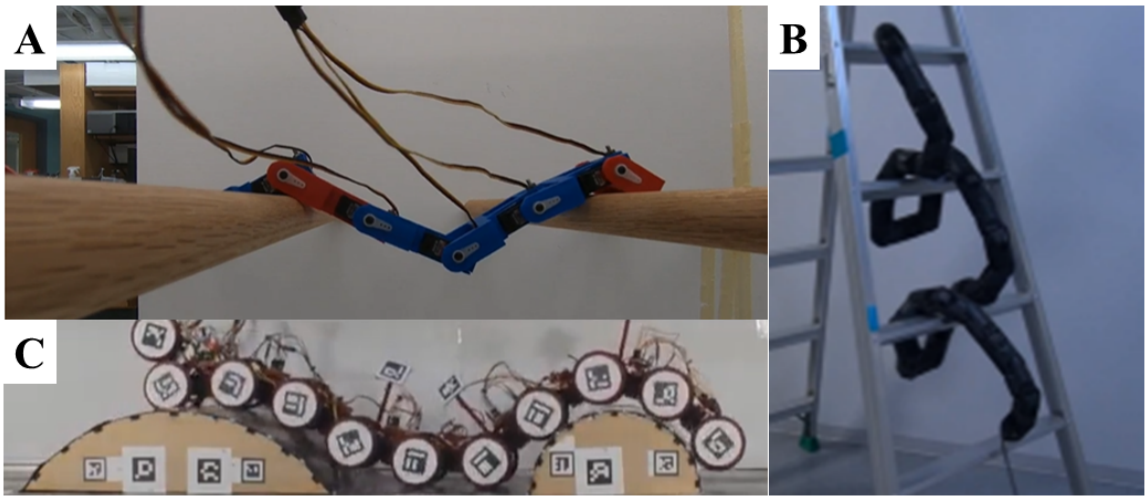

Figure 1.5: Vertical bending by snake robots to push against lateral obstacles. Snake robot vertically bending its body to push against the obstacles using **(A)** pre-defined shape open loop control, **(B)** operator aided control, and **(C)** contact force via sensory feedback. Reproduced from (Jurestovsky, Usher, and Astley, 2021; Takemori, Tanaka, and Matsuno, 2018b; Fu and Li, 2023).

vision to scan the environment and plan motions to adapt to its geometry (Tanaka and Tanaka, 2013; Pfotzer et al., 2015; Takemori, Tanaka, and Matsuno, 2018a; Fu and Li, 2020; Takemori, Tanaka, and Matsuno, 2021; Nakajima et al., 2018), mechanical (Takemori, Tanaka, and Matsuno, 2018a; Fu and Li, 2020; Kimura and Hirose, 2002)

and controlled compliance (Wang et al., 2020; Takemori, Tanaka, and Matsuno, 2018a; Travers, Whitman, and Choset, 2018) to maintain terrain contact. These methods only made robots slip more and move very slowly (Wang et al., 2020; Tanaka and Tanaka, 2013) in a complex terrain. These robots have used vertical bending to bridge height differences but it did not generate enough propulsion.

A few snake robots have been able to use vertical bending to push against the terrain for propulsion using a pre-defined shape open loop control (Jurestovsky, Usher, and Astley, 2021) or operator-aided control (Arai et al., 2008; Takemori, Tanaka, and Matsuno, 2018b; Takanashi et al., 2022; Takanashi et al., 2023) (Fig. 1.5A-B). To enable the snake robot to vertically bend its body to generate enough propulsion to move similar to snakes, contact force feedback is necessary. A few snake robots have used sensors that can detect forces or contact as feedback to help robots bridge height differences via vertical bending on 3-D terrain but not for generating propulsion directly (Hirose, 1993; Wu and Ma, 2011). A recent study studied propulsion generation using vertical bending via sensory feedback (Fu and Li, 2023) and found that contact force feedback increased the robustness of propulsion generated via vertical bending against various backward loads or unknown terrain geometry (Fig. 1.5C). Despite being able to generate the right propulsion via sensory feedback, the snake robot was equipped with discrete force sensors on its wheels which could potentially get caught onto the terrain asperities and could not sense forces on other parts of the robot body (Fu and Li, 2023). Hence there is a need for a sensorized snake robot whose body is smoother and has a large number of force sensors distributed along its body.

1.2.1.3 Model terrain to study snake locomotion

Complex 3-D terrains, the natural environment for some snakes, are filled with 3-D obstacles of different sizes and shapes (Gart, Mitchel, and Li, 2019; Jurestovsky, Usher, and Astley, 2021; Fu, Astley, and Li, 2022). To study how snakes use tactile sensing for vertical bending, the environment needs to be simplified with obstacles where only vertical bending can be used with no possibility of using lateral bending. A previous snake study used a wedge-shaped obstacle to study only vertical bending in snakes (Jurestovsky, Usher, and Astley, 2021). A half-cylindrical obstacle is an excellent 3-D terrain for studying vertical bending in snakes because it provides sufficient contact for the robot body to generate propulsion and prevents tactile sensors from getting damaged from sharp edges such as the tip of a wedge-shaped obstacle.

1.2.2 Amphibious fish locomotion on mud with different mud strengths

1.2.2.1 Appendage-based animals and robots use lateral bending for effective locomotion in a variety of environments

Some animals use lateral body and tail bending for effective locomotion either as part of their regular locomotion in the terrestrial environment or only when the environment becomes challenging. Some mammals such as ferrets use lateral body bending during walking (Kafkafi and Golani, 1998). Some studies have shown that reptiles such as lizards (Reilly and Delancey, 1997; Farley and Ko, 1997) and salamanders (Bennett, Simons, and Brainerd, 2001; Chong et al., 2021) regularly use axial bending in coordination with their limbs for effective locomotion (Fig. 1.6A).

Amphibious fishes also use lateral bending when walking with axial-appendicular-

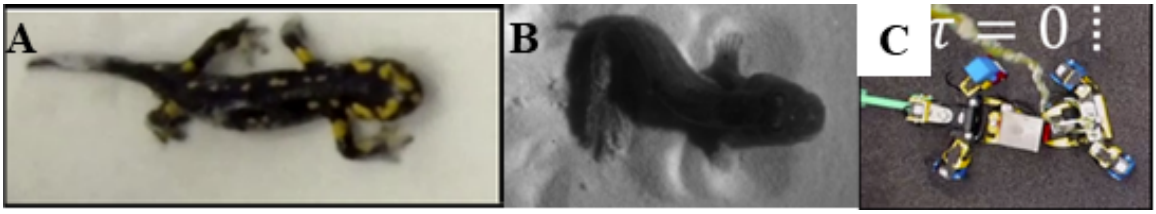

Figure 1.6: Use of Lateral body and tail bending in appendage-based locomotion. (A) Salamander using lateral body bending. **(B)** Mudskipper using lateral tail bending on 20° inclined sand substrate. **(C)** Salamander-inspired robot using lateral body bending. Reproduced from (Chong et al., 2021; Naylor and Kawano, 2022).

based locomotion (Bressman, Gibb, and Farina, 2018; Pace and Gibb, 2014; Du, Larsson, and Standen, 2016; Standen et al., 2016) and axial-based locomotion (Pace and Gibb, 2014; Clardy, 2012; Mehta et al., 2021; Sayer, 2005) on land. Studies have found that mudskippers use lateral tail bending (Fig. 1.6B) in combination with their appendicular-based locomotion to generate propulsion when moving in challenging environments such as sand surfaces with (Naylor and Kawano, 2022; McInroe et al., 2016) and without (Naylor and Kawano, 2022) inclination and on substrates such as gelatin (Wang et al., 2013).

Appendage-based robots developed with lateral body (Crespi et al., 2013) and tail (McInroe et al., 2016) bending capabilities have been shown to improve locomotion performance when body/tail bending is used (Fig. 1.6C). This suggests that lateral body and tail bending does help generate propulsion for effective locomotion. Therefore, amphibious fishes such as mudskippers likely use tail and lateral body bending to generate propulsion when locomotion becomes difficult on certain mud strengths. A systematic variation in the mud strength will show the emergence of the use of tail/body bending when locomotion becomes difficult.

1.2.2.2 Use of vertical bending by animals to enhance locomotion and propel against terrain/substrate

Some terrestrial animals are capable of bending their body vertically to improve locomotion on land. Some mammals such as cheetahs, kowari, grey short-tailed opossums, cuis, tree shrews, pikas, and cats regularly bend their spine vertically to enhance locomotion gaits such as galloping (Kamimura et al., 2022; Bertram and Gutmann, 2009; Schilling and Hackert, 2006) and half-bounding (English, 1980; Schilling and Hackert, 2006) (Fig. 1.7). By using vertical bending they increase their speed and stride length.

Previous studies on American eels have mentioned the use of a rendition of concertina locomotion in addition to lateral undulation on loose wet pebbles (Mehta

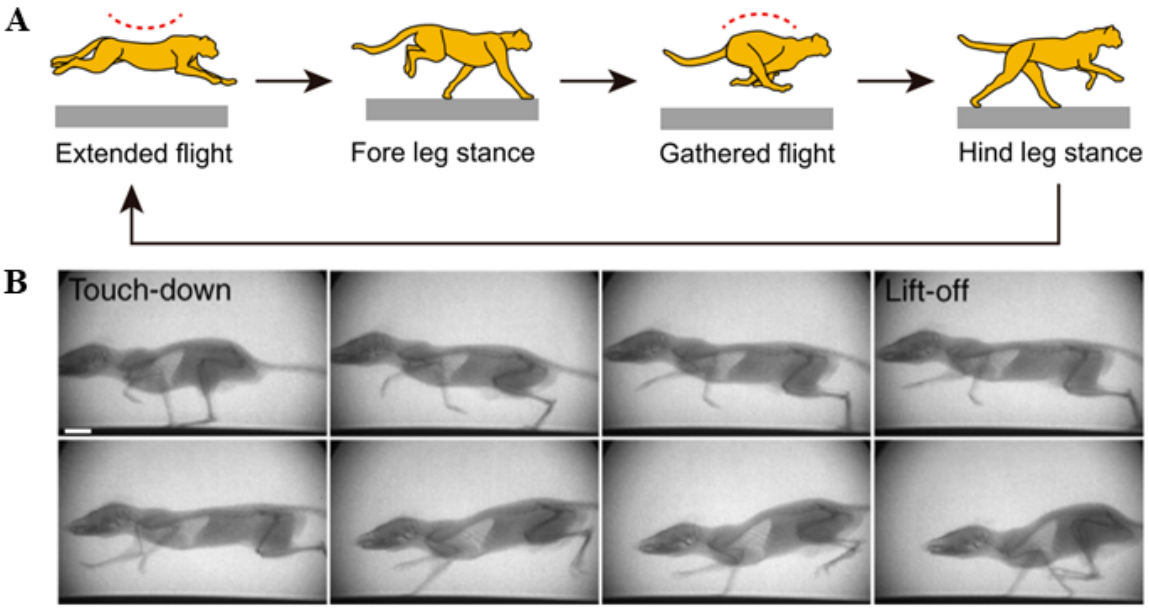

Figure 1.7: Use of vertical spine bending in legged locomotion. (A) Cheetah using vertical body bending to enhance galloping gait. **(B)** Kowari using vertical body bending to enhance half-bounding gait. Reproduced from (Kamimura et al., 2022; Schilling and Hackert, 2006).

et al., 2021), and the use of concertina-like movement of more burst movement on increased inclined wet sand and pebble substrates (Redmann et al., 2020). A study on snowflake moray mentioned the use of a rendition of sidewinding, a rendition of concertina locomotion, and a combination of lateral undulation and concertina locomotion on a wet sand substrate (Mehta et al., 2021). This suggests that elongated fishes start to use vertical bending and body lifting when it becomes difficult to locomote on substrates. Despite an observation of a small, local tail lifting in mudskippers on inclined sand (Naylor and Kawano, 2022), there is no study in lifting in fishes. A previous study on snakes found that they lift curved parts of their body to modulate ground friction (Hu et al., 2009). It is likely that elongated amphibious fishes also are capable of lifting parts of their body similar to snakes to modulate ground friction. A systematic variation in the mud strength will show the emergence of the use of vertical bending by amphibious fishes to lift body sections when locomotion becomes difficult.

1.2.2.3 Model substrate to study amphibious fish locomotion

Flowable substrates can have particles of varying sizes (Fig. 1.1D). Boulders and pebbles (Mehta et al., 2021; Standen et al., 2016) are larger compared to small amphibious fishes and hence are more like an uneven, mostly rigid terrain ($>$ 2 cm, Fig. 1.1D). Substrates with particles that flow when force is applied are considered to be flowable substrates. Substrates with particles ($<$ 2cm, Fig. 1.1D) can be categorized either as mostly coarse grains (gravel, coarse and fine sand), or mostly fine clay (silt and clay) (Coussot, 1997). Substrates with mostly coarse grains have no grain-grain cohesion and have weaker cohesion when water is added whereas mostly fine clay substrates have stronger cohesion between the particles and water due to colloidal

effects (Coussot, 1997).

Wet flowable substrates can also behave differently depending on water content. For example, mud with high water content acts like a viscous fluid whereas mud with low water content acts as a fractured solid. The solid-fluid transition occurs at the intermediate concentration of water in mud. We can control this water content using solid volume fraction which is defined as the volume of solid by the volume of both solid and water prior to mixing. The natural habitat of amphibious fishes at the water–land interface often has wet flowable substrates such as mud or wet sand (Clack, 2012; Perry et al., 2015; Wendt et al., 1997) which vary in solid composition and wetness. It is challenging to move on such substrates because they can behave similarly to a solid or flow similar to a liquid depending on the forces applied relative to yield strength (Coussot, 1997; Goldman, 2014; Li et al., 2009; Li, Hsieh, and Goldman, 2012; Mazouchova et al., 2010; Sharpe, Kuckuk, and Goldman, 2015; Winter, Deits, and Hosoi, 2012). This yield strength at which the solid–fluid transition occurs also varies depending on the water content of the substrate (Coussot, 1997). Wet flowable substrates such as mud can also have a strong cohesion due to colloidal effects (Coussot, 1997). This causes the substrate to stick to the animal's body and appendages which can affect the animal's locomotion. Despite these challenges, amphibious fishes can easily transition between different strategies and adapt to substrate variation on which they locomote by adjusting their body and appendages as they interact with the substrate.

Some amphibious fish locomotion studies have started quantifying the kinematics (Naylor and Kawano, 2022; Redmann et al., 2020) and muscle control (Horner and Jayne, 2014; Lutek and Standen, 2021) to help better understand how fishes locomote

on wet flowable substrates. Several previous studies have investigated animal and robot locomotion on sand varying from dry (Li, Hsieh, and Goldman, 2012; Maladen et al., 2009; McInroe et al., 2016; Naylor and Kawano, 2022), partly wet (Kudrolli, Ramirez, and Weitz, 2019; Sharpe, Kuckuk, and Goldman, 2015) to fully saturated sand (Dorgan, 2018; Redmann et al., 2020). Some amphibious fish studies have investigated locomotion on viscous solids such as gelatin (Wang et al., 2013) and viscous fluids made of polymers methyl cellulose (Lutek and Standen, 2021), and Poly-Bore (Horner and Jayne, 2008) mixed with water. Yet there are only a few animal locomotion studies on mud (Falkingham and Horner, 2016; Horner and Jayne, 2014; Lutek and Standen, 2021; Naylor and Kawano, 2022), especially in the solid-fluid transition concentration with no variation and controlling of mud strength.

To fully understand how the locomotor morphology, control, and kinematics permit performance it is necessary to quantify the environmental interaction between the fish and mud which requires controlling and maintaining mud strength. Natural mud can consist of both fine clay and some coarse grains. This complicates the controllability of natural mud because its strength is a function of not only the solid volume fraction but also a percentage of fine clay among the solid particles. Clay mud with no coarse grains is an excellent model substrate because it behaves qualitatively similar to natural mud yet its strength is only a function of solid volume fraction (Coussot, 1997).

It is important to prepare the substrate at a desired strength and control and maintain the substrate strength throughout the animal study to help understand the substrate-locomotor interaction mechanics. This is especially important in animal studies that take several days. Tools and methods to control and maintain the

substrate strength have been well established for dry sand which uses an air fluidized bed (Li et al., 2009; Maladen et al., 2009) to prepare and maintain sand at the desired volume fraction (Fig. 1.8A) and wet sand which uses a wet media preparation method and sieve apparatus (Sharpe, Kuckuk, and Goldman, 2015) (Fig. 1.8B). There have been some robot studies that have systematically varied the water content of mud-sand mixtures (Liu, Huang, and Qian, 2023) and mud (Liang et al., 2012; Zhang et al., 2016), yet there are no methods or equipment established for preparing, controlling,

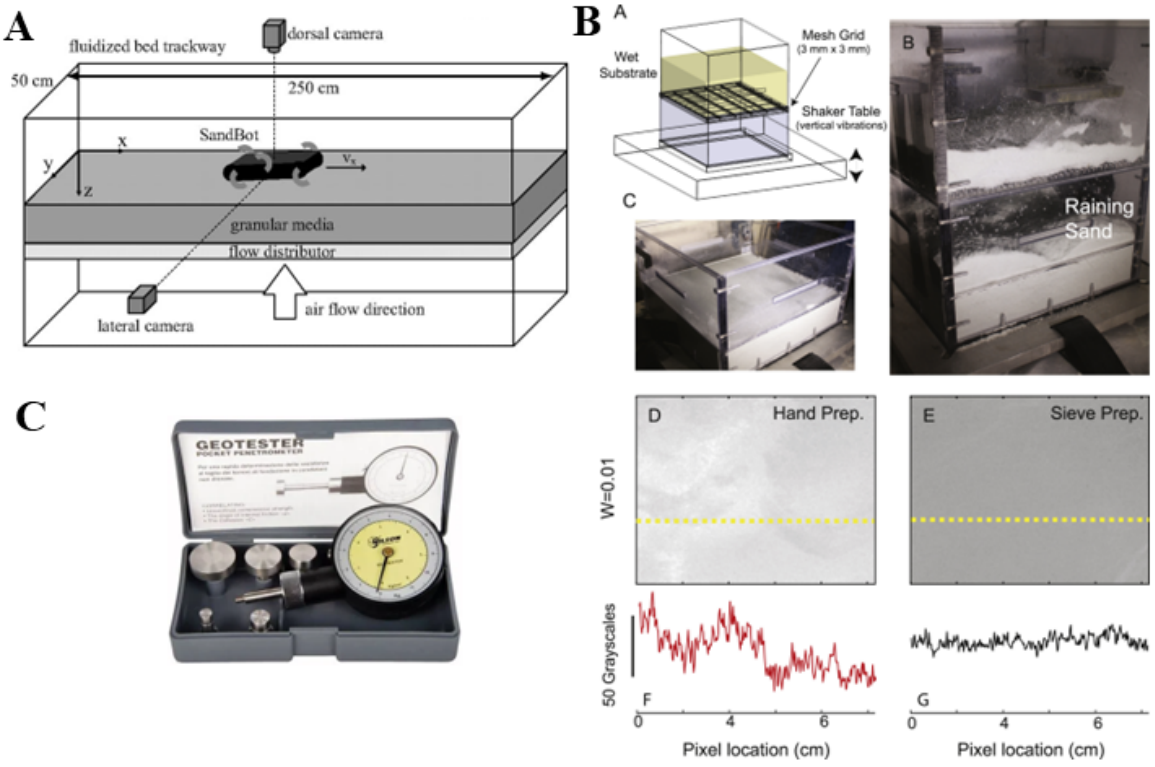

Figure 1.8: Equipments to control and maintain solid volume fraction. (A) Air fluidized bed for dry sand. **(B)** Sieve apparatus for wet sand. **(C)** Geotester pocket penetrometer for measuring penetration resistance in soil. Image Courtesy of (C) Gilson Company. (A-B) reproduced from (Li et al., 2009; Sharpe, Kuckuk, and Goldman, 2015).

and maintaining mud strength during the study and storage.

Commercially available penetrometers (Fig. 1.8C) have been used in measuring the penetration resistance of the substrate to estimate the strength of the soil. However, these penetrometers are not sensitive enough to measure the force on weaker mud. We can develop a device that uses a similar mechanism to help measure force and depth during penetration into the mud with the capability to modify the probe area suitable for each mud strength.

1.2.2.4 Amphibious fish's sustained locomotion strategies when moving on solid ground

Amphibious fishes regularly make foray onto land using three distinct sustained terrestrial locomotion strategies (Pace and Gibb, 2014) at the water–land interface. The three distinct strategies are defined based on the use of their pectoral fins and lateral body bending on solid ground as follows:

1. **Appendicular-based locomotion:** Mudskippers (Fig. 1.9B, E) are the only known amphibious fish to use this strategy (Wicaksono et al., 2018; Wang et al., 2013; Swanson and Gibb, 2004; Pace and Gibb, 2009; Kawano and Blob, 2013). The animal is slightly elongate (Fig. 1.9A, i) with relatively large pectoral fins (Swanson and Gibb, 2004; Pace and Gibb, 2009; Kawano and Blob, 2013)(Fig. 1.9A, ii). Appendicular-based locomotion is analogous to humans' motion when using crutches (Kawano and Blob, 2013; Pace and Gibb, 2014) and hence is also known as crunching gait. Here the animal uses the pectoral fins to lift its body and propel it forward by vaulting over the fins which act as a pivot in one cycle with minimal lateral body bending when moving on solid ground (Harris, 1960; Pace

and Gibb, 2014).

2. **Axial-based locomotion:** Elongate fishes (Fig. 1.9A, i) with relatively small fins and very elongated body (Fig. 1.9A, ii) such as ropefish, American eel, gunnel, prickleback, etc. use body lateral bending with minimal dorsoventral body bending

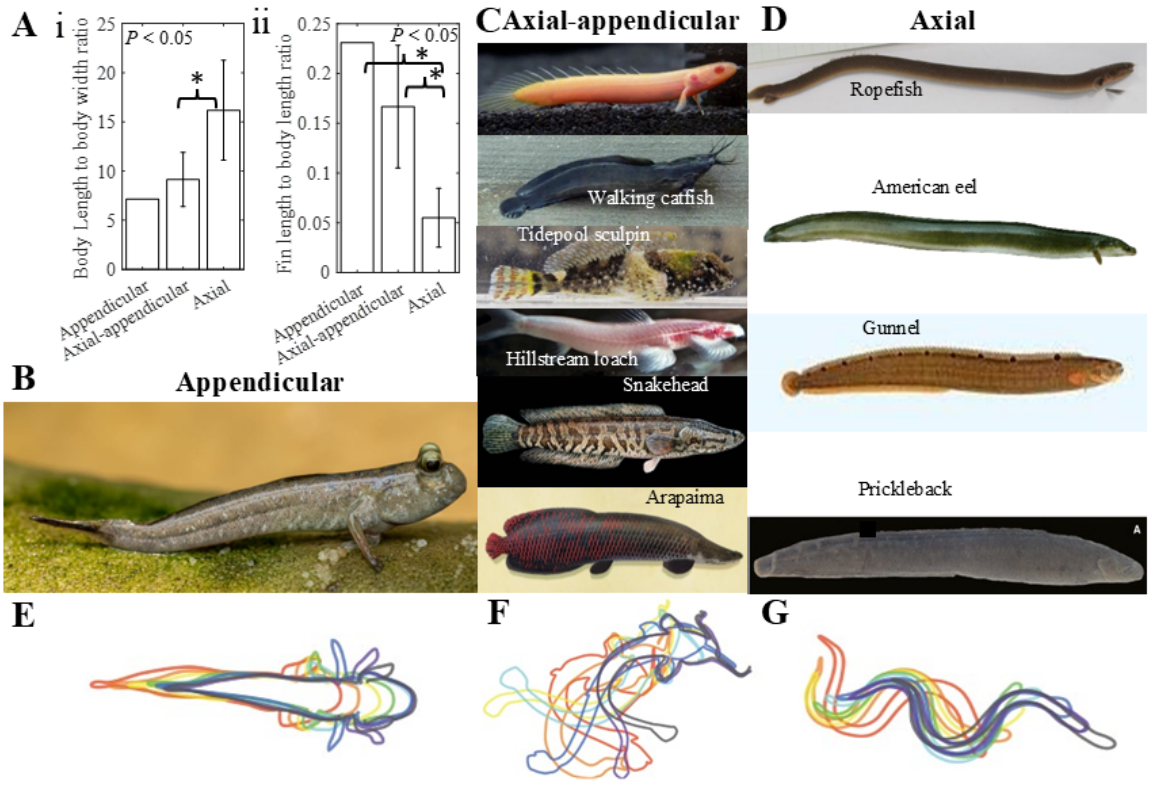

Figure 1.9: Amphibious fishes using three distinct strategies. (A) (i) Body length to body width ratio of amphibious fishes that use three distinct terrestrial locomotion strategies. (ii) Fin length to body length ratio of amphibious fishes that use three distinct terrestrial locomotion strategies. Amphibious fishes that use **(B)** appendicular-based , **(C)** axial-appendicular-based and **(D)** axial-based locomotion. **(E-G)** Overlapped frames of animal moving with **(B)** appendicular-based, **(C)** axial-appendicular-based and **(D)** axial-based locomotion. Image Courtesy of (B-D) Pexels, Aquatic Arts, Jules Bohanon, The BioFiles - Bill Hubick, Google Images, Missouri Department of Conservation, Animal Crossing New Horizons, Sierra Leone and Russell Brian Tate (CE fish essentials), squarepond.org, and NatureGate and reproduced from (Clardy and Hilton, 2016). (E-G) reproduced from (Pace and Gibb, 2014).

(Fig. 1.9D, G) to propel forward on solid ground (Pace and Gibb, 2011; Clardy, 2012; Mehta et al., 2021; Sayer, 2005; Gillis, 1998; Gillis, 2000; Watz et al., 2019; Ward et al., 2015). This is analogous to lateral undulation by snakes (Schiebel et al., 2019).

3. **Axial-appendicular-based locomotion:** Intermediately elongate fishes (Fig. 1.9A, i) with relatively medium pectoral fins (Fig. 1.9A, ii) such as bichir, walking catfish, tidepool sculpin, hillstream loach, snakehead, and arapaima, etc. use this strategy (Fig. 1.9C, F) to locomote on solid ground (Bressman, Gibb, and Farina, 2018; Bressman et al., 2019; Du, Larsson, and Standen, 2016; Standen et al., 2016; Ward et al., 2015; Crawford et al., 2020; Bressman, Morrison, and Ashley-Ross, 2021; Flammang et al., 2016; Johnels, 1957; Crawford et al., 2020; Standen, Du, and Larsson, 2014). Here, the animal uses a combination of lateral body undulation and pectoral fins alternatively over each cycle to propel forward which is analogous to army crawling (Bressman, Gibb, and Farina, 2018; Bressman et al., 2019; Du, Larsson, and Standen, 2016; Standen et al., 2016; Davenport and Matin, 1990; Bressman, Morrison, and Ashley-Ross, 2021; Flammang et al., 2016; Johnels, 1957; Crawford et al., 2020; Standen, Du, and Larsson, 2014).

1.2.3 Model organism for representative environments

1.2.3.1 Generalist snake - Model organism for complex 3-D terrain

Generalist snakes are those snakes that can live in a variety of habitats in the natural environment. They likely use sensory feedback to control body bending to push against the terrain in 3-D to generate contact forces along the desired direction (Fu, Astley,

and Li, 2022). Snakes have cutaneous mechanoreceptors distributed on their body which likely are used for tactile sensing and have proprioceptors within their muscles and tendons that provide information about the internal position, movement, and force sensing (Von During, 1979; Crowe, 1992; Crowe-Riddell et al., 2019; Proske, 1969). Despite having these capabilities, it is still unknown how these sensors are used by snakes to detect body position or environmental forces to control their locomotion. This lack of knowledge makes it difficult to study and understand how snakes detect and use contact forces as feedback to generate propulsion in complex 3-D terrain. We will develop a snake robot to study the use of tactile sensing in bending the body vertically in response to terrain contact.

1.2.3.2 Mudskipper - Model organism for appendicular-based locomotion on mud

Mudskipper (*Periophthalmus barbarus*) (Fig. 1.10A) is an excellent model organism to study appendicular-based locomotion because its natural environment is the mudflats which often have mud mixed with some silt and sand with natural variation in the wetness of the mud. There have been several extensive studies on different species of mudskipper locomotion on land in terms of kinematics and muscle control (Kawano and Blob, 2013; Pace and Gibb, 2009; Wang et al., 2013). Mudskipper is also the

Figure 1.10: Model organisms on mud. (A) Mudskipper (*Periophthalmus barbarus*). **(B)** Ropefish (*Erpetoichthys calabaricus*). **(C)** Bichir (*Polypterus senegalus*).

only known fish that uses this strategy. The transitioning between strategies or modifications to its sustained terrestrial locomotion strategy with variation in mud strength will help interpret its locomotion, connect to the previous work, and provide novel insights on its adaptation to mud strength variation.

The crutch walking gait is the mudskipper's sustained locomotion on land (Kawano and Blob, 2013; Pace and Gibb, 2009; Wicaksono et al., 2018). When using this gait, the mudskipper uses its two pectoral fins in phase with each other to lift the body and crutch forward with minimum to no body bending. The animal's sustained locomotion in water is swimming where it laterally bends its body to generate thrust (De and Nandi, 1984; Jaafar and Murdy, 2017; Pace and Gibb, 2009; Wang et al., 2013). This likely means that the mudskipper can either start to modify its appendicular-based locomotion by combining it with lateral body bending or start to show a new strategy to help it move as it interacts with the substrate.

Earlier studies have observed mudskippers using other types of locomotion in the natural environment (De and Nandi, 1984; Dijk, 1960; Jaafar and Murdy, 2017; Stebbins and Kalk, 1961). Mudskippers switch from swimming to burst locomotion such as skipping on water surfaces where the animal bends its tail to help propel itself forward (De and Nandi, 1984; Jaafar and Murdy, 2017; Stebbins and Kalk, 1961) or fast-starts, which is also known as C-starts where the animal forms a C shape with its body upon seeing a threat or perturbation and swims fast in a different direction (Jaafar and Murdy, 2017; Swanson and Gibb, 2004).

The animal's escape response on land upon seeing a threat is jumping, where it laterally bends its tail to thrust itself off the substrate over several body lengths (Dijk, 1960; Harris, 1960; Stebbins and Kalk, 1961; Swanson and Gibb, 2004). Some studies

have observed variation in the normal crutch walk mode when gelatin was used as a substrate (Wang et al., 2013) or when inclination was added to a mud (McInroe et al., 2016; Naylor and Kawano, 2022) and sand surface (Naylor and Kawano, 2022). In both cases, the animal bent its tail laterally likely to help generate propulsive forces to move forward. The use of different locomotion strategies by the mudskipper suggests that the animal is capable of transitioning to other strategies when the sustained locomotion fails.

1.2.3.3 Ropefish - Model organism for axial-based locomotion on mud

Studies have extensively investigated ropefish's (*Erpetoichthys calabaricus*) (Fig. 1.10B) terrestrial locomotion to better understand the kinematics and muscle control (Pace and Gibb, 2011; Ward et al., 2015) during terrestrial locomotion, making it an excellent model organism for axial-based locomotion. On land, ropefish uses lateral undulation with minimal dorsoventral bending (Pace and Gibb, 2014), which is less precise than snake's lateral undulation, likely due to the differences in musculature and morphology (Pace and Gibb, 2011). When swimming, the ropefish's anterior body has relatively linear forward movement, and its posterior body and tail have a cyclic lateral movement with paddling of pectoral fins (Pace and Gibb, 2011; Pace and Gibb, 2014). A study found that as the water depth reduces, the animal starts to have an increased magnitude of lateral excursions and wave amplitude in the anterior part of the body (Pace and Gibb, 2011). The animal's body is capable of modifying the wave number and amplitude of the lateral bending.

The ropefish's elongated body likely has the capability of lifting similar to snake's. Previous studies on American eels have mentioned the use of a rendition of concertina

locomotion in addition to lateral undulation on loose wet pebbles (Mehta et al., 2021), and the use of concertina-like movement of more burst movement on increased inclined wet sand and pebble substrates (Redmann et al., 2020). A study on snowflake moray mentioned the use of a rendition of sidewinding, a rendition of concertina locomotion, and a combination of lateral undulation and concertina locomotion on a wet sand substrate (Mehta et al., 2021). This suggests that elongated fishes start to use vertical bending and body lifting when it becomes difficult to locomote on substrates. A previous study found that snakes lift curved parts of their body to modulate ground friction (Hu et al., 2009). Ropefish may also have this capability and could likely use vertical lifting in combination with lateral bending on higher mud strengths when the mud starts to act more similar to a solid. There has been only one observation of a small, local tail lifting in mudskippers on inclined sand (Naylor and Kawano, 2022). Hence, the use of lifting some body sections by ropefish with systematic variation in mud strength is a novel strategy.

1.2.3.4 Bichir - Model organism for axial-appendicular-based locomotion on mud

Bichir (*Polypterus senegalus*) (Fig. 1.10C) has been extensively studied in terms of kinematics and muscle control compared to other fishes that use axial-appendicular-based locomotion on land in (Foster, Dhuper, and Standen, 2018; Standen, Du, and Larsson, 2014; Standen et al., 2016; Du and Standen, 2017; Du and Standen, 2020; Wilhelm et al., 2015; Du, Larsson, and Standen, 2016) and hence an excellent model organism to study this locomotion strategy. During terrestrial locomotion on land, the animal uses a combination of traveling and standing waves to generate body undulation and uses the placement of alternating pectoral fins to lift the body over

each cycle to propel forward (Pace and Gibb, 2014; Standen et al., 2016). When swimming, bichirs use pectoral fins to generate thrust with irregular body undulation that provides minimum thrust (Standen et al., 2016). Bichirs also use axial-based locomotion similar to snake lateral undulation on pebble surfaces (Standen et al., 2016). This shows that the animal is likely capable of modifying its body bending and body-fin coordination with mud strength variation.

1.2.4 Using robophysical models to study animal locomotion

Compared to animals, robots can be used for performing systematic and controlled experiments and help obtain repeatable results. They have been useful as active physical models of animals for studying locomotion in different environments, especially complex environments where it is difficult to create tractable theoretical models (Aguilar et al., 2016; Ijspeert, 2014; Long, 2012; Gravish and Lauder, 2018).

Snakes likely use tactile sensing to bend their body in 3-D via sensory feedback when traversing 3-D complex terrains. A sensorized snake robot can be used to study and understand the principles behind how the body deforms in response to terrain contact to generate the right forces via sensory feedback and develop better control strategies to help robots traverse complex 3-D terrains similar to snakes.

Amphibious fishes likely are capable of using vertical bending for propelling in the sagittal plane and lifting body sections to modulate ground friction on different mud strengths. A fish robophysical model with vertical lifting and lateral bending capabilities can be used to help understand how amphibious fishes use vertical bending to lift their bodies in coordination with lateral bending.

1.2.5 Measuring forces on the locomotor's body during interaction with obstacles/substrates

Contact force measurements have been extensively used in different aspects of robot locomotion and manipulation tasks and have helped advance their understanding and performance (Roberts, Zadan, and Majidi, 2021). This includes object identification (Sundaram et al., 2019), slip detection (Wang et al., 2019), tactile sensing (Yao et al., 2020; Zhu et al., 2020), exploration and interaction with cluttered environments (Gruebele et al., 2020), and terrain identification and classification (Shill et al., 2014; Wu et al., 2019).

Snake robots have been equipped with different types of sensors for the detection of forces or obstacle contact (Kano and Ishiguro, 2013; Liljebäck et al., 2011; Liljebäck, Pettersen, and Stavdahl, 2010; Hirose, 1993; Kamegawa et al., 2020; Wu and Ma, 2011; Tadokoro, 2019; Thandiackal et al., 2021; Liljebäck et al., 2012b; Taal, Yamada, and Hirose, 2009; Gonzalez-gomez et al., 2010). To improve contact, the sensors distributed along the entire length of the snake robot's body must be sufficiently flexible to allow the compliant body segments to conform passively to the 3-D terrain (Fu and Li, 2020). The sensors must provide sufficient coverage on each robot segment to accommodate contact variation in complex 3-D terrain.

Sensors such as strain gauges (Thandiackal et al., 2021; Liljebäck et al., 2012b), optical sensors (Taal, Yamada, and Hirose, 2009), and switches (Hirose, 1993) are quite rigid and not ideal for contact sensing (Fig. 1.11A). Sensors made of pressure-sensitive materials are flexible and more suitable for placing on the robot body. Such sensors that are commercially available (Kano and Ishiguro, 2013; Liljebäck, Pettersen, and Stavdahl, 2010; Liljebäck et al., 2011; Wu and Ma, 2011) come in specific sizes and

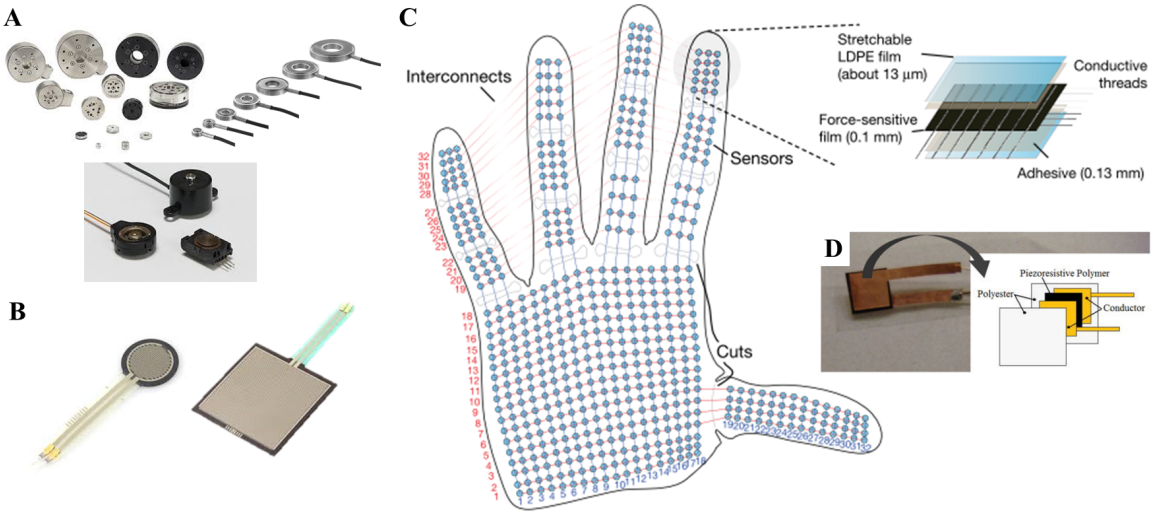

Figure 1.11: Contact force sensors. (A) Rigid force sensors. **(B)** Commercially available flexible piezo-resistive sensors, Force Sensitive Resistor (FSR) sensors. **(C-D)** Custom-made, flexible, low-cost, piezo-resistive pressure sensors. Image Courtesy of (A) ATI Industrial Automation, TE Connectivity, Thermax Power & Energy Supplies and Equipment Inc., and (B) Sparks Fun. (C-D) reproduced from (Sundaram et al., 2019; Kalantari et al., 2011).

shapes which makes them less suitable for high coverage (Fig. 1.11B). Despite providing high coverage, custom-made sensors with pressure-sensitive materials (Kamegawa et al., 2020; Tadokoro, 2019; Gonzalez-gomez et al., 2010) require substantial effort and special equipment for manufacturing. Recent studies have developed low-cost, piezo-resistive pressure sensor design (Sundaram et al., 2019; Kalantari et al., 2011) that can be custom-made to any shape for maximal coverage and is easy to manufacture (Fig. 1.11C-D). This sensor design will meet the requirements for a sensorized snake robot.

Piezo-resistive sensors, including the commercially available ones, under a constant load, exhibit creep behavior in the sensor response that occurs before settling to a constant value due to the viscoelastic nature of the piezo-resistive material (Kalantari

et al., 2011; Brinson and Brinson, 2015). This takes longer than the typical periods ($10^{-1} - 10^{1}$ s) of most robot locomotion, although soft robots in particular can be as slow as the creep behavior (Rus and Tolley, 2015). Because of this, creep behavior was not considered in most previous mobile robot studies that use piezo-resistive force sensors (Liljebäck, Pettersen, and Stavdahl, 2010; Shill et al., 2014; Wu et al., 2019; Kamegawa et al., 2020; Li et al., 2021). The characteristic time of this creep behavior is large and can be comparable to the timescale of robot locomotion, especially when the robot can become stuck in a complex 3-D terrain which results in sustained contact. This can be challenging for dynamic force measurement. Hence it is necessary to use a sensor model that considers sensor creep behavior for estimating dynamic forces accurately.

No fundamental theories exist to estimate the drag and lift forces for understanding the locomotor-substrate interaction mechanics on flowable substrates. Resistive force theory can be useful in finding force laws empirically analogous to theoretical force laws (the Navier-Stokes Equation) in fluids and aerodynamics. Previous studies have used resistive force theory to understand how the animals and robots interact with substrates by estimating drag and lift forces on the locomotor's body for dry (Astley et al., 2020; Ding et al., 2012; Ding, Li, and Goldman, 2013; Goldman, 2014; Li, Zhang, and Goldman, 2012; Li, Hsieh, and Goldman, 2012; Li, Zhang, and Goldman, 2013; Maladen et al., 2009; Maladen et al., 2011; Mazouchova et al., 2010; Mazouchova, Umbanhowar, and Goldman, 2013; McInroe et al., 2016; Zhang and Goldman, 2014) and wet (Sharpe, Kuckuk, and Goldman, 2015; Winter, Deits, and Hosoi, 2012) sand. Recent animal studies have also been able to apply resistive force theory in estimating thrust and drag forces on the animal's appendages during interaction with substrates

(Chong et al., 2021; Chong et al., 2023). Such force laws have not yet been developed for mud due to the difficulty in preparing and maintaining mud at a desired mud strength. Through resistive force theory, we can better understand the locomotor-mud interaction mechanics with variations in mud strength.

1.3 Research objectives and questions

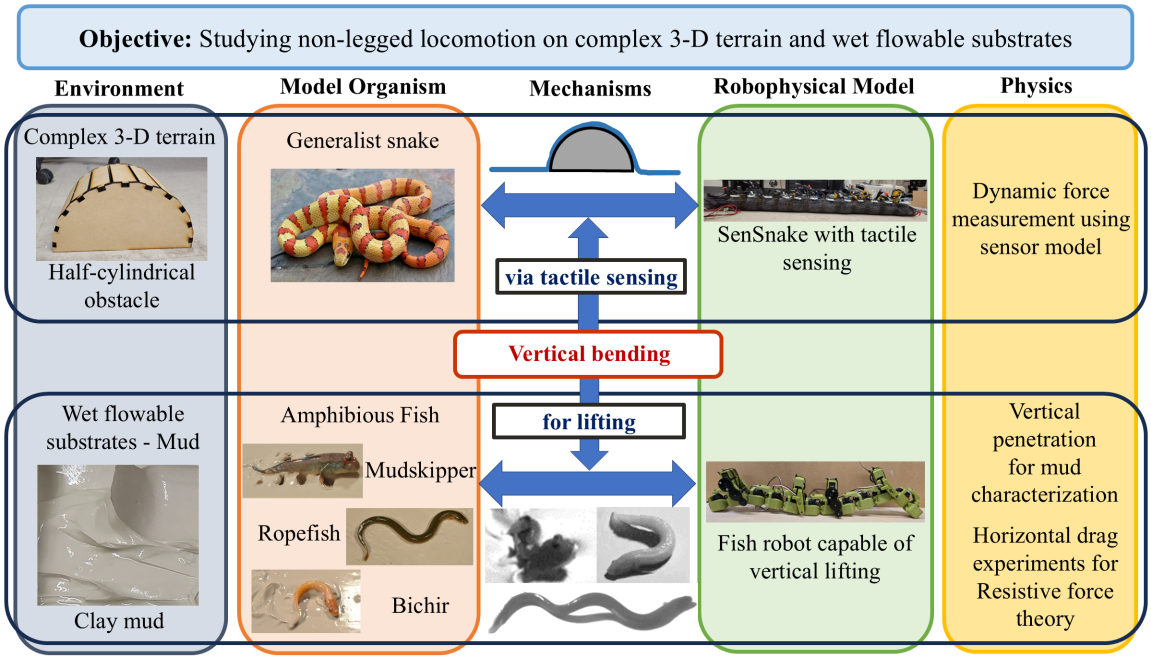

Figure 1.12: Research objective and approach for this dissertation. Image Courtesy of vivid reptiles.

The overall objective of this dissertation is to study non-legged locomotion on complex 3-D terrain and wet flowable substrates (Fig. 1.12). We will integrate biology, robotics, and physics to help achieve the research objective and answer questions in this dissertation. We have divided the objective into two parts based on the environment (complex 3-D terrain and mud) and chose model organisms that move well in each

environment to study (Fig. 1.12): (1) development of a robot to study the use of tactile sensing by snakes for 3-D body bending as sensory feedback in complex 3-D terrain and (2) understanding amphibious fishes moving on mud with variation in mud strength. The following shows how we will achieve the specific goals and questions over each chapter:

1. Chapter 2 details the robotic and force measurement studies to understand snake locomotion on complex 3-D terrain.
2. Chapter 3 details the tools and methods developed and the force measurement experiments to control and maintain mud strength.
3. Chapter 4 details the biological study to understand mudskipper locomotion with variation in mud strength.
4. Chapter 5 details the biological, robotic, and force measurement studies to understand ropefish locomotion with variation in mud strength.
5. Appendices 7.1 details the preliminary biological study to understand bichir locomotion with variation in mud strength.

Chapter 2: Sensorized robot to directly measure contact forces for 3-D body bending

To establish a robotic platform to study how to use contact sensing to modulate 3-D body bending to propel against 3-D terrain for locomotion similar to snakes, we first developed a sensorized robophysical model that can sense direct terrain contact forces. Through robot experiments, we showed that the robot can measure contact forces with high repeatability which will be helpful for systematic studies to understand the physics principles behind snake locomotion. We performed experiments to calibrate

the sensors on the robot to improve the accuracy of estimated force and inform the future design of terrain testbeds for studying complex 3-D terrain traversal. We also showed that we can obtain dynamic force measurements using a sensor model that takes into account the creep behavior that can be comparable to the timescale of robot locomotion.

Chapter 3: Tools and techniques to prepare and maintain mud strength

As a first step towards understanding the locomotor-mud interaction mechanics, we showed how we can prepare large quantities of mud systematically for different mud strengths. We also showed how well we can maintain the mud strength from our mud characterization methods and tools developed which the previous studies were unable to do. We then showed that we can perform systematic and controlled experiments through mud characterization.

Chapters 4: Mudskipper adapting to different mud strengths by modifying its sustained strategy or transitions to other strategies

We performed a systematic study of the mudskipper moving on different mud strengths which has not been performed until now. We used high-speed camera videos to measure and quantify the animal's performance during the crutch walking mode. We investigated the variation in the crutch walking gait through kinematics from 3-D tracking as the mud strength varied. We also performed statistical and 2-D kinematic analyses for the different strategies that emerged with mud strength variation.

Chapter 5: Ropefish adapting to different mud strengths

We performed a systematic study of the ropefish moving on different mud strengths using the same experiment protocol as the mudskipper study. We used high-speed camera videos to measure and quantify the animal's performance on different mud strengths. We investigated the coordination of novel body lifting and lateral bending in ropefishes through kinematics from 3-D tracking. We performed horizontal drag force measurements for resistive force theory on mud which will help calculate the modulation of lift and drag forces by body lifting. We have developed a fish robophysical model that will be used in studying body lifting and lateral bending coordination.

Appendices 7.1: Bichir adapting to different mud strengths

We performed a preliminary study of the bichir moving on mud with different mud strengths using the same experiment protocol as the mudskipper and ropefish studies. We used high-speed camera videos to measure and quantify the animal's performance during its terrestrial locomotion on different mud strengths. We used 2-D kinematics to compare the performance across different mud strengths.

Chapter 2

SenSnake: A snake robot with contact force sensing for studying locomotion in complex 3-D terrain

This chapter was previously published as an article entitled *SenSnake: A snake robot with contact force sensing for studying locomotion in complex 3-D terrain*, authored by Divya Ramesh, Qiyuan Fu, and Chen Li, in IEEE International Conference on Robotics and Automation (Ramesh, Fu, and Li, 2022). We re-used the article in this chapter with slight changes of the format under CC BY 4.0 and with permissions from all authors.

2.1 Author Contributions

Divya Ramesh developed robot, conducted experiments, analyzed data, and developed model; Qiyuan Fu developed robot control and assisted robot design and experimental setup; Divya Ramesh and Chen Li wrote the paper.

2.2 Acknowledgment

We thank Xiangyu Peng, Nikhil Murty and Kaiwen Wang for early sensor and robot prototyping; Yaqing Wang for calibration setup development; and Yaqing Wang, Ratan Othayoth, and Henry Astley for discussion.

This work was supported by an Arnold and Mabel Beckman Foundation Beckman Yong Investigators Award, a Burroughs Wellcome Fund Career Award at the Scientific Interface, a Johns Hopkins University Catalyst Award, and the JHU Whiting School

of Engineering start-up funds.

2.3 Summary

Despite advances in a diversity of environments, snake robots are still far behind snakes in traversing complex 3-D terrain with large obstacles. This is due to a lack of understanding of how to control 3-D body bending to push against terrain features to generate and control propulsion. Biological studies suggested that generalist snakes use contact force sensing to adjust body bending in real time to do so. However, studying this sensory-modulated force control in snakes is challenging, due to a lack of basic knowledge of how their force sensing organs work. Here, we take a robophysics approach to make progress, starting by developing a snake robot capable of 3-D body bending with contact force sensing to enable systematic locomotion experiments and force measurements. Through two development and testing iterations, we created a 12-segment robot with 36 piezo-resistive sheet sensors distributed on all segments with compliant shells with a sampling frequency of 30 Hz. The robot measured contact forces while traversing a large obstacle using vertical bending with high repeatability, achieving the goal of providing a platform for systematic experiments. Finally, we explored model-based calibration considering the viscoelastic behavior of the piezoresistive sensor, which will for useful for future studies.

2.4 Introduction

Snake robots hold the promise as a versatile platform for traversing in a variety of environments for critical applications (Walker, Choset, and Chirikjian, 2016; Liljebäck

et al., 2012a). However, despite snakes' remarkable locomotor capacities in 3-D terrain with large obstacles (Gart, Mitchel, and Li, 2019; Schiebel, Hubbard, and Goldman, 2020; Fu et al., 2020), snake robots still suffer slower speeds and larger slip (Wang et al., 2020; Tanaka and Tanaka, 2013) in similar terrain. Some snake robots use vision to scan the terrain and plan motions to adapt to its geometry (Tanaka and Tanaka, 2013; Pfotzer et al., 2015; Takemori, Tanaka, and Matsuno, 2018a; Fu and Li, 2020; Takemori, Tanaka, and Matsuno, 2021; Nakajima et al., 2018). Others use mechanical (Takemori, Tanaka, and Matsuno, 2018a; Fu and Li, 2020; Kimura and Hirose, 2002) or controlled (Wang et al., 2020; Takemori, Tanaka, and Matsuno, 2018a; Travers, Whitman, and Choset, 2018) compliance to maintain terrain contact. However, despite progress on using 2-D lateral bending to push against vertical asperities on flat surfaces to generate propulsion (Kano and Ishiguro, 2013; Liljebäck et al., 2011; Liljebäck, Pettersen, and Stavdahl, 2010; Hirose, 1993), we know little about how to use 3-D body bending to push against complex 3-D terrain to generate propulsion.

An ability to sense and adjust contact forces against the terrain likely contributes to generalist snakes' superior performance. When using 2-D lateral bending to push against vertical structures, generalist snakes can adjust their body bending in real time to maintain contact and control the direction of propulsion (Schiebel, Hubbard, and Goldman, 2020; Kano et al., 2012), suggesting that this is a sensory-modulated process. Snakes possess both cutaneous mechanoreceptors (i.e., skin tactile sensing) and proprioceptors within the muscles and tendons (i.e., internal position, movement, and force sensing) (Von During, 1979; Crowe, 1992; Crowe-Riddell et al., 2019; Proske, 1969; Schaeffer and Waters, 1996), yet it remains unknown how these sensors are used to detect body position or environmental forces to control locomotion. Such a lack of

basic knowledge makes it difficult to study snakes to understand how to sense and control contact forces to generate propulsion in complex 3-D terrain.

Robots have proven very useful as physical models of animals for studying locomotion, especially in complex environments, where it is difficult or impossible to create tractable theoretical models (Aguilar et al., 2016; Ijspeert, 2014; Long, 2012; Gravish and Lauder, 2018). In addition, contact force measurements (Roberts, Zadan, and Majidi, 2021) have advanced understanding and performance of many aspects of locomotion and manipulation tasks, including object identification (Sundaram et al., 2019), slip detection (Wang et al., 2019), tactile sensing (Yao et al., 2020; Zhu et al., 2020), exploring and interacting with cluttered environments (Gruebele et al., 2020), and terrain identification and classification (Shill et al., 2014; Wu et al., 2019). Here, to establish a robotic platform for studying the physical principles of sensing and controlling contact forces to generate propulsion in complex 3-D terrain and ultimately improve snake robot performance, we developed a snake robot, SenSnake, capable of 3-D body bending with contact force sensing along its body.

Our sensors have two design requirements. First, they must be sufficiently flexible to allow compliant body segments to passively conform to 3-D terrain to improve contact (Fu and Li, 2020). Second, they must provide sufficient coverage of each segment to accommodate variable contact in complex 3-D terrain. A variety of sensors have been used to detect forces or contact for snake robots (Kano and Ishiguro, 2013; Liljebäck et al., 2011; Liljebäck, Pettersen, and Stavdahl, 2010; Hirose, 1993; Kamegawa et al., 2020; Wu and Ma, 2011; Tadokoro, 2019; Thandiackal et al., 2021; Liljebäck et al., 2012b; Taal, Yamada, and Hirose, 2009; Gonzalez-gomez et al., 2010). Sensors based on strain gauges (Thandiackal et al., 2021; Liljebäck et al.,

2012b), optics (Taal, Yamada, and Hirose, 2009), and switches (Hirose, 1993) are rigid. Sensors based on pressure sensitive materials are flexible and more suitable for our needs. Among these, off-the-shelf ones (Kano and Ishiguro, 2013; Liljebäck et al., 2011; Liljebäck, Pettersen, and Stavdahl, 2010; Wu and Ma, 2011) come in specific sizes and shapes and are less suitable for high coverage; custom ones (Kamegawa et al., 2020; Tadokoro, 2019; Gonzalez-gomez et al., 2010) provide high coverage but require substantial effort and special equipment to manufacture. Here, we chose a low-cost piezo-resistive pressure sensor design that can be custom made to any shape for maximal coverage and is easy to manufacture, following recent work (Sundaram et al., 2019; Kalantari et al., 2011).

We first developed and tested an initial robot prototype (Sec. 2.5). Based on limitations revealed from the testing, we refined the robot and sensor design (Sec. 2.6). This enabled the robot to move over a large obstacle and measure contact forces with high repeatability (Sec. 2.6), achieving our major goal of providing a robotic platform for systematic experiments (rather than optimizing robot performance as in many robotics studies). In addition, we performed experiments to calibrate the sensors on the refined robot, which can improve force estimate accuracy and inform future design of terrain testbeds for studying complex 3-D terrain traversal (Sec. 2.7). Finally, we summarize contributions and discuss future work (Sec. 2.8).

2.5 Initial sensor & robot development

2.5.1 Initial robot prototype

The initial robot prototype, SenSnake v1 (0.9 m long, 0.044 m cross-sectional radius, 4.6 kg), had 12 alternating pitch and yaw segments to bend in 3-D (Fig. 2.1A). Each segment had a servo motor (Dynamixel XM430-W350-R) fully enclosed in a soft shell casted from silicone (Ecoflex 00-30, Smooth-On Inc.) (Fig. 2.1C, black) attached

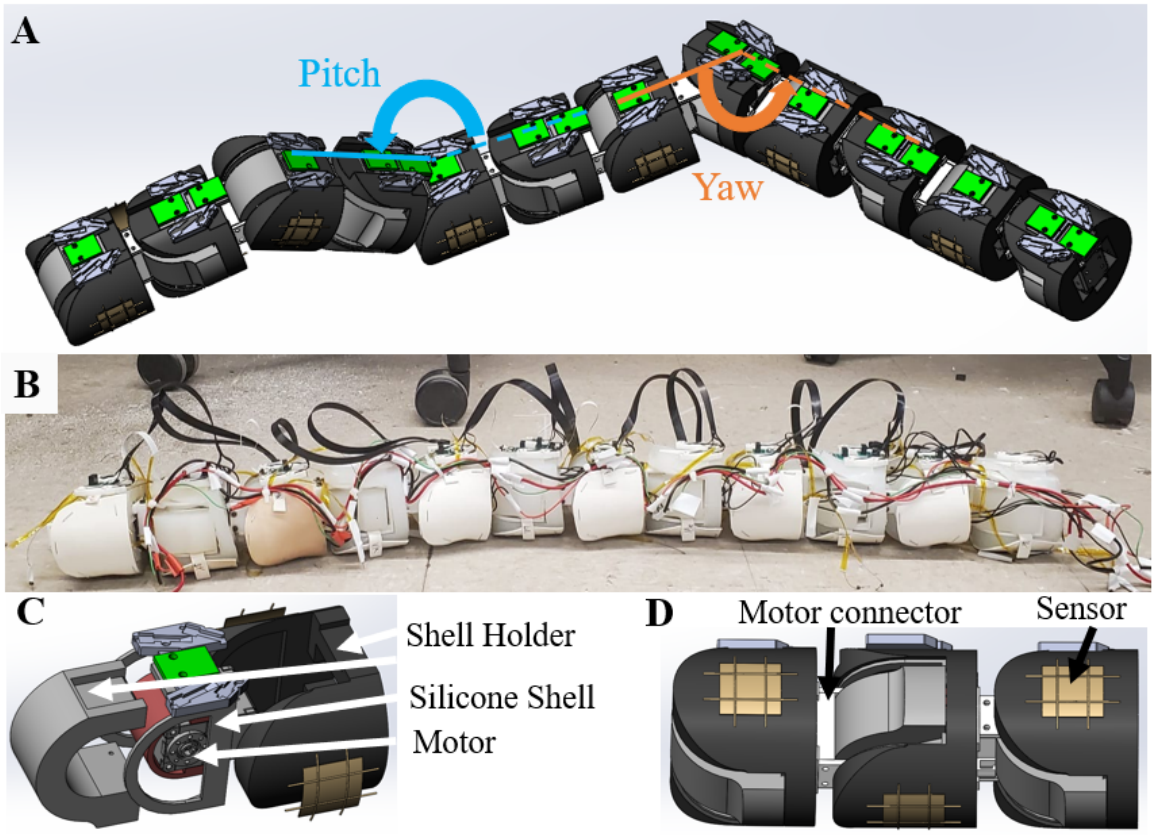

Figure 2.1: SenSnake v1. **(A)** CAD showing 3-D bending with pitch and yaw degrees of freedom. **(B)** Photo of robot without sleeve. **(C)** Exploded view of a segment. **(D)** Side view CAD of three segments with sensors on the side of yaw and bottom of pitch segments.

via 3-D printed shell holders (Fig. 2.1C). On the outside of the soft shell, each pitch segment had an array of four sensors (in a 2×2 arrangement) on its bottom, whereas each yaw segment had two such arrays on both sides (Fig. 2.1D). This resulted in a total of 72 sensors, which could be recorded at a sampling frequency of 17 Hz (see Sec. 2.5, C). The soft shell was intended to deform passively during terrain interaction to improve terrain sensor contact.

The robot was powered by a 12 V DC power supply. The motors were daisy-chained and controlled via a USB communication convertor (U2D2, Dynamixel). A rubber layer covered each sensor to prevent sensor wear and tear (Fig. 2.1B). A PolyEthylene Terepthalate braided sleeve (Flexo Pet, Techflex) covered the robot to reduce friction. Eighteen 8-pin FFC cable adapter to 8-DIP adapter PCB boards (green in Fig. 2.1A, C) were attached to the top part of the shell holder to connect sensors to a Data Acquisition board (DAQ).

2.5.2 Sensor fabrication

The sensor array consisted of seven layers (Fig. 2.2A). A piezo-resistive film (3M Velostat, 0.1 mm thickness, Adafruit Industries) was sandwiched between parallel stainless steel conductive threads (3 ply, 0.25 mm thickness, Adafruit Industries) above and below, placed perpendicular to each other (Fig. 2A). A crossing of thread above and below forms a single sensor. An adhesive sheet (Gizmo Dorks 468MP, 2.54 mm thickness, 3M) was placed over the conductive threads (Fig. 2.2A) and adhered to the piezo-resistive film, followed by a sheet of plastic wrap.

Each sensor experiences a reduction in resistance R_s on application of normal force. The sensor conductance, $C_s = 1/R_s$, increases linearly with the force applied

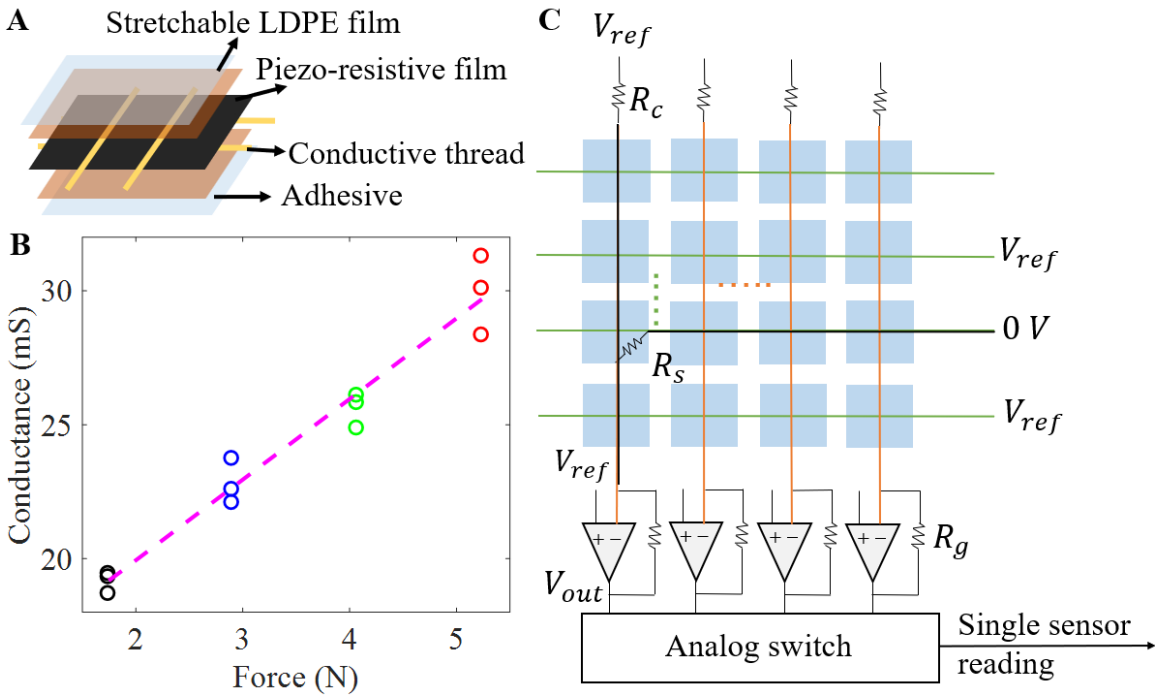

Figure 2.2: Sensor fabrication, calibration, and data acquisition. (A) Piezo-resistive sensor design. **(B)** Average conductance between 225 s and 300 s as a function of force applied (3 trials each) from calibration experiments in Sec. 2.7. Dashed line is best linear fit. **(C)** Signal isolation circuit to collect the sensor readings. Blue squares are piezo-resistive sheets. $V_{ref} = 2.5$ V, $R_g = 1000\ \Omega$, $R_C = 900\ \Omega$.

(Fig. 2.2B):

$$C_s = mF + d \tag{2.1}$$

where m and d are constants (multimedia material, video 1).

2.5.3 Sensor data acquisition

To obtain sensor resistance R_s, we replicated the DAQ designed in (Sundaram et al., 2019), which uses a signal isolation circuit to scan through sensors one at a time using a multiplexer and a demultiplexer (Fig. 2.2C) and minimize sensor crosstalk,

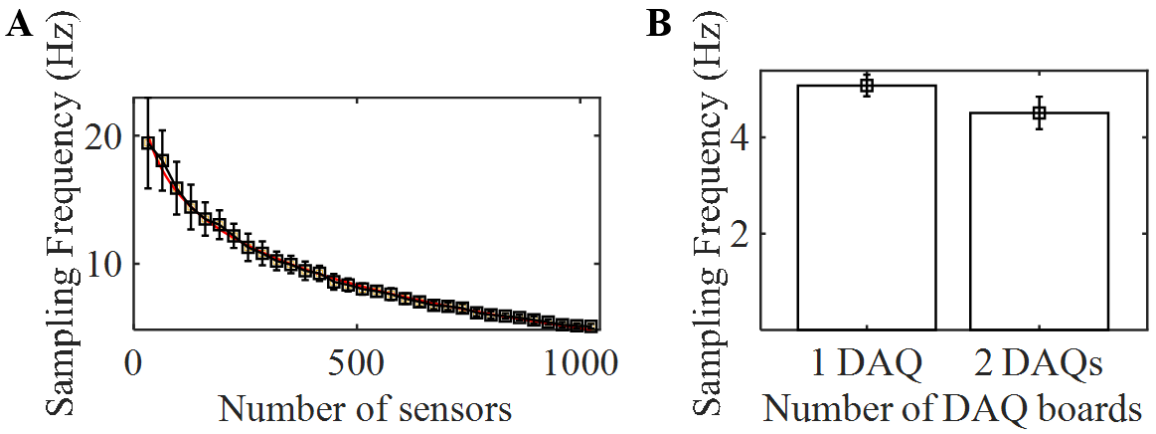

Figure 2.3: Sampling frequency of sensor data acquisition. (A) Sampling frequency as a function of the number of sensors (mean ± s.d. over 100 sampling cycles). **(B)** Comparison of sampling frequency between one and two DAQ used. 1024 sensors were scanned for each case.

an undesirable effect that sensors close to each other affect each other's resistance (D'Alessio, 1999). We characterized the sampling frequency of the DAQ, defined as the frequency at which data from all sensors being tested can be received. As expected, sampling frequency decreased monotonically with the number of sensors (Fig. 2.3A), starting at about 20 Hz for one sensor, decreasing to 10 Hz for 300 sensors, and approaching only a few Hz for 1000 sensors. When two DAQ were used, sampling frequency decreased but only slightly (Fig. 2.3B).

2.5.4 Experiments and issues revealed

We tested SenSnake v1 on flat rigid ground and a pile of small wooden blocks using lateral undulation (15.24 cm long, 5.08 cm wide, 3.38 cm tall: Fig. 2.4A-B). In both cases, the robot did not progress forward due to a lack of anisotropic friction necessary for undulating on smooth flat surfaces (Hu et al., 2009). We observed constant forces

when the robot remained stationary for the first 10 s (Fig. 2.4C-D). During lateral undulation, forces oscillated periodically on flat ground (Fig. 4C) and not so regularly

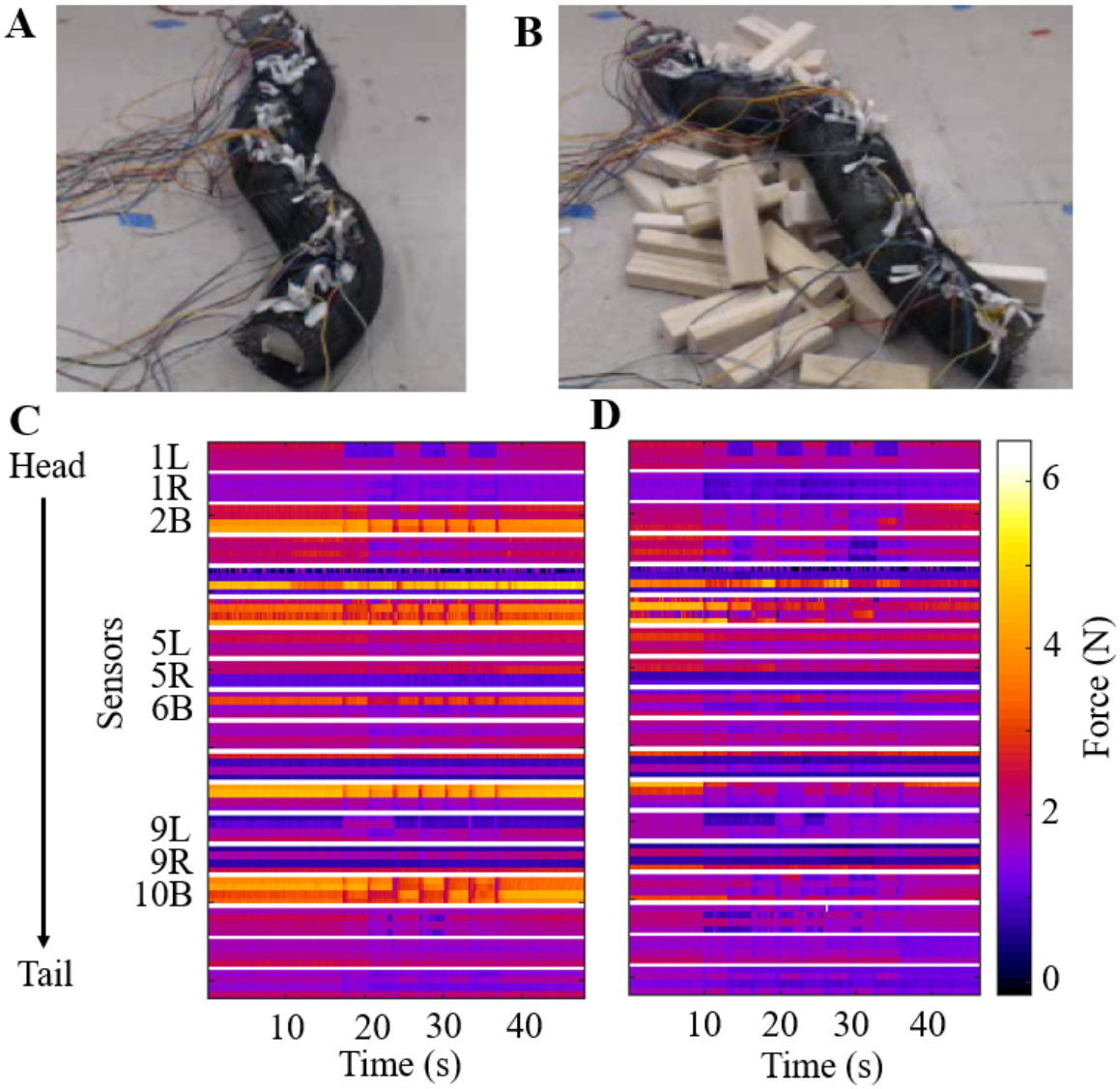

Figure 2.4: Initial robot prototype experiment. **(A)** Lateral undulation on flat ground. **(B)** Lateral undulation on rubble of wooden blocks. **(C)** Force readings varying with time on flat ground. **(D)** Force readings varying with time on rubble of wooden blocks. 1L and 1R indicate 1st segment left and right, 2B indicates 2^{nd} segment bottom.

on blocks (Fig. 2.4D). These results showed that the sensors can detect the expected forces during locomotion (multimedia material, video 2).

However, these tests also revealed several issues. First, we observed small signals on a large portion of force sensors on the body segments in contact with the block pile. This suggested that the silicone shell did not deform sufficiently to distribute highly localized stresses at terrain contact points widely to reach the exact locations of the sensors. Because each sensor covered only a small area at the crossing of the perpendicular conductive threads, it could not detect a large force signal. Contrary to expectation, the differences between the four sensors within each 2×2 sensor array on the block pile were similar to those on flat ground (Fig. 2.4C-D) likely a result of the lack of direct contact at the sensor point. This further showed that the intended high sensor spatial resolution did not outweigh the small sensor area limitation. Moreover, some of the sensors developed substantially noisy reading during experiments (Sensors 3R, 4B, 11L in Fig. 2.4C-D) because the sensor-chipboard connection wires became loose.

We also tested the robot traversing a single large obstacle as high as $0.28\times$ robot length by propagating a vertical bending shape that conforms to the obstacle down its body, a strategy inspired by recent animal observations (Jurestovsky, Usher, and Astley, 2021). Although the robot was able to generate the desired shape evolution on its own, it failed to use it against the large obstacle to propel forward. Examination of motor angle data revealed that the motors could not reach the desired positions during obstacle interaction. This was likely because pushing against the large obstacle resulted in high contact forces concentrated on segments contacting the forward half of the obstacle. To propel the entire robot forward, these segments must sustain these

large contact forces to overcome the large frictional drag from the substantial robot weight from the silicone layers. This large force requirement, together with restrictions from the sleeves, probably resulted in motor overload and trigged motor to give to prevent damage.

2.6 Refined sensor & robot development

We made several design and fabrication improvements to address these issues in a refined robot. These include: (1) replacing the solid silicone shell with a more compliant, hollow shell to reduce robot weight and sleeve restriction and improve body/sensor-terrain conformation; (2) replacing each 2 × 2 sensor array with a single sheet sensor (Kalantari et al., 2011) for more reliable force detection, further increasing sampling frequency; (3) adding a sensor to the left, right, and bottom sides of each segment to improve overall body sensor coverage; and (4) embedding wiring inside the robot to minimize disturbance during locomotion.

2.6.1 Refined sensors

We switched to a piezo-resistive sheet sensor to reduce the number of sensors, improve wire packaging, and increase sensor area. The sheet sensor is similar to the sensor array in design and working principle, except that the conductive threads (Fig. 2.2A) were replaced with a copper conductive sheet (Copper foil sheet with conductive adhesive, 0.07 mm thickness, Adafruit Industries) on either side (Fig. 2.5A).

2.6.2 Refined robot

The refined robot, SenSnake v2 (0.96 m long, 0.036 m segment radius, 2.4 kg), has 12 segments (Fig. 2.5B) with same joint structures as the initial robot (Fig. 2.5A). To make the robot lighter, the silicone shell was replaced with a compliant, hollow shell

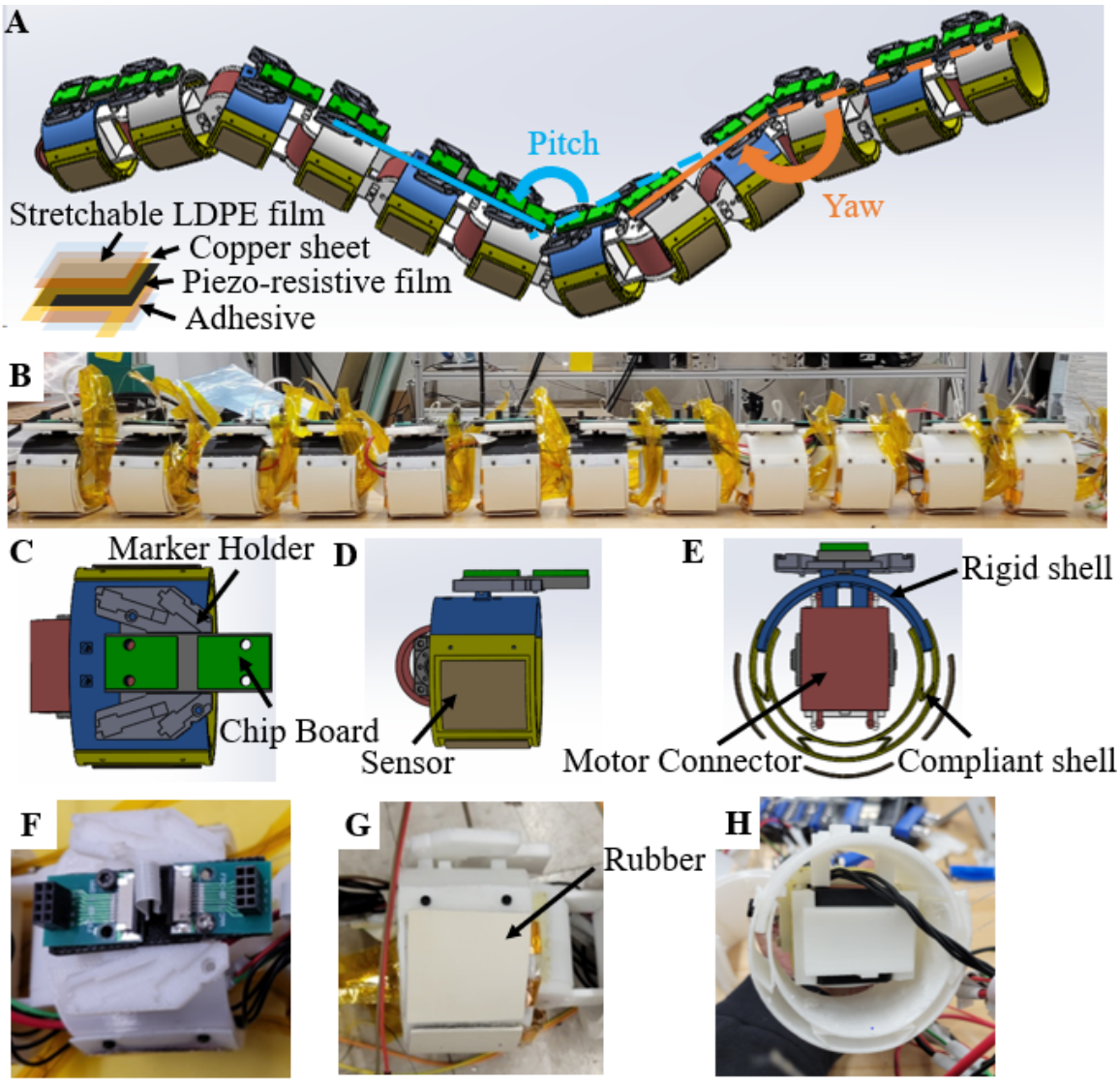

Figure 2.5: SenSnake v2 design. (A) CAD showing 3-D bending of robot. **(B)** Robot photo. Top, side, and front view CAD **(C-E)** and photos **(F-H)** of a segment.

to evenly distribute the force on the sensor (Fig. 2.5E). Because only the sides and bottom of the robot came in contact with the terrain obstacles during traversal, the rigid upper part of the shell was 3-D printed using PLA (Fig. 2.5C, blue), whereas the rest of the shell was 3-D printed soft using TPU (Fig. 2.5D, yellow).

Three sheet sensors (4 cm long, 3.5 cm wide) were distributed over majority of the soft shell (Fig. 2.5E) to detect forces on the left, right and bottom sides of each segment, totaling 36 sensors with a sampling frequency of 30 Hz. A rubber layer covered each sensor to prevent sensor wear and tear (Fig. 2.5G). We improved wiring to be enclosed inside the shell for better protection (Fig. 2.5F, H). We installed 3-D printed holders to mount LED motion capture markers to track each segment.

2.6.3 Experiments

To test how well our sensor and robot improvements solved the problems in the initial prototype and demonstrate its usefulness for understanding locomotion in complex terrain, we tested the refined robot on wooden half-cylindrical obstacle constructed from assembling laser cut boards (Fig. 2.6A-B). To reduce friction, we covered the entire surface with plastic sheet (0.254 mm polytetrafluroethylene sheet, McMaster, USA). Eight motion capture cameras (PhaseSpace IMPULSE X2) tracked 4 unique LED markers on each segment to obtain 3-D kinematics at 960 Hz (Fig. 2.5C).

We used feedforward control using Robot Operating System at a frequency of 50 Hz to propagate a pre-defined vertical bending shape down the body at 0.034 rad/s in a follow-the-leader manner. This pre-defined shape was generated by manually pushing the robot down to conform to the obstacle and recording the motor angles. The controller used linear interpolation of motor angles over time to propagate the

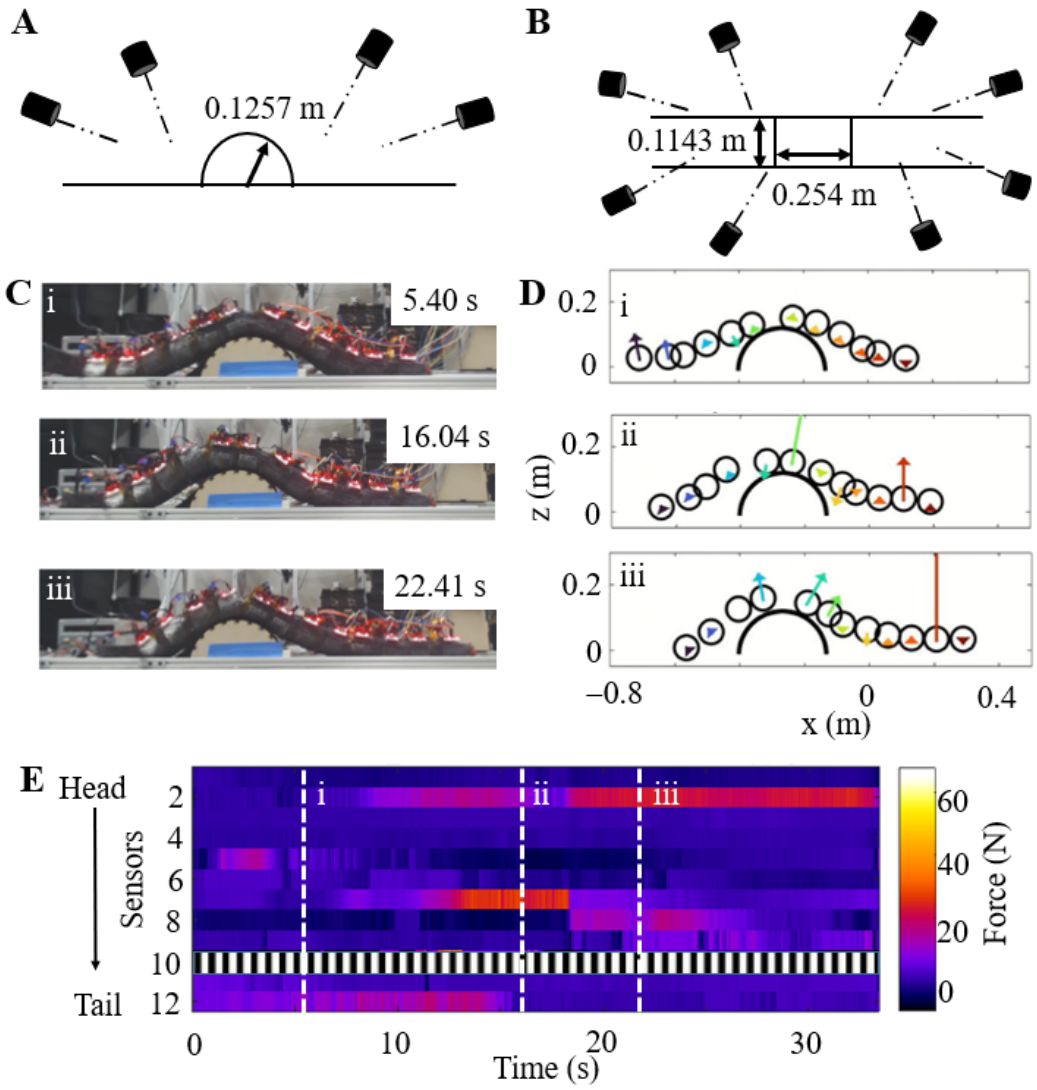

Figure 2.6: Force response generation during robot vertical bending. (A, B) Experimental setup. **(C)** Side view snapshots of robot traversing a large half-cylindrical obstacle. **(D)** Side view reconstruction of segment positions from motion capture data. **(E)** Measured force as a function of time for all sensors on bottom of the robot. White lines in B correspond to snapshot times in A. We note that sensor 10 does not give reliable force measurement due to loose sensor connection. Each sensor is individually calibrated (Eqn. 2.1). Each sensor's force data were offset by the absolute value of minimal negative value to remove artifacts of "negative pressure" from small sensor drift due to disturbance from the robot's self-deformation.

shape down the body. The robot started with the 6^{th} segment on top of middle of the obstacle, because on a flat ground a vertical bending could not generate sufficient propulsion to move it forward.

Overall, the robot conformed well to the obstacle and generated sufficient propulsion to propel itself forward to traverse the large obstacle. As the robot moved forward, all the contact forces patterns propagated backward relative to the robot (Fig. 2.6E). For the first 10 seconds after the robot started moving, forward motion was smooth (Fig. 2.6Ci), with substantial normal forces (5 N, 22% robot weight) on the segments contacting the front of the obstacle and the horizontal surface (Fig. 2.6Di). Besides supporting part of the robot weight, the normal force against the front side of the obstacle also resulted in forward propulsion.

Until the middle of the robot passed over the middle of the obstacle (Fig. 2.6Ci), the robot slowed down momentarily on the obstacle, presumably due to a relative contact. As the robot continued to propagate bending backward, the segment contacting the front side of the obstacle pushed harder and generated a very large force (23 N, 98% robot weight) (Fig. 2.6ii). This buildup of forward propulsion eventually helped the robot overcome frictional drag and slip forward rapidly, after which it resumed steady motion (Fig. 2.6C-Eiii). See multimedia material, video 3 for an example video.

We performed three trials and found excellent repeatability in the robot's motion and sensor data (Fig. 2.7A-B), achieving our main goal of providing a robotic platform for systematic experiments to understand principles (Aguilar et al., 2016; Ijspeert, 2014; Long, 2012; Gravish and Lauder, 2018).

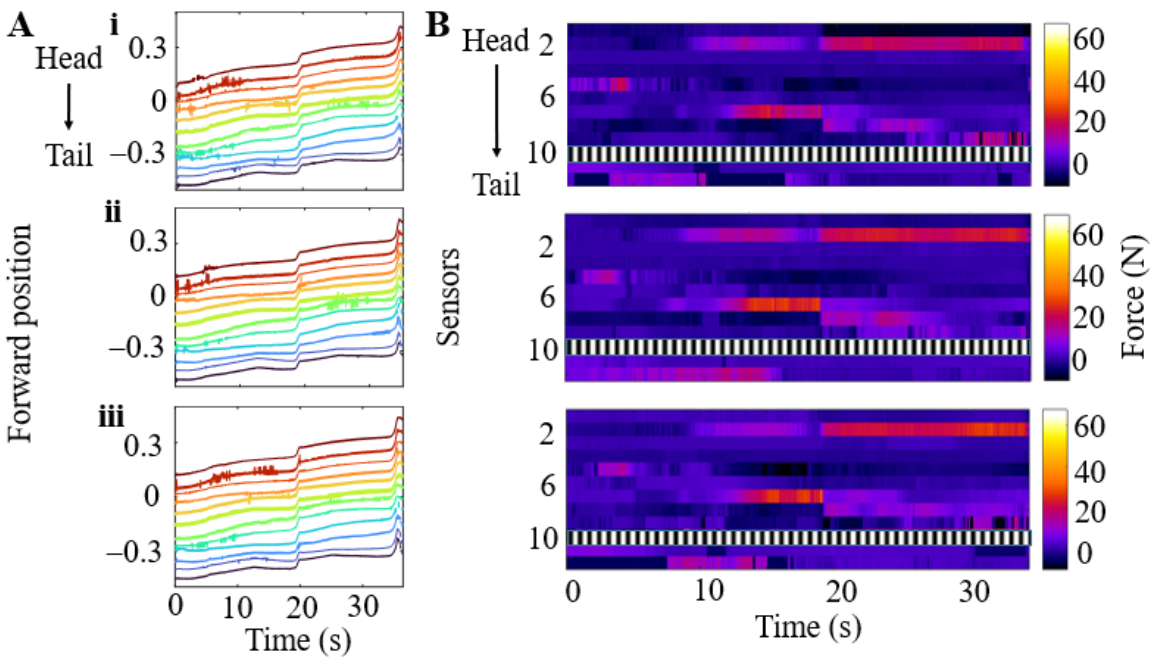

Figure 2.7: High system repeatability for robophysics studies. **(A)** Segment forward position as a function of time. **(B)** Force as a function of time for all bottom sensors. Sensor 10 does not give reliable force measurement due to loose connection.

2.7 Model-based sensor calibration

With proper design and fabrication, piezo-resistive force sensors enabled our snake robot to detect contact forces when traversing large obstacles. This is consistent with previous success in snake robots doing so against large vertical structures on horizontal surfaces (Kano and Ishiguro, 2013; Liljebäck et al., 2011; Liljebäck, Pettersen, and Stavdahl, 2010; Hirose, 1993). One distinction is that these previous studies focused mainly on using sensor data to generate locomotion in a robot. Our robot sensor development is not only to help generate locomotion, but also to provide quantitatively accurate measurements necessary for understanding the physical principles of snake propulsion generation using 3-D body bending.

For our goal, it is useful to consider the viscoelastic nature of piezo-resistive material, which causes a creep behavior of the sensor reading after force application (Brinson and Brinson, 2015). We carried out sensor modeling and calibration experiments to obtain high-fidelity force information from sensing reading, following recent work in developing a physics-based sensor model (Kalantari et al., 2011)).

2.7.1 Sensor model

Various models have been developed to model creep behaviors in viscoelastic materials under a constant stress (Brinson and Brinson, 2015). Simpler 2-parameter solid models

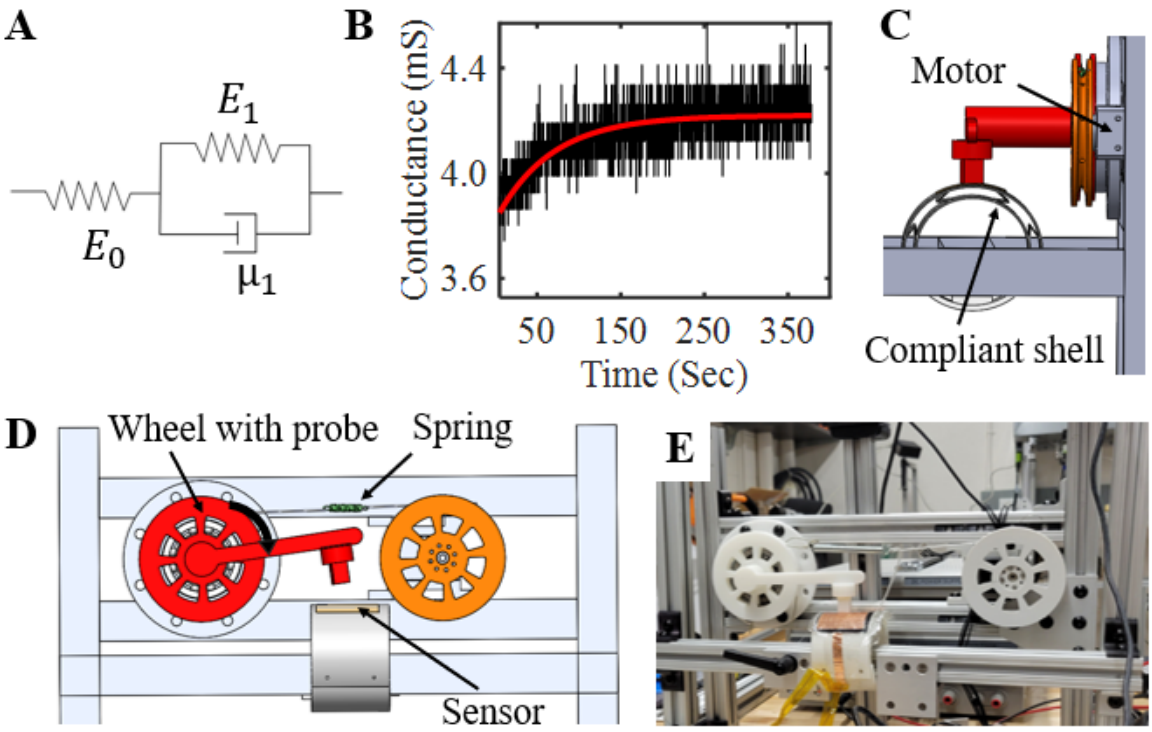

Figure 2.8: Calibration setup. (A) Sensor model. **(B)** Sensor conductance vs. time (black) and exponential fit (red) using Eqn. 9. **(C, D)** Front and side view schematics of calibration setup. **(E)** Front view photo of calibration setup.

such as Maxwell or Kelvin-Voigt models do not accurately describe creep or relaxation, respectively (Brinson and Brinson, 2015). Here, we used the 3-parameter Kelvin-Voigt representation of standard linear solid model (Fig. 2.8A) (Kalantari et al., 2011; Brinson and Brinson, 2015), which was demonstrated to accurately describe creep and relaxation in piezo-resistive material (Kalantari et al., 2011). The stress-strain dynamics from this model is:

$$\sigma + \frac{\mu_1}{E_0 + E_1}\dot{\sigma} = \frac{E_0 E_1}{E_0 + E_1}\varepsilon + \frac{\mu_1 E_0}{E_0 + E_1}\dot{\varepsilon} \tag{2.2}$$

where $\sigma = F/A$ is the stress applied, ε is the induced strain, E_0 and E_1 are elastic coefficients and μ_1 is viscous coefficient of the piezo-resistive material, F is the force applied, and A is the sensor's active area that is being deformed. Note that E_0, E_1, and μ_1 are model fitting parameters that linearly increase with the force applied (Kalantari et al., 2011), not constant material properties.

In addition, a previously developed physics model well describes the physical mechanism of how sensor deformation leads to resistance change (Kalantari et al., 2011). The resistance-strain relationship from this model is:

$$R_s = \frac{\rho_1 + \rho_2}{2}\sqrt{\frac{\pi H}{F}} + R_0(1-\varepsilon)e^{-\gamma D\varepsilon[\frac{\pi}{6\phi}\frac{1}{3}-1]} \tag{2.3}$$

where R_s is the total resistance measured, ρ_1 and ρ_2 are the resistivities of the piezo-resistive and conductive materials, respectively, H is the hardness of the material that measures the material's resistance to localized plastic deformation, R_0 is the initial resistance of the piezo-resistive material (2.58 kΩ), D is the filler particle diameter

(500 nm), and ϕ is the volume fraction of filler particles (0.2873). γ is defined by:

$$\gamma = \frac{4\pi}{h}\sqrt{2m_e\varphi} \tag{2.4}$$

where h is the Plank's constant, m_e is the mass of an electron, and φ is the potential barrier height between two adjacent filler particles (0.05 eV). Parameter values are from (Kalantari et al., 2011).

2.7.2 Model parameter estimation

The sensor model parameters E_0, E_1, and μ_1 are estimated using the least squares parameter estimation method (Soderstrom and Stoica, 1989). The strain ε is estimated using the Eqn. 2.3 for a given constant force and the measured R_s. The stress-strain dynamics in Eqn. 2.2 can be rewritten as:

$$\sigma + a\dot{\sigma} = b\varepsilon + c\dot{\varepsilon} \tag{2.5}$$

where:

$$a = \frac{\mu_1}{E_0 + E_1}, b = \frac{E_0 E_1}{E_0 + E_1}, a = \frac{\mu_1 E_0}{E_0 + E_1} \tag{2.6}$$

The stress-strain system can be further rearranged:

$$\sigma = \phi\theta, \phi = \begin{bmatrix} \varepsilon & \dot{\varepsilon} & -\dot{\sigma} \end{bmatrix} \tag{2.7}$$

If ϕ is a non-singular matrix, then the following equation can be used to estimate θ and the model fitting parameters:

$$\hat{\theta} = (\phi^T \phi)^{-1} \phi^T \sigma = \begin{bmatrix} \hat{b} & \hat{c} & \hat{a} \end{bmatrix}^T \tag{2.8}$$

An exponential fit of the sensor conductance C_{fit} was used to estimate the sensor model parameters:

$$C_{fit} = c_1 + c_2 e^{-c_3 t} \tag{2.9}$$

We estimated c_1, c_2 and c_3 for each trial by finding the least root mean square error fit while constraining their ranges so that the fit visually matched maximal and minimal conductance values.

2.7.3 Calibration setup

We developed a calibration system to calibrate the sensors systematically and repeatedly. A servo motor rotates a 3-D printed wheel (Fig. 2.8D, orange), which tries to rotate another wheel through a cable with a spring (stiffness = 246 N/m) to push a probe against the sensor. The spring allows the pushing wheel (Fig. 2.8D, red) to stop rotating while generating a controlled force that can be measured by measuring spring deformation. During calibration, we attached a fully assembled segment onto an aluminum beam and actuated the motor to apply a constant force for 370 s at a sampling frequency of 6 Hz. We tested four different constant forces, 1.75, 3, 4 and 5.25 N, and collected 3 trials each (multimedia material, video 4).

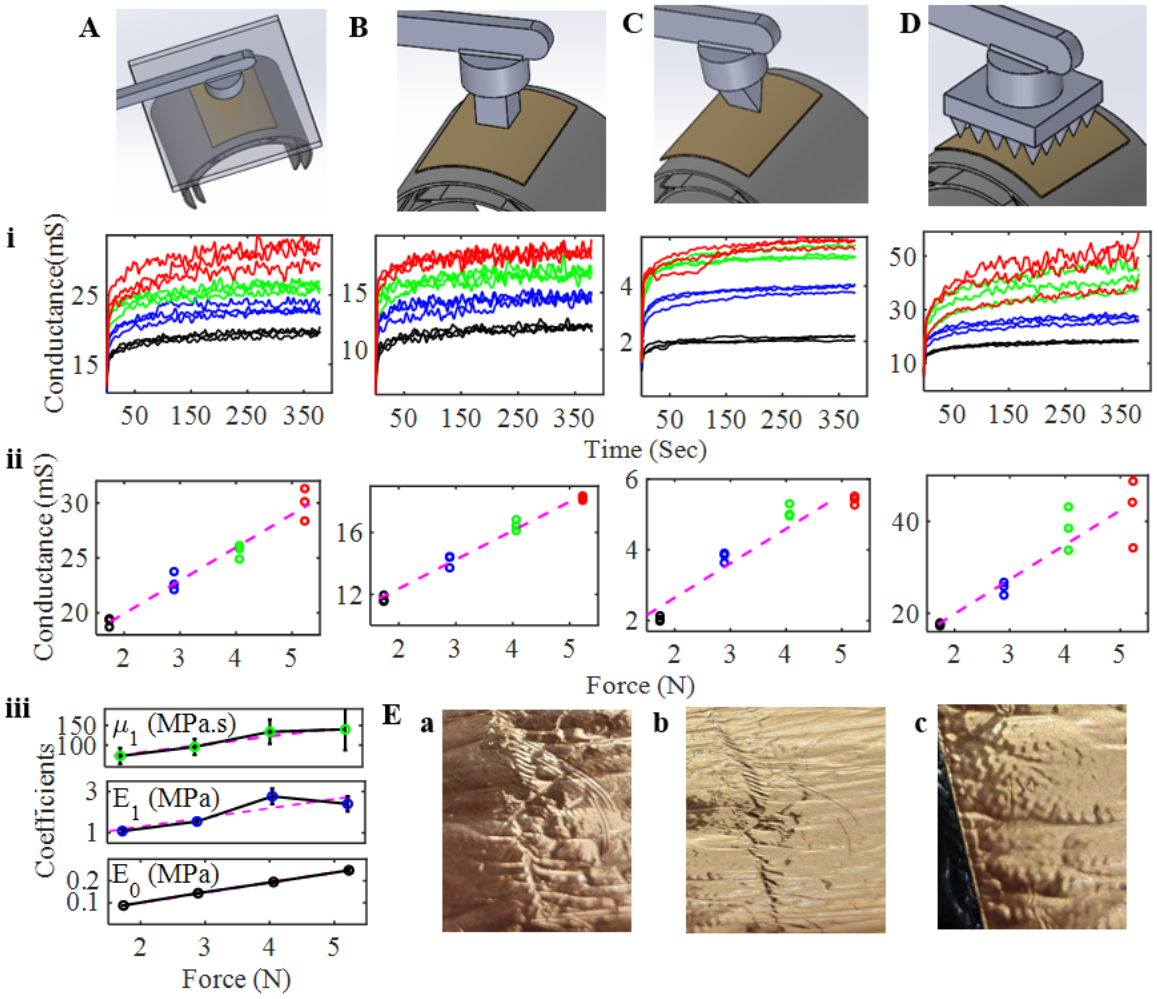

Figure 2.9: Model-based sensor calibration results. **(A)** Large flat probe. **(B)** Small flat probe. **(C)** Sharp edge probe. **(D)** Multi-point probe. (i) Measured sensor conductance as a function of time for four different constant forces. (ii) Average conductance after 300 s using data in (i) as a function of applied force. (iii) Model fitted sensor parameters (Eqn. 2.6) as a function of applied force using large flat probe. **(E)** Damaged sensor from multiple trials using probes in B-D. The dashed lines in (ii) and (iii) indicate linear fit lines. Black, blue, green, and red are for applied forces of 1.75, 3, 4, and 5.25 N.

2.7.4 Choice of calibration probe

In complex 3-D terrain, the robot may push against various objects, resulting in flat surface (Fig. 2.9A-B), edge (e.g., Fig. 2.9C), corner, or point (Fig. 2.9D) contact. These diverse contact conditions may affect the repeatability of the sensors and fidelity of sensor model, but few studies considered their effects (Kalantari et al., 2011; Cholleti et al., 2021). To test how robust our sensors and model-based calibration is, we tested four probes simulating different types of contact: a large flat probe covering the entire sensor (Fig. 2.9A), a small flat probe (Fig. 2.9B), a sharp edge probe (Fig. 2.9C), and a multi-point probe (Fig. 2.9D).

For the large and small flat probes, all three estimated parameters increased linearly with force (Fig. 2.9A, B, iii), consistent with previous observations (Kalantari et al., 2011). However, for the sharp edge and multi-point probes, the estimated parameters increased less linearly as force increased (Fig. 2.9C, D, ii). In addition, the piezo-resistive sensor layer creased substantially after repeated calibration tests with the small flat, sharp edge, and multi-point probes (Fig. 2.9E). Close observations of probe-sensor interaction during calibration showed that the local shape of the compliant shell changed significantly with forces concentrated on small contact areas, likely contributing to sensor creases (multimedia material, video 5).

These observations are informative for our future systematic robophysics experiments. To ensure high-fidelity force data to gain principled understanding of locomotion in complex 3-D terrain, it is more practical to design terrain testbeds with large obstacles that are sufficiently smooth to minimize edge or corner contact so that the resulting forces can be well described by the sensor model. Certainly, sensors more robust to such contacts inevitable in the real world still need to be developed

for robotic applications.

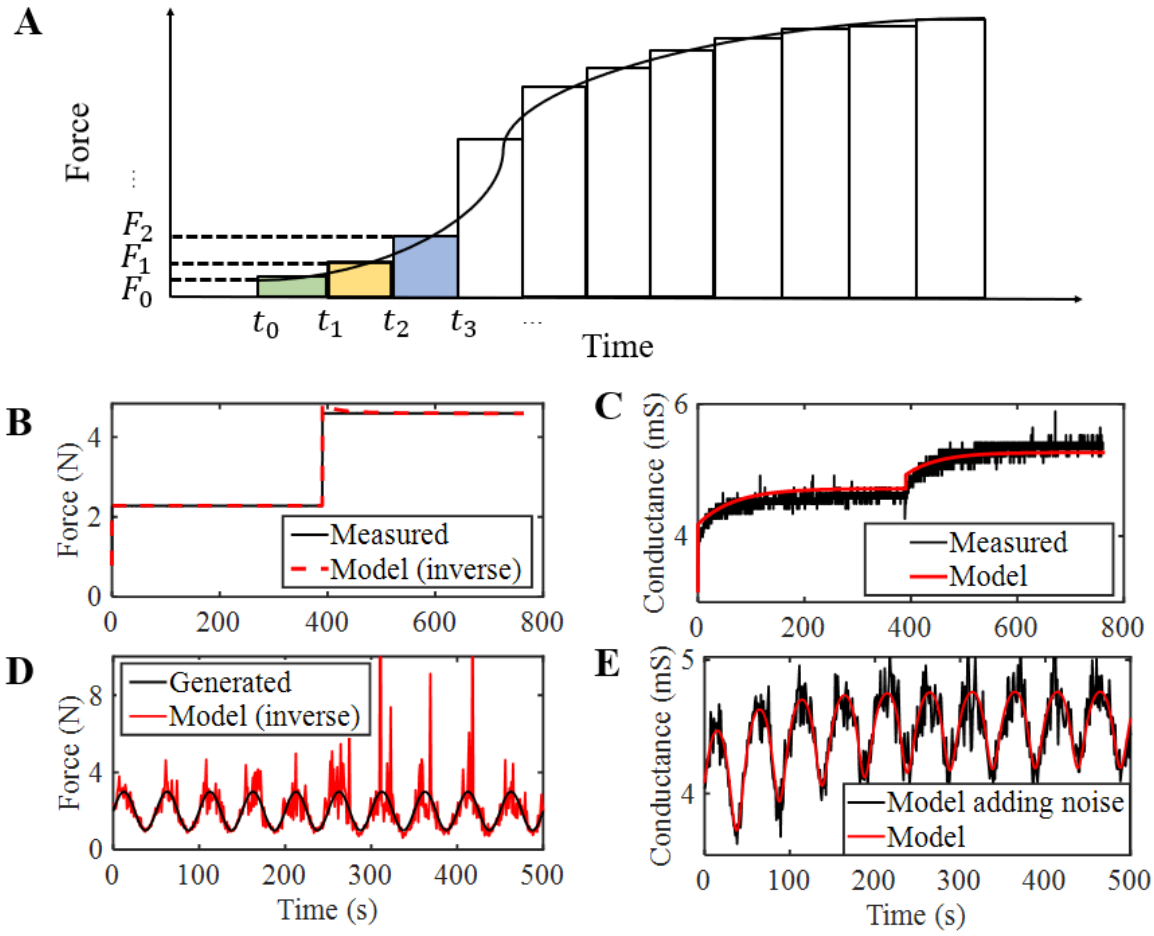

Figure 2.10: Proof of concept of model-based dynamic force estimation. **(A)** Idea of dynamic force decomposition using Boltzmann superposition principle. **(B, C)** Proof of concept using 2-step force input. **(B)** 2-step force measured using calibration setup (black) vs. estimated from model (red). **(C)** Sensor conductance measured (black) vs. estimated (red) using 2-step force. **(D, E)** Proof of concept using sinusoidal force. **(D)** Sinusoidal force input generated mathematically (black) vs. estimated from model (red). **(E)** Sensor conductance estimated using sinusoidal force (red), with Gaussian noise added (E, black) to simulate real data.

2.7.5 Dynamic force measurement using the sensor model

The piezo-resistive sensor's creep occurs with a characteristic time of 102 s (Fig. 2.8B), longer than typical periods (10^{-1}–10^{1} s) of most robot locomotion (although soft robots can be as slow as this creep behavior (Rus and Tolley, 2015)). Because of this, creep behavior was not considered in most previous mobile robot studies with piezo-resistive force sensors (Liljebäck, Pettersen, and Stavdahl, 2010; Shill et al., 2014; Wu et al., 2019; Kamegawa et al., 2020; Li et al., 2021). In preliminary experiments, we found that the snake robot can easily become stuck when attempting to move in complex 3-D terrain resulting in sustained contact. In this case, considering sensor creep behavior is necessary for estimating dynamic forces accurately.

To do so, we can decompose dynamic forces into multiple infinitesimal phases and fitting the sensor model to each phase, using the Boltzmann superposition principle (Brinson and Brinson, 2015; Huseby and Matsuoka, 1967) (Fig. 2.10A):

$$\varepsilon(t) = \sigma_0 J(t) + \int_{0^+}^{t} J(t-\tau)\frac{d\sigma(\tau)}{d\tau}d\tau \tag{2.10}$$

where σ_0 is the initial stress applied at $t = 0$, τ is the time that measures dynamic changes in stress $\sigma(t)$ (which does not exist for a constant force), 0^+ denotes the time after the initial stress is applied, and $J(t)$ is defined as:

$$J(t) = \frac{\varepsilon(t)}{\sigma(t)} = \frac{1}{E_0} + \frac{1}{E_1}(1 - e^{-\frac{E_1}{\mu_1}t}) \tag{2.11}$$

For example, the resulting strain for the force in Fig. 2.10A is (where A is sensor

active area):

$$\varepsilon(t) = \frac{F_0}{A} J(t) + \frac{F_1 - F_0}{A} J(t - t_1) + \frac{F_2 - F_1}{A} J(t - t_2) + \dots \tag{2.12}$$

We first tested how well this works for a simple 2-step force input (Fig. 2.10B, black) measured from the calibration setup. We applied the model (Eqns. 2.2 and 2.3) using the superposition principle (Eqn. 2.10) to estimate the resulting sensor conductance (Fig. 2.10C, red), which well matched the measured conductance (Fig. 2.10C, black). We then applied the model using the superposition principle in the reverse direction, using the measured sensor conductance (Fig. 2.10C, black) as input to estimate the force applied (Fig. 2.10B, red), which well matched the measured force (Fig. 2.10B, black).

Next, we tested how well this works for a dynamic, sinusoidal force input (Fig. 2.10D, black), which is generated mathematically and free of noise. We applied the model using the superposition principle to estimate the resulting conductance (Fig. 2.10E, red), which is also noise-free. Next, we added Gaussian noise to the resulting conductance (Fig. 2.10E, black) to simulate real measured conductance data. Then we applied the model using the superposition principle in the reverse direction, using the simulated sensor conductance (Fig. 2.10C, black) as input to estimate the force applied (Fig. 2.10D, red). Despite the noise, it well matched the sinusoidal force input (Fig. 2.10D, black).

2.8 Summary & future work

To provide a platform for studying how to use contact force sensing to modulate 3-D body bending to propel against 3-D terrain for locomotion, we developed a snake robot with contact force sensors distributed along its entire body. Through two development and testing iterations, our robot was able to obtain contact force measurements while moving over a large obstacle with high repeatability required for systematic studies. Our next step is to add feedback control using force estimated by the model from the sensor readings, so that the robot can adjust body bending to better conform to and push against complex 3-D terrain (Fu and Li, 2021).

Chapter 3

Control and characterization of mud strength for studying locomotion on wet flowable substrates

This chapter is to be submitted as an article entitled *Control and characterization of mud strength for studying locomotion on wet flowable substrates*, authored by Divya Ramesh, Gargi Sadalgekar, Qiyuan Fu, Zachary Souders, Jack Rao, and Chen Li, in the Journal of Experimental Biology (Ramesh et al., 2024a). It will be in revision at the time of submission of this dissertation.

3.1 Author Contributions

Conceptualization: Chen Li; methodology: Divya Ramesh, Qiyuan Fu, Jack Rao, Chen Li; validation: Divya Ramesh, Qiyuan Fu, Gargi Sadalgekar, Zachary Souders; investigation: Divya Ramesh, Gargi Sadalgekar; data curation: Divya Ramesh; writing: Divya Ramesh, Chen Li; visualization: Divya Ramesh, Chen Li; supervision: Chen Li; project administration: Chen Li; funding acquisition: Chen Li.

3.2 Acknowledgment

We thank Luke Moon and Mia Urban for the preliminary mud experiments, Kapi Ketan Mehta for assisting in the mud experiments, Lucas An and Milla Ivanova for mud preparation for experiments, and Jiangqi Tan for helping in mud characterization during animal experiments.

This study was funded by the Burroughs Wellcome Fund Career Award at the

Scientific Interface and a Johns Hopkins University Bridge Grant.

3.3 Summary

Some animals regularly interact with mud of varying strengths in muddy terrains, riverbeds, and at the water–land interface. Despite mud being challenging to move on, animals can adapt to substrate variation as they interact with the substrate. To understand this substrate-locomotor interaction mechanics, it is important to prepare substrate at desired strength and, control and maintain the strength throughout the animal study because the yield strength varies with water content. Tools and methods have been established for controlling and maintaining the substrate strength of dry and wet sand, but it is still yet to be established for mud due to difficulty in controlling and maintaining desired strength. There has been no previous study of animal locomotion on mud with varying mud strength yet. In this study, we developed tools and methods to control and characterize mud and have shown we can control and maintain mud strength during experiments.

3.4 Introduction

Some animals regularly interact with various substrates of different sizes ranging from boulders, pebbles, gravel, sand, silt, clay, and snow in nature. These substrates are considered flowable if the particle size is much smaller than the size of the animal. Substrates with particles that flow when force is applied are considered to be flowable substrates. The natural environment often contains a mixture of flowable substrates which makes the animal-substrate interaction complex and difficult to study.

Flowable substrates can have particles of varying sizes (Fig. 3.1A). Boulders and pebbles (Mehta et al., 2021; Standen et al., 2016) are larger compared to small animals and hence are more close to uneven, mostly rigid terrain ($>$ 2 cm, Fig. 3.1A). We only consider substrates with particles that are much smaller in size compared to animals to be flowable substrates ($<$ 2cm, Fig. 3.1A). These particles (Fig. 3.1A) can be categorized either as mostly coarse grains (gravel, coarse and fine sand), or mostly fine clay (silt and clay) (Coussot, 1997). Substrates with mostly coarse grains have no grain-grain cohesion and have weaker cohesion when water is added whereas mostly fine clay substrates have stronger cohesion between the particles and water due to colloidal effects (Coussot, 1997). This makes fine clay substrates much weaker compared to mostly coarse grains substrates.

Wet flowable substrates can also behave differently depending on the water content. For example, mud with high water content acts similar to a viscous fluid (Fig. 3.1C-D) whereas mud with low water content acts as a fractured solid (Fig. 3.1C-D). The solid–fluid transition occurs at the intermediate concentration of water in mud (Fig. 3.1C-D). We can control this water content using solid volume fraction (ϕ) which is defined as the volume of solid by the volume of both solid and water prior to mixing. Natural mud can consist of both fine clay and some coarse grains, which complicates the controllability of this mud because its strength is a function of not only the solid volume fraction but also a percentage of fine clay among the solid particles. Clay mud with no coarse grain is an ideal choice for a controllable wet flowable substrate because it behaves qualitatively similar to that of natural mud and its strength is only a function of the solid volume fraction.

Wet flowable substrates such as mud and wet sand vary in solid composition

and wetness and are often found in muddy terrains, riverbeds, and at the water–land interface (Clack, 2012; Perry et al., 2015; Wendt et al., 1997). These substrates can behave similarly to a solid or flow similar to a liquid depending on the forces applied relative to yield strength (Coussot, 1997) which makes it a challenge for the animal to locomote. This yield strength at the solid–fluid transition also varies depending on the wetness or dryness of the substrate. Wet substrates such as mud can also stick to the animal's body and appendages due to strong cohesion from colloidal effects (Coussot, 1997) which then affects the animal's locomotion. Despite these challenges, animals can transition between different strategies and adapt to substrate variation

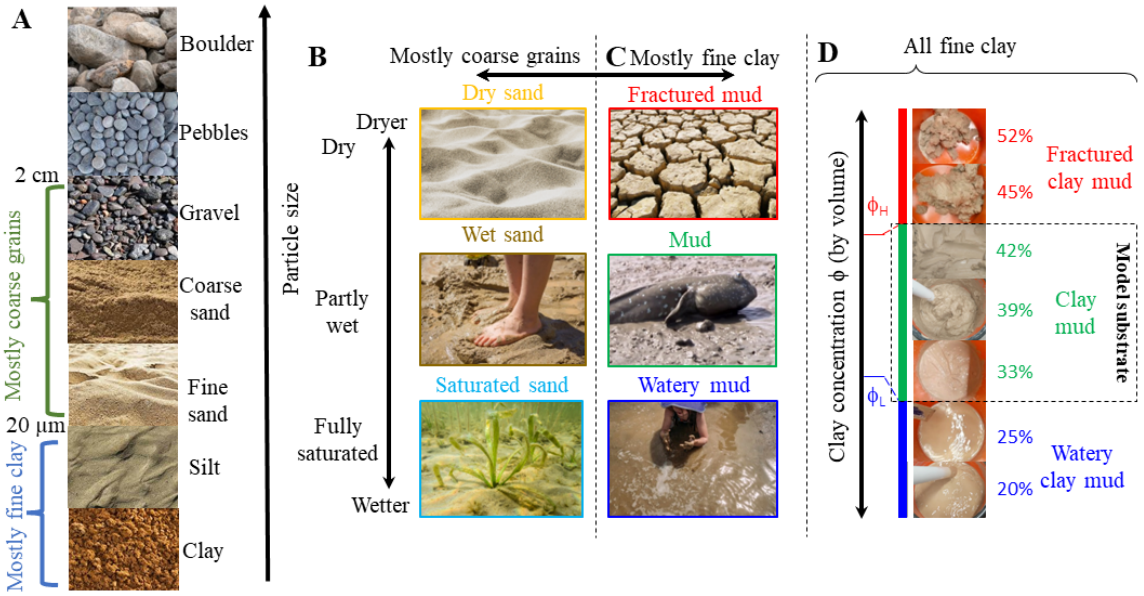

Figure 3.1: Substrate types. (A) Types of substrates vary in particle size (Image courtesy of Google images). **(B)** Mostly coarse grains such as sand varied with strength. **(C)** Mostly fine clay such as mud varied with strength. **(D)** Clay mud varied with strength which is dependent on solid volume fraction (ϕ) only. ϕ_H is the upper bound and ϕ_L is the lower bound for the solid–fluid transition regime for Georgia Kaolin mud. Image Courtesy of (A) Google Images, Getty Images, CMM Landscape Supply, Wikipedia, and Bryan's Lawn Maintenance, (B) Google Images and iStock, (C) Posterazzi, BBC, and Google Images.

during locomotion as they interact with the substrate.

To understand the animal-substrate interaction mechanics for a specific substrate, several animal and robot studies have been performed in a lab setting (Astley et al., 2020; Dorgan, 2018; Mazouchova et al., 2010; Naylor and Kawano, 2022; Redmann et al., 2020). There have been many animal and robot locomotion studies on dry (Astley et al., 2020; Hall, McGowan, and Lin, 2022; Li, Hsieh, and Goldman, 2012; Maladen et al., 2009; Mazouchova et al., 2010; McInroe et al., 2016; Naylor and Kawano, 2022; Schiebel et al., 2020; Tao, Huang, and Tang, 2020; Marvi et al., 2014), wet (Kudrolli, Ramirez, and Weitz, 2019; Sharpe, Kuckuk, and Goldman, 2015), and saturated sand (Dorgan, 2018; Redmann et al., 2020; Tao, Huang, and Tang, 2020) but only a few studies have focused on mud (Falkingham and Horner, 2016; Godon et al., 2024; Horner and Jayne, 2008; Liang et al., 2012; Lutek and Standen, 2021; Naylor and Kawano, 2022; Zhang et al., 2016) especially in the solid–fluid transition regime. There are only a few studies in amphibious fishes on thick clay mud (Falkingham and Horner, 2016; Standen et al., 2016; Horner and Jayne, 2014; Naylor and Kawano, 2022) and only two studies have investigated amphibious fishes moving on viscous fluids that behave similar to mud with different viscosities (Horner and Jayne, 2008; Lutek and Standen, 2021). There are no animal studies on mud with systematic variation of mud strength yet where the interaction mechanics have been investigated due to difficulty in controlling and maintaining mud strength.

To understand the substrate-locomotor interaction mechanics, it is important to prepare the substrate at a desired strength and control and maintain the substrate strength throughout animal study. This is especially important in animal studies whose duration spans several days. These tools and methods have been well established

for dry sand by using an air fluidized bed (Li et al., 2009; Maladen et al., 2009) to prepare and maintain sand at the desired volume fraction using air blown into the testbed at different pulses and wet sand using a sieve apparatus (Sharpe, Kuckuk, and Goldman, 2015) that uses a shaker table to allow the media to fall easily through the sieve from the vibration generated by the shaker. Despite having a systematic variation in the water content of mud-sand mixtures (Liu, Huang, and Qian, 2023) and mud (Liang et al., 2012; Zhang et al., 2016) in some robot studies, there are no methods or equipment established yet for preparing, controlling, and maintaining mud strength during the study and storage.

In this study, we will show how we can systematically prepare mud with different mud strengths in large quantities and how well we can maintain mud strength from our mud characterization methods and tools which the previous studies were unable to do. We will characterize mud using the penetration resistance which is often used in measuring the strength of soil. Through the mud characterization, we will show that we can perform systematic and controlled experiments enabling us to study how the animal copes with varying mud strength and how the mud sticking to the animal's body and appendages affect locomotion which has been difficult to do till now.

3.5 Materials and Methods

3.5.1 Choice of clay mud for the study and its preparation

Because kaolin mud (Coussot, 1997) is readily available, we used Georgia Kaolin (China Clay, Old Hickory Clay Company, Florida, USA) as the choice of clay mud for mud characterization and Edgar Plastic Kaolin (EPK) clay (Edgar Minerals,

USA) for our preliminary mud experiments. To prepare mud uniformly, we developed an automatic mixing system (Fig. 3.2A-B). This system consists of an automated stand mixer (ACA, model A86208, JEAHII, Guangzhou KeYue Technology Co. Ltd., Guangzhou, China) to mix the mud evenly. It also has a custom-made dipper that pushes the mud powder into the bowl filled with water periodically every 0.5 seconds using a rotating cam that is controlled by a 12 V DC motor. Based on the desired ϕ, we estimated the weight of kaolin needed for a given weight of tap water. We used mud with mud strength varying in the intermediate regime ($\phi_L < \phi < \phi_H$). We characterized mud strength with ϕ = 20%, 25%, 27%, 34%, 39%, 41%, and 42% for Georgia Kaolin mud characterization and ϕ = 14%, 27%, 34%, and 39%, for EPK mud characterization.

3.5.2 Experimental testbed with higher mud depth to reduce boundary effects

We used a container (HOMZ, Chicago, IL, USA) that is 1.02 m in length, 0.51 m in width, and 0.16 m in height to hold the clay mud during experiments and storage

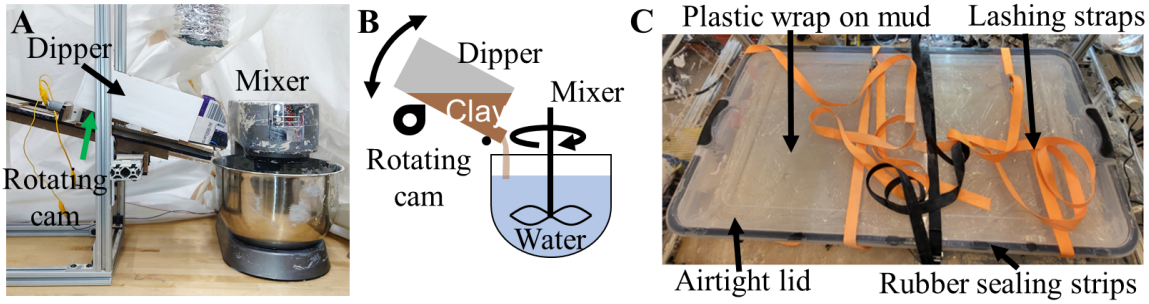

Figure 3.2: Mud preparation and storage during experiments. (A) Automated mud preparation system. **(B)** Schematic of the automated mud preparation system. **(C)** Sealed testbed to prevent and reduce water loss between experiments.

(Fig. 3.2C). When there is mud with low depth in the tub (Fig. 3.6A), the intruder during mud characterization will be affected by boundary effects from the bottom of the tub. Boundary effects are defined as artifact forces applied on an object as it moves near the container's boundary (Coussot, 1997). This hence causes an increase in the slope of the force as a function of depth profile when the intruder is close to the boundary (Fig. 3.6B). To avoid the effects, the container was filled with mud up to at least $3/4^{th}$ of the tub height.

3.5.3 Sealing method to minimize water loss during storage

The sides of the lid of the container used for the experiments were covered with rubber sealing strips (CloudBuyer) to further make the lid airtight and prevent water drops from escaping through the sides of the lid (Fig. 3.2C). We placed a plastic wrap directly over the mud to minimize water evaporation at the mud surface to the top of the lid during storage (Fig. 3.2C). We then placed lashing straps (ACE-Lashing Straps, Acelane) around the closed container to tighten the lids further onto the container (Fig. 3.2C).

To test how well the sealing method works, we characterized EPK mud with ϕ = 39% on four different locations (3 trials each) over the course of 1 hour (7 trials with an interval of 10 minutes) using a geotester pocket penetrometer (Gilson company inc, Ohio, USA), which is the normal duration of animal experiments in a day. The penetration force measured for each location was then used for spatial comparison of mud strength. The penetration force across the four locations was averaged for each time interval for temporal comparison. The deviation of the force averaged spatially and temporally was then overlaid with force measurement for ϕ = 39% and

compared with averaged force measurements for $\phi = 14\%$, 27%, and 34% from mud characterization at a depth of 0.64 cm.

3.5.4 Automated vertical penetration device to characterize mud

We developed an automated vertical penetration device to characterize mud (Fig. 3.3A-B) by measuring force as a function of depth across different ϕ. This device consists of a Dynamixel motor (XM430-W350-R) programmed to move the intruder by 4.96 cm into and out of the mud at 0.31 cm/s. The motor rotation is translated to linear displacement using a threaded rod (12" lead screw, 1/4"-16 thread size,

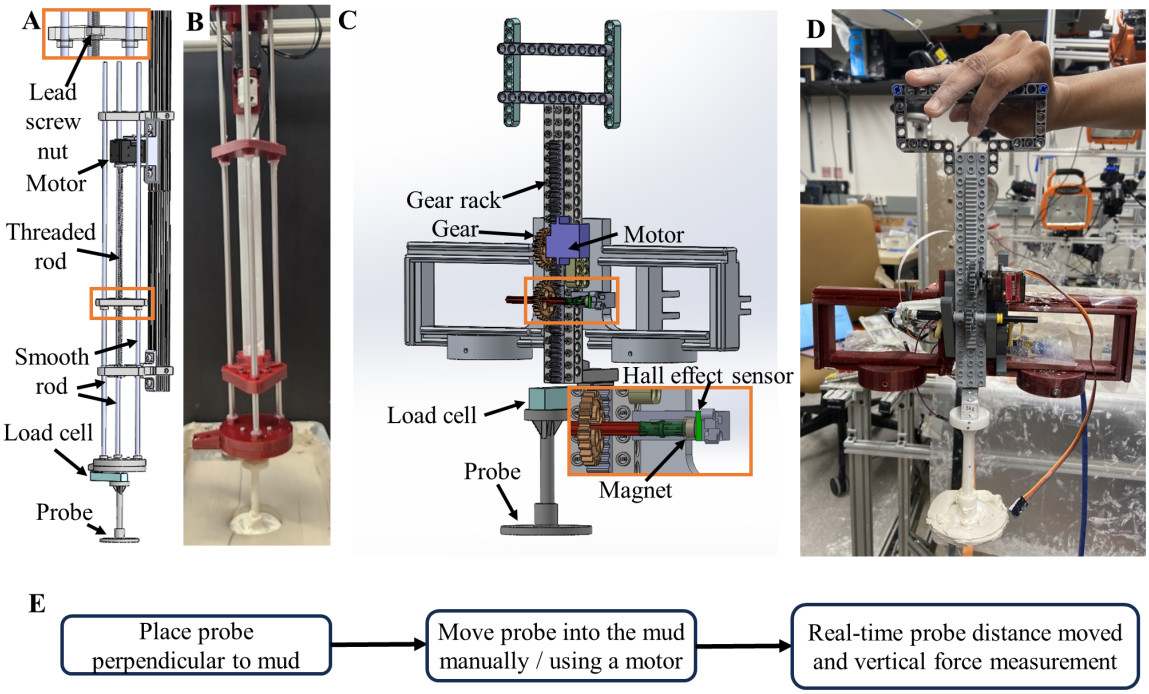

Figure 3.3: Mud characterization tools. (A) Automated vertical penetration device CAD. **(B)** Automated vertical penetration device. **(C)** Custom portable penetrometer CAD. **(D)** Custom portable penetrometer. **(E)** Block diagram of the penetration device control system.

McMaster-Carr, Princeton, NJ, USA) connected to the motor shaft (Fig. 3.3A). A 1-D force sensor (Strain gauge load cell, 5 kg, S18X4) is connected to the intruder to estimate forces. The load cell mount is connected to the threaded rod using three smooth rods (24" Linear Motion Shaft, 1/4" diameter, McMaster-Carr, Princeton, NJ, USA) and is fixed to the threaded rod by a lead screw nut (Fig. 3.3A). The probe area was reduced for higher ϕ to make it easier for the probe to penetrate the mud without large resistance. The automated penetration device was secured to a frame made up of T-slotted framing (McMaster-Carr, Princeton, NJ, USA) to ensure that the probe was placed perpendicular to the mud surface (Fig. 3.3E). The load cell readings were collected using an Arduino nano (Arduino.cc). We used MATLAB to control the motor and collect the load cell reading in real time (Fig. 3.3E).

The force estimated from the load cell had small oscillations in the data due to the small movement in the threaded rod which were removed by filtering the data using a band stop filter. The displacement was estimated from the motor position. The force and displacement data were synchronized using time from the motor data and then cropped to start when the intruder contacted the mud surface using the load cell measurements. The force readings were then normalized such that all the forces were based on the same probe area. To ensure that the displacement measured is perpendicular to the mud surface, it was calibrated so that the displacement reading was closer to the ground truth displacement using the linear relationship between the two displacements. The ground truth displacement was measured from the position of the intruder tracked using DLTdv digitizing tool (Hedrick, 2008; https://biomech.web.unc.edu/dltdv/) from the side view camera video taken during penetration over 3 trials.

3.5.5 Custom portable penetrometer to maintain mud strength during animal study

To perform animal experiments over several days, we need to track the water loss each day and maintain the mud strength during experiments. To maintain repeatability, we needed to characterize the mud strength at the end of each animal trial on disturbed mud. This was difficult to do using the automated vertical penetration device due to its bulkiness. The commercial penetrometers available are lightweight but are not sensitive enough to detect forces on weaker mud. So, we developed a custom portable penetrometer that uses the same mechanism as the automated vertical penetration device to characterize mud across multiple locations on the testbed (Fig. 3.3C-D).

The custom portable penetrometer also uses a 1-D force sensor (Strain gauge load cell, 5 kg, S18X4) that is connected to the intruder probe to detect forces. A gear rack and a gear (LEGO, Billund, Denmark) were used to convert the motor rotation into a linear motion (Fig. 3.3C-D). A servo motor (MG90S) was used to passively add resistance when powered to help move the probe slowly on mud with weaker ϕ (Fig. 3.3C-D). To measure the displacement of the probe, a hall effect sensor (AS5048B, AMS, Austria) was used (Fig. 3.3C). One end of the axle connected to the gear is attached with a magnet whose rotation is detected using the hall effect sensor (Fig. 3.3C). We used an Arduino Nano (Arduino.cc) to get the load cell and hall effect sensor readings and MATLAB to receive the data in real-time (Fig. 3.3E). The diameter of the probe used for higher ϕ was reduced to penetrate the mud easily without much resistance. We placed the penetrometer over a frame made up of T-slotted framing to ensure that the probe was perpendicular to the mud surface.

The linear displacement was measured using the angular displacement readings

from the hall effect sensor. The load cell reading was used to find the initial contact with the mud by the probe during penetration. The initial contact with the mud was then used to crop the linear displacement and vertical force data to start at the initial contact. The linear displacement was corrected using displacement calibration. The vertical force was then split into penetration force and extraction force by estimating the end of penetration, start, and end of lift force using the displacement and time data. The penetration force and displacement were first cropped to have the data up to 3 cm in depth. The force was then interpolated to have the same range of displacement across different trials. This force was then normalized such that all the forces were based on the same probe area. The interpolated penetration force was averaged across different trials and locations for each penetration test completed in a day. To compare across all the mud strengths, the penetration force ranged over 0 to 1 cm in depth. We also tested the performance of the custom portable penetrometer by comparing its mud characterization with the mud characterization from the automated vertical penetration device.

3.5.6 Mud characterization to choose mud strength for animal experiments and tracking mud strength during animal experiments

Clay mud with mud strengths varying from $\phi = 20\%$ (weak mud) to $\phi = 42\%$ (strong mud) was characterized using the automated vertical penetration device to choose different ϕ that varied drastically in terms of penetration force for experiments. We chose $\phi = 27\%$ because it is close to the lower limit of the solid–fluid transition regime. We also chose $\phi = 34\%$, 39%, and 42% which are in the solid–fluid transition regime. We also chose dry mud (very high ϕ) in the fractured mud regime. We prepared the

dry mud by drying out the water content over several days after the wet mud was flattened in a container.

We performed animal experiments and collected penetrometer data over a total of 6, 8, 5, 8, and 1 day for ϕ = 27%, 34%, 39%, 42%, and dry mud respectively. We used the custom portable penetrometer to characterize mud strength spatially on the disturbed mud after animal trials every 1 hour for over 18 locations for the first three penetration tests on Day 1 and 4 locations after Day 1 because the mud was found to be spatially uniform. For days when we had very few animal trials that lasted less than an hour, we only completed one penetration test over 18 locations. On ϕ = 39%, we still performed penetration tests over 18 locations for each day because the penetrometer was improved despite showing spatial uniformity to ensure repeatability in the mud characterization results. We characterized mud across 4 locations with 3 trials each for dry mud.

3.6 Results

3.6.1 Comparison of automated vertical penetration device and custom portable penetrometer

During intrusion, when the intruder is pushed into the mud, there is a lift force due to the hydro-static-like pressure from the mud. During extraction, when the intruder comes out of the mud, there is a force exerted from the hydro-static-like pressure in the opposite direction due to mud sticking to the intruder's base. This lift force increases with depth when the intruder is pushed in. There is a decrease in negative force as depth reduces when the intruder is lifted off the mud (Fig. 3.4A-B). Our

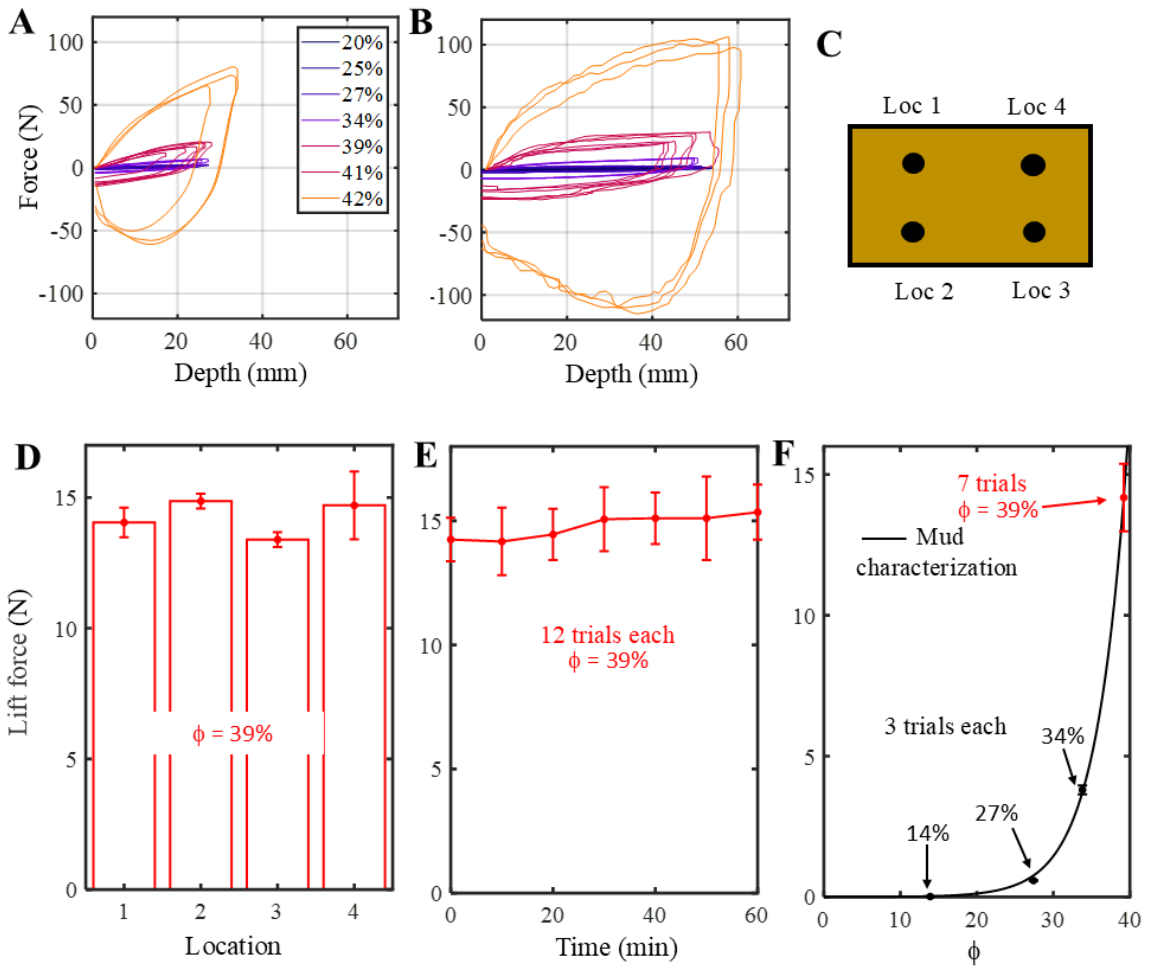

Figure 3.4: Mud characterization. **(A)** Mud strength for Georgia Kaolin is characterized by vertical force from penetration and extraction as a function of depth measured using an automated vertical penetration device. **(B)** Mud strength for Georgia Kaolin is characterized by vertical force from penetration and extraction as a function of depth estimated using a custom portable penetrometer. Color in (A) and (B) for each mud strength is a function of force at 1 cm. **(C)** A schematic of the four locations on mud used to test water loss during storage. **(D)** Lift force over the four locations with 3 trails each shows spatial uniformity after resetting disturbed mud. **(E)** Lift force as a function of time over four locations with 3 trials each showing minimal drift in force due to evaporation. **(F)** Lift force deviation from the sealing test (red) compared with the penetration force (black, curve is an exponential fit) at 0.64 cm depth from EPK mud characterization of different ϕ with 3 trials each. Error bar in E and F corresponds to the mean $\pm$ s.d. The drift in the force is small compared to the strength varying with ϕ.

mud characterization experiments using the automated vertical penetration device showed that as ϕ increased, the vertical penetration (lift) force also increased for a given depth (Fig.3.4A-B).

In comparison to the automated vertical penetration device mud characterization (Fig. 3.4A), the vertical penetration force as a function of depth profile for each ϕ measured from the custom portable penetrometer (Fig. 3.4B) was close to each other. This shows that the custom portable penetrometer can be used in our experiments to track water loss and characterize mud in place of the automated penetration device.

3.6.2 Sealing method provides minimal water loss during storage

We found the mud to be spatially uniform across the 4 locations (Fig. 3.4C-D) during the mud characterization for testing the sealing method. The drift in force as it varied with time showed a small water loss due to evaporation over 1 hour which is the normal duration of our experiments (Fig. 3.4E). But this variation in strength for mud with given ϕ was much smaller (red square marker, Fig. 3.4F) compared to the strength difference when ϕ was varied and hence was still within the deviation (black square marker, Fig. 3.4F). This shows that the sealing method can overall help us control and maintain mud strength during our experiments to enable repeatable experiments over several days.

3.6.3 Maintaining and controlling mud strength during animal experiments

The vertical penetration force during each penetrometer test had a minimum standard deviation for each day (each curve in Fig. 3.5A-E), which shows that the mud was

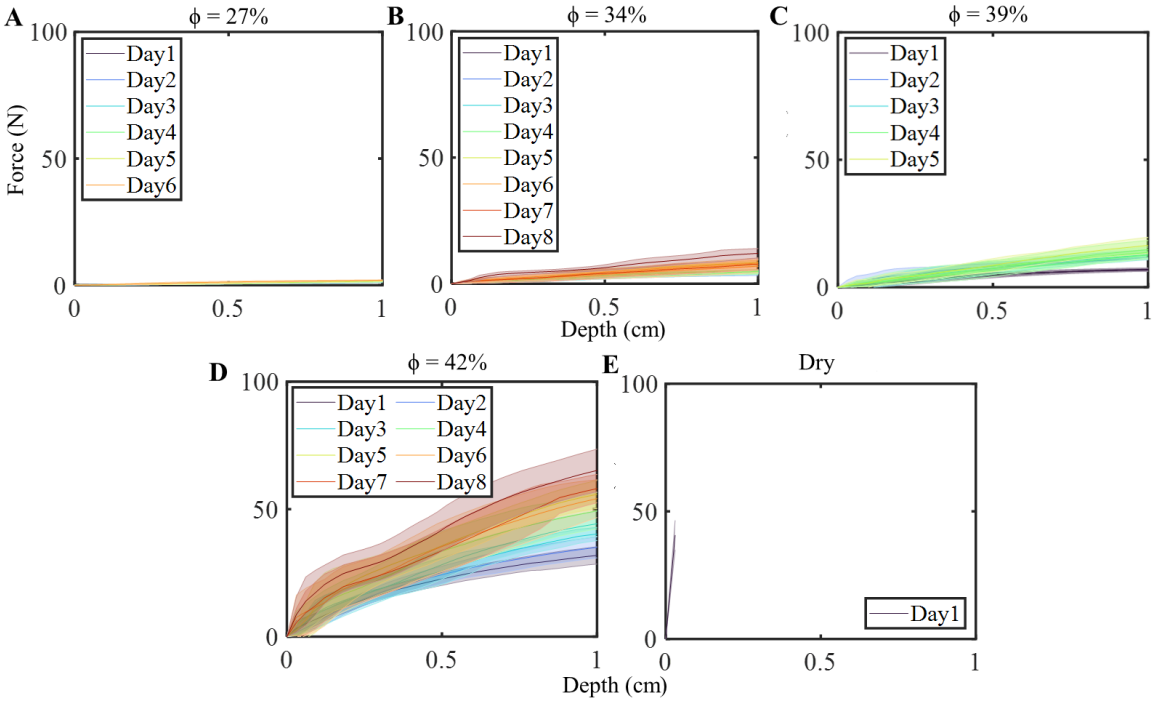

Figure 3.5: Controlling mud strength during experiments. Vertical penetration force averaged over all the locations as a function of depth during penetration for mud up to 1 cm with **(A)** $\phi = 27\%$, **(B)** $\phi = 34\%$ **(C)** $\phi = 39\%$ **(D)** $\phi = 42\%$ and **(E)** dry mud. Each color corresponds to a day. Penetration testing curves for the same day have the same color. The shaded error bars indicate mean $\pm$ s.d.

spatially uniform over each penetrometer test. The overlapping of the curves of all the penetrometer tests completed in a day shows that the mud was temporally consistent (same colored curves in Fig.3.5A-D). A gradual increase in the vertical penetration force over each day (different colored curves, Fig. 3.5A-D) for mud strengths with $\phi = 27\%$, 34%, 39%, and 42% indicates small water loss over each day. Because the number of days the animal was tested on $\phi = 34\%$ was greater than that of $\phi = 39\%$, there was more water loss on $\phi = 34\%$.

3.7 Discussion

To achieve the goal of quantifying animal-mud interaction and understanding the underlying interaction mechanics during the animal locomotion on mud, we developed tools and methods to help maintain and control mud strength during the experiments as a first step. The results in Sec. 3.6.1 show that they would help us in performing more repeatable and systematic experiments. These tools and methods developed will help study animal locomotion over a broader scale and explore the different locomotion strategies seen in amphibious fishes.

3.7.1 Mud preparation system to prepare mud more uniformly

Locomotion on substrates such as sand has been extensively studied due to the development and use of an air fluidized testbed (Li et al., 2009; Maladen et al., 2009) and sieve apparatus (Sharpe, Kuckuk, and Goldman, 2015) to control dry and wet sand respectively. There have been no animal studies yet on mud where the strength of mud was systematically varied due to the difficulty in preparing different mud strengths for animal experiments. There are some robot studies on mud with varying mud strength (Liang et al., 2012; Zhang et al., 2016), but no preparation methods or equipment have been established yet for mud. In this study, we have developed an automated mud preparation system that will help in preparing mud with different strengths in large quantities (Fig. 3.2A-B).

3.7.2 Tools to characterize mud strength to track water loss during animal experiments

We have developed an automated vertical penetration device (Fig. 3.3A-B) to help characterize mud which allows us to estimate the force as a function of the depth profile (Fig. 3.4A). Using this profile, we have shown that we keep track of the mud strength (Fig. 3.5) during the experiments using the custom portable penetrometer (Fig. 3.3C-D). To ensure the repeatability of the force as a function of depth profile, we need to be careful in ensuring that the probe is always perpendicular to the mud surface and is always cleaned before every use. To avoid boundary effects (Fig. 3.6), the device was always placed away from the walls of the container at a sufficient distance and was only penetrated up to a depth well above the bottom of the container. When using the penetrometer, we need to be careful in pushing the probe steadily at a slow speed to ensure that the hall effect sensor tracks the magnet's rotation accurately, especially on lower ϕ. Despite using a motor to increase the penetration resistance the operator still needs to move the probe slowly to ensure accurate reading from the sensor.

3.7.3 Improvements made to the automated vertical penetration device

We made a few improvements to the automated vertical penetration device as it was tested on mud. The first prototype (Version 1) of the automated vertical penetration device had a shorter threaded rod and a 3D-printed flange (Fig. 3.7A-B) to connect the threaded rod to the motor shaft (Fig. 3.7A-B). Version 2 of the prototype replaced the 3D-printed flange with a shaft coupler because it was hard to align the motor shaft with the screws very accurately. One end of the threaded rod was hot glued to

the shaft coupler to secure the rod and prevent it from moving. The threaded rod was also supported by two parts (Fig. 3.7C-D) mounted onto the T -slotted framing from both ends instead of one part (Fig. 3.7A-B) to prevent the linear slider from wobbling. Version 3 (Final version) of the prototype had a longer threaded rod to help the probe have a larger displacement (Fig. 3.7E-F).

3.7.4 Improvements made to custom portable penetrometer

We made several improvements to the custom portable penetrometer as it was tested on mud during the animal experiments. We added a frame with 100 g weight on either side in the Version 0 prototype (Fig. 3.8B) because the prototype (Fig. 3.8A) was difficult to hold and place it perpendicular to the mud surface. A motor attached to a gear was also added to the gear rack to provide resistance when it was powered as the probe was pushed into the mud with weaker ϕ (Fig. 3.8B). We improved the handle that helps in pushing the probe into the mud and the frame in the Version 1 prototype (Fig. 3.8C) to help hold the penetrometer better.

We added a thicker gear rack to the Version 2 prototype to reduce the bending of the gear rack and adjusted the frame to increase the range of motion (Fig. 3.8D). We also tested a smaller gear in the Version 2 prototype, but it did not have enough resistance even with the motor powered on in the mud with lower ϕ (Fig. 3.8D). To reduce the side-to-side movement of the gear rack, we made it wider in the Version 3 prototype (Fig. 3.8E). We also added a stronger frame with a better weight holder in this prototype (Fig. 3.8E). We improved the frame with better wire management in the Version 4 prototype (Fig. 3.8F) because the wires kept getting caught during the mud characterization.

All of the previous versions of the prototype were built mainly of LEGO parts, with different parts hot glued together. During experiments, the hot glue started to fail in keeping parts together when force was applied to push the probe into the mud. Over time, the hot-glued LEGO parts did not have sufficient adhesion and came apart. The axle to which the magnet was connected also moved often because it was attached using LEGO parts. This resulted in the hall effect sensor having inaccurate readings. To improve the prototype's robustness, we replaced the LEGO parts with machine-made and 3D-printed parts (Fig. 3.8G-F).

3.7.5 A sealing method to help minimize water loss

We have shown that the sealing method (Fig. 3.2C) developed minimizes water loss from evaporation spatial-temporally (Fig. 3.4D-F). Despite this water loss being minimal, it is difficult to prevent water evaporation completely. In nature, the mud strength varies constantly and is a continuous variable. Thus, even with a small water loss, the overall mud strength relatively remains the same. Using these tools and methods we have developed we have shown that we can control and maintain the mud strength which was difficult to do previously and allow us to perform animal and robot studies on mud with repeatability over several days.

3.8 Future work

Our tools and methods developed for locomotion studies with systematic variation in mud strength despite showing successfully maintaining, controlling and tracking mud strength during experiments can still be improved further. First, the latest

version of the custom portable penetrometer is yet to be tested during mud and animal experiments. A better wire management still needs to be made for the penetrometer with the circuit board enclosed inside a shell on the penetrometer. Currently, the wires and the circuit boards are still exposed on the latest version of the penetrometer for quick debugging during experiments. These improvements will make the penetrometer more robust. The hall effect sensor's detection of the magnet rotation is consistent only when the probe is pushed into the mud at a slow velocity. This can be improved by using better hall effect sensors or using other types of linear position tracking sensors. This will help perform mud characterization at different velocities which will help in studying how animals cope with disturbed mud.

Second, the automated mud preparation system can only mix small quantities each time. This will be useful for robot experiments that need a much larger mud testbed depending on their size which needs a much larger mud mixing system. Third, the sealing method is yet to be tested for maintaining mud strength for a substantial amount of time which is crucial for performing animal studies which lake longer durations of time spanning over several months.

3.9 Appendix

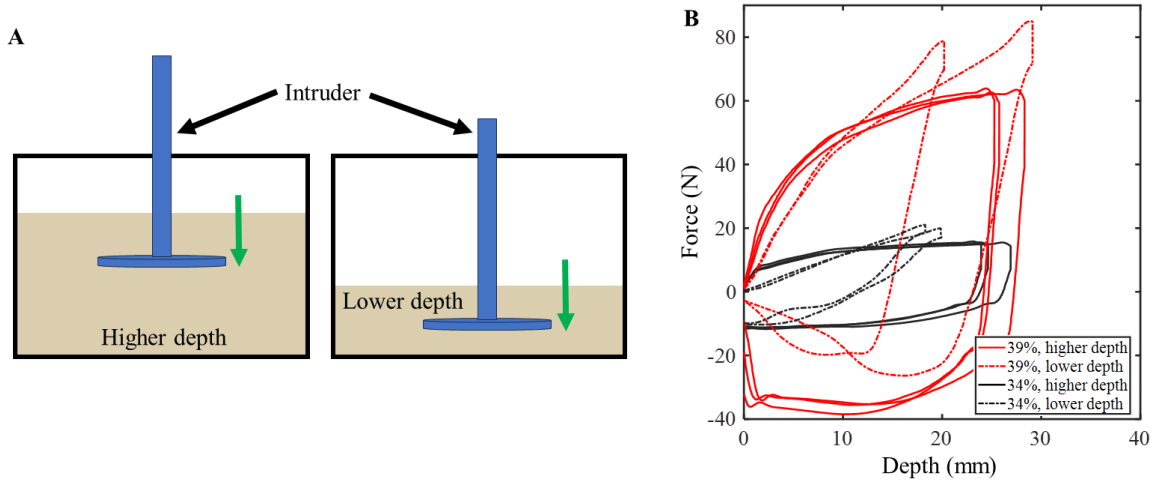

Figure 3.6: Boundary (A) Intruder pushing into the mud for a higher depth and lower depth filled container. **(B)** Force as a function of depth profile for $\phi = 34\%$ (Black) and 39% (Red) for lower depth (dashed-dotted line) and higher depth (Solid line) filled container.

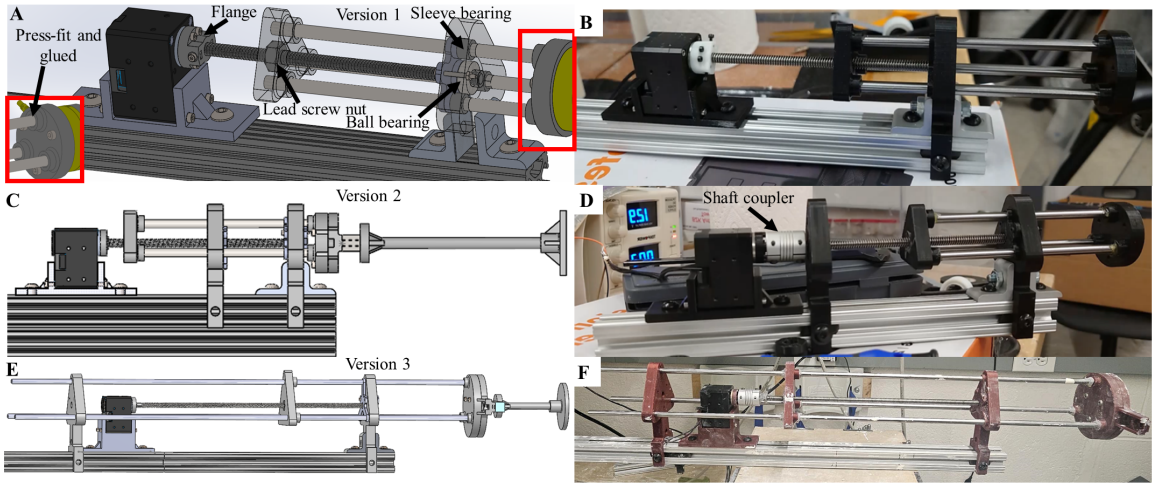

Figure 3.7: Improvements to the automated vertical penetration device. **(A)** Version 1 prototype CAD. **(B)** Photo of Version 1 prototype. **(C)** Version 2 prototype CAD. **(D)** Photo of Version 2 prototype. **(E)** Version 3 prototype (Final version) CAD. **(F)** Photo of Version 3 prototype (Final version).

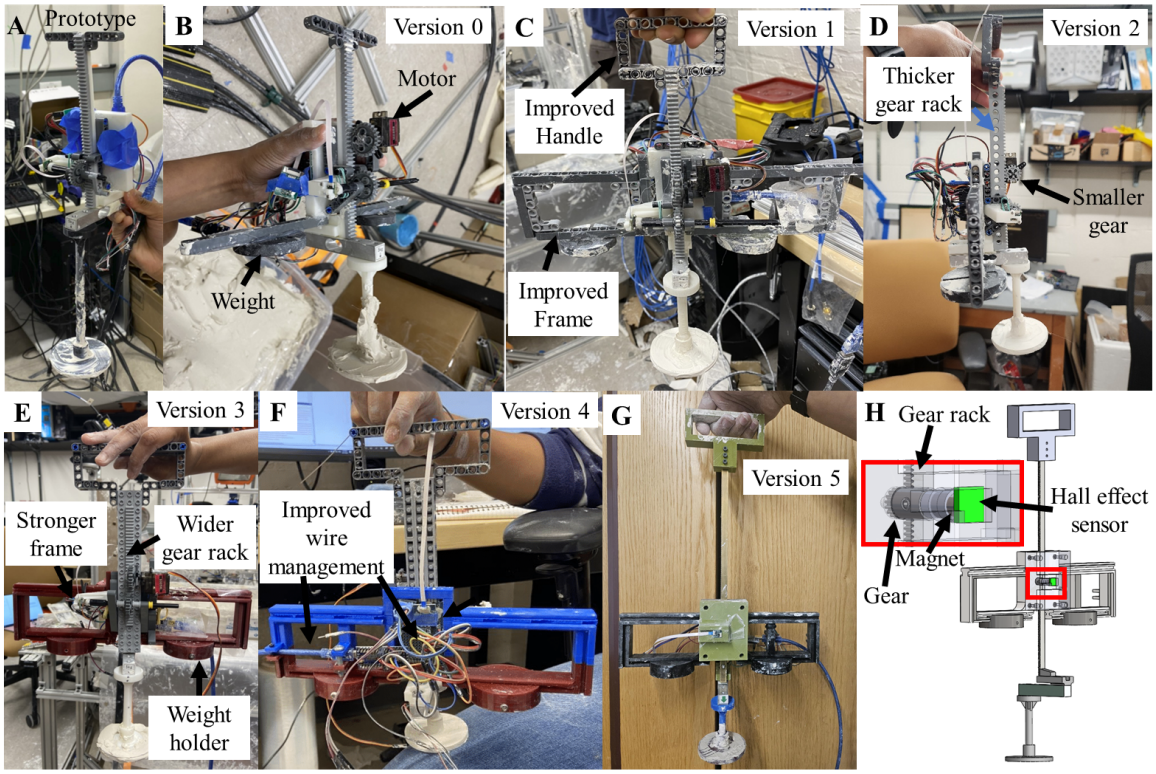

Figure 3.8: Improvements to the automated custom portable penetrometer. **(A)** Photo of the prototype. **(B)** Photo of the Version 0 prototype. **(C)** Photo of the Version 1 prototype. **(D)** Photo of the Version 2 prototype. **(E)** Photo of the Version 3 prototype. **(F)** Photo of the Version 4 prototype. **(G)** Photo of the Version 5 prototype. **(H)** Version 5 prototype CAD.

Chapter 4

Terrestrial locomotion by mudskippers on wet flowable substrate of varying strength

This chapter is to be submitted as an article entitled *Terrestrial locomotion by mudskippers on wet flowable substrate of varying strength*, authored by Divya Ramesh, Gargi Sadalgekar, Jiangqi Tan, and Chen Li, in the Journal of Experimental Biology (Ramesh et al., 2024b). It will be in revision at the time of submission of this dissertation.

4.1 Author Contributions

Conceptualization: Chen Li; methodology: Divya Ramesh, Chen Li; validation: Divya Ramesh, Gargi Sadalgekar; investigation: Divya Ramesh, Gargi Sadalgekar, Jiangqi Tan; data curation: Divya Ramesh; writing: Divya Ramesh, Chen Li; visualization: Divya Ramesh, Chen Li; supervision: Chen Li; project administration: Chen Li; funding acquisition: Chen Li.

4.2 Acknowledgment

We thank Qiyuan Fu for helping with the preliminary study and animal care. We thank Luke Moon for helping with the experimental setup, animal experiments, and animal care, Mia Urban for helping with the experimental setup, assisting in preliminary animal experiments, and animal care, Milla Ivanova for assisting in the animal experiments and helping with animal care, Lei An, Dennis Lin, and Catherine

Pollard for assisting in data analysis and Lucas An for helping with mud preparation for the experiments and animal care. We thank Kapi Ketan Mehta, Jack Rao, Chiadika Vincent, Luna Liu, and Yaqing Wang for helping with animal care. We thank Noah Bressman, Sandy Kawano, Noah Cowan, Jeremy Brown, and Yannis Kevrekidis for the helpful discussion. This study was funded by the Burroughs Wellcome Fund Career Award at the Scientific Interface and a Johns Hopkins University Bridge Grant.

4.3 Summary

Amphibious fishes can transition between different strategies as they traverse substrates of varying strength when they regularly make foray onto land. Mudskippers are likely capable of transitioning between strategies as they interact with the natural environment. We hypothesize that the mudskipper starts to adapt its locomotion strategy by either modifying the crutch walking gait or showing emergence of new gaits to help cope with variation of the wet substrate strength. We allowed the animal to move over mud of 5 different mud strengths. From our observations, we found that the animal started to sink more, had more contact length and hence moved slower and had reduced distance as the mud strength decreased from strong to weak mud. This is likely due to more mud starting to stick to the animal's body and appendages as the mud got weaker. This enabled the animal to use jump mode more often. On the weakest mud, the failure of the jump mode led to the emergence of variants of the crutch walk mode that involved tail bending. On the strongest mud, despite high mud strength, the speed of the animal decreased due to the mucus on the animal's body and appendages quickly drying up. This caused the animal to use the jump mode

more often.

4.4 Introduction

Amphibious fishes can transition from swimming in water to crawling on land (Astley and Jayne, 2007; Bressman, 2022; Pace and Gibb, 2014; Sayer, 2005) when making forays onto land at the water–land interface. Previous studies have revealed how amphibious fishes use morphologies and control systems originally made for swimming in walking or crawling on solid surfaces (Bressman, 2022; Bressman, Gibb, and Farina, 2018; Bressman et al., 2019; Bressman, Morrison, and Ashley-Ross, 2021; Pace and Gibb, 2011; Redmann et al., 2020; Standen et al., 2016).

The natural habitat of amphibious fishes often has wet flowable substrates such as mud or wet sand (Clack, 2012; Perry et al., 2015; Wendt et al., 1997) with varying solid composition and wetness. It is challenging to move on such substrates because they can behave similarly to a solid or flow similar a liquid depending on the forces applied relative to yield strength (Coussot, 1997; Goldman, 2014; Li et al., 2009; Li, Hsieh, and Goldman, 2012; Mazouchova et al., 2010; Sharpe, Kuckuk, and Goldman, 2015; Winter, Deits, and Hosoi, 2012). This yield strength at which the solid–fluid transition occurs also varies as the substrate gets dryer or wetter (Coussot, 1997). Wet substrates such as mud can also have a strong cohesion due to colloidal effects (Coussot, 1997) that make it stick to the animal's body and appendages which can affect the animal's locomotion. To adapt to these challenges, amphibious fishes amphibious fishes may adjust their body and appendages or even transition to other locomotor strategies.

Recent studies have started quantifying kinematics (Naylor and Kawano, 2022; Redmann et al., 2020) and muscle control (Horner and Jayne, 2014; Lutek and Standen, 2021) to better understand how fishes move on wet flowable substrates. Despite several previous animal and robot studies on sand varying from dry (Li, Hsieh, and Goldman, 2012; Maladen et al., 2009; McInroe et al., 2016; Naylor and Kawano, 2022), partly wet (Kudrolli, Ramirez, and Weitz, 2019; Sharpe, Kuckuk, and Goldman, 2015) to fully saturated sand (Dorgan, 2018; Redmann et al., 2020), there are only a few animal studies on mud (Falkingham and Horner, 2016; Horner and Jayne, 2014; Naylor and Kawano, 2022; Standen et al., 2016) especially in the solid–fluid transition concentration. Some amphibious fish studies have used viscous solids such as gelatin (Wang et al., 2013) and viscous fluids such as methyl cellulose (Lutek and Standen, 2021) and Poly-Bore (Horner and Jayne, 2008) when water is mixed as substrates. To fully understand how the locomotor morphology, control, and kinematics permit performance it is necessary to quantify the environmental interaction between the fish and the wet flowable substrates to help understand how fishes generate forces to locomote. There have been no studies yet on mud-animal interaction mechanics unlike on sand (Li, Hsieh, and Goldman, 2012; Maladen et al., 2009; Sharpe, Kuckuk, and Goldman, 2015).

For this study we will focus on appendicular-based locomotion which is one of the three distinct strategies found in amphibious fishes when walking on land (Pace and Gibb, 2014). We chose mudskipper (Fig. 4.1A) as the model organism because they are found in mudflats, their natural environment, which often has mud mixed with some silt and sand with natural variation in the wetness of the mud (Sayer, 2005). There have been extensive studies on their locomotion on land in terms of kinematics

and muscle control (Kawano and Blob, 2013; Pace and Gibb, 2009; Wang et al., 2013) and is the only known fish that use this strategy. The study's results and findings will help interpret the animal's locomotion, connect to the previous work, and provide novel insights on the animal's adaptation to variation in mud strength. Mudskipper's sustained locomotion on land is the crutch walking gait (Kawano and Blob, 2013; Pace and Gibb, 2009; Wicaksono et al., 2018). In this gait, they use their two pectoral fins in phase with each other to lift the body and crutch forward with minimum to no body bending. During swimming, their sustained locomotion in water, they laterally bend their body to generate thrust (De and Nandi, 1984; Jaafar and Murdy, 2017; Pace and Gibb, 2009; Wang et al., 2013). This likely means that the mudskippers can either start to modify their appendicular-based locomotion by combining it with body bending along the lateral plane or start to show a new strategy to help them move as they interact with the substrate.

Earlier studies have observed mudskippers using other types of locomotion apart from their sustained locomotion in the natural environment (De and Nandi, 1984; Dijk, 1960; Jaafar and Murdy, 2017; Stebbins and Kalk, 1961). In water, upon encountering

Figure 4.1: Choice of model organism. (A) Mudskipper moving on mud.

a threat, mudskippers switch from swimming to burst locomotion such as skipping on water surfaces where the animal bends its tail to help thrust itself forward (De and Nandi, 1984; Jaafar and Murdy, 2017; Stebbins and Kalk, 1961D) or fast-starts which is also known as C-starts where the animal forms a C shape with its body upon seeing a threat or perturbation and swims fast in a different direction (Jaafar and Murdy, 2017; Swanson and Gibb, 2004). On land, upon seeing a threat the animal's escape response is jumping where it laterally bends its tail to thrust itself off the substrate over several body lengths (Dijk, 1960; Harris, 1960; Stebbins and Kalk, 1961; Swanson and Gibb, 2004). Variation from the normal crutch walk mode has been observed in studies where gelatin was used as a substrate (Wang et al., 2013) or when inclination was added to a mud (McInroe et al., 2016; Naylor and Kawano, 2022) and sand surface (Naylor and Kawano, 2022). In both cases, the animal bent its tail laterally to likely help generate propulsive forces to move forward. The different locomotion strategies used by the mudskipper suggest that the animal is capable of transitioning to other strategies when sustained locomotion fails (Clack, 2012; Perry et al., 2015; Wendt et al., 1997). Our hypothesis is that the animal starts to adapt its locomotion strategy by either modifying the crutch walking gait or showing emergence of new gaits or modes to help cope with variation of the wet substrate strength.

To test the hypothesis, we allowed the mudskipper to traverse mud with different mud strengths and used high-speed cameras to track the animal to help measure the kinematics of the animal body and appendages. We hypothesized that (1) the animal when using the crutch walk mode starts to walk slower as the mud gets weaker. This is likely due to the increase in the adhesive force from mud sticking to the animal's ventral body and drag arising from mud sticking on the animal's dorsal body,

appendages, and tail which prevents the animal from lifting itself to move forward. (2) This likely causes the animal to start to either modify the crutching gait or use a new strategy to help it move forward. To test hypothesis (1), we used high-speed camera videos to measure and quantify the animal's performance during the crutch walking mode. To test hypothesis (2) we estimated how often the animal uses an emergent locomotion strategy over different mud strengths.

4.5 Materials and Methods

4.5.1 Animal testbed and controlling mud strength during experiments

We used Georgia Kaolin (China Clay, Old Hickory Clay Company, Florida, USA) as the choice of clay mud for our animal study because it is qualitatively similar to that of natural mud (Coussot, 1997). We prepared the clay mud using an automatic mixing system (Fig. 4.2A) developed for our mud characterization (Ramesh et al., 2024a). A container (HOMZ, Chicago, IL, USA) that is 1.02 m in length, 0.51 m in width, and 0.16 m in height with an airtight lid was used to hold the clay mud to perform experiments and during storage (Fig. 4.2D). We used the custom portable penetrometer (Fig. 4.2B) to track the water loss each day and maintain the mud strength during experiments (Ramesh et al., 2024a). When there is little mud in the tub, the animal locomotion and the intruder during mud characterization will be affected by boundary effects from the bottom of the tub. Boundary effects are defined as artifact forces applied on an object as it moves near the container's boundary (Coussot, 1997). To avoid this, the container had mud up to least $3/4^{th}$ of the tub height. We used sealing methods developed and tested in our previous study (Ramesh

et al., 2024a) to minimize the water loss. As part of the sealing method, the sides of the lid were covered with rubber sealing strips (CloudBuyer) to further make the lid airtight and prevent water drops from escaping through the sides of the lid (Fig. 4.2D). To minimize water evaporation from the mud surface to the top of the lid during storage, a plastic wrap was placed directly over the mud. Lashing straps (ACE-Lashing Straps, Acelane) were placed around the closed container to tighten

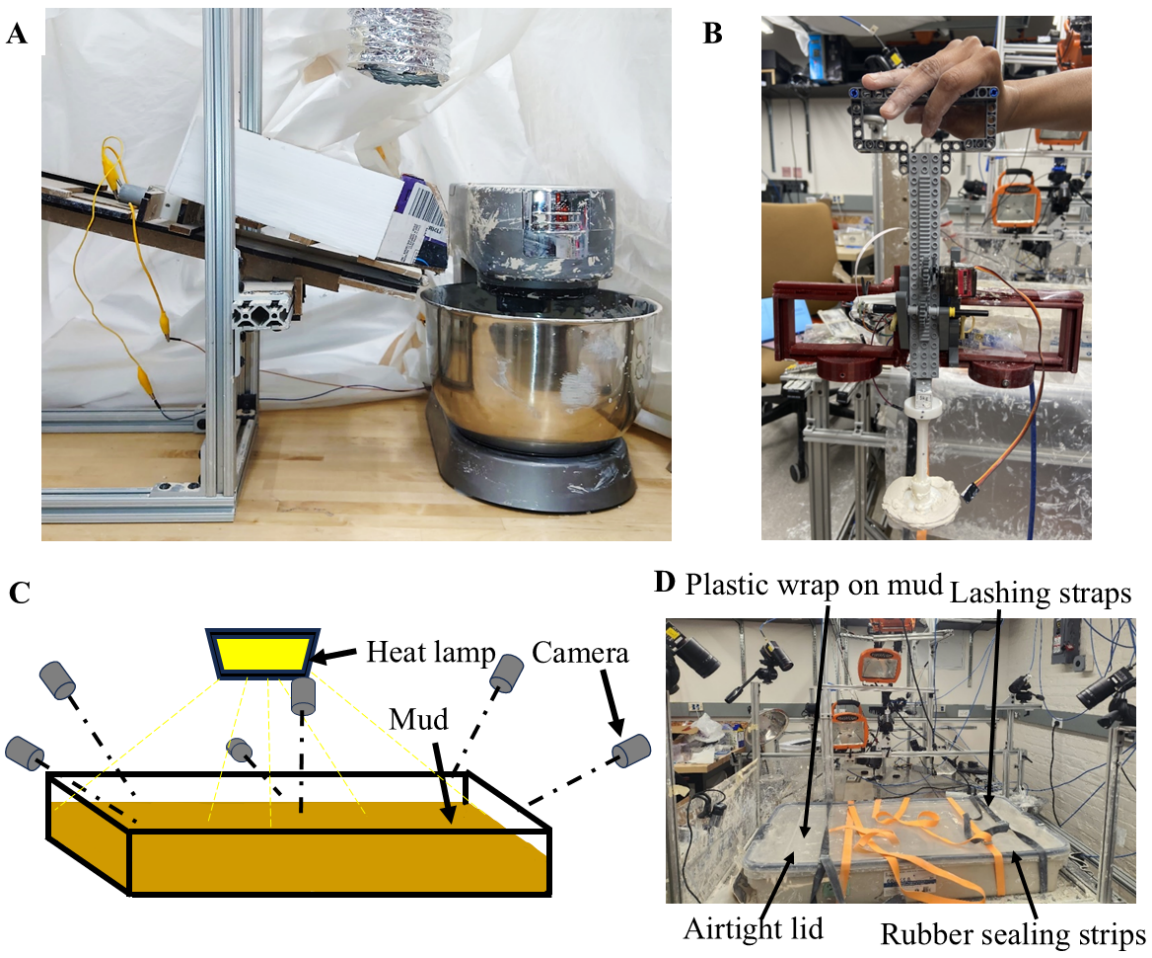

Figure 4.2: Experimental setup. **(A)** Automated mud preparation system. **(B)** Custom portable penetrometer. **(C)** A schematic of the experimental setup. **(D)** Photo of the experimental setup.

the lids further onto the container (Fig. 4.2D).

4.5.2 Choice of mud strength for experiments

For the animal experiments, we chose $\phi = 27\%$ (close to the lower limit of the solid–fluid transition regime), $\phi = 34\%$, 39%, and 42% which are in the solid–fluid transition regime from the mud characterization using the automated vertical penetration device (Ramesh et al., 2024a). We also chose dry mud with a very high ϕ in the fractured mud regime which was prepared by drying out the water content over several days after wet mud was flattened in a container.

4.5.3 Experimental setup, sample size and protocol to perform animal locomotion

We used 6 synchronized high-speed cameras (N-5A100 17 Gm/CXP-6-1.0, Adimec, Eindhoven, The Netherlands) to track animal locomotion and for 3-D reconstruction (Hedrick, 2008) at 60 frames per second for trials taken over the first few days and 100 frames per second for remaining trials (Fig. 4.2A-B). We also recorded top view and side view videos using webcams (Logitech and HP) at 30 frames per second to capture the entire animal study completed in a day. The experimental setup was well lit and heated using a heat lamp (500 Watt Portable Halogen Work Light, Woods) (Fig. 4.2A). The heat lamp was switched off between each trial to maintain the temperature.

We used 5 mudskippers (*Periophthalmus barbarous*) for this study. All animals were approved by and in compliance with The Johns Hopkins University Animal Care and Use Committee (protocol FI21E163). The animals were fed daily with dried shrimp pellets and housed in well-lit, well-heated aquarium tanks filled with brackish

Trial count for analysis	A1	A2	A3	A4	A5	Total trials	No. of Treatments	Trials per treatment (27%, 34%, 39%, 42%, Dry mud)
Walk trials for forward displacement and speed at each cycle	34	34	37	33	34	172	5	28, 50, 41, 28, 25
Walk trials for Trials for jumps count and jumps per animal for jumps displacement	15	15	15	15	15	75	5	15, 15, 15, 15, 15
Trials for mode transition analysis on $\phi = 27\%$, 34%, 42%	15	15	15	15	15	75	3	25, 25, -, 25, -
Trials for mode transition analysis on $\phi = 39\%$	4	4	4	4	4	20	1	-, -, 20, -, -
Trials for mode transition analysis on dry mud	3	3	3	3	3	15	1	-, -, -, -, 15
No. of cycles for sinkage and contact length	15	15	15	15	15	75	5	15, 15, 15, 15, 15
Walk trials with < 4 cycles	11	11	11	10	9	52	5	28, 17, 7, 0, 0
Walk trials with 4 cycles	2	1	1	1	3	8	5	0, 5, 3, 0, 0
Walk trials with 5+ cycles	21	22	25	22	22	112	5	0, 28, 31, 28, 25
Walk trials tracked for kinematics	22	21	21	21	20	105	4	-, 27, 25, 28, 25

Table 4.1: Sample size for different analysis. A1 corresponds to Animal 1

water. The animals were allowed to get accustomed to each mud strength for a few minutes on the first day of experiments.

The length, height, and weight of the animals were recorded after the experiment concluded each day. The length and height were estimated using ImageJ software. The animals were weighed using a digital weighing scale (American weigh scales, USA). The weight of the animals was 19.33 ± 4.76 g (mean ± s.d.). The length and height of the animals were 12.73 ± 1.65 cm and 2.334 ± 0.48 cm respectively. The average temperature of the experimental setup recorded at the start of each trial was 25 ± 0.92° C.

We defined a trial from when the animal was first placed on the mud until when it was finally taken off the mud. We recorded each trial using high-speed cameras. We started recording the videos before the animal was first placed on the mud and stopped the recording after the animal was finally taken off the mud in a trial. During each trial, the animal was gently prodded by hand to make the animal move. When the animal was drying out or had too much mud covering the body, it was taken off the mud, placed and cleaned in water for a few seconds before being placed it back on the mud. If the animal escaped from the testbed by jumping, it was cleaned and placed back onto the mud. The animal was taken off the mud at the end of each trial after 5 minutes. The animal was allowed to rest for some time (10 – 15 minutes) before each trial. After the mud was disturbed by fish during each trial, the mud was mixed using a metal spatula with beveled edges (Homi Styles) and manually flattened by hand using a piece of plexiglass (McMaster-Carr, Princeton, NJ, USA).

The custom portable penetrometer was used to characterize mud strength spatially on the disturbed mud after animal trials (Ramesh et al., 2024a). We defined

walk trials as those trials where the mudskipper walked continuously in consecutive cycles in a straight line. We rejected walk trials where the animal was close to the testbed boundary due to boundary effects. For kinematics analysis, we chose walk trials that had at least 4 cycles with at least 5 walk trials for each animal and which can be seen on three camera views needed for 3-D reconstruction. We defined cycle trials as those trials where the animal walks over one cycle. For sinkage and contact length analysis, we used cycle trials. See Table 4.1 for details on sample size for each analysis.

4.5.4 Tracking and 3-D kinematics reconstruction

All 2-D analysis used data that were manually tracked using DLTdv digitizing tool in MATLAB (Hedrick, 2008; https://biomech.web.unc.edu/dltdv/). For 3-D kinematics, the animal's nose tip (N), tail tip (T), and 4 points on the body between the head and tail were tracked (Fig. 4.3D, E) on top view and 2 other views for each animal trial. Both left and right pectoral fin's tip and shoulder where the pectoral fins attached to the body were also tracked (Fig. 4.3D, E). The points were tracked using DeepLabCut (https://www.mackenziemathislab.org/deeplabcut; Mathis et al., 2018). For each camera view for tracking using DLC, we manually tracked the markers on the animal body for several video frames and used this data as training sample to train the neural network. We examined each tracked video visually and manually re-tracked some video frames for those videos that had bad tracking and re-trained the training sample. We then converted the DLC tracked points to DLTdv tracked points for further processing of data and analysis in MATLAB.

Outliers from bad tracking of the 2-D positions of the tracked points over 3 views

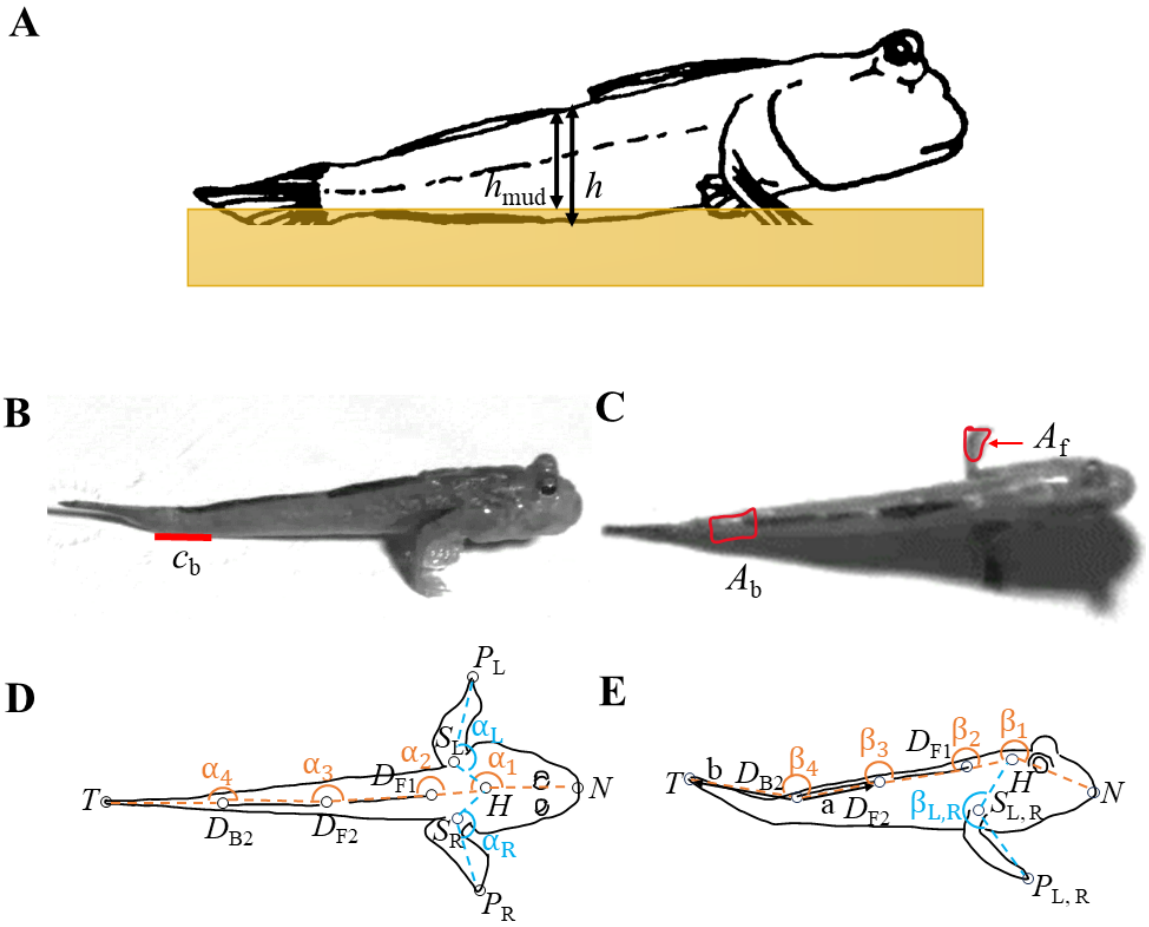

Figure 4.3: Animal tracking, sinkage and contact length. **(A)** Schematic of animal sinkage on mud (Image reproduced and modified from Sayer, 2005). **(B)** Animal body contact length (c_b, red line) on a snapshot of the animal during mid-stance. **(C)** Animal body (A_b) and fin contact area (A_f) on a snapshot of the animal during mid-stance. **(D)** Top view schematic of tracked markers and definitions of lateral bending angles on the animal body. **(E)** Side view schematic of tracked markers and definitions of vertical bending angles on the animal body. Vertical bending body angles (orange, β_i) and fin-body angles (blue, $\beta_{L,R}$) on the sagittal plane. L and R denote the left and right pectoral fins. a and b vectors are the direction vectors used in finding the body and fin-body angles. The black circles indicate tracked markers – Nose tip (N), head (H), first dorsal fin front (D_{F1}), second dorsal fin front (D_{F2}) and back (D_{B2}), tail (T), shoulder left (S_L) and right (S_R), pectoral fin tip left (P_L) and right (P_R). Lateral bending body angles (orange, α_i) and fin-body angles (blue, $\alpha_{L,R}$) on the transverse plane.

for each animal trial were removed using a criterion. This was done by finding the 2-D displacement for each point over time and removing any point with a displacement greater than 10.

These filtered 2-D positions were then converted to 3-D kinematics using the direct linear transformation method and DLTdv digitizing tool. We built a calibration object made up of lego bricks (The Lego Group, Billund, Denmark) to facilitate the 3-D calibration. We rotated the coordinate system to always have the forward axis to be x-axis, have the animal walk from left to right and face upwards using Principal Component Analysis (PCA) (Ma'ckiewicz and Ratajczak, 1993).

Due to bad tracking in some data caused by 3-D reconstruction, we further added four rotation criteria to rotate the data to have the animal walk from left to right and stay upright. We first used the fin-to-body vertical displacement to rotate the data along the x-axis by 90 or -90° to ensure the animal's vertical data is on the frontal plane with the left fin on the left and the right fin on the right of the animal body. We then used the fin-to-body vertical displacement to ensure the animal movement was not inverted on the sagittal plane by rotating the data along the x-axis by 180 degrees.

We then rotated the data about the z-axis by 180 degrees if the initial x-axis position is greater than the final x-axis position in a trajectory of a tracked point to ensure the animal moved from left to right. Using the slope between the x-z initial and final positions of a tracked point trajectory we rotated the dataset along the y-axis to have the animal trajectory parallel to the sagittal plane. A few trials were manually rotated through manual inspection of the trajectory of the dataset.

The newly rotated 3-D position dataset was first filtered by removing y and z

data points whose absolute displacement from the mean of y and z data was above a threshold of 30. We then filtered the data using a moving median filter for x-position and a median filter for both the y and z-position to remove outliers were caused by 3-D reconstruction. The artificial artifacts that were not filtered out were then removed manually after visual inspection from the 3-D position data.

4.5.5 Fore-aft displacement and speed over each cycle estimation analysis

The locomotor's forward displacement at each cycle (d) was calculated for walk trials for all 5 mud strengths (sample size in Table 4.1) using the following:

$$d = ((x_i - x_{i-1})^2 + (y_i - y_{i-1})^2)^{1/2} \tag{4.1}$$

Where (x_{i-1}, y_{i-1}) and (x_i, y_i) are the forward and lateral positions of the mudskipper's nose tip at the start of cycle i and end of cycle i respectively, tracked on top view videos for 2-D analysis. The forward speed (v_{xy}) was calculated using the following:

$$v_{xy} = \frac{d}{\Delta t}, f = (\Delta t)^{-1} \tag{4.2}$$

Where Δt is the duration of a walk cycle and f is the frequency of a walk cycle. The forward displacement, speed, and frequency were then averaged over all cycles in a walk trial.

4.5.6 Jump count and displacement analysis

The number of jumps was counted through manual inspection from the webcam video observations for each trial for all 5 mud strengths (sample size in Table 4.1). The total duration of the entire trial between when the animal was put onto and taken off the testbed was used to estimate the total number of jumps per minute. The jump displacement was also measured using Eqn. 4.1 between the tracked forward and lateral positions of the mudskipper at the start and end of the jump using the top view videos from webcams for $\phi = 42\%$ and from high-speed cameras for $\phi = 27\%$, 34%, 39% and on dry mud.

4.5.7 Mode transition analysis

To quantify the different mode transitions, we manually recorded the transitions as a sequence from webcam video observations for each trial for all 5 mud strengths (sample size in Table 4.1). We calculated the total number of times the animal has transitioned between modes. We then calculated the relative frequency which is defined as the ratio of total number of transitions between 2 modes to the total number of transitions starting from start mode. A mode transition diagram was created using GraphWiz and was simplified by only including the non-self-transitions with a frequency higher than 0.089 and those that emerged for the first time at a mud strength.

4.5.8 Walk mode and its variants use count on weakest and strongest mud

We calculated the total number of times a mode occurs from the sequence to estimate the number of times the animal walked using the normal crutch mode, with a small

tail bending and with a large tail bending for each trial for all 5 mud strengths (sample size in Table 4.1). We measured the relative frequency which is defined as the ratio of the number of times a type of walk mode occurs and the total number of times all three of the walking modes occur for comparison across the different mud strengths.

4.5.9 Sinkage and contact length analysis

The videos showing the animal locomotion from a side view were used in estimating the animal sinkage for each cycle trial for all 5 mud strengths (sample size in Table 4.1). To measure the sinkage, the animal's body height visible (h_{mud}) was measured using Eqn. 4.1 using a tracked point on top of the animal along the starting edge of the second dorsal fin, and another tracked point at the bottom of the animal along the starting edge of the second dorsal fin on mud at mid-aerial phase where sinkage was maximum (Fig. 4.3A). The actual height of the animal (h) was measured with points tracked like those tracked for h_{mud} but when the animal was completely off the mud (Fig. 4.3A). The sinkage (Δh) was calculated using the following:

$$\Delta h = h - h_{mud} \tag{4.3}$$

The body contact length (c_b) was measured to see how much the animal body was lifted for each cycle trial for all 5 mud strengths (sample size in Table 4.1) by manual measurement from a side view video (Fig. 4.3B) during mid-stance of the animal where there is maximum lifting in a cycle for each trial. It was normalized to body length (BL) of the animal. To measure how much the fins sink for each cycle trial for all 5 mud strengths (sample size in Table 4.1), the fin contact area (A_f) and the body

contact area (A_b) were measured manually using ImageJ from a side view video (Fig. 4.3B, C) during mid-stance of the animal. The fin contact length (c_f) was estimated to measure fin sinkage using the following:

$$c_f = c_b.\frac{A_f}{A_b} \tag{4.4}$$

The force at 1 cm from mud characterization (Ramesh et al., 2024a) was inverted (F^{-1}) for mud with $\phi = 27\%$ to $\phi = 42\%$. The inverse of force for dry mud was considered to be 0 because the force is very high on dry mud. The body contact length (c_b) and sinkage (Δh) were multiplied together for each mud strength to get the product of body contact length and sinkage ($c_b.\Delta h$).

4.5.10 Kinematic analysis

All the trials started with the animal's first cycle beginning with the stance phase. The 3-D positions of the tracked points were used in calculating the velocity in all three-axis (v_x, v_y, v_z) using the following:

$$\begin{bmatrix} v_x \\ v_y \\ v_z \end{bmatrix} = \begin{bmatrix} \frac{dx}{dt} \\ \frac{dy}{dt} \\ \frac{dz}{dt} \end{bmatrix} \tag{4.5}$$

where t is time, x, y and z are the fore-aft, lateral, and vertical positions. v_x, v_y and v_z are the fore-aft, lateral, and vertical velocities of the tracked points. The total

velocity (v) was calculated using the following:

$$v = (v_x^2 + v_y^2 + v_z^2)^{1/2} \tag{4.6}$$

The lateral bending body (α_i) and fin-body ($\alpha_{L,R}$) angles on the transverse plane (Fig. 4.3D) were calculated using the following:

$$\alpha = \tan^{-1}(\frac{(\vec{a} \times \vec{b}).\hat{n}}{\vec{a}.\vec{b}}) \tag{4.7}$$

where α is the lateral bending angle, n is the unit vector of the cross product, a and b are the vectors between the tracked points on the transverse plane (Fig. 4.3E). The lateral fin-body angle of the pectoral right fin (α_R) is the conjugate of the fin-body angle found using Eqn. 4.7 for aligning the directions of the left and right fin-body angles visually. All lateral bending body and fin-body angles were wrapped between [0°, 360°). The vertical bending body (β_i) and fin-body ($\beta_{L,R}$) angles on the sagittal plane were found using the following:

$$\beta = \tan^{-1}(\frac{-1.((\vec{a} \times \vec{b}).\hat{n})}{\vec{a}.\vec{b}}) \tag{4.8}$$

where β is the vertical bending angle (Fig. 4.3E). All vertical bending body and fin-body angles were wrapped between [0°, 360°). We then filtered the angle data using a median filter to remove outliers.

Because the animal motions were periodic during the walk mode, we offset the time to start from zero at the start of each walk cycle. We then normalized the time to the duration of each cycle so that it can be the percentage of each cycle. We also

found periodic displacement along all three axes (x_c, y_c, z_c) by collapsing all the cycles to start from 0 by subtracting the positions with the starting position of each cycle.

We subtracted the x-y-z positions of the D_{F1} (Fig. 4.3D, E) from all the tracked points to estimate the positions with respect to the body (x_b, y_b, z_b). We then estimated the fore-aft, lateral, and vertical body velocities using Eqn. 4.5 and the total body velocity using Eqn. 4.6. The periodic displacements with respect to the body were estimated similarly to that of the periodic positions in the world frame.

We divided the animal's cycle into stance and aerial phases based on the pectoral fins being on the mud and off the mud respectively. We used the maximum vertical periodic displacement (z_c) of the nose tip to compare the normalized time when mid-stance occurs over different mud strengths. We filtered the lateral velocity (v_y) with a moving average filter. We then used the start of the rising slope and falling slope of the lateral velocity (v_y) of the left and right fin tip respectively to compare the normalized time when the animal starts the aerial phase over different mud strengths. We used the start of the raising slope and falling slope of the filtered lateral velocity (v_y) of the left and right fin tip combined to compare the normalized time when the mid-aerial phase occurs over different mud strengths. We used the maximum fore-aft periodic displacement (x_c) in the aerial phase for both left and right fins to compare fore-aft fin placement across different mud strengths. We used the maximum and minimum lateral periodic displacement (y_c) in the aerial phase for left and right fins respectively to compare lateral fin placement across different mud strengths.

4.5.11 Statistical analysis

We used one-way analysis of variance (ANOVA) in JMP Pro to find the significance between different treatments for forward displacement, speed, jump, sinkage, and contact length analysis. We included all individual data for significance in forward displacement and speed. For sinkage, contact length, product of contact length and sinkage, and jump analysis, we used data averaged over each individual for significance. We have reported this data as mean ± s.d. for each analysis. We also used Student's *t*-test to compare the significance between individual treatments. To compare the kinematics across different mud strength, the velocities, periodic displacements, body and fin-body angles were interpolated to have the same normalized time and averaged over all the trials for each mud strength. We used one-way analysis of variance (ANOVA) in JMP Pro to find significance between different treatments for kinematics analysis. All analysis except for the statistical tests were performed on MATLAB.

4.6 Results

4.6.1 Performance during crutch walk mode across substrates

In most trials the mudskipper used the normal crutching walk gait (Kawano and Blob, 2013). The mudskipper's walking speed increased as the strength of the mud became stronger from $\phi = 27\%$ to $\phi = 42\%$ (Fig. 4.4A, $P < 0.005$, one-way ANOVA). This can be seen by the slope (Fig. 4.4A, fit line) that decreased from mud with $\phi = 42\%$ to mud with $\phi = 27\%$. But on dry mud, the mudskipper slowed down to a speed that is lower than mud with $\phi = 39\%$ but higher than that of mud with $\phi = 34\%$

($P < 0.005$, one-way ANOVA). The mudskipper also did not use high frequency on the weakest mud (Fig. 4.4A) unlike on mud with other mud strengths. The animal's speed was not affected by the small water loss across all the days the walk trials were collected for all the mud strengths (Fig. 4.10A-E).

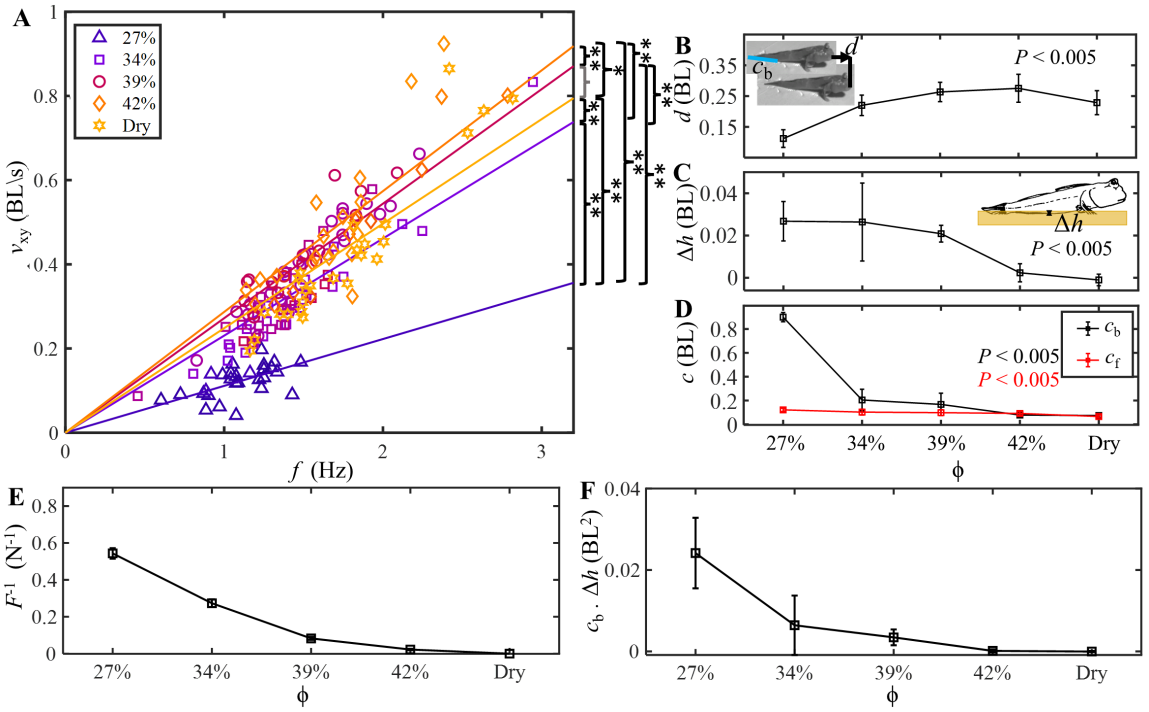

Figure 4.4: Mudskipper performance across ϕ. (A) Average speed (v_{xy}) of the animal's nose tip relative to frequency (f). Lines correspond to linear least-square fit lines. The color of fit line for each mud strength is a function of force at 1 cm from mud characterization. Each data point's color is a function of force at 1 cm measured using the penetrometer taken on the day of the walk trial. **(B)** Average forward displacement (d) of the animal's nose tip (N) as a function of ϕ. **(C)** Average sinkage (Δh) along the starting edge of the second dorsal fin as a function of ϕ. **(D)** Average body (black, c_b) and pectoral fin (red, c_f) contact length as a function of ϕ. **(E)** Inverse of force at 1 cm from mud characterization. **(F)** Average product of body contact length (c_b) and sinkage (Δh) as a function of ϕ. Square marker and error bar in B-D corresponds to mean ± s.d. Statistics performed using one-way ANOVA. ** $P < 0.005$, * $P < 0.05$, Student's t-test, one-way ANOVA.

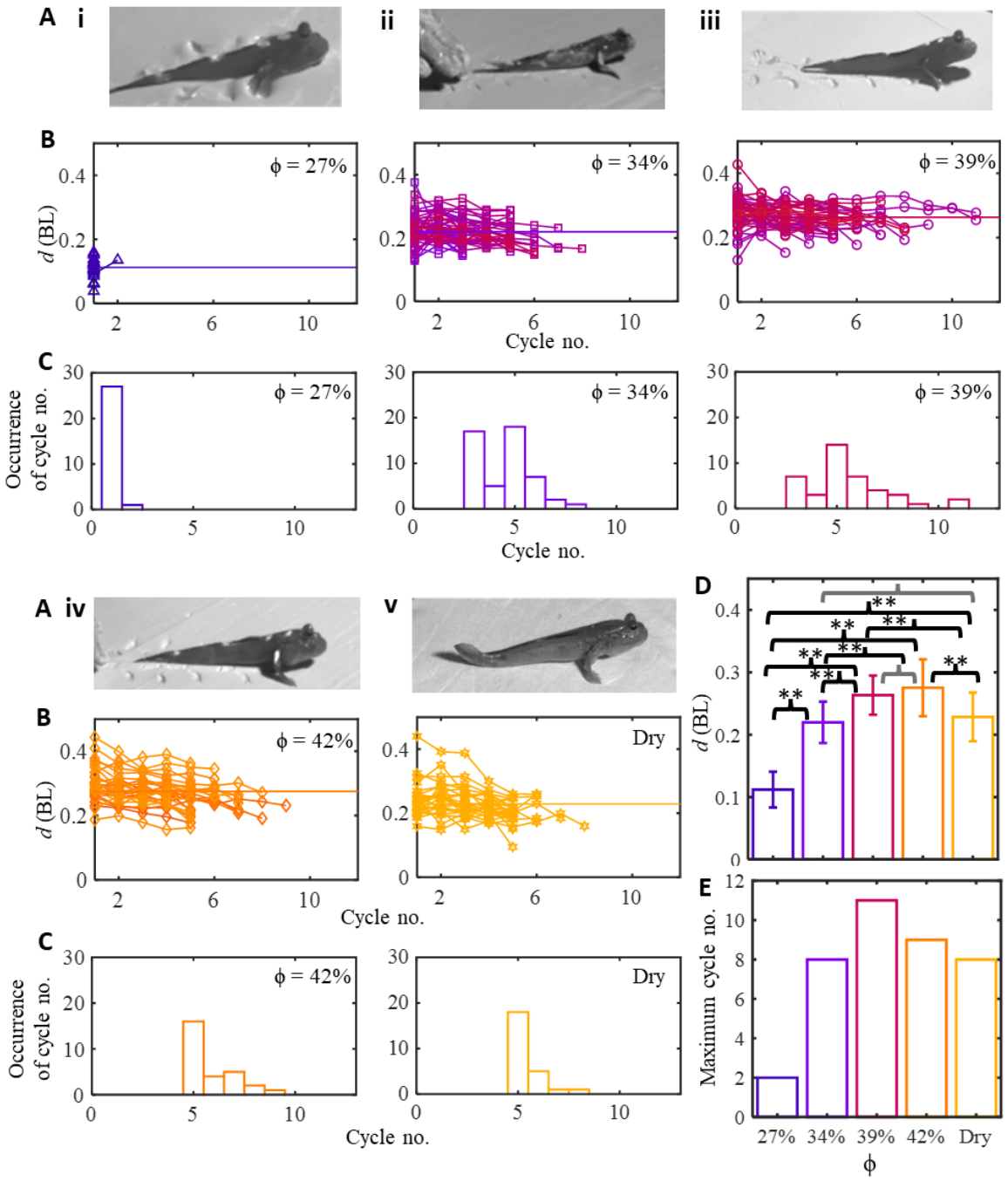

Figure 4.5: Mudskipper forward displacement over multiple cycles. (A) Snapshot of the mudskipper moving on mud with (i) $\phi = 27\%$, (ii) $\phi = 34\%$, (iii) $\phi = 39\%$, (iv) $\phi = 42\%$ and (v) dry mud. **(B)** Forward displacement (d) of the nose tip per cycle over each cycle and **(C)** histogram of the number of cycles the animal

walked across mud with (i) $\phi = 27\%$ (indigo color line, triangle marker), (ii) $\phi = 34\%$ (purple color line, square marker) (iii) $\phi = 39\%$ (magenta color line, circle marker) (iv) $\phi = 42\%$ (orange color line, diamond marker) and (v) dry mud (yellow color line, star marker). Line in B, i–v corresponds to the average forward displacement of nose tip (N) per cycle. The color of line for each mud strength is a function of force at 1 cm from mud characterization. Each data point's color is a function of force at 1 cm measured using the penetrometer taken on the day of the walk trial. **(D)** The average forward displacement of the nose tip (N) per cycle (lines in B, i-v) as a function of ϕ. Error bar corresponds to mean ± s.d. Statistics performed using one-way ANOVA. ** $P < 0.005$, * $P < 0.05$, Student's t-test, one-way ANOVA. **(E)** Maximum number of cycles the animal walked in a walk trial. Color in D-E corresponds to ϕ.

The forward displacement (Fig. 4.5B) also decreased over each cycle as the animal progressed forward for all 5 treatments (Fig. 4.5B, i-v). The slope of the fit line (Fig. 4.4A) indicates the average forward displacement per cycle (Fig. 4.4A, 4.5D). This forward displacement per cycle increased as the mud got stronger from $\phi = 27\%$ to $\phi = 42\%$ and then reduced on dry mud (Fig. 4.5B, i-iv). The mudskipper also started to sink in more (Fig. 4.4C) as the mud strength weakened which in turn increased the animal's body (Fig. 4.4D, black) and pectoral fin (Fig. 4.4D, red) contact length. The inverse of force at 1 cm from mud characterization (Fig. 4.4E) and the average product of body contact length (c_b) and sinkage (Δh) reduced (Fig. 4.4F) as the mud varied from $\phi = 27\%$ to dry mud.

The histogram of the number of cycles across mud (Fig. 4.5C, i-v) showed that the animal mostly walked 1 cycle on mud with $\phi = 27\%$ (Fig. 4.5C, i) and walked 5 cycles (Fig. 4.5C, ii-v) higher mud strengths. For mud with $\phi = 42\%$ and dry mud, we only considered walk trials with at least 5 cycles. Hence it is likely that the animal preferred to walk fewer cycles on these mud strengths. The maximum number of cycles the animal walked (Fig. 4.5E) increased as the mud got stronger from $\phi = 27\%$

to $\phi = 39\%$ and then reduced on mud with $\phi = 42\%$ and dry mud.

4.6.2 Animal's kinematics varying with mud strength

The fore-aft displacement of the animal's nose tip (N) collapsed over one cycle (Fig. 4.11A, i) showed that the animal's forward displacement in a cycle increased as mud

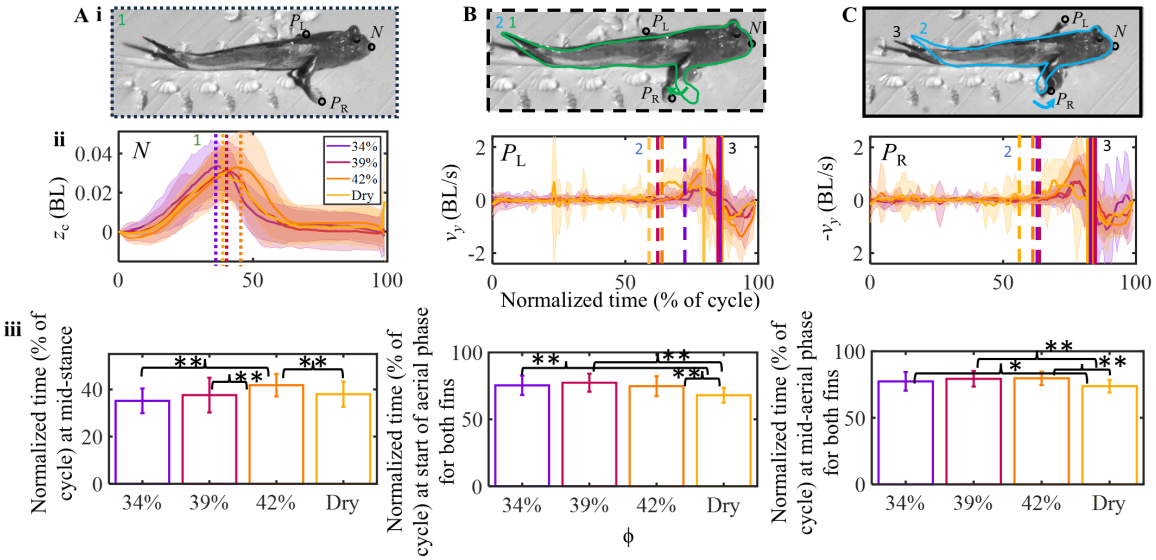

Figure 4.6: Mid-stance, start, and mid-aerial phase reached by the animal as a function of ϕ. (A) Mid-stance of the animal as a function of ϕ. (i) Snapshot of side view of the animal during mid-stance. (ii) Vertical periodic displacement (z_c) over one cycle of animal's nose tip (N) for $\phi = 34\%$ (purple curve), $\phi = 39\%$ (magenta curve), $\phi = 42\%$ (orange curve) and dry mud (yellow curve). Dotted line corresponds to maximum z_c in a cycle where mid-stance occurs. (iii) Average normalized time at mid-stance as a function of ϕ. **(B)** Start of aerial phase and (C) Mid-aerial phase of the animal as a function of ϕ. (i) Snapshot of the animal. (ii) Lateral velocity over one cycle of left (P_L) and right (P_R) pectoral fins for $\phi = 34\%$ (purple curve), $\phi = 39\%$ (magenta curve), $\phi = 42\%$ (orange curve) and dry mud (yellow curve). Dashed and solid lines correspond to the start of aerial phase and mid-aerial phase respectively. (iii) Average normalized time as a function of ϕ at the start of aerial phase and mid-aerial phase. Shaded error bar in (ii) and error bar in (iii) correspond to mean ± s.d. Statistics performed using one-way ANOVA. ** $P < 0.005$, * $P < 0.05$, Student's t-test, one-way ANOVA.

strength varied from $\phi = 34\%$ to $\phi = 42\%$ but then reduced on dry mud. The animal had minimal body lateral movement during each cycle (Fig. 4.11A, ii). The animal's body was lifted during the stance phase (Fig. 4.6A, ii) and reached a maximum value during mid-stance by the pectoral fins (Fig. 4.6A, i-ii) before lowering in height when the fins were off the ground during the aerial phase (Fig. 4.11A, iii) similar to when the animal moved on hard ground (Naylor and Kawano, 2022). The animal's vertical displacement on its nose tip (Fig. 4.11A, iii) showed the animal's body having a similar maximum vertical displacement on mud with $\phi = 34\%$ to $\phi = 42\%$ but this maximal vertical displacement was reduced on dry mud.

The average normalized time in reaching mid-stance by the animal's body (Fig. 4.6A, i-ii, dotted line) was similar for $\phi = 34\%$ and $\phi = 39\%$ but increased as the mud strength increased from $\phi = 39\%$ to $\phi = 42\%$ and then reduced on dry mud (Fig. 4.6A, iii, $P < 0.005$, one-way ANOVA). The average normalized time at the start of the aerial phase (Fig. 4.6B, i) for both pectoral fins (Fig. 4.6B-C, ii, dashed line) was similar for mud with mud strength increasing from $\phi = 34\%$ to $\phi = 42\%$ but was reduced on dry mud (Fig. 4.6B, iii, $P < 0.005$, one-way ANOVA). The average normalized time in reaching the mid-aerial phase (Fig. 6C, i) for both pectoral fins (Fig. 4.6B-C, ii, solid line) was also similar for mud with mud strength increasing from $\phi = 34\%$ to $\phi = 42\%$ but was reduced on dry mud (Fig. 4.6C, iii, $P < 0.005$, one-way ANOVA).

The animal's left pectoral fin tip (P_L), and right pectoral fin tip (P_R) had an increase in the fore-aft displacement over one cycle (Fig. 4.11B-C, i) for mud varying from $\phi = 34\%$ to $\phi = 39\%$ (Fig. 4.7C, i-iii, $P < 0.005$, one-way ANOVA). It remained similar between $\phi = 39\%$ and $\phi = 42\%$ but reduced on dry mud (Fig. 4.7C, i-iii, P

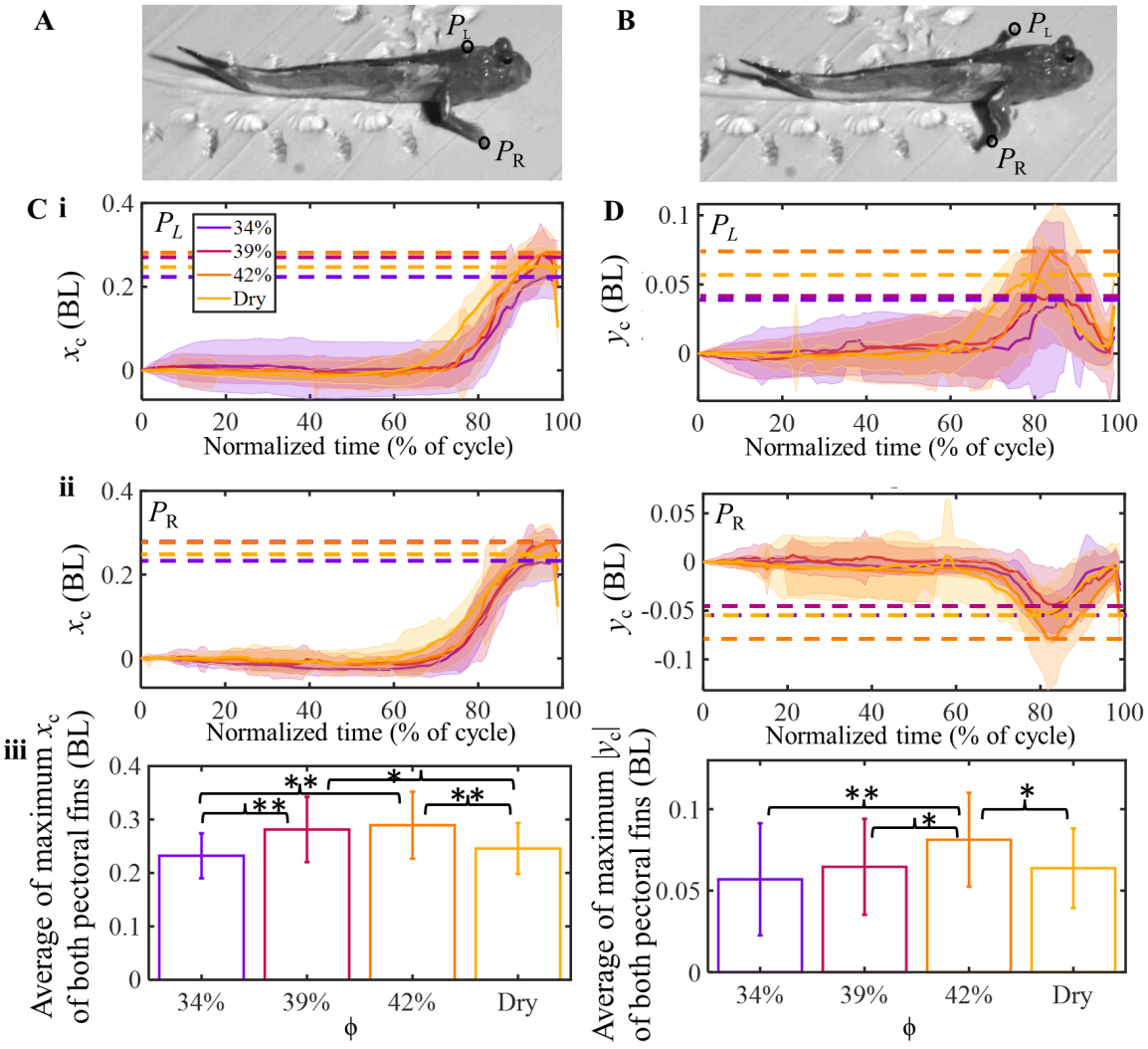

Figure 4.7: Pectoral fin displacement as a function of ϕ. (A) Snapshot of side view of animal during the end of aerial phase. **(B)** Snapshot of side view of animal during the mid aerial phase. **(C)** Fore-aft (x_c) and **(D)** lateral (y_c) periodic displacements of (i) left and (ii) right pectoral fins for ϕ = 34% (purple curve), ϕ = 39% (magenta curve), ϕ = 42% (orange curve) and dry mud (yellow curve). (iii) Average normalized time of maximum x_c (Dashed line in (i) and (ii)) and absolute of y_c (Dashed line in (i) and (ii)) as a function of ϕ. Shaded error bar in (i-ii) and error bar in (iii) correspond to mean ± s.d. Statistics performed using one-way ANOVA. ** $P < 0.005$, * $P < 0.05$, Student's t-test, one-way ANOVA.

< 0.005, one-way ANOVA). The lateral displacement over one cycle for the pectoral fins remained relatively the same from mud strength varying from $\phi = 34\%$ to $\phi = 39\%$ but increased on $\phi = 42\%$ and reduced on dry mud (Fig. 4.7D, i-iii, $P < 0.05$, one-way ANOVA). Due to error in tracking of fin tip especially when the fins are spread out on the lower mud strength, the statistics may not be very accurate.

The animal's left pectoral fin tip (P_L), and right pectoral fin tip (P_R) had minimal total velocity when on the mud, but it increased until the mid-aerial phase (Fig. 4.11B-C, vii) and then decreased after the mid-aerial phase when off the mud during the aerial phase for all mud strength (Fig. 4.11B-C, vii). The animal's body had increased total velocity until mid-stance, and it decreased as the animal reached the end of the stance phase and remained minimal during the aerial phase for all mud strengths (Fig. 4.11A, vii).

The maximum fore-aft velocity of the animal body increased as mud varied from $\phi = 34\%$ to $\phi = 39\%$ and remained relatively the same for higher mud strengths (Fig. 4.11A, iv). The fore-aft velocity of the left and right fin tips showed increased maximum fore-aft velocity for mud with $\phi = 42\%$ while it remained similar on other mud strengths (Fig. 4.11B-C, iv). The lateral velocity of the animal body was minimal for all mud strength (Fig. 4.11A, v). The maximum and minimum lateral velocities of the left and right pectoral fin tips increased and decreased respectively as the mud strength varied from $\phi = 34\%$ to $\phi = 42\%$ and then reduced and increased on dry mud respectively (Fig. 4.11B-C v). The vertical velocities of the animal body and fins were relatively similar across all the mud strengths (Fig. 4.11A-C, vi) starting from $\phi = 34\%$. The maximum total velocity on the nose tip increased as mud varied from $\phi = 34\%$ to $\phi = 39\%$, it remained the same at $\phi = 42\%$ and then reduced on

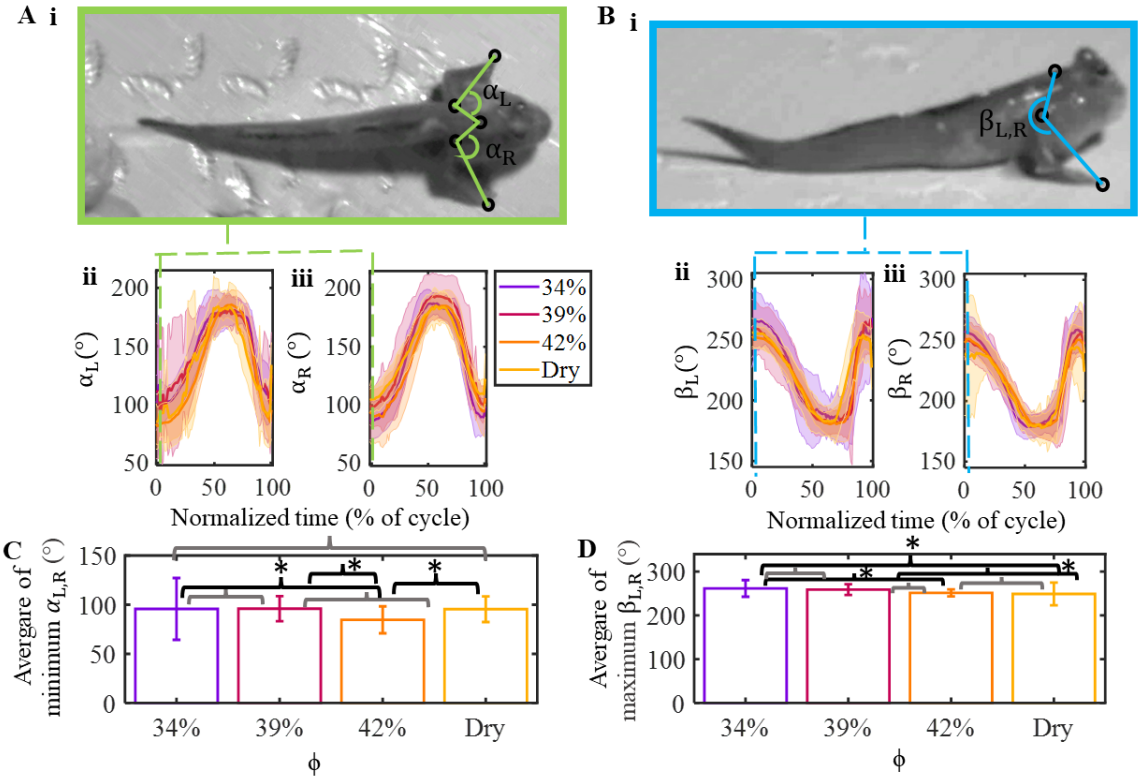

Figure 4.8: Fin rotation varying with ϕ. **(A)** Lateral fin-body angle as a function of ϕ. **(B)** Vertical fin-body angle as a function of ϕ. (i) Snapshot of top view and side view of the animal at the start of the stance phase. (ii) Left pectoral fin's lateral (α_L) and vertical fin-body angle (β_L), and (iii) right pectoral fin's lateral (α_R) and vertical fin-body angle (β_R) over one cycle for $\phi = 34\%$ (purple curve), $\phi = 39\%$ (magenta curve), $\phi = 42\%$ (orange curve) and dry mud (yellow curve). The shaded error bar corresponds to mean ± s.d. **(C)** Average of minimum α_L and minimum α_R as a function of ϕ. **(D)** Average of minimum β_L and minimum β_R as a function of ϕ. Error bar corresponds to mean ± s.d. Statistics performed using one-way ANOVA. * $P < 0.05$, Student's t-test, one-way ANOVA.

dry mud (Fig. 4.11A, vii). The maximum total velocity of the left and right fin tips increased as mud varied from $\phi = 34\%$ to $\phi = 42\%$ and then reduced on dry mud (Fig. 4.11B-C, vii).

The animal showed minimal body bending over one cycle on the transverse

plane (Fig. 4.12A, i-iv) for all mud with mud strengths varying from $\phi = 34\%$ to $\phi = 42\%$ and on dry mud. The head relative to the animal body (β_1), the upper (β_2) and lower (β_3) mid-body bending were relatively minimal on the sagittal plane (Fig. 4.12B, i-iii) for each cycle across all mud strengths varying from $\phi = 34\%$ to $\phi = 42\%$ and on dry mud. The tail relative to lower body (β_4) was bent throughout a cycle in most trials and had a small oscillation where the tail was slightly more bent during the stance phase compared to the aerial phase (Fig. 4.12B, iv) suggesting that the tail bending acted as a push-point to stabilize the animal during lift which were seen during our observations. This angle was relatively the same for each cycle across all mud strengths varying from $\phi = 34\%$ to $\phi = 42\%$ and on dry mud (Fig. 4.11B, iv). Both the left and right pectoral fins fully extended out (fin-body angle is 180 degrees) at the end of the stance phase across all mud strengths varying from $\phi = 34\%$ to $\phi = 42\%$ and on dry mud on both transverse (Fig. 4.8A, ii-iii) and sagittal (Fig. 4.8B, ii-iii) plane.

The average of the minimum lateral fin-body angles which is at the start of the stance phase (Fig. 4.8C) remained the same as mud strength varied from $\phi = 34\%$ to $\phi = 39\%$ but reduced on $\phi = 42\%$ and increased on dry mud (Fig. 4.8C, $P > 0.05$, one-way ANOVA). The average of the maximum vertical fin-body angles which is at the start of stance phase (Fig. 4.8D) remained the same as mud strength varied from $\phi = 34\%$ to $\phi = 39\%$ but reduced on $\phi = 42\%$ and dry mud (Fig. 4.8C, $P < 0.05$, one-way ANOVA). The statistics of the average of the minimum lateral and maximum vertical fin-body angles may be inaccurate due to the small shift in tracked fore-aft and lateral of the fin tips.

4.6.3 Animal transitioning to other modes to adapt to mud strength

The mudskipper displayed behavioral adaptations to overcome challenges on weaker mud and dry mud. The mudskipper jumped the most on dry mud and occasionally on mud with $\phi = 39\%$ and $\phi = 42\%$ (Fig. 4.9B, E). On the mud with $\phi = 34\%$, the number of jumps per minute got more frequent but still less than the count on dry mud ($P < 0.005$, one-way ANOVA). As the mud strength decreased from $\phi = 42\%$ to $\phi = 34\%$, the adhesive force of the mud increased (Ramesh et al., 2024a), and the mud started to stick more to the animal's body and appendages making it difficult to move forward due to drag. This likely caused the animal to jump more often due to the failure of crutch walk mode on the mud (Fig. 4.9E).

However, on mud with $\phi = 27\%$, the mudskipper jumped less frequently because more mud adhered to the animal body and fins making it difficult for it to jump (Fig. 4.9B). The jump displacement also increased as the mud got stronger (Fig. 4.9C) but decreased on dry mud ($P < 0.005$, one-way ANOVA). The animal also started to jump vertically with minimal forward displacement on dry mud (Fig. 4.9D, v).

Apart from jump mode, the mudskipper displayed two variants of the walk crutch mode the weakest mud ($\phi = 27\%$) to help move forward for more than one cycle which the animal was unable to do so using the normal crutch walk mode (Fig. 4.5B, i, 4.9E, i). These variants involved the mudskipper using its tail to thrust itself forward. The first variant is the walk crutch with small tail bending on the transverse plane. This mode did help the animal to move forward but was still ineffective because it could only move over one cycle. Despite the ineffectiveness, this mode (15.6%) was used more than the normal crutch mode (Fig. 4.9D). The second variant is the walk crutch with large tail bending. This variant is similar to jumping except that the

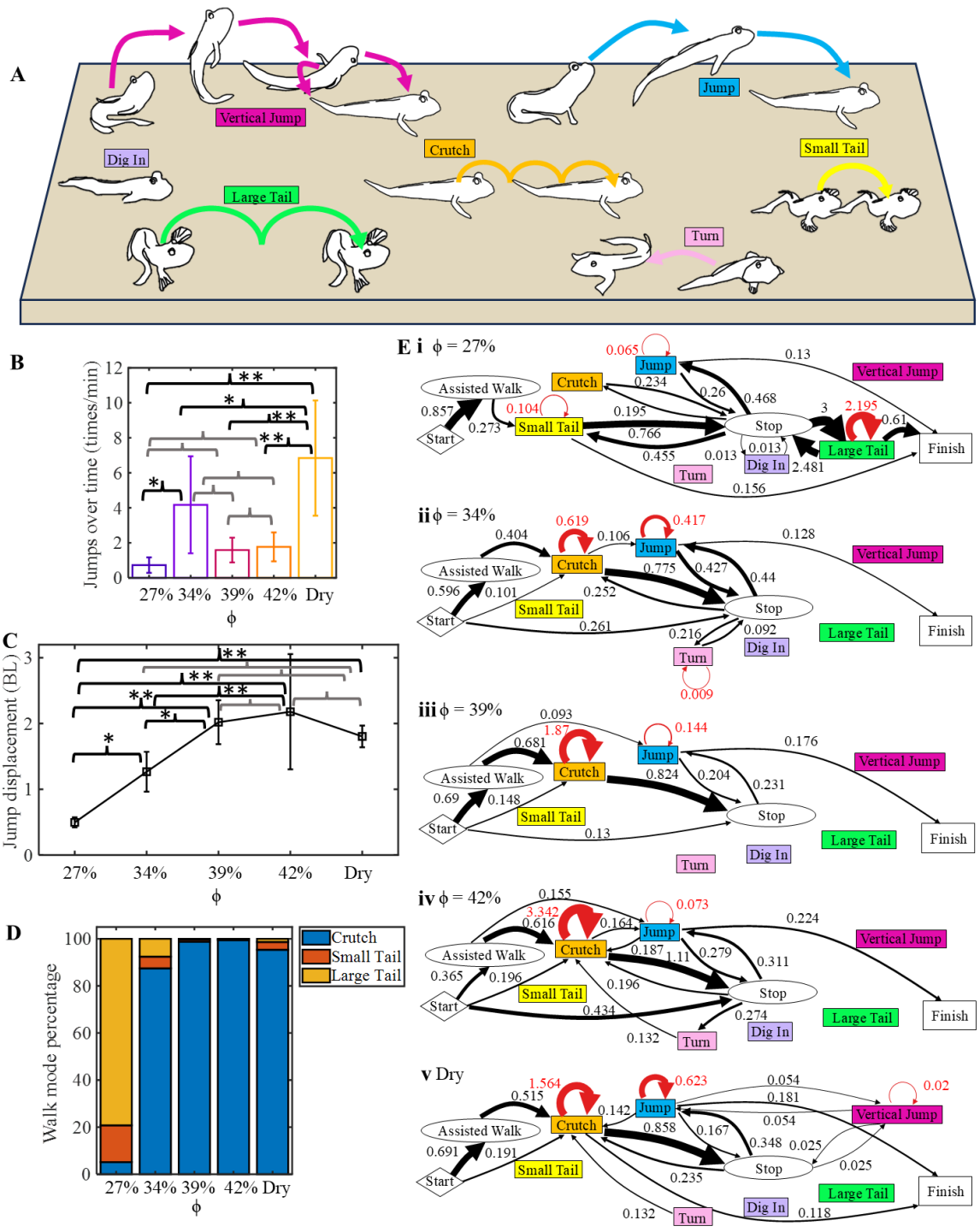

Figure 4.9: Behavioral adaptations. **(A)** Schematic of the mudskipper using

different modes on mud. Arrows indicate the movement direction in each locomotor mode. Each color corresponds to a mode. Vertical jump means the animal jumped vertically before turning and placing itself on the mud. **(B)** Jump count as a function of ϕ. **(C)** Jump displacement as a function of ϕ. **(D)** Crutch mode and its variant count percentage as a function of ϕ. **(E)** Mode transition diagram for (i) mud with (i) $\phi = 27\%$, (ii) $\phi = 34\%$, (iii) $\phi = 39\%$, (iv) $\phi = 42\%$ and (v) on dry mud. Red arrows and numbers correspond to transitioning to the same mode. The thickness of the arrows corresponds to frequency. A relative frequency greater than one means that on average it occurred more than once in each trial. Start corresponds to when the animal was put on the mud at the start of trial. Finish is when the animal is taken off the mud and placed back on mud or trial is finished. Stop means the animal stopped moving for some time. Assisted walk means the animal moved on mud with some parts in contact with the hand. Error bar in B-C corresponds to mean ± s.d. Statistics performed using one-way ANOVA. ** $P < 0.005$, * $P < 0.05$, Student's *t*-test, one-way ANOVA. See Table 4.1 for sample size.

body does not leave the surface. This variant of the crutch walk mode helped the mudskipper move over multiple cycles making this the most used walk mode (79.2%) on mud with $\phi = 27\%$ (Fig. 4.9D, 4.9E, i). When using the normal crutch mode on $\phi = 27\%$, the animal always stopped with the frequency of 0.234 after 1 cycle (Fig. 4.9E, i). The animal used the walk crutch mode with large tail bending more likely after stopping with a frequency of 3 (Fig. 4.9E, i).

The use of tail bending by the animal reduced as the mud strength increased from $\phi = 27\%$ and was minimal on $\phi = 39\%$ and $\phi = 42\%$ before starting to emerge again on dry mud (Fig. 4.9C). The small tail bending with walk mode (4.96%) was used less than walk mode with large tail bending (7.57%) on mud with $\phi = 34\%$ (Fig. 4.9D). The small tail bending with walk mode (3.28%) was used more than walk mode with large tail bending (1.38%) on dry mud (Fig. 4.9D). The crutch walk mode was still preferred by the animal to move forward compared to the two variants of the walk mode on $\phi = 34\%$ and dry mud with a frequency of 87.5% and 95.3% respectively

(Fig. 4.9D). The animal used the crutch walk mode from assisted walk with a high self-transition on all the mud strengths above $\phi = 27\%$ (Fig. 4.9D, ii-v).

4.7 Discussion

We measured the simple kinematics of the animal during each cycle of the crutching walk gait, the sustained terrestrial locomotion, seen in mudskippers. The different modes emergent in the animal locomotion to adapt to the variation of mud strength is likely due to the difficulty in traversing the mud using the crutch walking gait which is the preferred form of locomotion on land.

4.7.1 Failure of the crutch walk mode on weakest due to adhesive force

We hypothesized that the speed of the animal when using the crutch walk mode reduces as the mud gets weaker, likely due to the increase in the adhesive force of the mud and drag from mud sticking to the animal's body and appendages which in turn prevents the animal from lifting itself to move forward. This hypothesis was confirmed for mud strength decreasing from $\phi = 42\%$ to $\phi = 27\%$. This is because as the mud got weaker the animal had increased sinkage (Fig. 4.4C), body and fin contact length (Fig. 4.4D) and struggled more. This was seen in the decrease in the normalized time at mid-stance as mud strength decreased (Fig. 4.6A, ii-iii) which in turn reduced the forward displacement. This is likely due to insufficient lift force (F_L) needed to help the animal move forward (Fig. 4.13A).

For the animal to move forward, the lift force should be to be equal to its weight similar to other flowable substrates such as sand. On stronger mud, the mudskipper

sinks less (Fig. 4.13A) to generate the lift force (Fig. 4.13B) to move forward. The animal must sink in more to generate the same lift force on weaker mud (Fig. 4.13B). The pectoral fins of the animal also spread more as the mud strength reduced likely to increase the surface area of the fins which in turn would reduce the lift force. This was seen in the fin contact length (Fig. 4.4D, red) suggesting that the fins were more spread out on weaker mud.

Previous studies on sand found that the C-shaped legs of SandBot could move on flowable substrates fast similar to rigid ground if applied force is less than the yield force causing the substrate to resolidify (Li et al., 2009; Li et al., 2010). This has also been observed in studies on sea turtles and FipperBot moving sand similar to rigid ground by keeping the flipper applied force below the yield force to re-solidify the substrate (Mazouchova et al., 2010; Mazouchova, Umbanhowar, and Goldman, 2013). The mudskipper also likely has the capability of using its pectoral fins to resolidify the substrate. But unlike sand, mud can have large adhesive forces. Hence, if the mudskipper's pectoral fin motions are not adjusted then more mud sticks to the belly resulting in the difficulty of the animal to lift upwards due to a large adhesive force and drag. This in turn causes the forward displacement and speed (Fig. 4.4A-B) to decrease. This is likely why the animal took shorter normalized time to reach mid-stance (Fig. 4.6A, iii) and had reduced maximum fore-aft fin tip placement (Fig. 4.7C, iii) as the mud strength decreased from $\phi = 42\%$ to $\phi = 34\%$ which in turn reduced the forward displacement.

This lift force (F_L) is proportional to the horizontal contact area of the animal

which is the product of body contact length and body width, and the sinkage:

$$F_L = C_L.(c_b.w_b).\Delta h \tag{4.9}$$

where C_L is the lift coefficient that measures the mud strength and is proportional to the penetration force, w_b is the width of the animal which is constant. The product of body contact length (c_b) and sinkage (Δh) was shown to follow the same trend as the inverse of force at 1 cm from mud characterization (Fig. 4.4E-F) which in turn confirms our hypothesis.

4.7.2 Failure of the crutch walk mode on strongest mud strength due to lack of water

We hypothesized that the speed of the animal when using the crutch walk mode increases as the mud gets stronger. But the speed was reduced on dry mud (very high mud strength) likely because the mudskipper's body and fins started to stick to the surface of the dry mud causing the animal to slow down its speed (Fig. 4.4A). The sticking is likely due to the mucus on the animal's body or pectoral fins at surface contact area quickly drying up once the animal's wet body or pectoral fins came in contact with the mud surface. This likely caused the animal to quickly start the aerial phase (Fig. 4.6B, iii) and reach the mid-aerial phase (Fig. 4.6C, iii) to remove the fins faster and reduce the stance phase (Fig. 4.6A, iii) which reduced the forward displacement. In a previous study where the mudskipper moved on the surface of water and on gelatin, it was found that the speed of the mudskipper was smaller on the gelatin which was high in viscosity compared to the surface in water (Wang et al., 2013). In this study, we further found that if the strength, in other words viscosity was

increased from $\phi = 27\%$ to $\phi = 42\%$ then the speed increased and on the strongest mud (dry mud) strength the speed reduced.

4.7.3 Transition to jump mode when walking fails

Despite previous studies in observations of jump mode in mudskippers as a terrestrial escape response (Dijk, 1960; Jaafar and Murdy, 2017; Stebbins and Kalk, 1961) and quantifying kinematics of mudskipper jumping on a single substrate with no variation (Swanson and Gibb, 2004), there have been no systematic studies yet in jumping of mudskippers with mud strength variation. Here, we found that as the mud strength decreased from $\phi = 42\%$ to $\phi = 34\%$, the adhesive force of the mud increased, and the mud started to stick more to the animal's body and appendages making it difficult to move forward due to drag. This likely caused the animal to jump more often due to the failure of crutch walk mode on the mud (Fig. 4.9E, ii-iv).

When jumping, the animal bends its tail and pushes itself off the ground from the propulsive forces generated (Gibb, Ashley-Ross, and Hsieh, 2013). This likely helped the animal to get off the mud sticking to its body and appendages on mud with $\phi = 34\%$ to overcome the drag from the mud and helped remove itself from the surface of dry mud when the crutch walk mode failed. At $\phi = 27\%$, the jump mode likely failed to help generate enough propulsive forces to overcome the large adhesive force and drag the animal needed to push off the mud due to too much mud sticking onto the body and appendages. The jump mode was seen to be used the most often on dry mud (Fig. 4.9B). This is likely because the crutch walk mode failed on this mud due to the mucus on the animal's body and appendages quickly drying up as soon as it came in contact with the mud surface. This enabled the animal to jump to

lift its body off the surface to move. The animal also showed the emergence of vertical jumps on dry mud likely due to a lack of adhesive force and drag from the mud which enabled the animal to use a higher angle of attack during jumping (Fig. 4.9A, 4.9E, v).

Previous studies of escape responses in mudskippers (Swanson and Gibb, 2004) have shown that mudskippers can jump with an average displacement of 3 cm on hard surfaces. Here we found that on mud at all mud strengths, the animal can reach displacements greater than 3 cm (Fig. 4.9C). This shows that the animal likely generates larger thrust when pushing its tail onto the substrate which enables it to jump over a larger displacement. We also found that the jump displacement increased as mud strength increased from $\phi = 27\%$ to $\phi = 42\%$ and reduced on dry mud (Fig. 4.9C).

4.7.4 Tail bending to generate propulsive forces during crutch facilitates locomotion

On the weakest mud, the animal was unable to move with both the jump mode (Fig. 4.9A) and the crutch walk mode (Fig. 4.9C) likely due to generation of a large adhesive force and drag from mud sticking to animal's body and fins. This enabled the animal to start using tail bending along with the normal crutch mode. There have been observations of large tail bending with the normal crutch mode in mudskippers moving over inclined sand (McInroe et al., 2016; Naylor and Kawano, 2022) and observations of small tail bending with normal crutch mode on surface of water and gelatin (Wang et al., 2013). Despite observations of the animal using large (Naylor and Kawano, 2022) and small (Wang et al., 2013) tail bending, there have been no systematic study

yet on these modes. Here we showed through our systematic study that these walk mode variants emerge when normal crutch mode fails on the weakest ($\phi = 27\%$) mud and then reduces in occurrence on mud with $\phi = 34\%$ and is negligible on mud with $\phi = 39\%$ and $\phi = 42\%$ before increasing its occurrence on strongest (dry) mud (Fig. 4.9D). The animal likely used tail bending on weakest mud to generate propulsive forces to overcome the large adhesive force and drag as seen in the use of tail in MuddyBot, a robo-physical model developed to study the use of tail in mudskippers on inclined sand, where it was shown to help improve performance on inclined sand substrate (McInroe et al., 2016).

On the weakest mud, the walk crutch mode with small tail bending helped the animal to move but only over one cycle which is similar to the normal crutch mode. This likely enabled the animal to use walk crutch mode with large tail bending to help it move over multiple cycles on the mud. This behavior resembles skipping on water surfaces where the animal bends its tail to help thrust itself forward (De and Nandi, 1984; Dijk, 1960; Jaafar and Murdy, 2017). The animal also likely used small tail bending due to fatigue. We found that the animal used the large and small tail bending along with normal crutch mode sometimes on mud with mud strength increasing from $\phi = 34\%$ to $\phi = 42\%$ and the strongest (dry) mud when it was tired or struggling to move forward.

4.7.5 Transition to different modes when the primary locomotion fails shows capability of transition across substrates

We hypothesized that as the animal started to struggle more with variation in the mud strength, it would start to either modify the crutching gait or use a new strategy to help

it move forward. The observations in this study have confirmed the hypothesis. The primary locomotion of the animal, the crutch walk mode, as seen in our observations cannot be modified by the animal with variation in mud strength. This shows that the crutch walk mode can be considered as a stereotypical template for the animal and it can only be modulated by a very small amount due to which it fails on the weakest and strongest mud and different modes start to emerge. As the animal started to struggle more when the mud strength got weaker or extremely dry the primary locomotion, the crutch walk mode, started to fail and this enabled the emergence of the jump mode. As the jump mode started to fail on the weakest mud, the animal started to use a variant of the crutch walk mode by bending the tail to help the animal push itself forward during the propulsive phase of the crutch walk mode. This shows that the animal can easily transition over a continuum of substrates as seen in the natural environment. In the natural environment, the animal must swim in deep water and likely transitions to walking at the bottom of the water as it gets closer to the water–land transition zone. The animal can quickly adapt to the various mud strengths at this zone by transitioning to other modified crutch walking gaits or jump and even swimming modes before continuing to walk on land.

4.8 Future work

This study focuses more on the biological aspect of terradynamics. To help develop a better understanding of how mudskippers can adapt to variation in mud strength and change between strategies, our next step is to develop resistive force theory (RFT) to calculate forces on fish body and pectoral fins to help predict performance landscapes.

Resistive force theory has been found useful in finding force laws empirically analogous to theoretical force laws in fluids and aerodynamics. Previous studies have used RFT to understand how the animals interact with substrates such as dry (Astley et al., 2020; Ding et al., 2012; Ding, Li, and Goldman, 2013; Goldman, 2014; Li, Zhang, and Goldman, 2012; Li, Hsieh, and Goldman, 2012; Li, Zhang, and Goldman, 2013; Maladen et al., 2009; Maladen et al., 2011; Mazouchova et al., 2010; Mazouchova, Umbanhowar, and Goldman, 2013; McInroe et al., 2016; Zhang and Goldman, 2014) and wet (Sharpe, Kuckuk, and Goldman, 2015; Winter, Deits, and Hosoi, 2012) sand to generate the right forces. This will help in getting a better understanding of the locomotor-mud interaction mechanics as the mud strength is varied.

We have also developed a robo-physical model that moves similar to that of the mudskipper. We plan to use this robo-physical model to perform systematic and repeatable experiments and explore the parameter space to better understand why mudskippers use certain parameters and do not prefer to use other parameters. We have also added lifting segments to the robo-physical model which will help us further study the use of tail bending in the animal when using the normal crutch mode.

4.9 Appendix

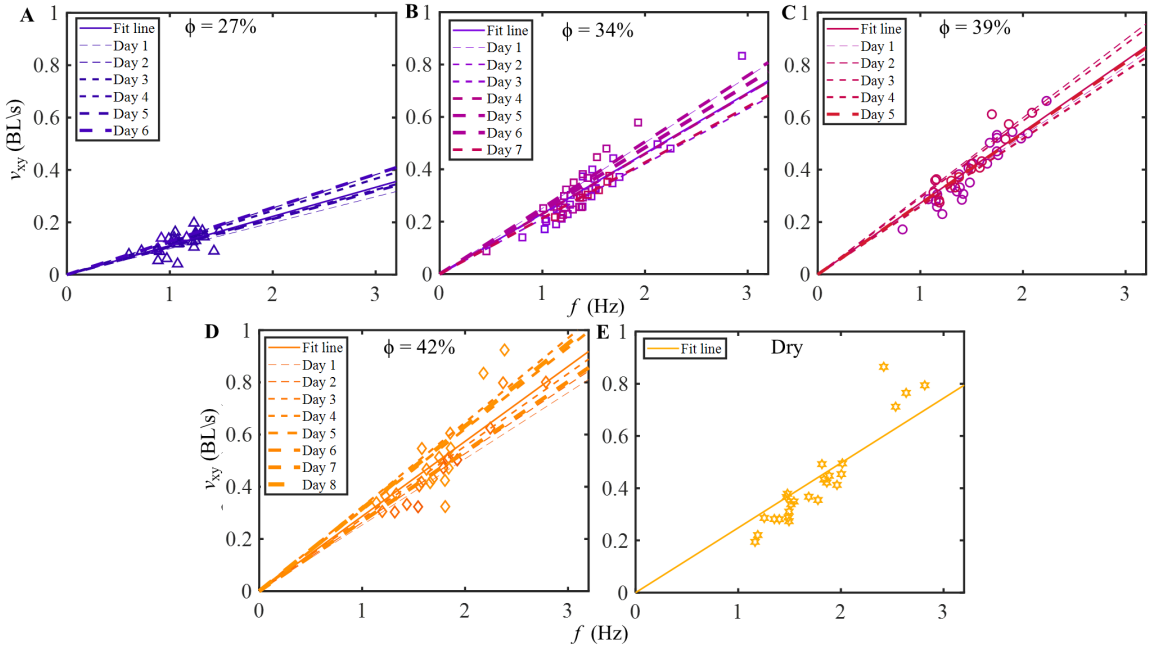

Figure 4.10: Animal performance over each day across ϕ. Average speed (v_{xy}) of the animal's nose tip relative to frequency (f) for **(A)** $\phi = 27\%$, **(B)** $\phi = 34\%$, **(C)** $\phi = 39\%$, **(D)** $\phi = 42\%$, and **(E)** dry mud. Solid lines correspond to linear least square fit lines of all the walk trials in a mud strength. The color of the fit line for each mud strength is a function of force at 1 cm from mud characterization. Each data point's color is a function of force at 1 cm measured using the penetrometer taken on the day of the walk trial. The dashed fit lines correspond to linear least square fit lines each day of the walk trials. The thickness of the dash lines is a function of the day number for each mud strength.

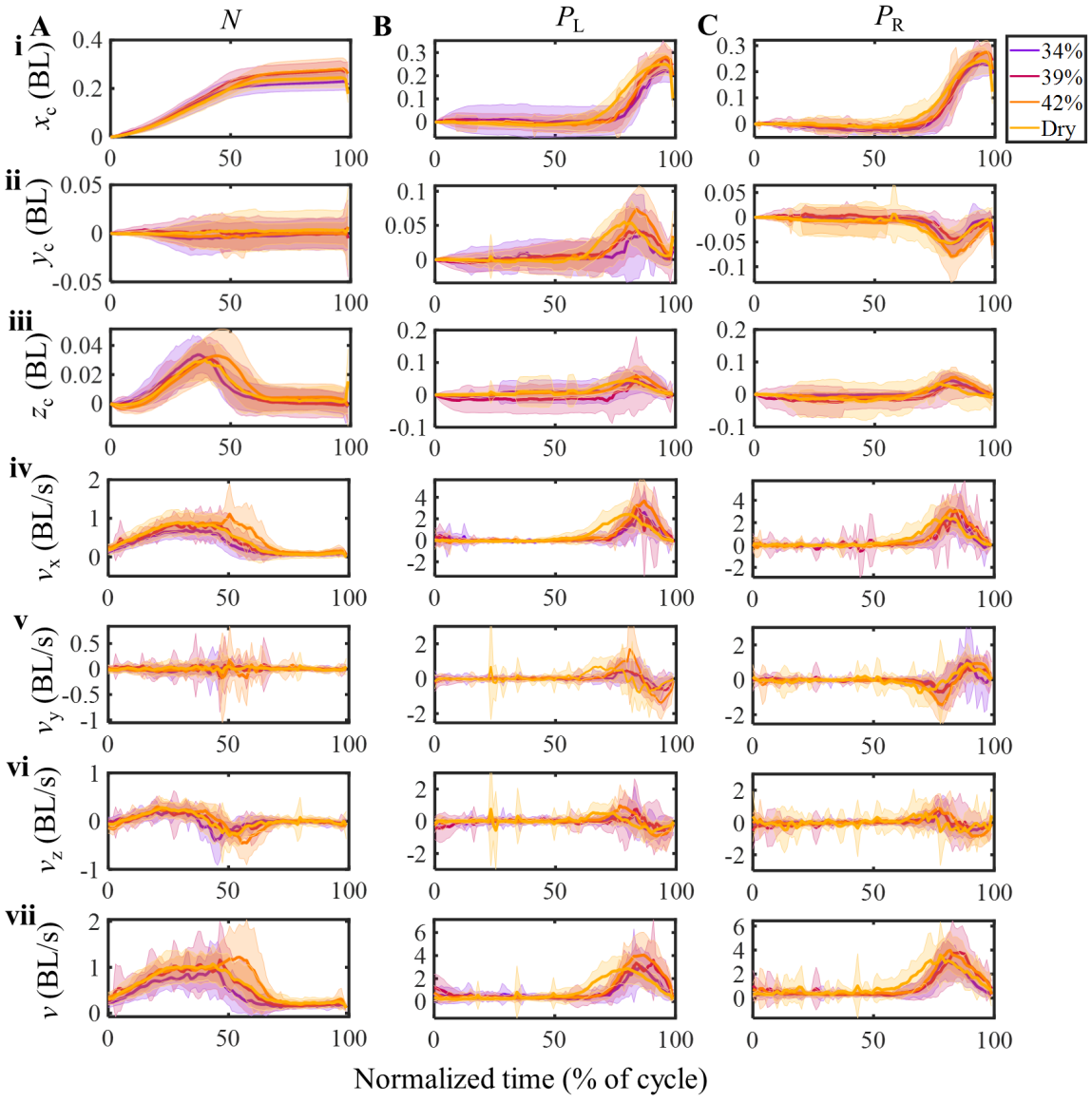

Figure 4.11: Animal kinematics over one cycle across ϕ. Animal's **(A)** nose tip (N), **(B)** left pectoral fin tip (P_L), and **(C)** right pectoral fin tip (P_R) kinematics. (i) Fore-aft periodic displacement (x_c), (ii) lateral periodic displacement (y_c), (iii) vertical periodic displacement (z_c), (iv) fore-aft velocity (v_x), (v) lateral velocity (v_y), (vi) vertical velocity (v_z) and (vii) total velocity (v) over normalized time on mud with $\phi = 34\%$ (purple curve), $\phi = 39\%$ (magenta curve), $\phi = 42\%$ (orange curve) and dry mud (yellow curve). The shaded error bar corresponds to mean $\pm$ s.d.

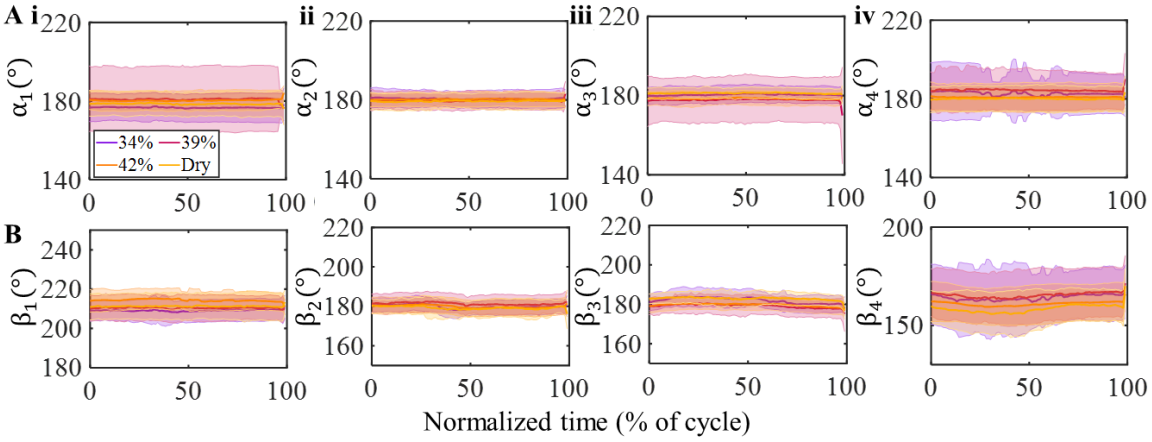

Figure 4.12: Body rotation varying with ϕ. (A) Lateral bending body angle as a function of ϕ. **(B)** Vertical bending body angle as a function of ϕ. (i) Head to body rotation on the lateral plane (α_1) and vertical plane (β_1), (ii) upper mid-body rotation on the lateral plane (α_2) and vertical plane (β_2), (iii) lower mid-body rotation on the lateral plane (α_3) and vertical plane (β_3), (iv) tail-body rotation on the lateral plane (α_4) and vertical plane (β_4) over one cycle for $\phi = 34\%$ (purple curve), $\phi = 39\%$ (magenta curve), $\phi = 42\%$ (orange curve) and dry mud (yellow curve). The shaded error bar corresponds to mean $\pm$ s.d.

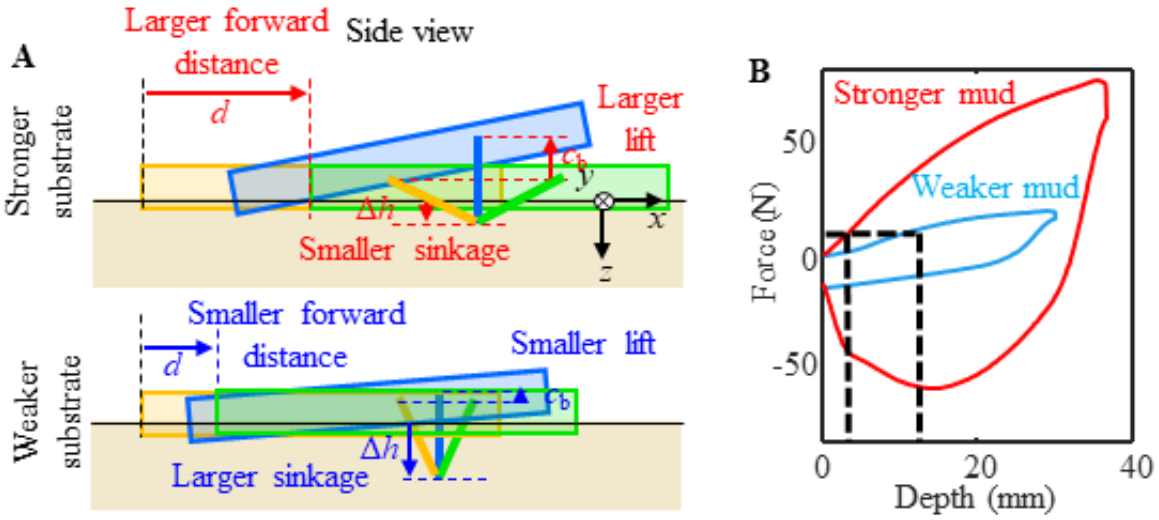

Figure 4.13: Animal sinkage when moving on stronger and weaker mud. **(A)** Schematic of the animal sinkage on stronger and weaker mud. Yellow corresponds to the initial animal position. Blue corresponds to mid-stance position and green corresponds to the end of stance phase. **(B)** Force as a function of depth profile for stronger and weaker mud.

Chapter 5

Body lifting by ropefish during terrestrial locomotion on mud with different strengths

This chapter is to be submitted as an article entitled *Body lifting by ropefish during terrestrial locomotion on mud with different strengths*, authored by Divya Ramesh, Daniel Collum, Abdulla Ubaydullaev, Hongbo Zhang, Alex Nath, Dami Kim, Catherine Pollard, Chiadika Vincent, Na Dai, and Chen Li.

5.1 Author Contributions

Divya Ramesh conducted and oversaw animal experiments and performed animal and force data analysis; Daniel Collum developed the horizontal drag force measurement device and conducted force measurement experiments; Abdulla Ubaydullaev assisted in force measurement experiments; Hongbo Zhang, Alex Nath, Dami Kim, and Na Dai helped conduct animal experiments and helped with animal data tracking; Catherine Pollard developed lifting robot and assisted in animal data tracking; Chiadika Vincent developed first prototype of horizontal drag force measurement device; Divya Ramesh and Chen Li wrote the paper.

5.2 Acknowledgment

We thank Qiyuan Fu for helping with the preliminary study and animal care; Gargi Sadalgekar, Dennis Lin, Aydin Mokaddem, Julie Le, Zheyu Zhou, Xiyuan Wang, Bill Wang, Luna Liu, Kyungmo Choi, and Yaqing Wang for helping with animal care. This

study was funded by the Burroughs Wellcome Fund Career Award at the Scientific Interface and a Johns Hopkins University Bridge Grant.

5.3 Summary

Amphibious fishes regularly encounter mud of different strengths when moving at the water–land interface which can be challenging. Ropefish like other elongated amphibious fishes regularly make forays onto land using axial-based locomotion (lateral bending). They are likely capable of vertically bending their body which many terrestrial animals do to enhance locomotion. Only one amphibious fish study has observed a small, local tail lifting in mudskippers on inclined sand. We hypothesize that the ropefish starts to lift sections of its body in coordination with lateral bending likely to modulate friction on higher mud strengths. To test this, we allowed the animal to move over the mud of 3 different mud strengths. We observed that the animal started to sink more and had a reduction in speed and larger contact length on the lowest mud strength. On mud of higher strength, the animal had increased speed and minimal sinkage with less body contact length due to large body sections lifting off the mud surface likely to overcome ground friction. We have performed horizontal drag force measurement experiments whose force measurements can be used in resistive force theory for mud to calculate the modulation of lift and drag force by body lifting. To better understand the coordination between body lifting and lateral bending, we have also developed a robophysical model.

5.4 Introduction

Amphibious fishes regularly make foray onto land by transitioning from swimming in water to crawling on land (Ashley-Ross et al., 2013; Bressman, 2022; Pace and Gibb, 2014; Sayer, 2005) at the water–land interface. They have been found to use morphologies and control systems that were originally made for swimming for walking or crawling on solid surfaces (Bressman, 2022; Bressman, Gibb, and Farina, 2018; Bressman et al., 2019; Bressman, Morrison, and Ashley-Ross, 2021; Pace and Gibb, 2011; Redmann et al., 2020; Standen et al., 2016). This water–land interface often has wet flowable substrates such as mud or wet sand (Clack, 2012; Perry et al., 2015; Wendt et al., 1997) that vary in solid composition and wetness. Such substrates can behave similarly to a solid or flow similar to a liquid based on the forces applied relative to the yield strength (Coussot, 1997; Goldman, 2014; Li et al., 2009; Li, Hsieh, and Goldman, 2012; Mazouchova et al., 2010; Winter, Deits, and Hosoi, 2012; Sharpe, Kuckuk, and Goldman, 2015). The moisture content of the substrate also causes variation in the yield strength (Coussot, 1997) at which the solid–fluid transition occurs which makes locomotion challenging. Mud, unlike sand, can have strong cohesion caused by colloidal effects (Coussot, 1997). This causes the mud to stick to the animal's appendages and body, which can affect its locomotion.

Amphibious fishes can adapt exceptionally well to substrate variation despite these challenges by adjusting their body and appendages and transitioning between strategies as they interact with the substrate. Recent studies have quantified the kinematics (Naylor and Kawano, 2022; Redmann et al., 2020) and muscle control (Horner and Jayne, 2014; Lutek and Standen, 2021) to understand better how fishes locomote on wet flowable substrates. Several studies have investigated animal and

robot locomotion/behavior on dry (Li, Hsieh, and Goldman, 2012; Maladen et al., 2009; McInroe et al., 2016; Naylor and Kawano, 2022), partly wet (Kudrolli, Ramirez, and Weitz, 2019; Sharpe, Kuckuk, and Goldman, 2015) and fully saturated sand (Dorgan, 2018; Redmann et al., 2020) unlike on mud, which only has a few animal studies (Falkingham and Horner, 2016; Horner and Jayne, 2014; Naylor and Kawano, 2022; Standen et al., 2016), especially in the solid–fluid transition concentration. Viscous fluids such as gelatin (Wang et al., 2013), methyl cellulose (Lutek and Standen, 2021), and Poly-Bore (Horner and Jayne, 2008) have also been used as substrates to study fish locomotion.

It is necessary to quantify the environmental interaction between fish and wet substrate to help fully understand the generation of forces on the animal's body and appendages, and how the locomotor morphology, control, and kinematics permit performance. The interaction mechanics between mud and animal is yet to be studied unlike on sand, where it has been extensively studied (Li, Hsieh, and Goldman, 2012; Maladen et al., 2009; Sharpe, Kuckuk, and Goldman, 2015). Our previous study (Ramesh et al., 2024a) has established tools and methods to systematically prepare, vary, and control mud of different strengths to facilitate this similar to methods that have been well established for controlling dry (Li et al., 2009; Maladen et al., 2009) and wet (Sharpe, Kuckuk, and Goldman, 2015) sand.

Resistive force theory (RFT) has been used in finding force laws empirically that are analogous to theoretical force laws in fluids and aerodynamics to help better understand the locomotor-substrate interaction mechanics. Although previous studies have used RFT to understand the locomotor-substrate interaction mechanics for dry (Li, Zhang, and Goldman, 2012; Li, Hsieh, and Goldman, 2012; Astley et al., 2020;

Ding et al., 2012; Ding, Li, and Goldman, 2013; Goldman, 2014; Li, Zhang, and Goldman, 2013; Maladen et al., 2009; Maladen et al., 2011; Mazouchova et al., 2010; Mazouchova, Umbanhowar, and Goldman, 2013; McInroe et al., 2016; Zhang and Goldman, 2014) and wet (Sharpe, Kuckuk, and Goldman, 2015; Winter, Deits, and Hosoi, 2012) sand, such force laws are yet to be developed for mud.

Amphibious fishes use three distinct strategies on land to locomote which are the appendicular-based, axial-appendicular-based, and axial-based locomotion (Pace and Gibb, 2014). Our previous study performed a systematic study of mudskipper which uses appendicular-based locomotion (crutching gait) on land, moving on mud with different strengths (Ramesh et al., 2024b) and found that the animal either modifies its crunching gait or transitions to another locomotion strategy with mud strength variation. In this study, we will focus on axial-based locomotion which is used by elongate amphibious fishes on land (Pace and Gibb, 2014). Elongate fishes laterally bend their body to propel forward on solid ground (Pace and Gibb, 2011; Clardy, 2012; Mehta et al., 2021; Sayer, 2005; Gillis, 1998; Gillis, 2000; Watz et al., 2019; Ward

Figure 5.1: Choice of model organism. (A) Ropefish moving on mud.

et al., 2015) similar to snake's lateral undulation (Schiebel et al., 2019). We chose ropefish (*Erpetoichthys calabaricus*) as the model organism for axial-based locomotion (Fig. 5.1) because they have been extensively studied in terms of kinematics and muscle control (Pace and Gibb, 2011; Ward et al., 2015) during terrestrial locomotion.

Studies have observed that ropefish use lateral bending with minimal dorsoventral bending on solid ground which is less precise compared to snakes likely due to differences in musculature and morphology (Pace and Gibb, 2011). When swimming, the animal's anterior body has a linear forward movement compared to the posterior body whereas, its posterior body and tail have a cyclic lateral movement and its pectoral fins paddle for forward propulsion (Pace and Gibb, 2011; Pace and Gibb, 2014). A study observed that as the water depth reduces, the ropefish's anterior body starts to have an increased magnitude of lateral excursions and wave amplitude (Pace and Gibb, 2011). This shows that the animal can modify the wave number and amplitude of its lateral bending.

Many terrestrial animals can bend their body vertically to improve locomotion on land. Some mammals bend their spine vertically to enhance locomotion gaits such as galloping (Kamimura et al., 2022; Bertram and Gutmann, 2009; Schilling and Hackert, 2006) and half-bounding (English, 1980; Schilling and Hackert, 2006). Reptiles such as snakes use vertical bending in arboreal environments on lateral obstacles (Jurestovsky, Usher, and Astley, 2021; Astley and Jayne, 2009; Astley and Jayne, 2007), in complex 3-D terrain(Fu, Astley, and Li, 2022), and in gliding (Yeaton et al., 2020). Ropefish may also have the capability to vertically bend its elongated body similar to snakes. A previous study on snakes found that they lift curved parts of their body to modulate ground friction (Hu et al., 2009). It is likely that ropefish

can also lift parts of their body in combination with lateral bending on higher mud strengths for a similar function. Despite an observation of a small, local tail lifting in mudskippers on inclined sand (Naylor and Kawano, 2022), there is no study yet with observation of elongate amphibious fishes lifting sections of their body with systematic variation in mud strength.

We hypothesize that the animal starts to modify its terrestrial locomotion as the mud strength increases. To test the hypothesis, we allowed the ropefish to locomote on mud with different mud strengths and used high-speed cameras to track the animal body and pectoral fins to help measure the kinematics. We hypothesized that (1) the animal when using the lateral bending (axial-based locomotion) starts to traverse slower as the mud gets weaker. This is likely due to the increase in the adhesive force caused by mud sticking to the animal's lower body and drag arising from mud sticking on the animal's upper body which prevents the animal from lifting itself to progress forward. (2) The animal starts to lift parts of its body in coordination with lateral bending to improve or maintain its performance. To test hypothesis (1), we used high-speed camera videos to measure and quantify the animal's performance during axial-based locomotion. To test hypothesis (2), we performed kinematics to help understand the body lifting and lateral bending coordination. We also performed horizontal drag force experiments to develop a resistive force theory for mud which can be used to calculate the modulation of lift and draft forces by body lifting.

5.5 Materials and Methods

5.5.1 Animal experimental testbed, choice of mud substrate, and mud characterization during experiments

We used Georgia Kaolin (China Clay, Old Hickory Clay Company, Florida, USA) as the substrate for our animal and force measurement experiments because clay mud behaves quantitatively similar to natural mud (Coussot, 1997). The clay mud was prepared using an automated mixing system (Fig. 5.2A) that was developed and used in our previous studies (Ramesh et al., 2024a; Ramesh et al., 2024b). The experimental testbed consisted of a container (HOMZ, Chicago, IL, USA) that is 1.02 m in length, 0.51 m in width, and 0.16 m in height with an airtight lid was used to hold the clay mud to perform experiments and during storage (Fig. 5.2D). To track the water loss and maintain the mud strength throughout the study, we used the custom portable penetrometer (Ramesh et al., 2024a) during the animal and horizontal drag force measurement experiments (Fig. 5.2B).

We filled the container up to at least $3/4^{th}$ of the tub height to prevent boundary effects from affecting the animal locomotion and the intruder during mud characterization. Boundary effects are defined as artifact forces applied on an object as it moves near the container's boundary (Coussot, 1997). We also used sealing methods that were developed and used in our previous study to help minimize water loss (Ramesh et al., 2024a). This method consisted of the sides of the lid covered with rubber sealing strips (CloudBuyer) to further make the lid airtight and to prevent water drops from escaping from the sides of the lid (Fig. 5.2D). A plastic wrap was placed directly on the mud surface to minimize the evaporation of water from the surface to the top

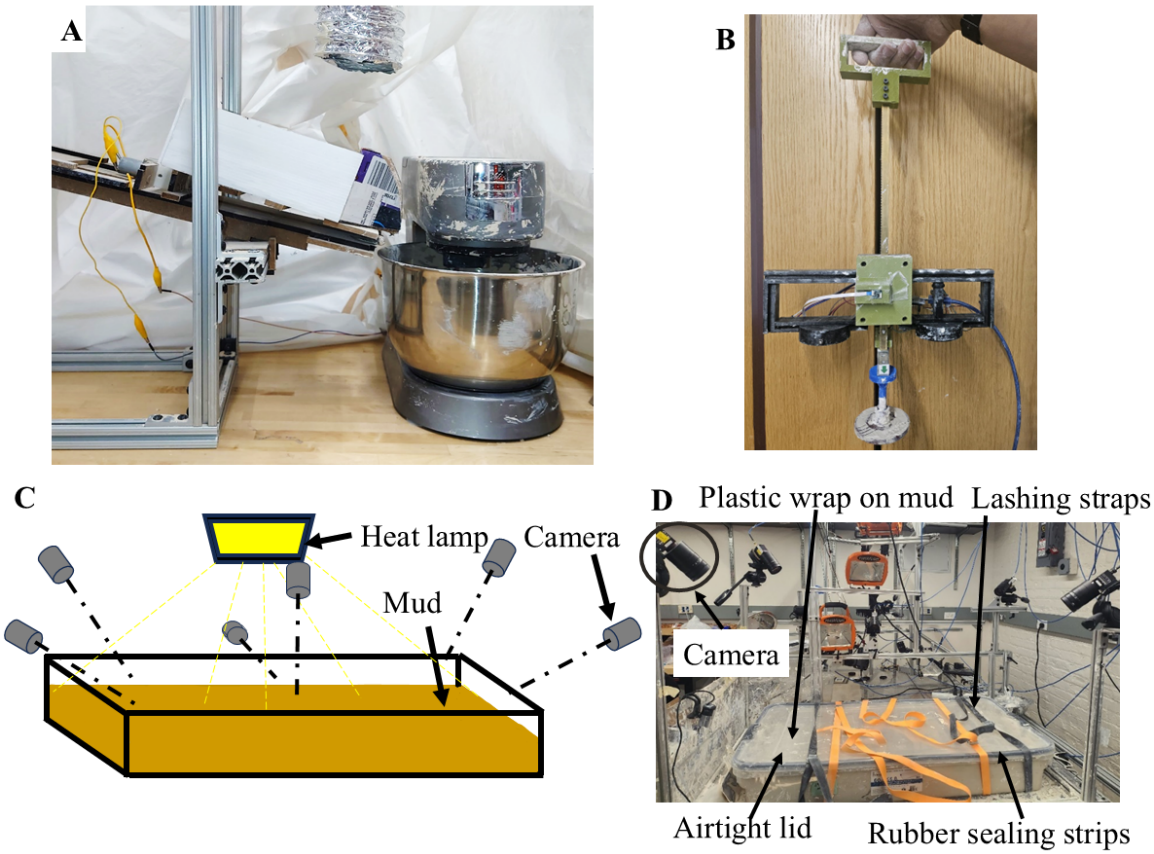

Figure 5.2: Experimental setup. (A) Automated mud preparation system. **(B)** Custom portable penetrometer. **(C)** A schematic of the experimental setup. **(D)** Photo of the experimental setup. Reproduced from Ramesh et al., 2024b

of the lid. We also placed lashing straps (ACE-Lashing Straps, Acelane) around the closed container to tighten the lids further onto the container (Fig. 5.2D).

5.5.2 Different mud strengths used for experiments

We chose $\phi = 27\%$ which is closer to the lower limit of the solid–fluid transition regime and $\phi = 39\%$ which is in the solid–fluid transition regime based on the mud characterization using the automated vertical penetration device (Ramesh et al.,

Trial count for analysis	A1	A2	A3	A4	A5	Total trials	No. of Treatments	Trials per treatment (27%, 39%, Cracked dry mud)
Walk trials for forward displacement and speed at each cycle	13	8	9	15	17	62	3	8, 13, 41
No. of cycles for sinkage and contact length	8	4	7	8	12	39	3	8, 16, 15
Walk trials tracked for kinematics	3	1	2	4	3	13	1	-, 13, -

Table 5.1: Sample size for different analysis. A1 corresponds to Animal 1

2024a). We also chose cracked dry mud that has a very high ϕ in the fractured mud regime. It was prepared by drying out the water content after the wet mud was flattened in a container over several days. We chose $\phi = 27\%$, 34% (which is also in the solid–fluid transition regime), and 39% for the horizontal drag force measurement experiments.

5.5.3 Experimental setup, sample size and protocol for animal locomotion

We tracked the animal locomotion using 6 synchronized high-speed cameras (N-5A100 17 Gm/CXP-6-1.0, Adimec, Eindhoven, The Netherlands) and used it for 3-D

reconstruction (Hedrick, 2008) at 100 frames per second for all trials (Fig. 5.2C-D). We also used two webcams (Logitech and HP) to record top view and side view videos at 30 frames per second to capture the entire animal study completed in a day. The experimental setup was well lit and heated using a heat lamp (500 Watt Portable Halogen Work Light, Woods) (Fig. 5.2C). The heat lamp was switched off between each trial to maintain the temperature.

We used 5 ropefishes (*Erpetoichthys calabaricus*) for this study. We chose to use this species because they have been extensively studied in previous studies which will allow us to use our results and findings to connect to the previous work and provide novel insights on the animal's adaptation to varying mud strength. All animals were approved by and in compliance with The Johns Hopkins University Animal Care and Use Committee (protocol FI21E163 and FI24E75). The animals were fed daily with dried shrimp pellets and housed in well-lit, well-heated aquarium tanks filled with fresh water. The animals were allowed to get accustomed to each mud strength for a few minutes on the first day of experiments. Due to the difficulty of the animal locomoting on $\phi = 27\%$, we could only collect data for 3 individuals.

We also recorded the length, height, and weight of the animals after the experiment concluded each day. The length and height were estimated using ImageJ software. The animals were weighed using a digital weighing scale (American weigh scales, USA). The weight of the animals was 14.03 ± 1.47 g (mean $\pm$ s.d.). The length and height of the animals were 22.2 ± 1.06 cm and 1.16 ± 0.18 cm respectively. The average temperature of the experimental setup recorded at the start of each trial was $25 \pm 0.6^\circ$ C.

Here we defined a trial from when the animal was first placed on the mud until

when it was finally taken off the mud. We recorded each trial using high-speed cameras. We started recording the videos before the animal was first placed on the mud and stopped the recording after the animal was finally taken off the mud in a trial. During each trial, we gently prodded the animal by hand to make the animal move. When the animal was drying out or had too much mud covering the body, we removed it off the mud and placed and cleaned it in water for a few seconds before being placed back on the mud. The animal was taken off the mud at the end of each trial after 2–3 minutes. The animal was allowed to rest for some time (10 – 15 minutes) before each trial. We mixed the mud using a metal spatula with beveled edges (Homi Styles) and manually flattened by hand using a piece of plexiglass (McMaster-Carr, Princeton, NJ, USA) after the mud was disturbed by fish during each trial.

The custom portable penetrometer was used to characterize mud strength spatially on the disturbed mud after animal trials (Ramesh et al., 2024a). We defined walk trials as those trials where the ropefish moved continuously in consecutive lateral undulation cycles. We rejected walk trials where the animal was close to the testbed boundary due to boundary effects. For kinematics analysis, we chose walk trials which can be seen on two camera views needed for 3-D reconstruction. We defined cycle trials as those trials where the animal laterally undulates over one cycle. For sinkage and contact length analysis, we used cycle trials. See Table 5.1 for details on the sample size for each analysis.

5.5.4 Animal tracking and 3-D reconstruction

We used DLTdv digitizing tool (Hedrick, 2008; https://biomech.web.unc.edu/dltdv/) in MATLAB to manually track data for all the 2-D analysis. We tracked 10 points

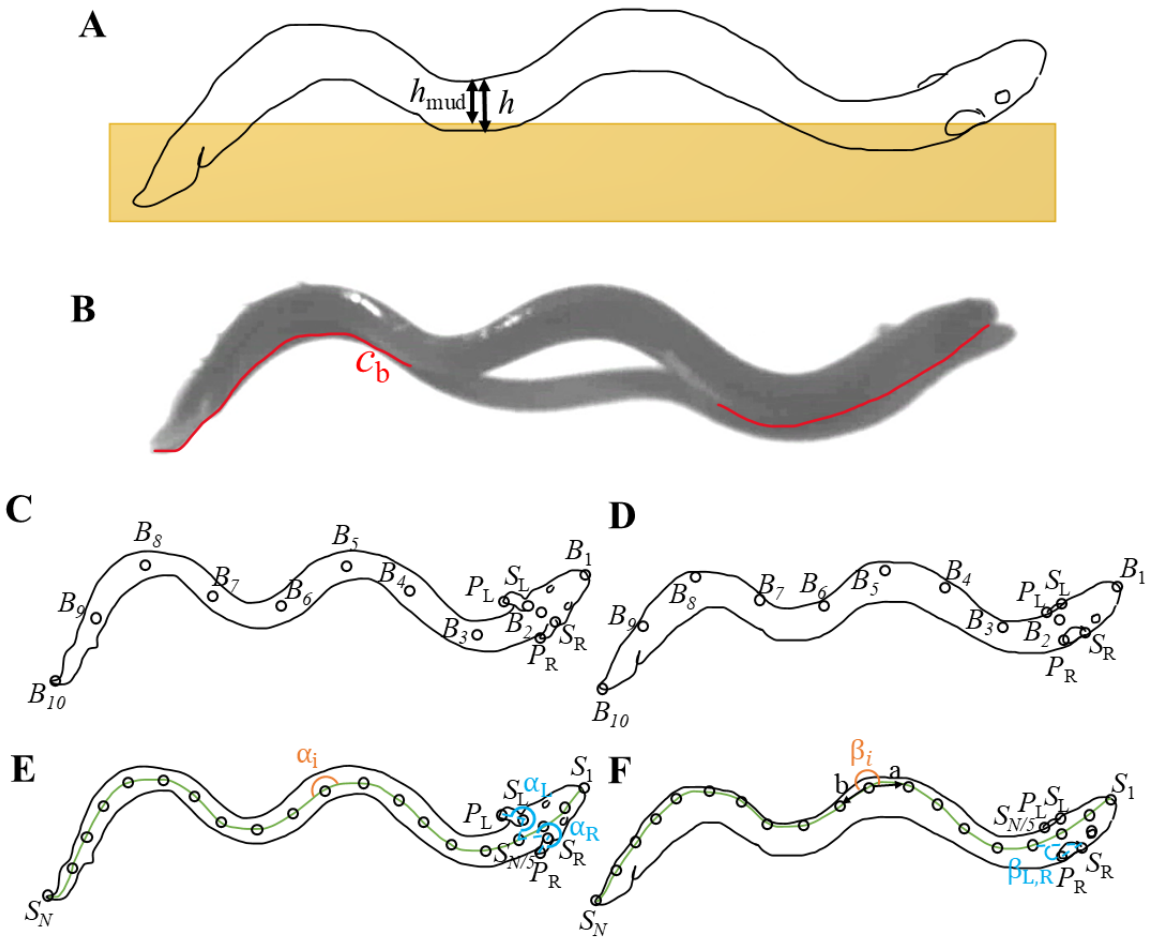

Figure 5.3: Animal tracking, sinkage, and contact length. (A) Schematic of animal sinkage on mud. **(B)** Animal body contact length (c_b, red line) on a snapshot of the animal during maximum lifting in a trial. **(C)** Top view schematic of tracked markers. The black circles indicate tracked markers starting from nose tip (B_1) till tail tip (B_{10}), shoulder left (S_L) and right (S_R), pectoral fin tip left (P_L) and right (P_R). **(D)** Sideview view schematic of tracked markers. The black circles indicate tracked markers starting from nose tip (B_1) till tail tip (B_{10}), shoulder left (S_L) and right (S_R), pectoral fin tip left (P_L) and right (P_R). **(E)** Top view schematic of the markers from the spline curve (green curve) and definitions of lateral bending angles on the animal body. The black circles indicate the markers from the spline curve starting from the nose tip (S_1) till the tail tip (S_N, $N = 20$), shoulder left (S_L) and right (S_R), pectoral fin tip left (P_L) and right (P_R). Lateral bending body angles (orange, α_i) and fin-body angles (blue, $\alpha_{L,R}$) on the transverse plane. **(F)** Side view schematic of the markers from the spline curve (green curve) and definitions of vertical bending angles on the animal

body. Vertical bending body angles (orange, β_i) and fin-body angles (blue, $\beta_{L,R}$) on the sagittal plane. L and R denote the left and right pectoral fins. a and b vectors are the direction vectors for finding the body and fin-body angles.

on the animal body starting from the nose tip (B_1) until the tail tip (B_{10}) for 3-D kinematics on top view (Fig. 5.3C) and another view where the locomotion is along the side view (Fig. 5.3D). We also tracked the left (P_L) and right (P_R) pectoral fin tips and the shoulder ($S_{L,R}$) where the pectoral fins are attached to the animal body (Fig. 5.3C-D). The points were tracked using DeepLabCut (https://www.mackenziemathislab.org/deeplabcut; Mathis et al., 2018). For tracking using DLC, we manually tracked the markers on the animal body for several video frames. We used this data as a training sample to train the neural network in DeepLabCut for each camera view. We then examined each tracked video visually and manually re-tracked some video frames for videos with bad tracking and re-trained the training sample. We then converted the tracked DLC data to DLTdv tracked points for further processing of data and analysis in MATLAB.

The 2-D positions of the tracked points over the 2 views for each animal trial were first used to generate a body curve (spline curve) at each time interval using the spaps function in MATLAB (Fig. 5.3E-F). The curve was used to extract 20 equidistant 2-D positions from nose tip to tail tip (S_1 to S_N) for each camera view to ensure that the points are placed in the same locations in all views for accurate 3-D tracking (Fig. 5.3E-F). We then converted these 2-D positions to 3-D kinematics using the direct linear transformation method and DLTdv digitizing tool. We built a calibration object that consists of lego bricks (The Lego Group, Billund, Denmark) to facilitate the 3-D calibration.

We used Principal Component Analysis (PCA) (Ma'ckiewicz and Ratajczak, 1993) to rotate the coordinate system always to have the forward axis be the x-axis, have the animal locomote from left to right, and face upwards. We further added rotation criteria to ensure the animal faced in the forward direction which the PCA was not able to do. This consisted of rotating the data about the z-axis by 180 degrees if the animal's nose tip's x-axis position is less than the animal's tail tip's x-axis position.

5.5.5 Fore-aft displacement and speed analysis

We calculated the animal's forward displacement at each cycle (d) for walk trials for all 3 mud strengths (sample size in Table 5.1) using the following:

$$d = ((x_i - x_{i-1})^2 + (y_i - y_{i-1})^2)^{1/2} \tag{5.1}$$

Where (x_{i-1}, y_{i-1}) and (x_i, y_i) are the forward and lateral positions of the ropefish's nose tip at the start of cycle i and end of cycle i respectively, tracked on top view videos for 2-D analysis. The forward speed (v_{xy}) was calculated using the following:

$$v_{xy} = \frac{d}{\Delta t}, f = (\Delta t)^{-1} \tag{5.2}$$

Where Δt is the duration of a walk cycle and f is the frequency of a walk cycle. The forward displacement, speed, and frequency were then averaged over all cycles in a walk trial.

5.5.6 Sinkage and contact length analysis

We used videos showing the animal locomoting relatively in a side view to estimate the animal sinkage for each cycle trial for all 3 mud strengths (sample size in Table 5.1). To measure the sinkage, the animal's body height visible (h_{mud}) was measured using Eqn. 5.1 using a tracked point on top of the animal, and another tracked point at the bottom of the animal on mud (Fig. 5.3A) during minimal body lifting. We measured the actual height of the animal (h) by tracking points like those tracked for h_{mud} but when the animal was completely off the mud (Fig. 5.3A). The sinkage (Δh) was calculated using the following:

$$\Delta h = h - h_{mud} \tag{5.3}$$

Because there is no sinkage on the cracked dry mud, we have assumed all individuals have 0 cm depth. To measure the sections of body that were off the mud for each cycle trial for all 3 mud strengths (sample size in Table 5.1), we measured the body contact length (c_b) by manual measurement from a side view video (Fig. 5.3B) when maximum sections of the animal's body were lifted off the mud for each trial. We then normalized it to the body length (BL) of the animal.

5.5.7 Kinematics Analysis

We subtracted the x-y-z positions of the animal's nose tip (Fig. 5.3E-F) from all the points to estimate the positions with respect to the animal's body (x_b, y_b, z_b). We used the following equation to estimate the lateral bending body (α_i) and fin-body

($\alpha_{L,R}$) angles on the transverse plane (Fig. 5.3E):

$$\alpha = \tan^{-1}(\frac{(\vec{a} \times \vec{b}).\hat{n}}{\vec{a}.\vec{b}}) \tag{5.4}$$

where α is the lateral bending angle, n is the unit vector of the cross product, a and b are the vectors between the tracked points on the transverse plane (Fig. 5.3F). The lateral fin-body angle of the pectoral right fin (α_R) is the conjugate of the fin-body angle found using Eqn. 5.4 for aligning the directions of the left and right fin-body angles visually. All lateral bending body and fin-body angles were wrapped between [0°, 360°). We found the vertical bending body (β_i) and fin-body ($\beta_{L,R}$) angles on the sagittal plane were found using the following:

$$\beta = \tan^{-1}(\frac{-1.((\vec{a} \times \vec{b}).\hat{n})}{\vec{a}.\vec{b}}) \tag{5.5}$$

where β is the vertical bending angle (Fig. 5.3F). All vertical bending body and fin-body angles were wrapped between [0°, 360°). We then filtered the angle data using a median filter to remove outliers.

5.5.8 Horizontal drag force measurement device

We developed a horizontal drag force device based on the design of our automated vertical penetration device developed in our previous study (Ramesh et al., 2024a) to measure the forward and lateral forces as a function of displacement of the probe across different ϕ. The device consists of a Dynamixel motor (XM430-W350-R) programmed to move the probe that was placed on the mud at a given depth by 3.97 cm at 0.29 cm/s. The depth is defined as the height of the probe starting from base of the

probe that is immersed in the mud. A threaded rod (12" lead screw, 1/4"–16 thread size, McMaster-Carr, Princeton, NJ, USA) connected to the motor shaft was used to translate the motor rotation to linear displacement (Fig. 5.4A). Two 1-D force sensors (Strain gauge load cell, 5 kg, S18X4) were connected perpendicular to each other on the transverse plane with one end of a load cell connected to the probe to estimate

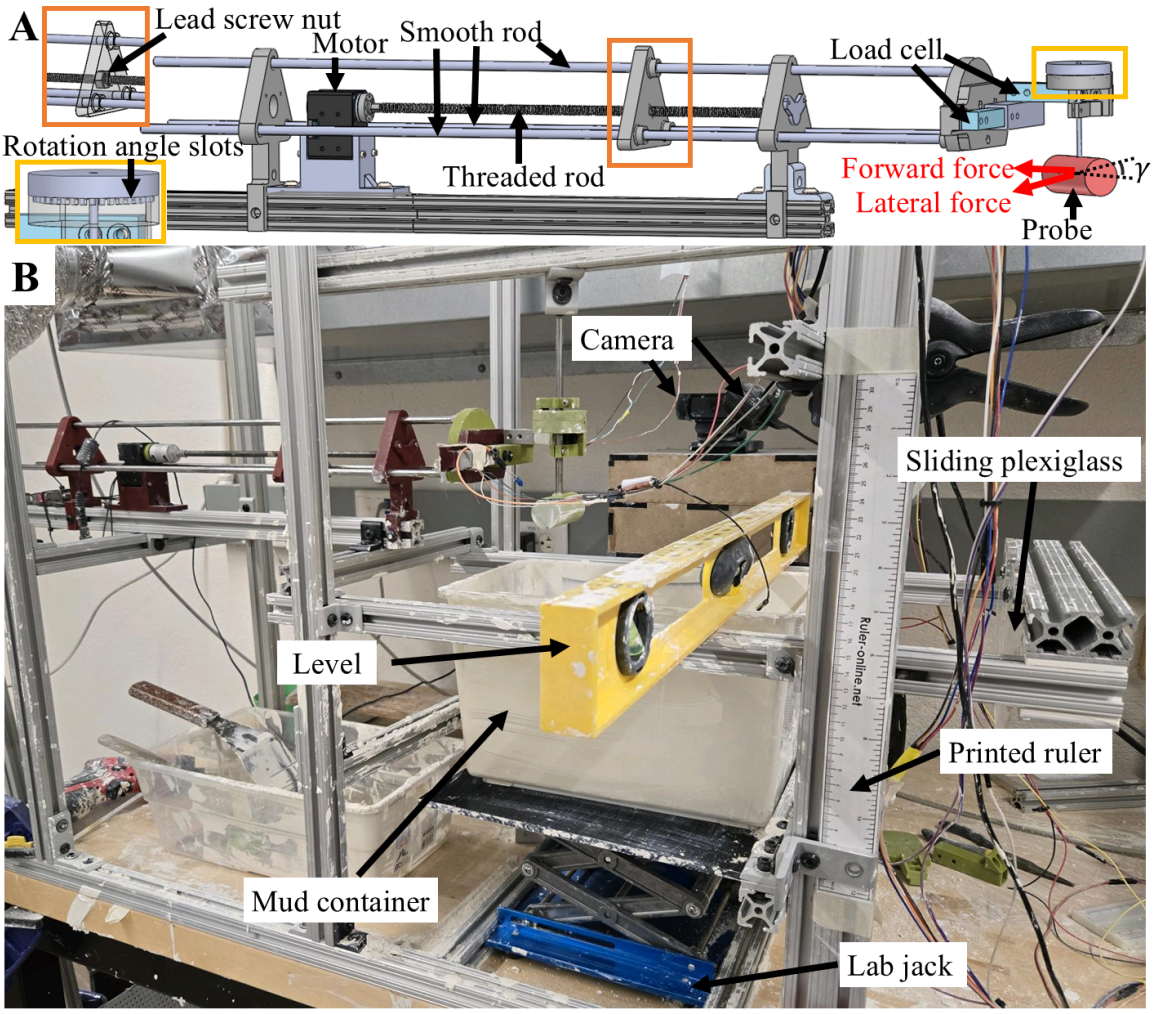

Figure 5.4: Horizontal drag force measurement device. (A) Horizontal drag force measurement device CAD. **(B)** Horizontal drag force measurement device.

the forward and lateral forces (Fig. 5.4A). The load cells mount was connected to the threaded rod using three smooth rods (24" Linear Motion Shaft, 1/4" diameter, McMaster-Carr, Princeton, NJ, USA) and was fixed to the threaded rod by a lead screw nut (Fig. 5.4A).

We used a cylindrical probe (Fig. 5.4A) that is 2.6 cm in diameter and 6 cm in length and placed it on the mud surface with depths of 0.2, 0.5, and 1 cm. The orientation of the probe (γ) was varied from 0° to 90° in increments of 10° where 0° indicates that the length of the probe is perpendicular to the forward motion of the probe (Fig. 5.4A). The horizontal drag force measurement device was secured using a frame made up of T-slotted framing (McMaster-Carr, Princeton, NJ, USA) to ensure the probe moved parallel to the mud surface. The mud was held in a rigid container that is 28 cm in length, 17 cm in height, and 17.5 cm in width (Fig. 5.4B). To prevent the force measurements from getting affected by boundary effects, the probe was placed in the middle of the container with enough distance from the container's boundaries. Boundary effects are defined as artifact forces applied on an object as it moves near the container's boundary (Coussot, 1997). The mud was mixed and flattened using a piece of plexiglass (McMaster-Carr, Princeton, NJ, USA) that was fixed using sliders (McMaster-Carr, Princeton, NJ, USA) after the mud was disturbed by the probe during each trial (Fig. 5.4B).

A lab jack (Wisamic Store) was used to change the depth of the probe sinkage by increasing the height of the lab jack and placing the probe in a fixed position (Fig. 5.4B). We used a level (Stanley, USA) to ensure that the mud container was leveled when the lab jack increased in height (Fig. 5.4B). A printed ruler was used to measure the depth (Fig. 5.4B). We also used webcams (Logitech) to record oblique top view

and side view videos at 30 frames per second for each trial (Fig. 5.4B). The load cell readings were collected using an Arduino nano (Arduino.cc). We used MATLAB to control the motor and collect the load cell readings in real time. We collected 3 trials for each depth and probe orientation, γ.

The force estimated from the load cell had small oscillations in the data due to the small movement in the threaded rod which were removed by filtering the data using a band stop filter. The displacement was estimated from the motor position. The force and displacement data were synchronized using time from the motor data and then cropped to start when the probe started to move on the mud surface using the load cell measurements. The force data was then interpolated to have the same range of displacement across different trials.

5.5.9 Statistical tests

We used one-way analysis of variance (ANOVA) in JMP Pro to find the significance between different treatments for forward displacement, speed, sinkage, and contact length analysis. We included all individual data for significance in forward displacement and speed. For sinkage and contact length analysis, we averaged data over each individual for significance and have reported this data as mean $\pm$ s.d. for each analysis. We also used Student's t-test to compare the significance between individual treatments. The interpolated force data from the horizontal drag force measurement experiments was averaged across different trials for each angle moved by the probe for comparison across the depth, angles swept, and ϕ. All analyses except for the statistical tests were performed on MATLAB.

5.6 Results

5.6.1 Animal's performance as a function of ϕ

The ropefish used lateral bending similar to snakes but with less precision as seen in previous studies (Pace and Gibb, 2011). The speed of the animal increased as the strength of the mud increased from $\phi = 27\%$ to cracked dry mud (Fig. 5.5A, $P < 0.05$, one-way ANOVA). This is indicated by the slope (Fig. 5.5A, fit line) that increases from mud with $\phi = 27\%$ to cracked dry mud. The forward displacement (Fig. 5.6B) also decreased over each cycle as the animal progressed forward for all treatments.

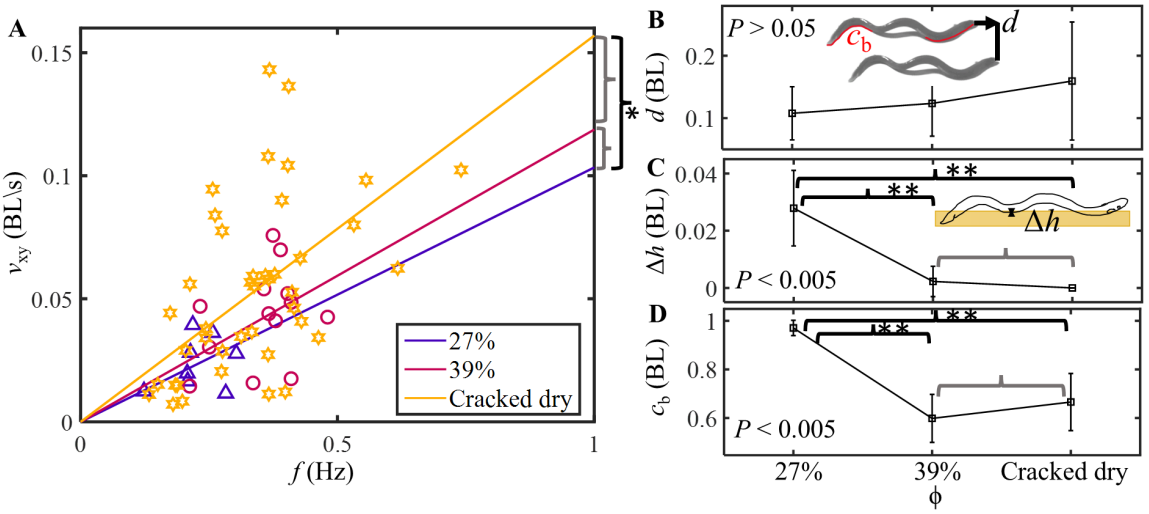

Figure 5.5: Ropefish performance across ϕ. (A) Average speed (v_{xy}) of the animal's nose tip relative to frequency (f). Lines correspond to linear least-square fit lines. The color of the fit line and each data point for each mud strength is a function of force at 1 cm from mud characterization. **(B)** Average forward displacement (d) of the animal's nose tip (B_1) as a function of ϕ. **(C)** Average sinkage (Δh) of the animal's body as a function of ϕ. **(D)** Average body contact length (c_b) as a function of ϕ. Square marker and error bar in B-D corresponds to mean $\pm$ s.d. Statistics performed using one-way ANOVA. ** $P < 0.005$, * $P < 0.05$, Student's t-test, one-way ANOVA.

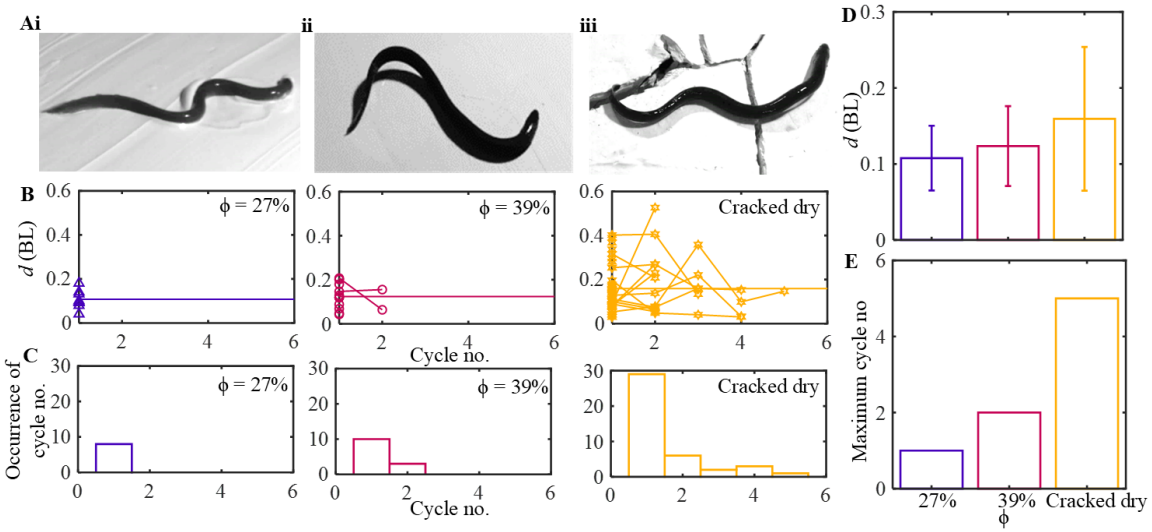

Figure 5.6: Ropefish forward displacement over multiple cycles. (A) Snapshot of the ropefish moving on mud with (i) $\phi = 27\%$, (ii) $\phi = 39\%$, and (iii) cracked dry mud. **(B)** Forward displacement (d) of the animal's nose tip per cycle over each cycle and **(C)** histogram of the number of cycles the animal walked across mud with (i) $\phi = 27\%$ (indigo color line, triangle marker), (ii) $\phi = 39\%$ (magenta color line, circle marker), and (iii) cracked dry mud (yellow color line, star marker). Line in B, i-iii corresponds to the average forward displacement of the animal's nose tip (B_1) per cycle. The color of line for each mud strength is a function of force at 1 cm from mud characterization. **(D)** The average forward displacement of the animal's nose tip (B_1) per cycle (lines in B, i-iii) as a function of ϕ. Error bar corresponds to mean $\pm$ s.d. **(E)** Maximum number of cycles the animal moved in a walk trial. Color in D-E corresponds to ϕ.

The average forward displacement did not have a significant change across all three treatments (Fig. 5.5B, 5.6D, $P > 0.05$).

The ropefish had more sinkage (Δh) on mud with $\phi = 27\%$ and had minimal sinkage on mud with $\phi = 39\%$ and on cracked dry mud (Fig. 5.5C, $P < 0.005$, one-way ANOVA). The animal had more body contact length (c_b) on mud with $\phi = 27\%$ compared to on mud with $\phi = 39\%$ and on cracked dry mud (Fig. 5.5D, $P < 0.005$, one way ANOVA). Almost all of the animal's body was in contact with the mud on ϕ

= 27% mud strength (Fig. 5.5D) indicating that the animal had minimal to no body lifting. The animal had smaller body contact length on mud with $\phi = 39\%$ and on cracked dry mud indicating that some sections of the animal's body were lifted off the mud surface (Fig. 5.5D) during locomotion.

The histogram of the number of cycles across mud (Fig. 5.6C, i-iii) showed that the animal mostly locomoted 1 cycle on mud with $\phi = 27\%$ and 39% (Fig. 5.6C, i-ii) whereas it locomoted up to 5 cycles on cracked dry mud (Fig. 5.6C, iii). The maximum number of cycles that the animal locomoted (Fig. 5.6E) increased as the mud got stronger from $\phi = 27\%$ to cracked dry mud.

5.6.2 Animal's kinematics to understand lateral bending and vertical lifting coordination

As a first step towards the comparison of the kinematics of the animal across all mud strengths to understand how the body lifting is in coordination with the lateral bending, we were able to generate the 3-D body curves for each trial both in the world frame (Fig. 5.7B) and the body frame (Fig. 5.7C), lateral and vertical bending body angles, and lateral and vertical pectoral fin-body angles for mud with $\phi = 39\%$. The body curves on the sagittal plane at some time frames have sections of the animal body that are off the mud surface in coordination with lateral bending on the transverse plane (Fig. 5.7C).

The lateral bending angles of the body segments from the body curve in a trial (Fig. 5.8B, i) show that there is a lateral wave that is propagated from head to tail to help generate propulsion for the animal to move forward. The vertical bending angles of the body segments from the body curve show that there is body bending in

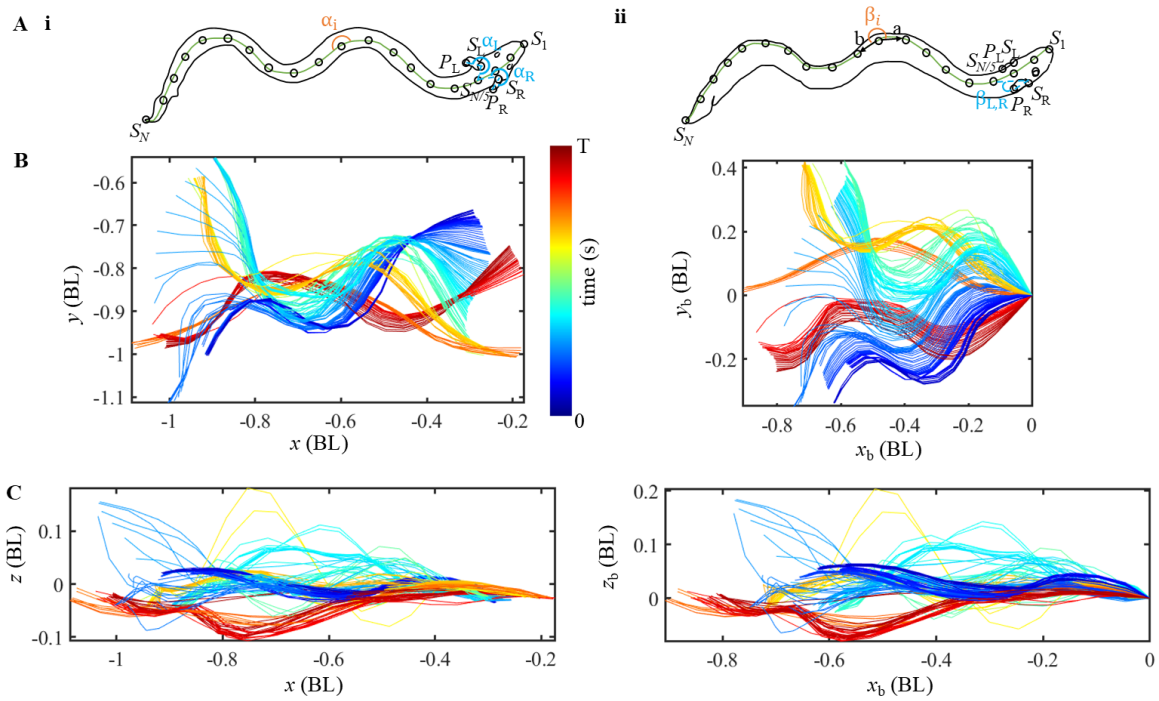

Figure 5.7: 3-D kinematics of the animal's body. **(A)** Schematic of the animal with the points extracted from the spline curve and tracked fin points on the (i) transverse plane and (ii) sagittal plane. **(B)** Animal's 3-D body curves (i) using the 3-D positions and (ii) 3-D positions with respect to the animal's body overlaid across time on the sagittal plane from one walk trial on $\phi = 39\%$. **(C)** Animal's 3-D body curves (i) using the 3-D positions and (ii) 3-D positions with respect to the animal's body overlaid across time on the transverse plane from one walk trial on $\phi = 39\%$. Color of the curves in B-C corresponds to time.

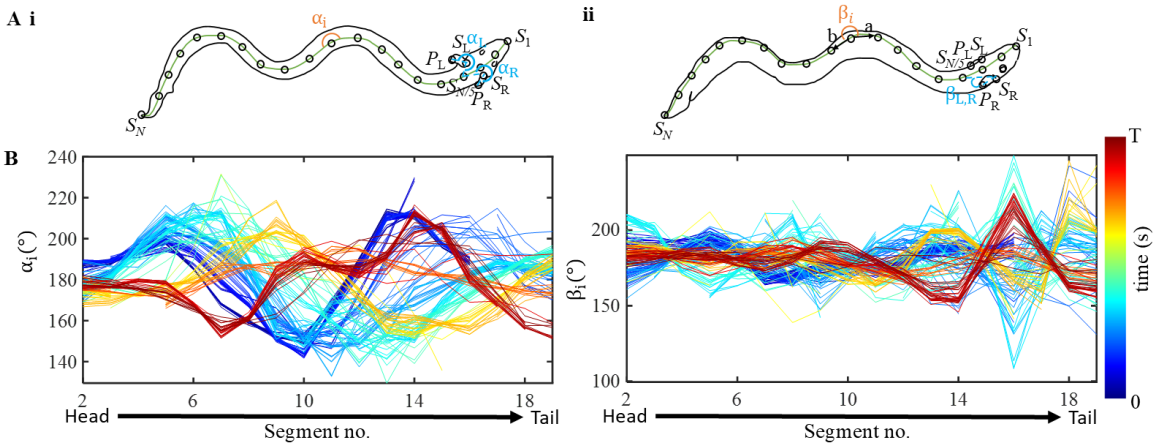

Figure 5.8: Lateral and vertical bending body and fin-body angle. (A) Schematic of the animal with the points extracted from the spline curve and tracked fin points and the angle definitions on the (i) transverse plane and (ii) sagittal plane. **(B)** Animal's (i) lateral and (ii) vertical bending body rotations as a function of segment number from one walk trial on $\phi = 39\%$. Color of the curves in B corresponds to time. Segment number in B starts from head to tail.

the sagittal plane which indicates that the animal lifts different parts of its body in a cycle likely to modulate friction from the mud surface (Fig. 5.8B, ii) to help progress forward. The pectoral fins of the animal are mostly folded onto the animal's body and sometimes are placed on the mud during lateral bending and body lifting from visual observations.

5.6.3 Forward and lateral force measurements for RFT

The forward force as a function of displacement of the probe on the mud surface profile reduced as the orientation of the probe increased from $\gamma = 0°$ to $\gamma = 90°$ at different depths and for all ϕ (Fig. 5.9). This force-displacement profile increased as mud became stronger ($\phi = 27\%$ to 39%) and as the depth increased (Fig. 5.9). The forward force during the probe's backward motion started to have a change in slope

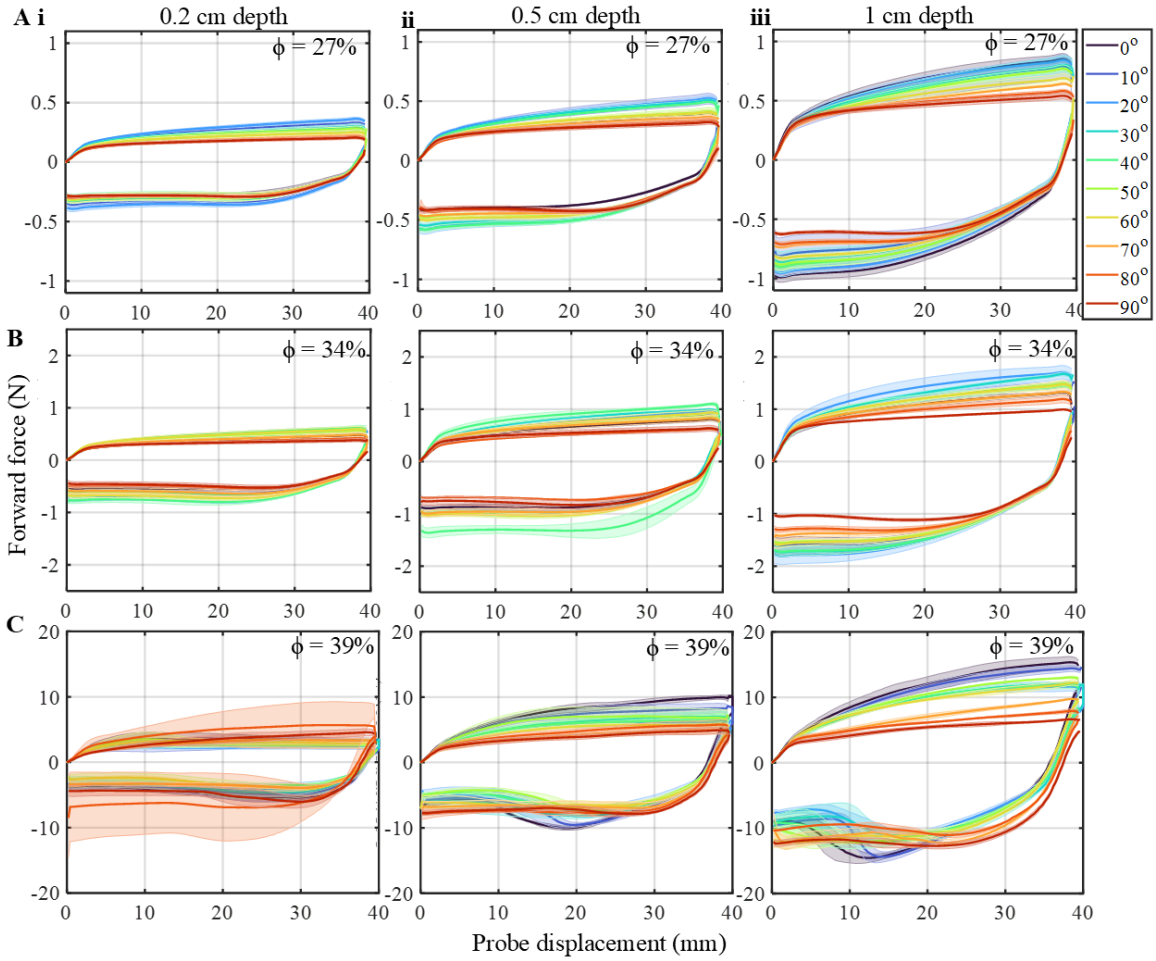

Figure 5.9: Forward force as a function of displacement of the probe across ϕ, depth and γ. Forward force as a function of displacement of the probe with different orientations ($\gamma = 0°$ to 90°) with depth (i) 0.2 cm, (ii) 0.5 cm and (iii) 1 cm on the mud surface of mud with **(A)** $\phi = 27\%$, **(B)** $\phi = 34\%$ and **(C)** $\phi = 39\%$. The shaded error bar corresponds to mean ± s.d. Color corresponds to γ.

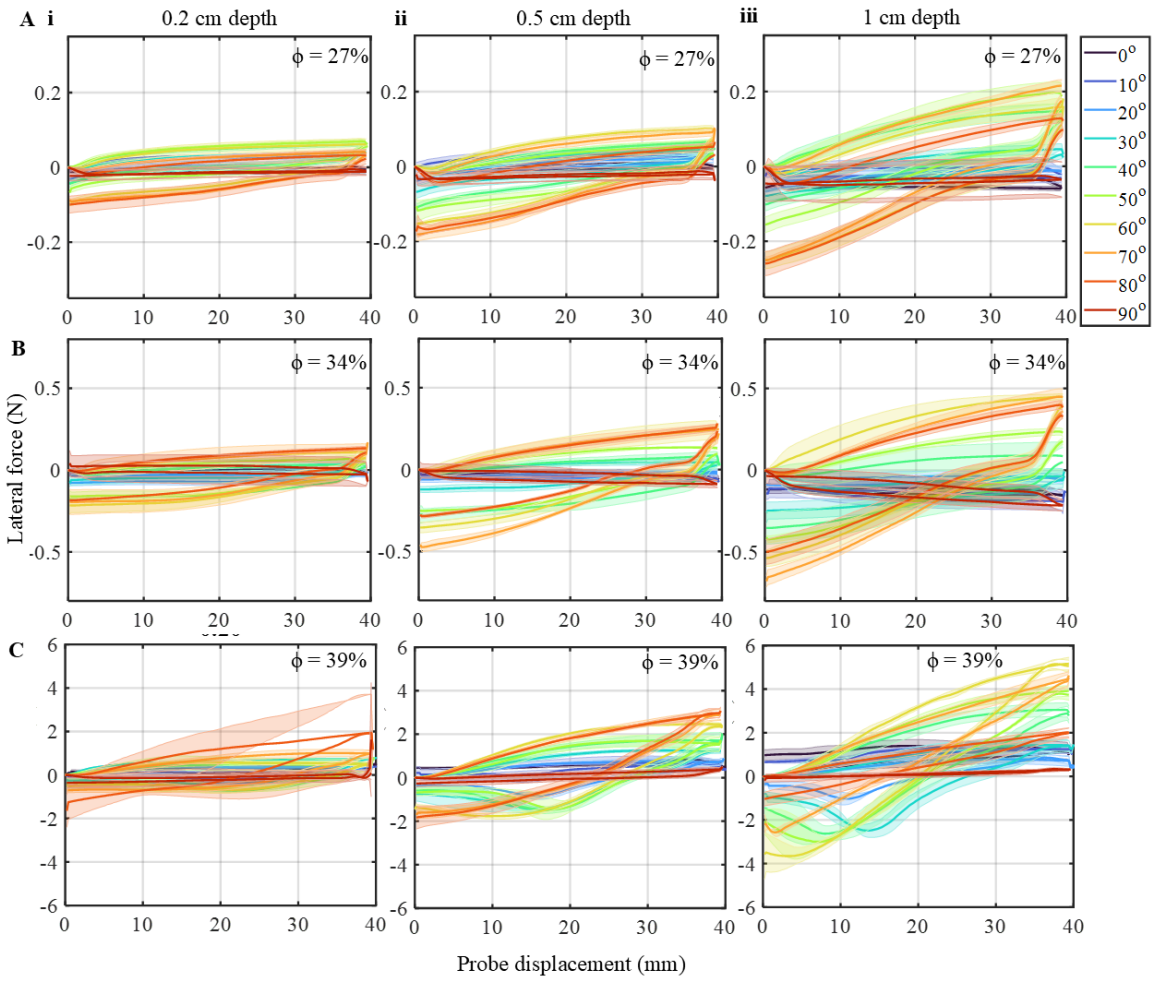

Figure 5.10: Lateral force as a function of displacement of the probe across ϕ, depth and γ. Lateral force as a function of displacement of the probe with different orientations ($\gamma = 0°$ to $90°$) with depth (i) 0.2 cm, (ii) 0.5 cm and (iii) 1 cm on the mud surface of mud with **(A)** $\phi = 27\%$, **(B)** $\phi = 34\%$ and **(C)** $\phi = 39\%$. The shaded error bar corresponds to mean ± s.d. Color corresponds to γ.

for $\phi = 39\%$ (Fig. 5.9C) because the mud fell off the probe from lack of adhesive force and too much mud sticking to the probe due to the mud not being sticky enough compared to the lower mud strengths.

The lateral force as a function of displacement of the probe on the mud surface profile increased as the orientation of the probe increased from $\gamma = 0°$ until $\gamma = 60°$ and then decreased from $\gamma = 60°$ until $\gamma = 90°$ for 0.2 cm depth for mud with $\phi = 27\%$ (Fig. 5.10A, i). This force-displacement profile increased from $\gamma = 0°$ to $\gamma = 70°$ and then reduced until $\gamma = 90°$ for 0.5 cm and 1 cm depths for mud with $\phi = 27\%$ (Fig. 5.10A, ii-iii). The lateral force as a function of displacement of the probe on the mud surface profile increased as the orientation of the probe increased from $\gamma = 0°$ until $\gamma = 80°$ and then reduced at $\gamma = 90°$ for all depths for mud with $\phi = 34\%$ (Fig. 5.10B, i-iii). This force-displacement profile increased as the orientation of the probe increased from $\gamma = 0°$ until $\gamma = 80°$ and then reduced at $\gamma = 90°$ for 0.2 cm and 0.5 cm depths for mud with $\phi = 39\%$ (Fig. 5.10C, i-ii). The force-displacement profile increased as the orientation of the probe increased from $\gamma = 0°$ until $\gamma = 60°$ and then reduced until $\gamma = 90°$ for 1 cm sinkage for mud with $\phi = 34\%$ (Fig. 5.10C, iii).

5.6.4 Robophysical model for a systematic study of understanding body lifting and lateral bending coordination in ropefish

We have developed a 12 segment lifting robophysical model that can laterally bend its body and lift sections of the body (Fig. 5.11). The robot consists of 4 lifting segments and 12 yaw segments. The robot is actuated using Hyperion motors (DS13-TMB). The lifting segments lift the yaw segments using a series of gears. Unlike our snake robot (Fu and Li, 2020; Fu and Li, 2023; Ramesh, Fu, and Li, 2022) that were

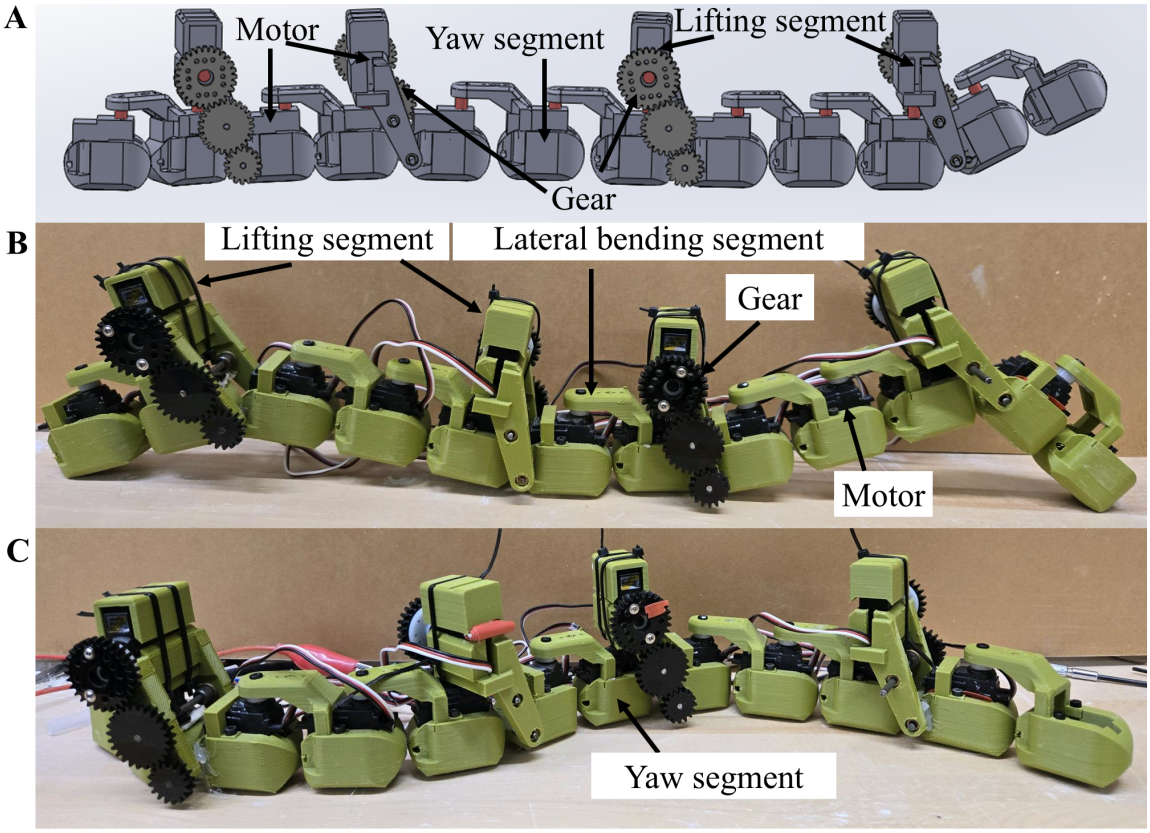

Figure 5.11: Lifting robophysical model. **(A)** A CAD of the lifting robophysical model. Photo of the Lifting robophysical model capable of **(B)** lifting and **(C)** lateral bending its body.

previously developed which had alternative lifting and yaw segments, this robot has all 12 segments to be yaw segments and each lifting segment is attached to a yaw segment. This helps in generating a smoother lateral curve during lateral bending and lifting as seen in the ropefish. We plan to use this robot for performing systematic experiments to help better understand the use of body lifting in ropefish in combination with lateral bending. We will systematically sweep body lifting and lateral bending parameters to understand how parameter variation affects the coordination and locomotion on different mud strengths.

5.7 Discussion and future work

We measured the simple kinematics of the animal during each cycle of the lateral bending which is used by ropefish to move on hard ground (Pace and Gibb, 2014). The emergent use of lifting sections of the animal's body in combination with lateral bending is likely due to the difficulty in traversing the mud of higher mud strengths and helping modulate ground friction.

5.7.1 Performance of the animal with variation in mud strength

We hypothesized that the ropefish starts to locomote slower as the mud becomes weaker, likely due to the increase in the adhesive force from the mud sticking to the animal's lower body and the drag that arises from mud sticking on the animal's upper body which prevents the animal from lifting itself to progress forward. This hypothesis was supported because the speed of the animal reduced as mud varied from cracked dry mud to $\phi = 27\%$ (Fig. 5.5A). Previous studies on American eels have found that the animal moves more effectively on flowable substrates such as wet sand compared to loose pebble substrates (Redmann et al., 2020). On lower mud strengths ($\phi = 27\%$), the mud behaves more similarly to a flowable substrate and hence the ropefish was able to push the substrate along the sides of the animal's body during lateral bending to progress forward similar to wet sand (Redmann et al., 2020; Gillis, 1998). Unlike sand, the cohesive nature of mud caused the substrate to stick to the sides of the animal which slows down the animal. Despite the increase in speed as the mud became stronger, the average forward displacement over each cycle of lateral bending did not have a significant increase in performance (Fig. 5.5B, 5.6D) likely due to the mud

becoming closer to rough ground and less similar to a flowable substrate.

5.7.2 Use of vertical bending in combination the axial-based locomotion to maintain the performance on higher mud strengths

We observed the use of vertical bending to lift sections of the animal's body when ropefish moved on higher mud strengths ($\phi = 39\%$ and cracked dry mud) (Fig. 5.5D). This is likely because, at higher mud strengths, mud behaves more similar to a solid and hence has higher friction on the mud surface. Snakes lift curved parts of their body during lateral undulation to modulate ground friction (Hu et al., 2009). Ropefish likely lift parts of their body for a similar function.

Previous studies on American eels have mentioned the use of a rendition of concertina locomotion in addition to lateral undulation on loose wet pebbles (Mehta et al., 2021), and the use of concertina-like movement of more burst movement on increased inclined wet sand and pebble substrates (Redmann et al., 2020). A study on snowflake moray mentioned the use of a rendition of sidewinding, a rendition of concertina locomotion, and a combination of lateral undulation and concertina locomotion on a wet sand substrate (Mehta et al., 2021). This suggests that elongated fishes start to use vertical bending and body lifting when it becomes difficult to locomote on substrates. Ropefish and other elongated fishes likely have a lower threshold in overcoming friction on uneven grounds, unlike snakes that have been well adapted to terrestrial environments. We will perform detailed kinematics as future work across the different mud strengths will help better understand how the ropefish coordinates the body lifting and lateral bending for effective locomotion.

5.7.3 Force as a function of mud strength and resistive force theory

The force and displacement of the probe profile for mud are different from dry (Marvi et al., 2014; Li, Zhang, and Goldman, 2013) and wet sand (Sharpe, Kuckuk, and Goldman, 2015). They are also more complex due to colloidal effects that are absent in sand when water is added (Coussot, 1997). The cohesive nature of mud makes it stick to the probe during reverse motion causing forces to be generated in the opposite direction (Fig. 5.9) which is absent in dry sand (Marvi et al., 2014; Li, Zhang, and Goldman, 2013) and smaller in wet sand (Sharpe, Kuckuk, and Goldman, 2015). For future work, we plan on using the force-displacement profile at different probe orientations, depths, and mud strengths for resistive force theory (RFT) which has not yet been performed on mud. We plan on using RFT to calculate the drag and lift forces on the locomotor's body to better understand body lifting and lateral bending coordination.

Chapter 6
Conclusions

6.1 General remarks

In this dissertation, we combined biological, robotic, and physics studies to investigate non-legged locomotion on complex 3-D terrain and wet flowable substrates (Fig. 1.12). We divided the objective into two parts based on the environment (complex 3-D terrain and mud) and chose a model organism that moves well in each. Thus, our two objectives are as follows: (1) develop a sensorized robot to study the use of tactile sensing by snakes for 3-D body bending via sensory feedback in complex 3-D terrain and (2) study amphibious fishes moving on mud with variation in mud strength.

For objective (1), we focused on the use of vertical bending by snakes via sensory feedback. To achieve this, by focusing on the use of direct body-terrain contact sensing for studying vertical bending in snakes, we developed a sensorized snake robot with high repeatability. We also gained insights on how to design terrain testbeds for this sensorized robot to study snake locomotion on 3-D complex terrain. Our experiments showed that we can use the sensorized robot for systematic studies because of its high repeatability. Our snake robot will help in developing direct contact force feedback control to help bend the robot body in 3-D similar to snakes when traversing any 3-D terrain. This will allow robots to traverse such terrains for various applications with minimal human control.

For objective (2), we focused on understanding how amphibious fishes, which are representative of each of the three known sustained strategies modified their strategy or transitioned to new strategies when locomoting on mud with different

strengths. As a first step towards systematic studies on mud, we developed novel tools and methods to maintain and control mud strength. We discovered that all three amphibious fishes started to use vertical bending for lifting to modulate ground friction or to propel off of the mud with their sustained strategy or new strategies on certain mud strengths which is novel in amphibious fishes with systematic variation in mud strength. Our systematic studies will inspire future research in understanding a variety of animals moving on mud and will help robots move on mud by modifying a strategy or transitioning between strategies based on mud strength variation.

6.2 Specific accomplishments

6.2.1 Snake robot design for direct body-terrain contact sensing and 3-D terrain testbed design for systematic studies

- Developed a sensorized snake robot equipped with custom-made, low-cost, flexible piezo-resistive sensors for direct body-terrain contact sensing (Chapter 2, Fig. 1.12).
- Confirmed repeatability of the contact force measurements by allowing the sensorized robot to traverse a half cylindrical obstacle using vertical bending (Chapter 2, Fig. 1.12).
- Showed the capability of measuring dynamic forces (Fig. 1.12) using a sensor model that takes into account the creep behavior seen in piezo-resistive sensors due to their viscoelastic behavior (Chapter 2).

6.2.2 Tools and methods to control and maintain mud strength for systematic and repeatable studies

- Developed an automated mud preparation system for uniform mixing of mud for different mud strengths (Chapter 3).
- Developed sealing methods and confirmed their effectiveness in maintaining mud strengths between experiments over several days by showing minimal water loss spatio-temporally (Chapter 3).
- Developed tools and confirmed their capability to characterize mud through force measurements from vertical penetration (Fig. 1.12) to track loss of water during animal experiments (Chapter 3).

6.2.3 Mechanisms that enhance amphibious fish locomotion on mud with different strengths

- Performed a systematic study of mudskipper (Chapter 4) and ropefish (Chapter 5), and a preliminary study of bichir (Appendices 7.1) on mud with different mud strengths.
- Confirmed the robustness of the crutch walk mode by the mudskipper against mud strength variation (Chapter 4).
- Confirmed transitioning to different strategies by the mudskipper when the animal is not able to use crutch walk mode, which is the primary locomotion with mud strength variation (Chapter 4).
- Discovered the use of tail bending to vertically lift and propel the mudskipper's body off the mud in the sagittal plane (Fig. 1.12) in some strategies that emerge due to difficulty in using crutch walk mode on weaker mud (Chapter 4).

- Discovered the use of vertical body lifting (Fig. 1.12) in ropefish (Chapter 5) and bichir (Appendices 7.1) on higher mud strengths during the use of their primary strategy.
- Developed a horizontal drag force measurement device and used it for repeatable force measurements with a systematic variation of probe orientation and sinkage depth for resistive force theory to estimate drag and lift forces (Chapter 5, Fig. 1.12).
- Developed a fish robophysical model that can laterally bend and vertically lift body segments for studying the novel vertical lifting in amphibious fishes (Chapter 5, Fig. 1.12).

6.3 Future directions

Studies in this dissertation contribute to studying snake locomotion on complex 3-D terrain via sensory feedback and systematic study of animal and robot locomotion on mud. There is much more research needed to achieve the goal of enabling limbless robots to move similarly to snakes on 3-D complex terrain, and robots to move similarly to amphibious fishes on mud in the natural environment. Below are some of the potential directions that can help advance our understanding of non-legged locomotion on complex 3-D terrain and wet flowable substrates:

6.3.1 Using sensory feedback via tactile sensing in snake robots for vertical bending to generate propulsion similar to snakes

Our sensorized robophysical model will help develop control strategies that allow the bending of the robot body in response to terrain contact via sensory feedback

to successfully traverse a complex terrain in the natural environment. The sensor model that takes into account the creep behavior in piezo-resistive sensors will also help accurately estimate dynamic forces when moving in the natural environment, especially if the robot gets stuck, which results in sustained contact. This model can be used to estimate the contact force from the tactile sensor response and the force can be used as feedback to control body bending.

6.3.2 Exploration of more complex 3-D terrains and applications in the real world environments

More systematic studies can be performed on different 3-D terrain setups to help understand the use of tactile sensing as sensory feedback in complex 3-D terrain to control 3-D body bending. The control strategies developed can then be used in a variety of real world applications such as pipe inspection, planet exploration, and search and rescue after an earthquake.

6.3.3 Other animal locomotion and behavior studies on mud with mud strength variation

We developed tools and methods to control and maintain mud strength (Chapter 3) similar to those developed for dry (Li et al., 2009; Maladen et al., 2009) and wet (Sharpe, Kuckuk, and Goldman, 2015) sand. We have also confirmed their capability in tracking and maintaining water loss during animal experiments (Chapter 3). Many other animals such as mud turtles and mud salamanders regularly move on mud in the natural environment. These tools and methods will be useful for understanding other animals coping on mud with systematic variations in mud strength.

6.3.4 Electromyography experiments to study muscle activation during strategies with variation in mud strength

Our study discovered the emergence of different strategies that involve the use of tail bending in mudskippers when the crutch walk mode fails on weaker mud and strongest mud (Chapter 4). Electromyography (EMG) measurements will help study the muscle activation during the different modes used by the mudskipper as a function of the mud strength. This will help gain more insights into the emergence and disappearance of some strategies as the animal starts to struggle on a particular mud strength.

6.3.5 Robots transitioning between strategies on mud with dynamic mud strength variation via force sensing and real world applications

Our amphibious fish studies with systematic variation of mud strength (Chapter 4, 5 and Appendices 7.1) have revealed that these animals start to use tail bending to lift their bodies in the sagittal plane to propel against weaker mud (Chapter 4) or lift parts of their body to overcome drag on stronger mud (Chapter 5 and Appendices 7.1). We can use force sensing in robots to sense mud strength variation and use these forces as feedback to help the robot switch between strategies and use tail bending or vertical lifting based on the mud strength. This will allow robots to traverse muddy terrain easily in the natural environment similar to amphibious fishes for various applications such as soil testing along rivers, exploration of muddy areas, and search and rescue after floods.

6.3.6 Resistive force theory and geometric mechanics for mud

The interaction mechanics for aquatic and aerial locomotion can be understood using the Navier-Stokes Equation. However, there exist no fundamental theories for understanding the locomotor-substrate interaction mechanics on flowable substrates. Previous locomotion studies on sand have used resistive force theory (RFT) to experimentally estimate drag and lift forces on the locomotor's body (Li, Zhang, and Goldman, 2013; Maladen et al., 2009; Schiebel et al., 2020) and appendages (Chong et al., 2021; Chong et al., 2023), which can be extended for mud.

Geometric mechanics is a general framework that links locomotor performance to how the locomotor moves its body and limbs in its own body frame (Hatton and Choset, 2015). A recent study has been able to apply geometric mechanics to axial-appendicular locomotion on dry sand (Chong et al., 2022). Geometric mechanics (Chong et al., 2021; Chong et al., 2023; Chong et al., 2022) can be used in understanding the effects of body-appendage coordination as a function of mud strength.

6.4 Final thoughts

It was a rewarding experience working with different animals. Studying animal movement helped me think more analytically and sharpen my observational skills. Coming from an electrical engineering background, through various aspects of my research, I gained immense knowledge, valuable skills, and keen intuition in mechanical design. I am lucky to have worked in biological, robotic, and physics aspects of terradynamics to discover mechanisms of animal locomotion and gained various skills along the way. I look forward to hearing about relevant work in the future.

Appendices

7.1 Bichir locomotion on mud with different strengths

Below are some preliminary results for bichir (Fig. 7.1) using axial-appendicular-based locomotion on different mud strengths.

7.2 Author Contributions

This work was authored by Divya Ramesh, Hongbo Zhang, Alex Nath, Dami Kim, and Chen Li. Divya Ramesh oversaw animal experiments and performed animal data analysis; Hongbo Zhang, Alex Nath, and Dami Kim helped conduct animal experiments and helped with animal data tracking; Divya Ramesh and Chen Li wrote the paper.

7.3 Acknowledgment

We thank Qiyuan Fu for helping with the preliminary study and animal care; Dennis Lin for helping with data analysis; Gargi Sadalgekar, Aydin Mokaddem, Julie Le, Luna Liu, Kyungmo Choi, and Yaqing Wang for helping with animal care. This study was funded by the Burroughs Wellcome Fund Career Award at the Scientific Interface and a Johns Hopkins University Bridge Grant.

Figure 7.1: Choice of model organism. (A) Bichir moving on mud.

7.3.1 Materials and methods for preliminary kinematic analysis

7.3.1.1 Animal experimental testbed, choice of mud substrate, and mud characterization during experiments

We used Georgia Kaolin (China Clay, Old Hickory Clay Company, Florida, USA) as the substrate for our preliminary animal experiments because clay mud behaves quantitatively similar to natural mud (Coussot, 1997). The clay mud was prepared using an automated mixing system (Fig. 7.2A) that was developed in the previous studies (Ramesh et al., 2024a; Ramesh et al., 2024b). The experimental testbed consisted of a container (HOMZ, Chicago, IL, USA) that is 1.02 m in length, 0.51 m in width, and 0.16 m in height with an airtight lid to hold the clay mud during experiments and storage (Fig. 7.2D). We used the custom portable penetrometer (Ramesh et al., 2024a) during the animal experiments (Fig. 7.2B) to track the water loss and maintain the mud strength throughout the study.

We filled the container up to at least $3/4^{th}$ of the tub height to prevent boundary effects from affecting the animal locomotion and the intruder during mud characterization. Boundary effects are defined as artifact forces applied on an object as it

moves near the container's boundary (Coussot, 1997). We also used sealing methods that were developed and used in our previous studies to minimize water loss (Ramesh et al., 2024a; Ramesh et al., 2024b). This method consisted of the sides of the lid covered with rubber sealing strips (CloudBuyer) to make the lid more airtight and to prevent water drops from escaping from the sides of the lid (Fig. 7.2D). We placed a plastic wrap directly on the mud surface to minimize the evaporation of water from the surface to the top of the lid. We also placed lashing straps (ACE-Lashing Straps,

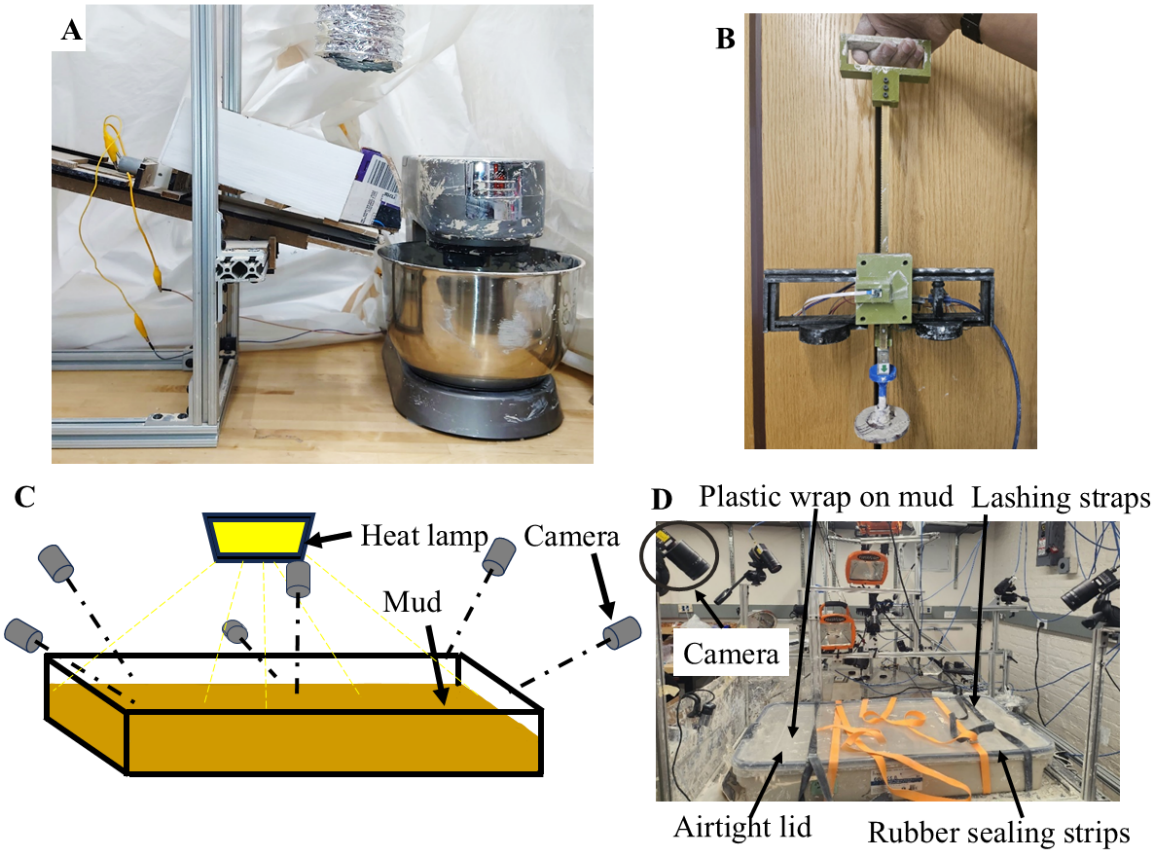

Figure 7.2: Experimental setup. **(A)** Automated mud preparation system. **(B)** Custom portable penetrometer. **(C)** A schematic of the experimental setup. **(D)** Photo of the experimental setup. Reproduced from Ramesh et al., 2024b

Acelane) around the closed container to tighten the lids further onto the container (Fig. 7.2D).

7.3.1.2 Different mud strengths used for experiments

We chose $\phi = 27\%$ which is closer to the lower limit of the solid-fluid transition regime and $\phi = 34\%$, 39% and 42% which are in the solid-fluid transition regime based on the mud characterization using the automated vertical penetration device (Ramesh et al., 2024a).

7.3.1.3 Experimental setup, sample size and protocol for animal locomotion

We tracked the animal locomotion using 6 synchronized high-speed cameras (N-5A100 17 Gm/CXP-6-1.0, Adimec, Eindhoven, The Netherlands) (Hedrick, 2008) at 100 frames per second for all trials (Fig. 7.2C-D). We also captured the entire animal study in a day by recording top view and side view videos using webcams (Logitech and HP) at 30 frames per second. We used a heat lamp (500 Watt Portable Halogen Work Light, Woods) to make the experimental setup well-lit and heated (Fig. 7.2C). We switched off the heat lamp between each trial to maintain the temperature.

We used 6 bichirs (*Polypterus senegalus*) for this study. We chose to use this species to study axial-appendicular-based locomotion because they have been extensively studied in previous studies which will allow us to use our results and findings to connect to the previous work and provide novel insights on the animal's adaptation to varying mud strength. All animals were approved by and in compliance with The Johns Hopkins University Animal Care and Use Committee (protocol FI21E163). The animals were fed daily with dried shrimp pellets and housed in well-lit, well-heated

aquarium tanks filled with fresh water. The animals were allowed to get accustomed to each mud strength for a few minutes on the first day of experiments.

We also recorded the length, height, and weight of the animals after the experiment concluded each day. The length and height were estimated using ImageJ software. The animals were weighed using a digital weighing scale (American weigh scales, USA). The weight of the animals was 5.3 ± 2.14 g (mean ± s.d.). The length and height of the animals were 9.24 ± 1.36 cm and 1.21 ± 0.17 cm respectively. The average temperature of the experimental setup recorded at the start of each trial was 24.96 ± 0.73° C.

Here we defined a trial from when the animal was first placed on the mud until when it was finally taken off the mud. We recorded each trial using high-speed cameras. We started recording the videos before the animal was first placed on the mud and stopped the recording after the animal was finally taken off the mud in a trial. During each trial, we gently prodded the animal by hand to make the animal move. When the animal was drying out or had too much mud covering the body, we removed it off the mud, placed and cleaned in water for a few seconds before being placed back on the mud. The animal was taken off the mud at the end of each trial after 2-3 minutes. The animal was allowed to rest for some time (10 – 15 minutes) before each trial. We mixed the mud using a metal spatula with beveled edges (Homi Styles) and manually flattened by hand using a piece of plexiglass (McMaster-Carr, Princeton, NJ, USA) after the mud was disturbed by fish during each trial.

The custom portable penetrometer was used to characterize mud strength spatially on the disturbed mud after animal trials (Ramesh et al., 2024a). We defined walk trials as those trials where the bichir moved continuously in consecutive

Trial count for analysis	A1	A2	A3	A4	A5	A6	Total trials	No. of Treatments	Trials per treatment (27%, 34%, 39%, 42%)
Walk trials for forward displacement and speed at each cycle	9	11	7	4	8	4	43	2	17, -, 26, -
No. of cycles for sinkage, contact length, and maximum bending analysis	9	6	6	3	3	3	30	4	9, 6, 9, 6

Table 7.1: Sample size for different analysis. A1 corresponds to Animal 1

cycles. We rejected walk trials where the animal was close to the testbed boundary due to boundary effects. We defined cycle trials as those trials where the animal locomotes over one cycle. We used cycle trials for sinkage, contact length, and maximum bending analysis and tracked data using DLTdv digitizing tool (Hedrick, 2008; https://biomech.web.unc.edu/dltdv/). See Table 7.1 for details on sample size for each analysis.

7.3.1.4 Fore-aft displacement and speed analysis

We calculated the animal's forward displacement at each cycle (d) for walk trials for all 2 mud strengths (sample size in Table 7.1) using the following:

$$d = ((x_i - x_{i-1})^2 + (y_i - y_{i-1})^2)^{1/2} \tag{7.1}$$

Where (x_{i-1}, y_{i-1}) and (x_i, y_i) are the forward and lateral positions of the bichir's mid-body at the start of cycle i and end of cycle i respectively, tracked on top view videos 2-D analysis. The forward speed (v_{xy}) was calculated using the following:

$$v_{xy} = \frac{d}{\Delta t}, f = (\Delta t)^{-1} \tag{7.2}$$

Where Δt is the duration of a walk cycle and f is the frequency of a walk cycle. The forward displacement, speed, and frequency were then averaged over all cycles in a walk trial.

7.3.1.5 Sinkage, contact length, and maximum bending analysis

We used videos showing the animal locomoting relatively in a side view to estimate the animal sinkage for each cycle trial for all 4 mud strengths (sample size in Table 7.1). To measure the sinkage, the animal's body height visible (h_{mud}) was measured using Eqn. 7.1 using a tracked point on top of the animal, and another tracked point at the bottom of the animal on mud (Fig. 7.4A) during minimal body lifting which was during the start of a cycle. We measured the actual height of the animal (h) by tracking points like those tracked for h_{mud} but when the animal was completely off

the mud (Fig. 7.4A). The sinkage (Δh) was calculated using the following:

$$\Delta h = h - h_{mud} \tag{7.3}$$

To measure the sections of body that were off the mud for each cycle trial for all 4 mud strengths (sample size in Table 7.1), we measured the body contact length (c_b) by manual measurement from a side view video (Fig. 7.4B) when maximum sections of the animal's body were lifted off the mud for each trial. We then normalized it to the animal's body length (BL). We measured the distance between the animal's nose-tip and tail-tip (d_c) using Eqn. 7.1 (Fig. 7.4C) at the start and end of a cycle which is when the maximum bending occurs and averaged the two distance measurements.

7.3.1.6 Statistics

We used one-way analysis of variance (ANOVA) in JMP Pro to find the significance between different treatments for forward displacement, speed, sinkage, contact length, and maximum bending analysis. We included all individual data for significance in forward displacement and speed. For sinkage, contact length, and maximum bending analysis, we averaged data over each individual for significance and have reported this data as mean ± s.d. for each analysis. We also used Student's t-test to compare the significance between individual treatments. All analyses except for the statistical tests were performed on MATLAB.

7.3.2 Results

7.3.2.1 Performance of animal with variation in mud strength

The bichir used axial-appendicular-based locomotion similar to previous studies (Pace and Gibb, 2014; Standen et al., 2016). The speed and average forward displacement of the animal did not have significant changes as the strength of the mud increased from $\phi = 27\%$ to $\phi = 39\%$ (Fig. 7.3A, E, $P > 0.05$, one-way ANOVA). The results may be inaccurate due to insufficient animal data. The forward displacement (Fig. 7.3C) decreased over each cycle as the animal progressed forward for both treatments.

The histogram of the number of cycles across mud (Fig. 7.3D, i-ii) showed that the animal mostly locomoted 1 cycle (Fig. 7.3D, i) with a maximum of 4 cycles (Fig. 7.3F) on mud with $\phi = 27\%$ whereas it mostly locomoted 2 cycles (Fig. 7.3D, ii) up to maximum of 6 cycles (Fig. 7.3F) on mud with $\phi = 39\%$. The maximum number of cycles that the animal locomoted (Fig. 7.3F) increased as the mud got stronger from $\phi = 27\%$ to $\phi = 39\%$.

Bichir had more sinkage (Δh) on mud with $\phi = 27\%$ and had a significant change in sinkage compared to other mud strengths (Fig. 7.4A, $P < 0.05$, one-way ANOVA, Student's t-test). There wasn't a significant change in sinkage between mud with $\phi = 34\%$ and other mud strengths with $\phi > 34\%$ (Fig. 7.4A). Mud with $\phi = 39\%$ and $\phi = 42\%$ also did not have significant changes in sinkage (Fig. 7.4A).

The animal had more body contact length (c_b) on mud with $\phi = 27\%$ compared to on mud with $\phi = 39\%$ and $\phi = 42\%$ (Fig. 7.4B, $P < 0.05$, one-way ANOVA, Student's t-test). Almost all of the animal's body was in contact with the mud on $\phi = 27\%$ mud strength indicating that the animal had minimal to no body lifting. The animal had

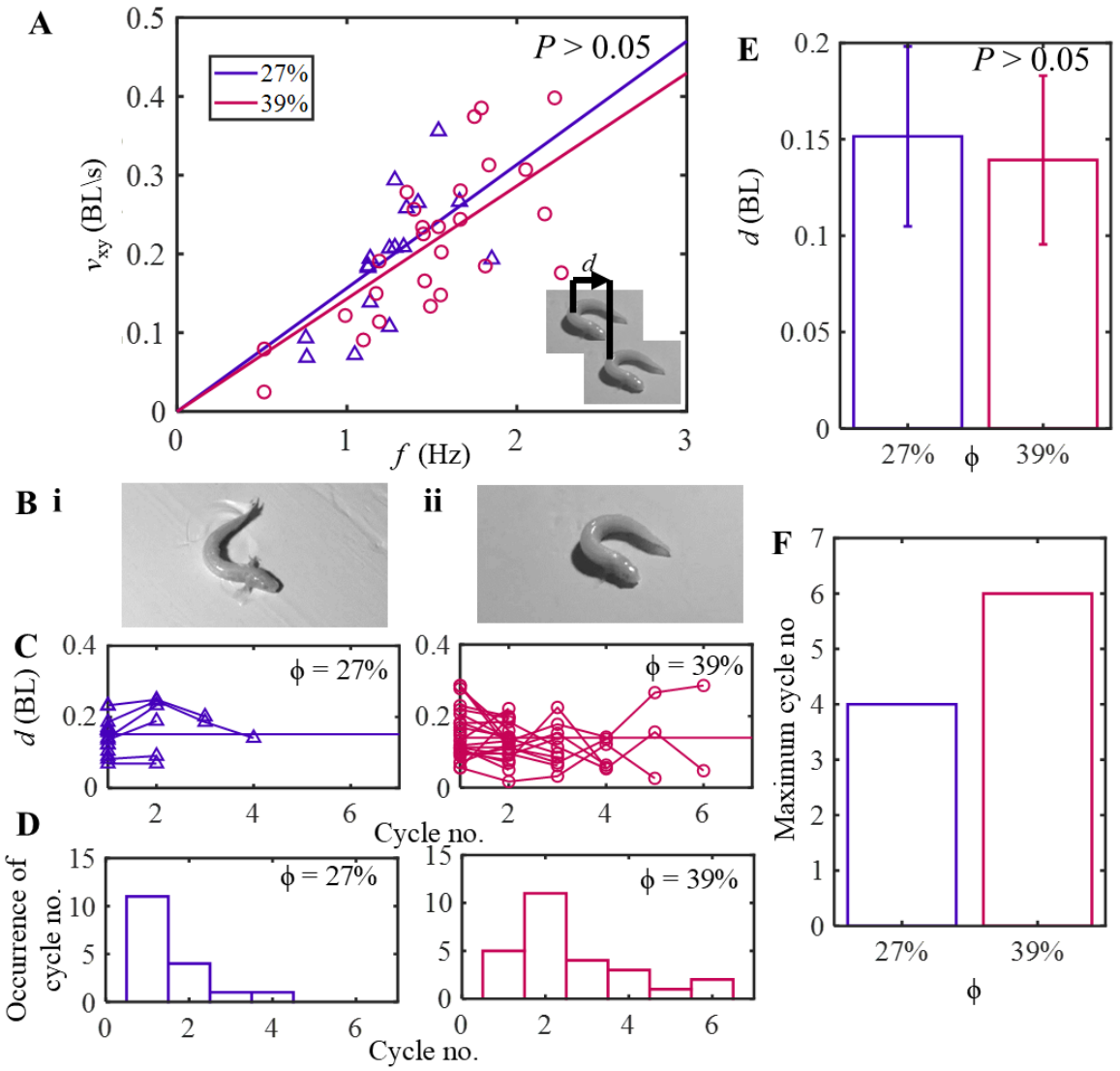

Figure 7.3: Bichir speed, forward displacement and total number of cycles across ϕ. (A) Average speed (v_{xy}) of the animal's mid-body relative to frequency (f). Lines correspond to linear least-square fit lines. The color of the fit line and each data point for each mud strength is a function of force at 1 cm from mud characterization. **(B)** Snapshot of the bichir moving on mud with (i) $\phi = 27\%$ and (ii) $\phi = 39\%$. **(C)** Forward displacement (d) of the animal's mid-body per cycle over each cycle and **(D)** histogram of the number of cycles the animal walked across mud with (i) $\phi = 27\%$ (indigo color line, triangle marker) and (ii) $\phi = 39\%$ (magenta color line, circle marker). Line in C, i-iii and fit lines in A correspond to the average forward displacement of

the animal's mid-body per cycle. The color of line for each mud strength is a function of force at 1 cm from mud characterization. **(E)** The average forward displacement of the animal's mid-body per cycle (lines in C, i-iii) as a function of ϕ. Error bar in E corresponds to mean $\pm$ s.d. **(F)** Maximum number of cycles the animal moved in a walk trial. Color in E-F corresponds to ϕ. Statistics were performed using one-way ANOVA.

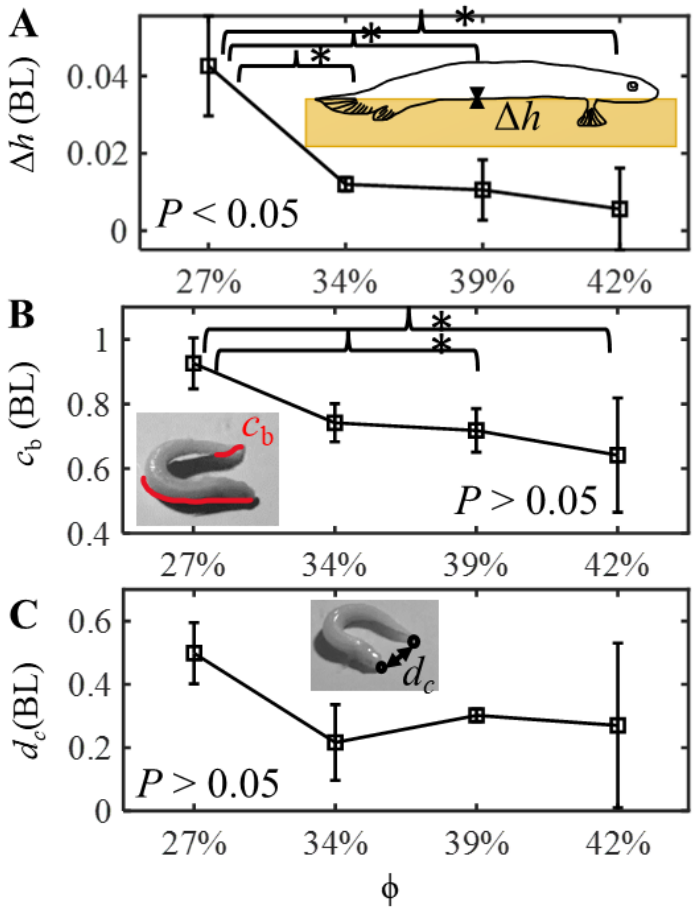

Figure 7.4: Bichir sinkage, contact length, and maximum bending as a function of ϕ. (A) Average sinkage (Δh) of the animal's body as a function of ϕ. **(B)** Average body contact length (c_b) as a function of ϕ. **(C)** maximum bending (d_c) as a function of ϕ. Square marker and error bar in A-C corresponds to mean $\pm$ s.d. Statistics performed using one-way ANOVA. * $P < 0.05$, Student's t-test, one-way ANOVA.

lesser body contact length on mud with $\phi > 27\%$ indicating that some sections of the animal's body were lifted off the mud surface (Fig. 7.4B) during locomotion. Video observations showed that the animal lifted its lower body (Fig. 7.4B) during each half cycle (twice in a cycle). The animal did not have a significant change in maximum bending (Fig. 7.4C). The results may be incorrect due to insufficient animal data.

7.4 Viscosity and stress measurements for mud with different strengths

Below are measurement results for viscosity, yield, and flow stress (Fig. 7.5) of mud with different mud strengths (ϕ = 27%, 34%, 39%, and 42%) that were measured using a rheometer (Anton Paar). They were not included in the previous chapters or other publications but they can be potentially useful for future research:

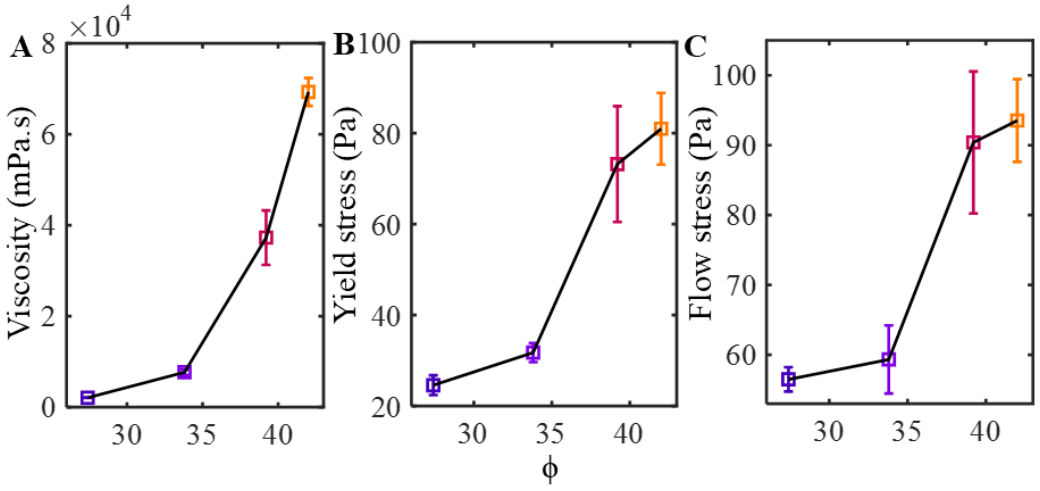

Figure 7.5: Viscocity and stress measurements for mud with different ϕ. **(A)** Viscosity as a function of ϕ. **(B)** Yield stress as a function of ϕ. **(C)** Flow stress as a function of ϕ. The color of the error bar and square marker for each mud strength is a function of force at 1 cm from mud characterization. Square marker and error bar in A-C corresponds to mean ± s.d.

7.5 3-D terrain setups for snake robot experiments

Below are 3-D terrain setups that were developed to study snake locomotion in 3-D complex terrains using the sensorized snake robot, SenSnake. They were not included in the previous chapters or other publications but they can be potentially useful for future research and inspire new ideas:

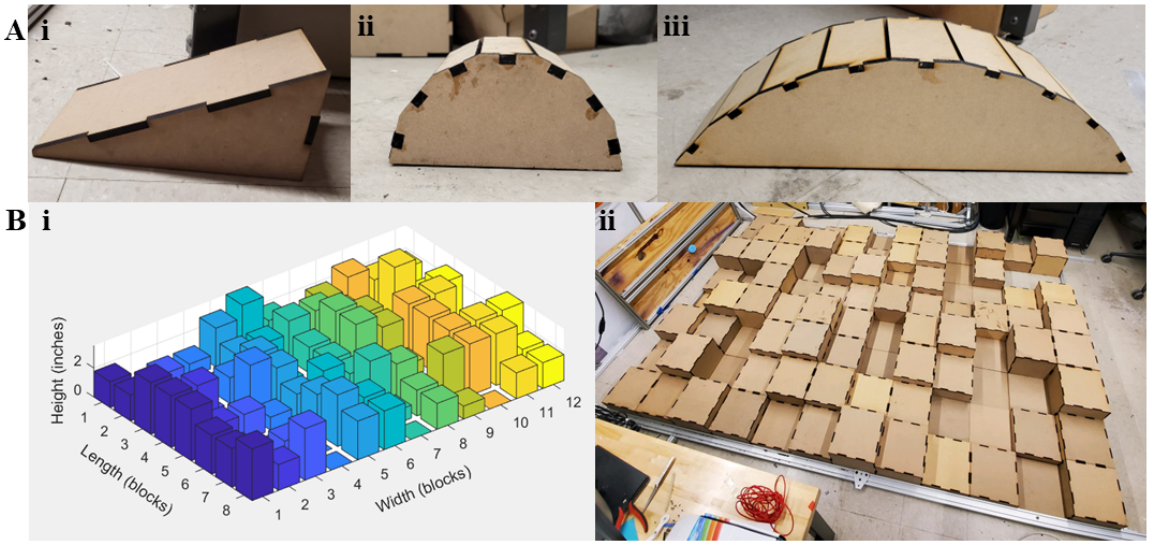

Figure 7.6: 3-D terrain setup. (A) 3-D obstacles. (i) Wedge, (ii) small half-cylindrical obstacle, and (ii) large half-cylindrical obstacle made up of laser cut wooden sheets (McMaster-Carr, Princeton, NJ, USA). **(B)** Complex 3-D terrain. (i) Randomized terrain blocks of different heights generated using MATLAB. (ii) Randomized terrain wooden blocks of different heights made up of laser cut wooden sheets (McMaster-Carr, Princeton, NJ, USA). Kaiwen Wang and Qiyuan Fu helped with the laser cutting of the wooden sheets. Kaiwen Wanng developed code for the generation of randomized terrain.

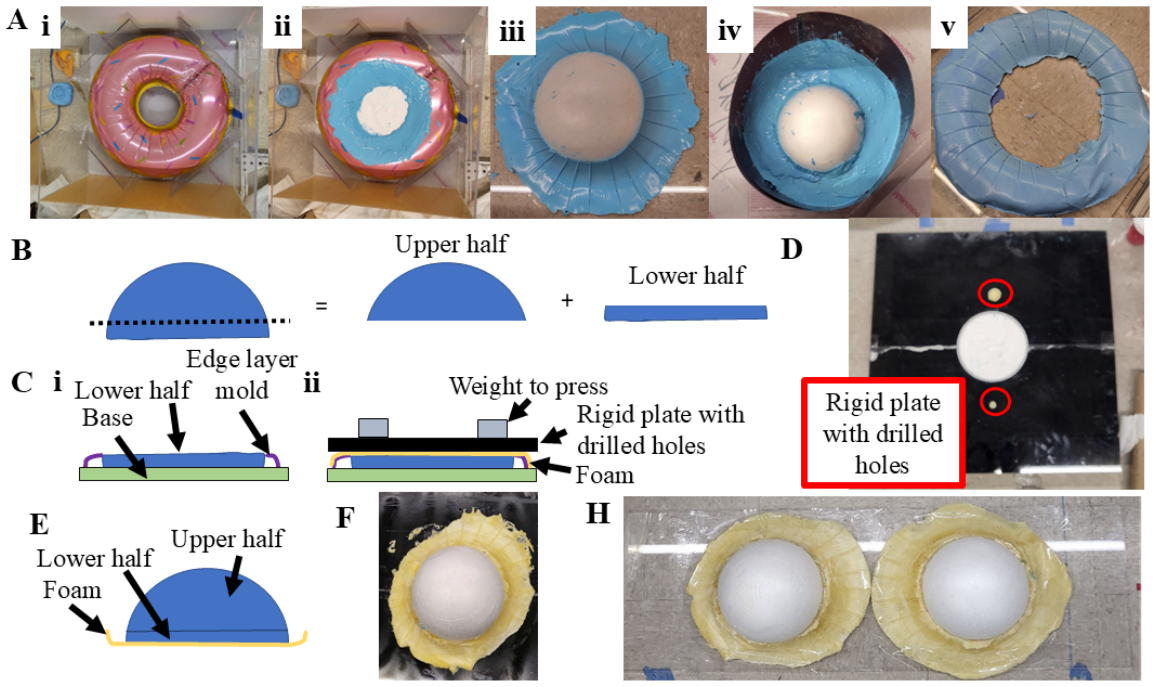

Figure 7.7: Smooth terrain development. (A) Terrain hill edge layer mold development. (i) A donut-shaped balloon (GGDE Store) for making a terrain hill edge layer mold. (ii) Donut-shaped balloon with a smooth half sphere made up of Polystyrene foam (MT Products Store) and smooth edge layer mold made of liquid rubber (Smooth-on, Inc., Pennsylvania, USA) set to cure. (iii) Smooth half sphere and edge layer after curing. (iv) Setup for making the edge layer mold made of liquid rubber (Smooth-on, Inc., Pennsylvania, USA) set to cure. (v) Terrain hill edge layer mold. **(B)** Schematic of the half sphere split into two parts. **(C)** Schematic of the smooth terrain hill development. (i) Placement of the lower half of the half sphere and the edge layer mold. (ii) Rigid Polyurethane foam (Smooth-on, Inc., Pennsylvania, USA) poured onto the edge layer mold and pressed using weights. textbf(D) Snapshot of the top view of the smooth terrain hill development setup. textbf(E) Schematic of the smooth terrain hill with the upper half glued onto the lower half of the half sphere. textbf(F) Smooth terrain hill. textbf(F) Two smooth terrain hills glued onto a plexiglass (McMaster-Carr, Princeton, NJ, USA) to make a smooth valley for a smooth terrain.

Bibliography

Aguilar, Jeffrey, Tingnan Zhang, Feifei Qian, Mark Kingsbury, Benjamin McInroe, Nicole Mazouchova, Chen Li, Ryan Maladen, Chaohui Gong, Matt Travers, Ross L. Hatton, Howie Choset, Paul B. Umbanhowar, and Daniel I. Goldman (2016). "A review on locomotion robophysics: The study of movement at the intersection of robotics, soft matter and dynamical systems." In: *Reports on Progress in Physics* 79.11, p. 110001. ISSN: 00344885. DOI: 10.1088/0034-4885/79/11/110001.

Arai, Masayuki, Yoshinori Tanaka, Shigeo Hirose, Hiroyuki Kuwahara, and Shingo Tsukui (Jan. 2008). "Development of "Souryu-IV" and "Souryu-V:" serially connected crawler vehicles for in-rubble searching operations." In: *Journal of Field Robotics* 25.1-2, pp. 31–65. ISSN: 15564959. DOI: 10.1002/rob.20229.

Ashley-Ross, Miriam A., S. Tonia Hsieh, Alice C. Gibb, and Richard W. Blob (Aug. 2013). "Vertebrate land invasions-past, present, and future: An introduction to the symposium." In: *Integrative and Comparative Biology*. Vol. 53. 2, pp. 192–196. DOI: 10.1093/icb/ict048.

Astley, Henry C. and Bruce C. Jayne (Nov. 2007). "Effects of perch diameter and incline on the kinematics, performance and modes of arboreal locomotion of corn snakes (Elaphe guttata)." In: *Journal of Experimental Biology* 210.21, pp. 3862–3872. ISSN: 00220949. DOI: 10.1242/jeb.009050.

Astley, Henry C. and Bruce C. Jayne (Mar. 2009). "Arboreal habitat structure affects the performance and modes of locomotion of corn snakes (Elaphe guttata)." In: *Journal of Experimental Zoology Part A: Ecological Genetics and Physiology* 311.3, pp. 207–216. ISSN: 19325223. DOI: 10.1002/jez.521.

Astley, Henry C., Joseph R. Mendelson, Jin Dai, Chaohui Gong, Baxi Chong, Jennifer M. Rieser, Perrin E. Schiebel, Sarah S. Sharpe, Ross L. Hatton, Howie Choset, and Daniel I. Goldman (2020). *Surprising simplicities and syntheses in limbless self-propulsion in sand*. DOI: 10.1242/jeb.103564.

Bennett, Wallace O., Rachel S. Simons, and Elizabeth L. Brainerd (2001). "Twisting and bending: The functional role of salamander lateral hypaxial musculature during locomotion." In: *Journal of Experimental Biology* 204, pp. 1979–1989.

Bertram, John E.A. and Anne Gutmann (June 2009). "Motions of the running horse and cheetah revisited: Fundamental mechanics of the transverse and rotary gallop."

In: *Journal of the Royal Society Interface* 6.35, pp. 549–559. ISSN: 17425662. DOI: 10.1098/rsif.2008.0328.

Borenstein, Johann, Malik Hansen, and Adam Borrell (July 2007). "The OmniTread OT-4 serpentine robot - Design and performance." In: *Journal of Field Robotics* 24.7, pp. 601–621. ISSN: 15564959. DOI: 10.1002/rob.20196.

Bressman, N. R., J. W. Love, T. W. King, C. G. Horne, and M. A. Ashley-Ross (2019). "Emersion and terrestrial locomotion of the northern snakehead (Channa argus) on multiple substrates." In: *Integrative Organismal Biology* 1.1. ISSN: 25174843. DOI: 10.1093/iob/obz026.

Bressman, Noah R (Dec. 2022). "Terrestrial Capabilities of Invasive Fishes and Their Management Implications." In: *Integrative and Comparative Biology* 62.5, pp. 1377–1394. ISSN: 1540-7063. DOI: 10.1093/icb/icac023.

Bressman, Noah R., Alice C. Gibb, and Stacy C. Farina (Dec. 2018). "A walking behavior generates functional overland movements in the tidepool sculpin, Oligocottus maculosus." In: *Zoology* 131, pp. 20–28. ISSN: 09442006. DOI: 10.1016/j.zool.2018.10.003.

Bressman, Noah R., Callen H. Morrison, and Miriam A. Ashley-Ross (Aug. 2021). "Reffling: A Novel Locomotor Behavior Used by Neotropical Armored Catfishes (Loricariidae) in Terrestrial Environments." In: *Ichthyology and Herpetology* 109.2, pp. 608–625. ISSN: 27661520. DOI: 10.1643/i2020084.

Brinson, Hal F. and L. Catherine Brinson (2015). *Polymer engineering science and viscoelasticity: An introduction, Second edition*, pp. 1–482. ISBN: 9781489974853. DOI: 10.1007/978-1-4899-7485-3.

Cholleti, Eshwar Reddy, Jonathan Stringer, Piaras Kelly, Chris Bowen, and Kean Aw (2021). "Studying the creep behaviour of strechable capacitive sensor with barium titanate silicone elastomer composite." In: *Sensors and Actuators, A: Physical* 319, p. 112560. ISSN: 09244247. DOI: 10.1016/j.sna.2021.112560. URL: https://doi.org/10.1016/j.sna.2021.112560.

Chong, Baxi, Yasemin Ozkan Aydin, Chaohui Gong, Guillaume Sartoretti, Yunjin Wu, Jennifer M. Rieser, Haosen Xing, Perrin E. Schiebel, Jeffery W. Rankin, Krijn B. Michel, Alfredo Nicieza, John R. Hutchinson, Daniel I. Goldman, and Howie Choset (Apr. 2021). "Coordination of lateral body bending and leg movements for sprawled

posture quadrupedal locomotion." In: *International Journal of Robotics Research* 40.4-5, pp. 747–763. ISSN: 17413176. DOI: 10.1177/0278364921991158.

Chong, Baxi, Juntao He, Shengkai Li, Eva Erickson, Kelimar Diaz, Tianyu Wang, Daniel Soto, and Daniel I. Goldman (2023). "Self-propulsion via slipping: Frictional swimming in multilegged locomotors." In: *Proceedings of the National Academy of Sciences* 120.11. DOI: 10.1073/pnas. URL: http://www.pnas.org/lookup/suppl/doi:10.1073/pnas.2213698120/-/DCSupplemental..

Chong, Baxi, Tianyu Wang, Eva Erickson, Philip J Bergmann, and Daniel I Goldman (2022). "Coordinating tiny limbs and long bodies: Geometric mechanics of lizard terrestrial swimming." In: DOI: 10.1073/pnas. URL: https://doi.org/10.1073/pnas.2118456119.

Clack, Jennifer A (2012). *Gaining Ground: The Origin and Evolution of Tetrapods*. Indiana University Press.

Clardy, Todd R. (Dec. 2012). "Aquatic and Terrestrial Locomotion of the Rock Prickleback, Xiphister mucosus (Cottiformes: Zoarcoidei: Stichaeidae)." In: *Northwestern Naturalist* 93.3, pp. 203–210. ISSN: 1051-1733. DOI: 10.1898/11-19.1.

Clardy, Todd R. and Eric J. Hilton (Apr. 2016). "Osteology of the prickleback genus Xiphister (Cottiformes: Zoarcoidei: Stichaeidae)." In: *Acta Zoologica* 97.2, pp. 211–231. ISSN: 14636395. DOI: 10.1111/azo.12118.

Coussot, Philippe (1997). *Mudflow rheology and dynamics*. Routledge.

Crawford, Callie H., Zachary S. Randall, Pamela B. Hart, Lawrence M. Page, Prosanta Chakrabarty, Apinun Suvarnaraksha, and Brooke E. Flammang (Oct. 2020). "Skeletal and muscular pelvic morphology of hillstream loaches (Cypriniformes: Balitoridae)." In: *Journal of Morphology* 281.10, pp. 1280–1295. ISSN: 10974687. DOI: 10.1002/jmor.21247.

Crespi, Alessandro, Konstantinos Karakasiliotis, Andre Guignard, and Auke Jan Ijspeert (2013). "Salamandra Robotica II: An amphibious robot to study salamander-like swimming and walking gaits." In: *IEEE Transactions on Robotics* 29.2, pp. 308–320. ISSN: 15523098. DOI: 10.1109/TRO.2012.2234311.

Crowe, Alan (1992). "Muscle spindles, tendon organs, and joint receptors." In: *Sensorimotor integration. Chicago: University of Chicago Press. p*, pp. 454–95.

Crowe-Riddell, Jenna M., Ruth Williams, Lucille Chapuis, and Kate L. Sanders (2019). "Ultrastructural evidence of a mechanosensory function of scale organs (sensilla) in sea snakes (Hydrophiinae)." In: *Royal Society Open Science* 6.4, p. 182022. ISSN: 20545703. DOI: 10.1098/rsos.182022.

D'Alessio, Tommaso (1999). "Measurement errors in the scanning of piezoresistive sensors arrays." In: *Sensors and Actuators, A: Physical* 72.1, pp. 71–76. ISSN: 09244247. DOI: 10.1016/S0924-4247(98)00204-0.

Davenport, J. and A. K.M.Abdul Matin (1990). "Terrestrial locomotion in the climbing perch, Anabas testudineus (Bloch) (Anabantidea, Pisces)." In: *Journal of Fish Biology* 37.1, pp. 175–184. ISSN: 10958649. DOI: 10.1111/j.1095-8649.1990.tb05938.x.

De, J K and N C Nandi (1984). "A NOTE ON THE LOCOMOTORY BEHAVIOUR OF THE MUDSKIPPER BOLEOPHTHALMUS BODDARTI." In: *Indian Journal of Fisheries* 31, pp. 407–409.

Dijk, Van D.E. (1960). "Locomotion and attitudes of the mudskipper, Periophthalamus, a semi-terrestrial fish." In: *South African Journal of Science* 56.7, pp. 158–162.

Ding, Yang, Nick Gravish, Chen Li, Ryan D. Maladen, Nicole Mazouchova, Sarah S. Sharpe, Paul B. Umbanhowar, and Daniel I. Goldman (2012). "Comparative studies reveal principles of movement on and within granular media." In: *Natural Locomotion in Fluids and on Surfaces: Swimming, Flying, and Sliding*. The IMA Volumes in Mathematics and its Applications 155. Ed. by Stephen Childress, Anette Hosoi, William W. Schultz, and Jane Wang, pp. 281–292. DOI: 10.1007/978-1-4614-3997-4. URL: https://link.springer.com/10.1007/978-1-4614-3997-4.

Ding, Yang, Chen Li, and Daniel I. Goldman (Nov. 2013). "Swimming in the desert." In: *Physics Today* 66.11, pp. 68–69. ISSN: 00319228. DOI: 10.1063/PT.3.2189.

Dorgan, Kelly M. (May 2018). "Kinematics of burrowing by peristalsis in granular sands." In: *Journal of Experimental Biology* 221.10. ISSN: 00220949. DOI: 10.1242/jeb.167759.

Du, T. Y., H. C.E. Larsson, and E. M. Standen (Mar. 2016). "Observations of terrestrial locomotion in wild Polypterus senegalus from Lake Albert, Uganda." In: *African Journal of Aquatic Science* 41.1, pp. 67–71. ISSN: 16085914. DOI: 10.2989/16085914.2015.1125337.

Du, Trina Y. and Emily M. Standen (Oct. 2017). "Phenotypic plasticity of muscle fiber type in the pectoral fins of Polypterus senegalus reared in a terrestrial environment." In: *Journal of Experimental Biology* 220.19, pp. 3406–3410. ISSN: 00220949. DOI: 10.1242/jeb.162909.

Du, Trina Y. and Emily M. Standen (June 2020). "Terrestrial acclimation and exercise lead to bone functional response in Polypterus senegalus pectoral fins." In: *Journal of Experimental Biology* 223.11. ISSN: 14779145. DOI: 10.1242/jeb.217554.

English, Arthur Wm (1980). "The functions of the lumbar spine during stepping in the cat." In: *Journal of Morphology* 165.1, pp. 55–66. ISSN: 10974687. DOI: 10.1002/jmor.1051650106.

Falkingham, Peter L. and Angela M. Horner (Sept. 2016). "Trackways produced by lungfish during terrestrial locomotion." In: *Scientific Reports* 6. ISSN: 20452322. DOI: 10.1038/srep33734.

Farley, Claire T. and T. Christine Ko (1997). "Mechanics of locomotion in lizards." In: *Journal of Experimental Biology* 200, pp. 2177–2188.

Flammang, Brooke E., Apinun Suvarnaraksha, Julie Markiewicz, and Daphne Soares (Mar. 2016). "Tetrapod-like pelvic girdle in a walking cavefish." In: *Scientific Reports* 6. ISSN: 20452322. DOI: 10.1038/srep23711.

Foster, Kathleen L., Misha Dhuper, and Emily M. Standen (Sept. 2018). "Fin and body neuromuscular coordination changes during walking and swimming in Polypterus senegalus." In: *Journal of Experimental Biology* 221.17. ISSN: 00220949. DOI: 10.1242/jeb.168716.

Fu, Qiyuan, Henry C. Astley, and Chen Li (May 2022). "Snakes combine vertical and lateral bending to traverse uneven terrain." In: *Bioinspiration and Biomimetics* 17.3. ISSN: 17483190. DOI: 10.1088/1748-3190/ac59c5.

Fu, Qiyuan, Sean W. Gart, Thomas W. Mitchel, Jin Seob Kim, Gregory S. Chirikjian, and Chen Li (2020). "Body lateral deformation and compliance help snakes and snake robots stably traverse large steps." In: *Integrative and Comparative Biology* 60.

Fu, Qiyuan and Chen Li (2020). "Robotic modelling of snake traversing large, smooth obstacles reveals stability benefits of body compliance." In: *Royal Society Open Science* 7.2, p. 191192. ISSN: 20545703. DOI: 10.1098/rsos.191192.

Fu, Qiyuan and Chen Li (2021). "Snake robot traversing large obstacles using vertical bending with contact force feedback." In: *arXiv preprint arXiv:2112.07815*.

Fu, Qiyuan and Chen Li (Sept. 2023). "Contact feedback helps snake robots propel against uneven terrain using vertical bending." In: *Bioinspiration and Biomimetics* 18.5. ISSN: 17483190. DOI: 10.1088/1748-3190/ace672.

Gart, Sean W., Thomas W. Mitchel, and Chen Li (2019). "Snakes partition their body to traverse large steps stably." In: *Journal of Experimental Biology* 222.8. ISSN: 00220949. DOI: 10.1242/jeb.185991.

Gibb, Alice C., Miriam A. Ashley-Ross, and S. Tonia Hsieh (Aug. 2013). "Thrash, flip, or jump: The behavioral and functional continuum of terrestrial locomotion in teleost fishes." In: *Integrative and Comparative Biology*. Vol. 53. 2, pp. 295–306. DOI: 10.1093/icb/ict052.

Gillis, Gary B. (Mar. 1998). "Environmental Effects on Undulatory Locomotion in the American Eel Anguilla Rostrata: Kinematics in Water and on Land." In: *Journal of Experimental Biology* 201.7, pp. 949–961.

Gillis, Gary B. (Jan. 2000). "Patterns of white muscle activity during terrestrial locomotion in the American Eel (Anguilla Rostrata)." In: *Journal of Experimental Biology* 203.3. ISSN: 1477-9145.

Godon, Simon, Carlos Prados, Ahmed Chemori, Asko Ristolainen, and Maarja Kruusmaa (2024). "Walking in Mud: Modelling, Control and Experiments of Quadruped Locomotion." In: *TechRxiv*. DOI: 10.36227/techrxiv.172047167.78902329/v1. URL: https://doi.org/10.36227/techrxiv.172047167.78902329/v1.

Goldman, Daniel I. (July 2014). "Colloquium: Biophysical principles of undulatory self-propulsion in granular media." In: *Reviews of Modern Physics* 86.3, pp. 943–958. ISSN: 15390756. DOI: 10.1103/RevModPhys.86.943.

Gonzalez-gomez, Juan, Javier Gonzalez-quijano, Houxiang Zhang, and Mohamed Abderrahim (2010). "Toward the sense of touch in snake modular robots for search

and rescue operations." In: *Proc. ICRA 2010 Workshop "Modular Robots: State of the Art*, pp. 63–68.

Gravish, Nick and George V. Lauder (2018). "Robotics-inspired biology." In: *Journal of Experimental Biology* 221.7. ISSN: 00220949. DOI: 10.1242/jeb.138438.

Gray, J and H W Lissmann (Feb. 1950). "The Kinetics of Locomotion of the Grass-Snake." In: *Journal of Experimental Biology* 26.4, pp. 354–367. ISSN: 1477-9145.

Gruebele, Alexander, Jean Philippe Roberge, Andrew Zerbe, Wilson Ruotolo, Tae Myung Huh, and Mark R. Cutkosky (2020). "A stretchable capacitive sensory skin for exploring cluttered environments." In: *IEEE Robotics and Automation Letters* 5.2, pp. 1750–1757. ISSN: 23773766. DOI: 10.1109/LRA.2020.2969939.

Hall, Joseph K., Craig P. McGowan, and David C. Lin (2022). "Comparison between the kinematics for kangaroo rat hopping on a solid versus sand surface." In: *Royal Society Open Science* 9.2. ISSN: 20545703. DOI: 10.1098/rsos.211491.

Harris, Vernon A. (1960). "ON THE LOCOMOTION OF THE MUD-SKIPPER PERIOPHTHALMUS KOELREUTERI (PALLAS): (GOBIIDAE)." In: *Proceedings of the Zoological Society of London* 134.1, pp. 107–135. ISSN: 14697998. DOI: 10.1111/j.1469-7998.1960.tb05921.x.

Hatton, R. L. and H. Choset (Dec. 2015). "Nonconservativity and noncommutativity in locomotion: Geometric mechanics in minimum-perturbation coordinates." In: *European Physical Journal: Special Topics* 224.17-18, pp. 3141–3174. ISSN: 19516401. DOI: 10.1140/epjst/e2015-50085-y.

Hedrick, Tyson L. (Sept. 2008). "Software techniques for two- and three-dimensional kinematic measurements of biological and biomimetic systems." In: *Bioinspiration and Biomimetics* 3.3. ISSN: 17483182. DOI: 10.1088/1748-3182/3/3/034001.

Hirose, Shigeo (1993). *Biologically inspired robots: Snake-Like Locomotors and Manipulators*. Oxford University Press, Oxford.

Horner, Angela M. and Bruce C. Jayne (May 2008). "The effects of viscosity on the axial motor pattern and kinematics of the African lungfish (Protopterus annectens) during lateral undulatory swimming." In: *Journal of Experimental Biology* 211.10, pp. 1612–1622. ISSN: 00220949. DOI: 10.1242/jeb.013029.

Horner, Angela M. and Bruce C. Jayne (May 2014). "Lungfish axial muscle function and the vertebrate water to land transition." In: *PLoS ONE* 9.5. ISSN: 19326203. DOI: 10.1371/journal.pone.0096516.

Hu, David L., Jasmine Nirody, Terri Scott, and Michael J. Shelley (2009). "The mechanics of slithering locomotion." In: *Proceedings of the National Academy of Sciences* 106.25, pp. 10081–10085. ISSN: 00278424. DOI: 10.1073/pnas.0812533106.

Huseby, T. W. and S. Matsuoka (1967). "Mechanical properties of solid and liquid polymers." In: *Materials Science and Engineering* 1.6, pp. 321–341. ISSN: 00255416. DOI: 10.1016/0025-5416(67)90014-6.

Ijspeert, Auke J. (2014). "Biorobotics: Using robots to emulate and investigate agile locomotion." In: *Science*. Vol. 346. 6206, pp. 196–203. DOI: 10.1126/science.1254486.

Jaafar, Zeehan and Edward O Murdy (2017). *Fishes out of water: biology and ecology of mudskippers*. CRC Press.

Jayne, Bruce C (1986). *Kinematics of Terrestrial Snake Locomotion*. Tech. rep. 4, pp. 915–927. URL: https://www.jstor.org/stable/1445288.

Johnels, Alf G (1957). "The Mode of Terrestrial Locomotion in Clarias." In: *Oikos* 8.2, pp. 122–129. URL: https://www.jstor.org/stable/3564996.

Jurestovsky, Derek J., Logan R. Usher, and Henry C. Astley (2021). "Generation of propulsive force via vertical undulations in snakes." In: *Journal of Experimental Biology* 224.13. ISSN: 14779145. DOI: 10.1242/jeb.239020.

Kafkafi, Neri and Ilan Golani (1998). "A traveling wave of lateral movement coordinates both turning and forward walking in the ferret." In: *Biological Cybernetics* 78, pp. 441–453.

Kalantari, Masoud, Javad Dargahi, Jozsef Kövecses, Mahmood Ghanbari Mardasi, and Shahrzad Nouri (2011). "A new approach for modeling piezoresistive force sensors based on semiconductive polymer composites." In: *IEEE/ASME Transactions on Mechatronics* 17.3, pp. 572–581. ISSN: 10834435. DOI: 10.1109/TMECH.2011.2108664.

Kamegawa, Tetsushi, Taichi Akiyama, Yosuke Suzuki, Toru Kishutani, and Akio Gofuku (2020). "Three-Dimensional Reflexive Behavior by a Snake Robot with Full

Circumference Pressure Sensors." In: *2020 IEEE/SICE International Symposium on System Integration*, pp. 897–902. DOI: 10.1109/SII46433.2020.9026245.

Kamimura, Tomoya, Kaho Sato, Shinya Aoi, Yasuo Higurashi, Naomi Wada, Kazuo Tsuchiya, Akihito Sano, and Fumitoshi Matsuno (Apr. 2022). "Three Characteristics of Cheetah Galloping Improve Running Performance Through Spinal Movement: A Modeling Study." In: *Frontiers in Bioengineering and Biotechnology* 10. ISSN: 22964185. DOI: 10.3389/fbioe.2022.825638.

Kano, Takeshi and Akio Ishiguro (2013). "Obstacles are beneficial to me! Scaffold-based locomotion of a snake-like robot using decentralized control." In: *IEEE International Conference on Intelligent Robots and Systems*, pp. 3273–3278. ISSN: 21530858. DOI: 10.1109/IROS.2013.6696821.

Kano, Takeshi, Takahide Sato, Ryo Kobayashi, and Akio Ishiguro (2012). "Local reflexive mechanisms essential for snakes' scaffold-based locomotion." In: *Bioinspiration and Biomimetics* 7.4, p. 046008. ISSN: 17483182. DOI: 10.1088/1748-3182/7/4/046008.

Kawano, Sandy M. and Richard W. Blob (Aug. 2013). "Propulsive forces of mudskipper fins and salamander limbs during terrestrial locomotion: Implications for the invasion of land." In: *Integrative and Comparative Biology*. Vol. 53. 2, pp. 283–294. DOI: 10.1093/icb/ict051.

Kelley, K. C., S. J. Arnold, and J. Gladstone (1997). "The effects of substrate and vertebral number on locomotion in the garter snake Thamnophis elegans." In: *Functional Ecology* 11.2, pp. 189–198. ISSN: 02698463. DOI: 10.1046/j.1365-2435.1997.00077.x.

Kimura, Hitoshi and Shigeo Hirose (2002). "Development of Genbu: Active wheel passive joint articulated mobile robot." In: *IEEE International Conference on Intelligent Robots and Systems* 1, pp. 823–828. DOI: 10.1109/irds.2002.1041492.

Kudrolli, Arshad, Bernny Ramirez, and David A Weitz (Nov. 2019). "Burrowing dynamics of aquatic worms in soft sediments." In: *Proceedings of the National Academy of Sciences* 116.51. DOI: 10.1073/pnas.1911317116/-/DCSupplemental.y. URL: https://www.pnas.org.

Li, C., P. B. Umbanhowar, H. Komsuoglu, and D. I. Goldman (2010). "The effect of limb kinematics on the speed of a legged robot on granular media." In: *Proceedings*

of the Society for Experimental Mechanics, Inc. Vol. 67, pp. 1383–1393. DOI: 10.1007/S11340-010-9347-1.

Li, Chen, S. Tonia Hsieh, and Daniel I. Goldman (Sept. 2012). "Multi-functional foot use during running in the zebra-tailed lizard (Callisaurus draconoides)." In: *Journal of Experimental Biology* 215.18, pp. 3293–3308. ISSN: 00220949. DOI: 10.1242/jeb.061937.

Li, Chen, Paul B Umbanhowar, Haldun Komsuoglu, Daniel E Koditschek, and Daniel I Goldman (Mar. 2009). "Sensitive dependence of the motion of a legged robot on granular media." In: *Proceedings of the National Academy of Sciences* 106.9, pp. 3029–3034. URL: www.pnas.org/cgi/content/full/.

Li, Chen, Tingnan Zhang, and Daniel I Goldman (2012). "A resistive force model for legged locomotion on granular media." In: *Adaptive Mobile Robotics*, pp. 433–440.

Li, Chen, Tingnan Zhang, and Daniel I Goldman (2013). "A Terradynamics of Legged Locomotion on Granular Media." In: *Science* 339.6126, pp. 1408–1412. DOI: 10.1126/science.1229163. URL: https://www.science.org.

Li, Tinghua, Bayu Jayawardhana, Amar M. Kamat, and Ajay Giri Prakash Kottapalli (2021). "Source-Seeking Control of Unicycle Robots With 3-D-Printed Flexible Piezoresistive Sensors." In: *IEEE Transactions on Robotics*. ISSN: 1552-3098. DOI: 10.1109/tro.2021.3076964.

Liang, Xu, Min Xu, Lichao Xu, Peng Liu, Xiaoshuang Ren, Ziwen Kong, Jie Yang, and Shiwu Zhang (2012). "The AmphiHex: A novel amphibious robot with transformable leg-flipper composite propulsion mechanism." In: *IEEE International Conference on Intelligent Robots and Systems*, pp. 3667–3672. ISBN: 9781467317375. DOI: 10.1109/IROS.2012.6386238.

Liljebäck, P., K. Y. Pettersen, Ø. Stavdahl, and J. T. Gravdahl (2012a). "A review on modelling, implementation, and control of snake robots." In: *Robotics and Autonomous Systems* 60.1, pp. 29–40. ISSN: 09218890. DOI: 10.1016/j.robot.2011.08.010. URL: http://dx.doi.org/10.1016/j.robot.2011.08.010.

Liljebäck, Pål, Kristin Y. Pettersen, and Øyvind Stavdahl (2010). "A snake robot with a contact force measurement system for obstacle-aided locomotion." In: *IEEE International Conference on Robotics and Automation*, pp. 683–690. ISSN: 10504729. DOI: 10.1109/ROBOT.2010.5509839.

Liljebäck, Pål, Kristin Y. Pettersen, Øyvind Stavdahl, and Jan Tommy Gravdahl (2011). "Experimental Investigation of Obstacle-Aided Locomotion With a Snake Robot." In: *IEEE Transactions on Robotics* 27.4, pp. 792–800.

Liljebäck, Pål, Øyvind Stavdahl, Kristin Y. Pettersen, and Jan Tommy Gravdahl (2012b). "A modular and waterproof snake robot joint mechanism with a novel force/torque sensor." In: *IEEE International Conference on Intelligent Robots and Systems*, pp. 4898–4905. ISSN: 21530858. DOI: 10.1109/IROS.2012.6386115.

Liu, Shipeng, Boyuan Huang, and Feifei Qian (Dec. 2023). "Adaptation of Flipper-Mud Interactions Enables Effective Terrestrial Locomotion on Muddy Substrates." In: *IEEE Robotics and Automation Letters* 8.12, pp. 7978–7985. DOI: 10.1109/LRA.2023.3323123.

Long, John (2012). *Darwin's devices: what evolving robots can teach us about the history of life and the future of technology*. Basic Books (AZ).

Lutek, K. and E. M. Standen (2021). "Increasing Viscosity Helps Explain Locomotor Control in Swimming Polypterus senegalus." In: *Integrative Organismal Biology* 3.1, pp. 1–11. ISSN: 25174843. DOI: 10.1093/iob/obab024.

Ma'ckiewicz, Andrzej and Waldemar Ratajczak (1993). "PRINCIPAL COMPONENTS ANALYSIS (PCA)*." In: *Computers & Geosciences* 19.3, pp. 303–342.

Maladen, Ryan D, Yang Ding, Chen Li, and Daniel I Goldman (July 2009). "Undulatory Swimming in Sand:Subsurface Locomotion of theSandfish Lizard." In: *Science* 325.5938, pp. 314–318. ISSN: 00368075. DOI: 10.1126/science.1172490.

Maladen, Ryan D., Yang Ding, Paul B. Umbanhowar, Adam Kamor, and Daniel I. Goldman (Sept. 2011). *Mechanical models of sandfish locomotion reveal principles of high performance subsurface sand-swimming*. DOI: 10.1098/rsif.2010.0678.

Marvi, Hamidreza, Chaohui Gong, Nick Gravish, Henry Astley, David L Hu, and Daniel I Goldman (2014). "Sidewinding with minimal slip: Snake and robot ascent of sandy slopes." In: 346.6206.

Mathis, Alexander, Pranav Mamidanna, Kevin M. Cury, Taiga Abe, Venkatesh N. Murthy, Mackenzie Weygandt Mathis, and Matthias Bethge (Sept. 2018). "DeepLabCut: markerless pose estimation of user-defined body parts with deep

learning." In: *Nature Neuroscience* 21.9, pp. 1281–1289. ISSN: 15461726. DOI: 10.1038/s41593-018-0209-y.

Mazouchova, Nicole, Nick Gravish, Andrei Savu, and Daniel I. Goldman (June 2010). "Utilization of granular solidification during terrestrial locomotion of hatchling sea turtles." In: *Biology Letters* 6.3, pp. 398–401. ISSN: 1744957X. DOI: 10.1098/rsbl.2009.1041.

Mazouchova, Nicole, Paul B. Umbanhowar, and Daniel I. Goldman (June 2013). "Flipper-driven terrestrial locomotion of a sea turtle-inspired robot." In: *Bioinspiration and Biomimetics* 8.2. ISSN: 17483182. DOI: 10.1088/1748-3182/8/2/026007.

McInroe, Benjamin, Henry C. Astley, Chaohui Gong, Sandy M. Kawano, Perrin E. Schiebel, Jennifer M. Rieser, Choset Howie, Richard W. Blob, and Daniel I. Goldman (July 2016). "Tail use improves performance on soft substrates in models of early vertebrate land locomotors." In: *Science* 353.6295, pp. 154–158. ISSN: 10959203. DOI: 10.1126/science.aaf8800.

Mehta, R. S., K. Akesson, E. Redmann, M. McCarty-Glenn, R. Ortega, S. Syed, M. Yap-Chiongco, C. Jacquemetton, and A. B. Ward (Sept. 2021). "Terrestrial locomotion in elongate fishes: exploring the roles of morphology and substrate in facilitating locomotion." In: *Journal of Zoology* 315.1, pp. 2–18. ISSN: 14697998. DOI: 10.1111/jzo.12794.

Moon, Brad R. and Carl Gans (1998). "Kinematics, Muscular Activity and Propulsion in Gopher Snakes." In: *Journal of Experimental Biology* 201.19, pp. 2699–2684. ISSN: 1477-9145.

Nakajima, Mizuki, Motoyasu Tanaka, Kazuo Tanaka, and Fumitoshi Matsuno (2018). "Motion control of a snake robot moving between two non-parallel planes." In: *Advanced Robotics* 32.10, pp. 559–573. ISSN: 15685535. DOI: 10.1080/01691864.2018.1458653. URL: https://doi.org/10.1080/01691864.2018.1458653.

Naylor, Emily R and Sandy M Kawano (Dec. 2022). "Mudskippers Modulate their Locomotor Kinematics when Moving on Deformable and Inclined Substrates." In: *Integrative and Comparative Biology* 62.5, pp. 1335–1356. ISSN: 1540-7063. DOI: 10.1093/icb/icac084.

Othayoth, Ratan, George Thoms, and Chen Li (2020). "An energy landscape approach to locomotor transitions in complex 3D terrain." In: *Proceedings of the National Academy of Sciences*. DOI: 10.1073/pnas.1918297117/-/DCSupplemental.

Pace, C. M. and A. C. Gibb (July 2009). "Mudskipper pectoral fin kinematics in aquatic and terrestrial environments." In: *Journal of Experimental Biology* 212.14, pp. 2279–2286. ISSN: 00220949. DOI: 10.1242/jeb.029041.

Pace, C. M. and A. C. Gibb (Mar. 2014). "Sustained periodic terrestrial locomotion in air-breathing fishes." In: *Journal of Fish Biology* 84.3, pp. 639–660. ISSN: 00221112. DOI: 10.1111/jfb.12318.

Pace, Cinnamon M. and Alice C. Gibb (Feb. 2011). "Locomotor behavior across an environmental transition in the ropefish, Erpetoichthys calabaricus." In: *Journal of Experimental Biology* 214.4, pp. 530–537. ISSN: 00220949. DOI: 10.1242/jeb.047902.

Perry, C. T., P. S. Kench, M. J. O'Leary, K. M. Morgan, and F. Januchowski-Hartley (Apr. 2015). "Linking reef ecology to island building: Parrotfish identified as major producers of island-building sediment in the Maldives." In: *Geology* 43.6, pp. 503–506. ISSN: 19432682. DOI: 10.1130/G36623.1.

Pfotzer, L., M. Staehler, A. Hermann, A. Rönnau, and R. Dillmann (2015). "KAIRO 3: Moving over stairs & unknown obstacles with reconfigurable snake-like robots." In: *2015 European Conference on Mobile Robots (ECMR)*, pp. 3–8. DOI: 10.1109/ECMR.2015.7324209.

Proske, U. (1969). "An electrophysiological analysis of cutaneous mechanoreceptors in a snake." In: *Comparative Biochemistry And Physiology* 29.3, pp. 1039–1046. ISSN: 0010406X. DOI: 10.1016/0010-406x(69)91006-8.

Ramesh, Divya, Qiyuan Fu, and Chen Li (2022). "SenSnake: A snake robot with contact force sensing for studying locomotion in complex 3-D terrain." In: *Proceedings - IEEE International Conference on Robotics and Automation*, pp. 2068–2075. ISSN: 10504729. DOI: 10.1109/ICRA46639.2022.9812159.

Ramesh, Divya, Gargi Sadalgekar, Qiyuan Fu, Zachary Souders, Jack Rao, and Chen Li (2024a). "Control and characterization of mud strength for studying locomotion on wet flowable substrates." In: *Journal of Experimental Biology* (To be submitted).

Ramesh, Divya, Gargi Sadalgekar, Jiangqi Tan, and Chen Li (2024b). "Terrestrial locomotion by mudskippers on wet flowable substrate of varying strength." In: *Journal of Experimental Biology* (To be submitted).

Redmann, Erica, Alina Sheikh, Areej Alqahtani, Mica McCarty-Glenn, Shazrah Syed, Rita S. Mehta, and Andrea B. Ward (July 2020). "Terrestrial locomotion in American eels (Anguilla rostrata): How substrate and incline affect movement patterns." In: *Integrative and Comparative Biology*. Vol. 60. 1. Oxford University Press, pp. 180–189. DOI: 10.1093/icb/icaa016.

Reilly, S. M. and M. J. Delancey (1997). "Sprawling locomotion in the lizard Sceloporus clarkii: The effects of speed on gait, hindlimb kinematics, and axial bending during walking." In: *Journal of Zoology* 243.2, pp. 417–433. ISSN: 09528369. DOI: 10.1111/j.1469-7998.1997.tb02791.x.

Roberts, Peter, Mason Zadan, and Carmel Majidi (2021). "Soft Tactile Sensing Skins for Robotics." In: *Current Robotics Reports* 2.3, pp. 343–354. DOI: 10.1007/s43154-021-00065-2.

Rus, Daniela and Michael T. Tolley (2015). "Design, fabrication and control of soft robots." In: *Nature* 521.7553, pp. 467–475. ISSN: 14764687. DOI: 10.1038/nature14543.

Sayer, Martin D.J. (Sept. 2005). *Adaptations of amphibious fish for surviving life out of water*. DOI: 10.1111/j.1467-2979.2005.00193.x.

Schaeffer, Dorcas O. and R. Mark Waters (1996). "Neuroanatomy and neurological diseases of reptiles." In: *Seminars in Avian and Exotic Pet Medicine* 3.5, pp. 165–171. ISSN: 1055937X. DOI: 10.1016/s1055-937x(96)80005-3.

Schiebel, Perrin E., Henry C. Astley, Jennifer M. Rieser, Shashank Agarwal, Christian Hubicki, Alex M. Hubbard, Kelimar Diaz, Joseph R. Mendelson, Ken Kamrin, and Daniel I. Goldman (June 2020). "Mitigating memory effects during undulatory locomotion on hysteretic materials." In: *eLife* 9, pp. 1–32. ISSN: 2050084X. DOI: 10.7554/eLife.51412.

Schiebel, Perrin E, Alex M Hubbard, and Daniel I Goldman (2020). "Comparative study of snake lateral undulation kinematics in model heterogeneous terrain." In: *Integrative and Comparative Biology* 63, pp. 198–208. DOI: 10.1093/icb/icaa125.

Schiebel, Perrin E., Jennifer M. Rieser, Alex M. Hubbard, Lillian Chen, D. Zeb Rocklin, and Daniel I. Goldman (2019). "Mechanical diffraction reveals the role of passive dynamics in a slithering snake." In: *Proceedings of the National Academy of Sciences of the United States of America* 116.11, pp. 4798–4803. ISSN: 10916490. DOI: 10.1073/pnas.1808675116.

Schilling, Nadja and Rémi Hackert (Oct. 2006). "Sagittal spine movements of small therian mammals during asymmetrical gaits." In: *Journal of Experimental Biology* 209.19, pp. 3925–3939. ISSN: 00220949. DOI: 10.1242/jeb.02400.

Sharpe, Sarah S., Robyn Kuckuk, and Daniel I. Goldman (July 2015). "Controlled preparation of wet granular media reveals limits to lizard burial ability." In: *Physical Biology* 12.4. ISSN: 14783975. DOI: 10.1088/1478-3975/12/4/046009.

Shill, Jacob J., Emmanuel G. Collins, Eric Coyle, and Jonathan Clark (2014). "Terrain identification on a one-legged hopping robot using high-resolution pressure images." In: *Proceedings - IEEE International Conference on Robotics and Automation*, pp. 4723–4728. ISSN: 10504729. DOI: 10.1109/ICRA.2014.6907550.

Soderstrom, Torsten and Petre Stoica (1989). *System identification*. Prentice-Hall International.

Standen, Emily M., Trina Y. Du, Philippe Laroche, and Hans C.E. Larsson (Oct. 2016). "Locomotor flexibility of Polypterus senegalus across various aquatic and terrestrial substrates." In: *Zoology* 119.5, pp. 447–454. ISSN: 09442006. DOI: 10.1016/j.zool.2016.05.001.

Standen, Emily M., Trina Y. Du, and Hans C.E. Larsson (2014). "Developmental plasticity and the origin of tetrapods." In: *Nature* 513.7516, pp. 54–58. ISSN: 14764687. DOI: 10.1038/nature13708.

Stebbins, Robert C and Margaret Kalk (1961). *Observations on the Natural History of the Mud-Skipper, Periophthalmus sobrinus*. Tech. rep. 1, pp. 18–27. URL: https://www.jstor.org/stable/1440166?seq=1&cid=pdf-.

Sundaram, Subramanian, Petr Kellnhofer, Yunzhu Li, Jun Yan Zhu, Antonio Torralba, and Wojciech Matusik (2019). "Learning the signatures of the human grasp using a scalable tactile glove." In: *Nature* 569.7758, pp. 698–702. ISSN: 14764687. DOI: 10.1038/s41586-019-1234-z. URL: http://dx.doi.org/10.1038/s41586-019-1234-z.

Swanson, Brook O. and Alice C. Gibb (Nov. 2004). "Kinematics of aquatic and terrestrial escape responses in mudskippers." In: *Journal of Experimental Biology* 207.23, pp. 4037–4044. ISSN: 00220949. DOI: 10.1242/jeb.01237.

Taal, Stefan R., Hiroya Yamada, and Shigeo Hirose (2009). "3 Axial force sensor for a semi-autonomous snake robot." In: *IEEE International Conference on Robotics and Automation*, pp. 4057–4062. ISSN: 10504729. DOI: 10.1109/ROBOT.2009.5152366.

Tadokoro, Satoshi (2019). "Disaster Robotics: Results from the ImPACT Tough Robotics Challenge." In: *Springer* 128.

Takanashi, Takuro, Mizuki Nakajima, Tatsuya Takemori, and Motoyasu Tanaka (Oct. 2022). "Obstacle-Aided Locomotion of a Snake Robot Using Piecewise Helixes." In: *IEEE Robotics and Automation Letters* 7.4, pp. 10542–10549. ISSN: 23773766. DOI: 10.1109/LRA.2022.3194689.

Takanashi, Takuro, Mizuki Nakajima, Tatsuya Takemori, and Motoyasu Tanaka (2023). "Reaction Force Analysis for Obstacle-Aided Locomotion of Snake Robot Using Piecewise Helixes." In: *IEEE Access* 11, pp. 44150–44166. ISSN: 21693536. DOI: 10.1109/ACCESS.2023.3272751.

Takemori, Tatsuya, Motoyasu Tanaka, and Fumitoshi Matsuno (2018a). "Gait Design for a Snake Robot by Connecting Curve Segments and Experimental Demonstration." In: *IEEE Transactions on Robotics* 34.5, pp. 1384–1391. DOI: 10.1145/2786558.2786562.

Takemori, Tatsuya, Motoyasu Tanaka, and Fumitoshi Matsuno (2018b). "Ladder Climbing with a Snake Robot." In: *2018 IEEE/RSJ International Conference on Intelligent Robots and Systems (IROS)*, pp. 1–9. DOI: 10.1109/IROS.2018.8594411.

Takemori, Tatsuya, Motoyasu Tanaka, and Fumitoshi Matsuno (2021). "Hoop-Passing Motion for a Snake Robot to Realize Motion Transition Across Different Environments." In: *IEEE Transactions on Robotics* 37.5, pp. 1696–1711. ISSN: 19410468. DOI: 10.1109/TRO.2021.3063438.

Tanaka, Motoyasu and Kazuo Tanaka (2013). "Climbing and descending control of a snake robot on step environments based on kinematics." In: *IEEE International Conference on Intelligent Robots and Systems*, pp. 3285–3290. ISSN: 21530858. DOI: 10.1109/IROS.2013.6696823.

Tao, Junliang Julian, Sichuan Huang, and Yong Tang (Sept. 2020). "SBOR: a minimalistic soft self-burrowing-out robot inspired by razor clams." In: *Bioinspiration and Biomimetics* 15.5. ISSN: 17483190. DOI: 10.1088/1748-3190/ab8754.

Thandiackal, Robin, Kamilo Melo, Laura Paez, Johann Herault, Takeshi Kano, Kyoichi Akiyama, Frédéric Boyer, Dimitri Ryczko, Akio Ishiguro, and Auke J. Ijspeert (2021). "Emergence of robust self-organized undulatory swimming based on local hydrodynamic force sensing." In: *Science Robotics* 6.57. ISSN: 24709476. DOI: 10.1126/scirobotics.abf6354.

Travers, Matthew, Julian Whitman, and Howie Choset (2018). "Shape-based coordination in locomotion control." In: *International Journal of Robotics Research* 37.10, pp. 1253–1268. ISSN: 17413176. DOI: 10.1177/0278364918761569.

Von During, M (1979). "Sensory nerve endings of the skin and deeper structures." In: *Biology of the reptilia, neurology A* 9, pp. 407–441.

Walker, Ian D, Howie Choset, and Gregory S Chirikjian (2016). "Snake-like and continuum robots." In: *Springer handbook of robotics*. Springer, pp. 481–498.

Wang, Lei, Min Xu, Bo Liu, Tianyu Jiang, Shiwu Zhang, and Jie Yang (2013). "Experimental study on morphology and kinematics of mudskipper in amphibious environments." In: *2013 IEEE International Conference on Robotics and Biomimetics, ROBIO 2013*. IEEE Computer Society, pp. 1095–1100. DOI: 10.1109/ROBIO.2013.6739610.

Wang, Tianyu, Julian Whitman, Matthew Travers, and Howie Choset (2020). "Directional Compliance in Obstacle-Aided Navigation for Snake Robots." In: *American Control Conference (ACC)*, pp. 2458–2463. ISSN: 07431619. DOI: 10.23919/ACC45564.2020.9148021.

Wang, Yancheng, Xin Wu, Deqing Mei, Lingfeng Zhu, and Jianing Chen (2019). "Flexible tactile sensor array for distributed tactile sensing and slip detection in robotic hand grasping." In: *Sensors and Actuators, A: Physical* 297, p. 111512. ISSN: 09244247. DOI: 10.1016/j.sna.2019.07.036. URL: https://doi.org/10.1016/j.sna.2019.07.036.

Ward, Andrea B., Alyssa Costa, Stephanie L. Monroe, Robert J. Aluck, and Rita S. Mehta (Oct. 2015). "Locomotion in elongate fishes: A contact sport." In: *Zoology* 118.5, pp. 312–319. ISSN: 18732720. DOI: 10.1016/j.zool.2015.06.002.

Watz, J., P. A. Nilsson, E. Degerman, C. Tamario, and O. Calles (Oct. 2019). "Climbing the ladder: an evaluation of three different anguillid eel climbing substrata and placement of upstream passage solutions at migration barriers." In: *Animal Conservation* 22.5, pp. 452–462. ISSN: 14691795. DOI: 10.1111/acv.12485.

Wendt, Jobst, Zdzislaw Belka, Bernd Kaufmann, Renate Kostrewa, and Joerg Hayer (1997). "The world's most spectacular carbonate mud mounds (Middle Devonian, Algerian Sahara)." In: *Journal of Sedimentary Research* 67, pp. 424–436.

Wicaksono, Adhityo, Saifullah Hidayat, Bambang Retnoaji, Adolfo Rivero-Müller, and Parvez Alam (Dec. 2018). "A mechanical piston action may assist pelvic-pectoral fin antagonism in tree-climbing fish." In: *Journal of the Marine Biological Association of the United Kingdom*. Vol. 98. 8. Cambridge University Press, pp. 2121–2131. DOI: 10.1017/S0025315417001722.

Wilhelm, Benjamin C., Trina Y. Du, Emily M. Standen, and Hans C.E. Larsson (June 2015). "Polypterus and the evolution of fish pectoral musculature." In: *Journal of Anatomy* 226.6, pp. 511–522. ISSN: 14697580. DOI: 10.1111/joa.12302.

Winter, Amos G., Robin L.H. Deits, and A. E. Hosoi (June 2012). "Localized fluidization burrowing mechanics of Ensis directus." In: *Journal of Experimental Biology* 215.12, pp. 2072–2080. ISSN: 00220949. DOI: 10.1242/jeb.058172.

Wright, Cornell, Aaron Johnson, Aaron Peck, Zachary Mccord, Allison Naaktgeboren, Philip Gianfortoni, Manuel Gonzalez-Rivero, Ross Hatton, and Howie Choset (2007). "Design of a Modular Snake Robot." In: *IEEE/RSJ International Conference on Intelligent Robots and Systems*, pp. 2609–2614. DOI: 10.1109/IROS.2007.4399617.

Wu, X. Alice, Tae Myung Huh, Aaron Sabin, Srinivasan A. Suresh, and Mark R. Cutkosky (2019). "Tactile Sensing and Terrain-Based Gait Control for Small Legged Robots." In: *IEEE Transactions on Robotics* 36.1, pp. 15–27. ISSN: 19410468. DOI: 10.1109/TRO.2019.2935336.

Wu, Xiaodong and Shugen Ma (2011). "Development of a Sensor-driven Snake-like Robot SR -I." In: *IEEE International Conference on Information and Automation*, pp. 157–162.

Yao, Guo, Liang Xu, Xiaowen Cheng, Yangyang Li, Xin Huang, Wei Guo, Shaoyu Liu, Zhong Lin Wang, and Hao Wu (2020). "Bioinspired Triboelectric Nanogenerators as

Self-Powered Electronic Skin for Robotic Tactile Sensing." In: *Advanced Functional Materials* 30.6, p. 1907312. ISSN: 16163028. DOI: 10.1002/adfm.201907312.

Yeaton, Isaac J., Shane D. Ross, Grant A. Baumgardner, and John J. Socha (Sept. 2020). "Undulation enables gliding in flying snakes." In: *Nature Physics* 16.9, pp. 974–982. ISSN: 17452481. DOI: 10.1038/s41567-020-0935-4.

Zhang, Shiwu, Youcheng Zhou, Min Xu, Xu Liang, Jiming Liu, and Jie Yang (June 2016). "AmphiHex-I: Locomotory Performance in Amphibious Environments with Specially Designed Transformable Flipper Legs." In: *IEEE/ASME Transactions on Mechatronics* 21.3, pp. 1720–1731. ISSN: 10834435. DOI: 10.1109/TMECH.2015.2490074.

Zhang, Tingnan and Daniel I. Goldman (Oct. 2014). "The effectiveness of resistive force theory in granular locomotion." In: *Physics of Fluids* 26.10. ISSN: 10897666. DOI: 10.1063/1.4898629.

Zhu, Miaomiao, Mengna Lou, Ibrahim Abdalla, Jianyong Yu, Zhaoling Li, and Bin Ding (2020). "Highly shape adaptive fiber based electronic skin for sensitive joint motion monitoring and tactile sensing." In: *Nano Energy* 69, p. 104429. ISSN: 22112855. DOI: 10.1016/j.nanoen.2019.104429. URL: https://doi.org/10.1016/j.nanoen.2019.104429.

Vita

Divya Ramesh was born in Madurai, Tamil Nadu, India on 22nd June 1995, with a twin sister Rachita Ramesh, to Dr. Savithri Ramesh and Dr. Ramesh Ardhanari. She received her B.Tech degree in Electronics and Communication Engineering from VIT University, Vellore, India in 2017. She then received her MSE degree in Electrical Engineering from University of Pennsylvania, Philadelphia, USA in 2019. She started pursuing her Ph.D. degree in Mechanical Engineering from Johns Hopkins University in 2019 under the supervision of Prof. Chen Li. Her research is focused on studying and understanding animal and robot locomotion on 3-D complex terrain and wet flowable substrates. During her doctoral degree program, she received her MSE degree in Robotics in 2024. She has published in *IEEE RA-L* (presented at ICRA 2020) and presented at *ICRA* 2022. She was shortlisted for the Best Student Paper finalist (Division of Comparative Biomechanics) at the SICB Annual Meeting in 2023.